LANGLEY GRANT
IN-32-CR
93198
P-238

OSU

The Ohio State University

ANALYSIS AND MEASUREMENT OF ELECTROMAGNETIC SCATTERING

BY PYRAMIDAL AND WEDGE ABSORBERS

By

B.T. DeWitt
W.D. Burnside

The Ohio State University

ElectroScience Laboratory

Department of Electrical Engineering
Columbus, Ohio   43212

NOTICES

When Government drawings, specifications, or other data are used for any purpose other than in connection with a definitely related Government procurement operation, the United States Government thereby incurs no responsibility nor any obligation whatsoever, and the fact that the Government may have formulated, furnished, or in any way supplied the said drawings, specifications, or other data, is not to be regarded by implication or otherwise as in any manner licensing the holder or any other person or corporation, or conveying any rights or permission to manufacture, use, or sell any patented invention that may in any way be related thereto.

50272-101

REPORT DOCUMENTATION PAGE	1. REPORT NO.	2.	3. Recipient's Accession No.
4. Title and Subtitle			5. Report Date
ANALYSIS AND MEASUREMENT OF ELECTROMAGNETIC SCATTERING BY PYRAMIDAL AND WEDGE ABSORBERS			March 1986
			6.
7. Author(s)			8. Performing Organization Rept. No.
B.T. DeWitt, W.D. Burnside			716148-10
9. Performing Organization Name and Address			10. Project/Task/Work Unit No.
The Ohio State University ElectroScience Laboratory Department of Electrical Engineering 1320 Kinnear Road Columbus, Ohio 43212			11. Contract(C) or Grant(G) No. (C) (G) NSG 1613
12. Sponsoring Organization Name and Address			13. Type of Report & Period Covered
National Aeronautics and Space Administration Langley Research Center Hampton, Virginia 23665			Technical
			14.

15. Supplementary Notes

16. Abstract (Limit: 200 words)

By modifying the reflection coefficients in the Uniform Geometrical Theory of Diffraction coefficients a solution that approximates the scattering from a dielectric wedge is found. This solution agrees closely with the exact solution of Rawlins which is only valid for a few minor cases. This modification is then applied to the corner diffraction coefficient and combined with an equivalent current and Geometrical Optics solutions to model scattering from pyramid and wedge absorbers.

Measured results from 12" pyramid absorber from 2 to 18 GHz are compared to calculations assuming the returns add incoherently and assuming the returns add coherently. The measured results tend to be between the two curves. The pyramid calculated results are also compared to bistatic measurements. In the nose-on regions, all the terms are needed while, near grazing incidence, the tip diffraction dominates the return. Measured results from 8" wedge absorber is also compared to calculations with the return being dominated by the wedge diffraction.

The procedures for measuring and specifying absorber performance are discussed and calibration equations are derived to calculate a reflection coefficient or a reflectivity using a reference sphere. The absorbers studied tend to act highly dispersive, so specifying a reflectivity is preferred to specifying a reflection coefficient.

Shaping changes to the present absorber designs are introduced to improve performance based on both high and low frequency analysis. The change involves making the tips more pointed, curving the sides of the pyramid to break up the reflected fields, and making the base angle smaller. These changes have an overall effect of smoothing the transition between free space and the absorber material. Some prototypes were built and tested.

17. Document Analysis a. Descriptors

b. Identifiers/Open-Ended Terms

c. COSATI Field/Group

18. Availability Statement	19. Security Class (This Report)	21. No. of Pages
	Unclassified	233
	20. Security Class (This Page)	22. Price
	Unclassified	

TABLE OF CONTENTS

LIST OF TABLES

v

LIST OF FIGURES

x

CHAPTER I

INTRODUCTION

Work on free space absorbers began during World War II as radar became more important. Both Germany and the United States had projects which put absorbers in field operations. The German project was code named "Schornsteinfeger," which dealt with camouflaging submarine snorkels and periscopes. The US project was primarily directed towards improveing radar performance by reducing interfering reflections from nearby objects. An interesting discussion of this early work is presented by Emerson [1].

The late 40's was dominated by work on broad-band absorbers rather than the resonant absorber used in the war. The first anechoic chambers were not built until the early 50's as commercial absorber made of animal hair became available. The 60's marked the introduction of pyramid absorbers and better materials giving greatly improved performance over animal hair absorbers. During the 70's, little progress was made in absorber technology compared to the radar hardware advances. Today, electromagnetic absorbers and anechoic chambers are in widespread use throughout the world for radiation and scattering measurements. In fact, a wide range of absorbers for different frequency ranges and applications are readily available from several commerical sources.

Foam pyramid absorbers are mainly used in anechoic chambers today because they provide the best scattering performance for a wide range of incident angles and frequencies. However, with an increasing need to make more accurate measurements at lower signal levels a better understanding of absorber scattering is desirable. Specifically, in a compact range where bistatic and monstatic scattering off the side walls, ceiling, and floor is of interest. These terms cannot normally be time gated out unless the room is very large which makes the building expense unduly extravagant.

This report develops an high frequency analysis of scattering by free space absorber pyramids and wedges. The analysis is based on the Uniform Geometrical Theory of Diffraction (UTD) [2]. Normally, high frequency solutions are difficult to apply to dielectric materials because of ray splitting at boundaries and the lack of asymptotic solutions for the dielectric wedge. The dielectric slab has been studied by Burnside and Burgener [3] and Rojas-Teran [4]. Fortunately, the absorber material is high loss limiting the transmitted rays making a high frequency solution possible using presently available theoretical solutions.

The basic building block for the absorber scattering is based on the solution of Burnside and Burgener for dielectric plates [3]. Background material for this is presented in Chapter II. The construction of a tip diffraction model using corner diffraction is discussed and a UTD method of calculating scattering from a dielectric wedge is presented and compared to an exact solution for specific cases.

2

The method of modeling absorber pyramids and wedges using the equations from Chapter II is given in Chapter III. The chapter starts with the electrical properties of the absorber material and then studies the different mechanisms that contribute to the absorber scattering.

Chapter IV presents the results of measurements made on the absorbers and compares them with calculations using the models of Chapter III. Measurements of both pyramids and wedges are compared with calculated results.

The models presented can be used to predict absorber effects in range measurements. Using the predictions, the room shape or type of absorber could be changed to in order to improve performance.

Chapter V covers measurement procedures for free space absorbers and lists the problems encountered with measuring reflectivity and effective radar cross section. Derivations of the calibration equations for the suggested measurements are given.

Some changes in absorber shaping are presented in Chapter VI based on both low and high frequency analysis. The measured effects of the alternate shaping are shown and compared with standard pyramid absorber.

This report concludes with Chapter VII which summarizes the results of this work and gives conclusions made as a result of this study.

CHAPTER II

THEORETICAL BACKGROUND

A. INTRODUCTION

This chapter presents the basic equations used to calculate the scattering from a dielectric wedge and corner. First, the two-dimensional edge diffraction problem will be discussed leading to the three-dimensional scattering by a conducting wedge. Solutions for diffraction by a dielectric wedge are less developed than for the conducting wedge; nevertheless, some different solutions are reviewed in terms of their applicability to the absorber problem.

B. DIFFRACTION BY A WEDGE

The complete UTD field solutions for an electromagnetic line source illuminating a infinite wedge as shown in Figure 2.1 is composed of a direct signal from the source to the receiver, a reflected field from the wedge face or faces, plus a diffracted field which eminates from the edge. The direct plus reflected field terms constitute the classical geometrical optics (GO) solution. Keller showed that the discontinuities at the incident and reflected shadow boundaries of the GO solution must be compensated for by a set of edge diffraction terms.

Kouyoumjian and Pathak [2] found that the continuity of the total field across the shadow boundaries could be used to develop UTD solutions.

Referring to Figure 2.1, the following expressions are for an electric or magnetic line source located at (ρ', ϕ') with respect to the edge and a receiver located at (ρ, ϕ). The total UTD solution for this problem is given by

$$u^{TOTAL} = u^{INC} + u^{REF} + u^{DIF} \tag{2.1}$$

where u represents an electric scalar field for the electric line source case and a magnetic scalar field for the magnetic line source case. The incident field is given by

$$u^{INC} = \begin{cases} K \dfrac{e^{-jk\rho_i}}{\sqrt{\rho_i}} & \text{in regions I and II, and} \\ \\ 0 & \text{in region III} \end{cases} \tag{2.2}$$

where ρ_i is the distance from the line source to the receiver, and K is a complex constant. The reflected field is given by

$$u^{REF} = \begin{cases} \pm K \dfrac{e^{-jk\rho_r}}{\sqrt{\rho_r}} & \text{in region I , and} \\ \\ 0 & \text{in regions II and III} \end{cases} \tag{2.3}$$

where ρ_r is the distance from the image of the line source to the receiver. The + sign is used for the magnetic line source case and the - sign for the electric line source which are used to satisfy the
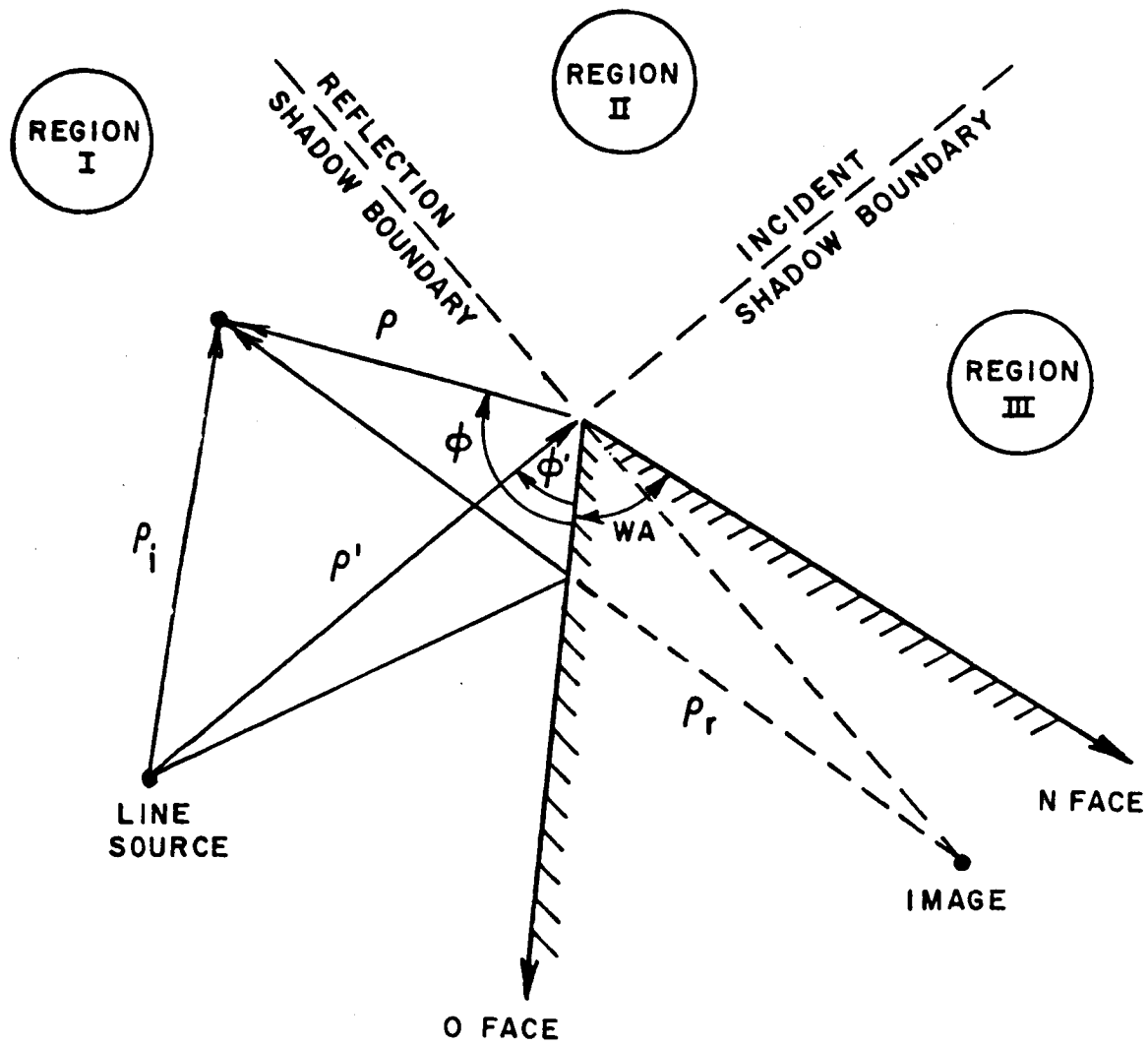
Figure 2.1. A line source radiating in the presence of a wedge. Note the wedge angle is WA=(2-n)π in the diffraction solution.

boundary conditions associated with perfectly conducting ground planes making up the wedge faces. The diffracted field is given by

$$u^{DIFF} = \left[D(\frac{\rho'\rho}{\rho'+\rho} , \phi-\phi', n) \pm D(\frac{\rho\rho'}{\rho'+\rho} , \phi+\phi', n) \right] K \frac{e^{-jk\rho'}}{\sqrt{\rho'}} \frac{e^{-jk\rho}}{\sqrt{\rho}}$$

(2.4)

where the + sign is used for the magnetic line source case and the - sign for the electric line source. The $D(\frac{\rho'\rho}{\rho'+\rho} , \phi-\phi', n)$ term is associated with the discontinuity at the incident shadow boundary; whereas, the $D(\frac{\rho'\rho}{\rho'+\rho} , \phi+\phi', n)$ term is associated with the reflection shadow boundary. Note, also, that the ± signs associated with the reflection coefficient are found in the diffraction solution multiplying the $\phi+\phi'$ term. The angles ϕ and ϕ' are measured from the "0 face" of the wedge.

To solve a three-dimensional wedge diffraction problem, the same procedure is used. The total solution is given by the sum of the incident, reflected, and diffracted fields. The three-dimensional problem is different in that spherical waves are being considered instead of cylindrical waves, and the field can be arbitrarily polarized instead of merely being a simple electric or magnetic line source.

To simplify the reflected field calculation, the incident field is split into perpendicular (⊥) and parallel (∥) components. The parallel component is defined as that part of the incident field parallel to the plane defined by the incident ray direction ($\hat{I}$) and the normal to the plate ($\hat{n}$). The perpendicular component is that part of the incident

7

field perpendicular to the plane defined by $\hat{I}$ and $\hat{n}$ as shown in Figure 2.2. The $E_\perp^i$ component corresponds to the 2D case of an electric line source, and $E_\parallel^i$ corresponds to the 2D case of a magnetic line source. The reflected field can now be written as

$$
\begin{bmatrix} E_\parallel^r \\ E_\perp^r \end{bmatrix} = \begin{bmatrix} R_{(M)} & 0 \\ 0 & R_{(E)} \end{bmatrix} \begin{bmatrix} E_\parallel^i \\ E_\perp^i \end{bmatrix} \sqrt{\frac{\rho_1^r \rho_2^r}{(\rho_1^r+s)(\rho_2^r+s)}} \; e^{-jks}
\tag{2.5}
$$

where ρ_1^r and ρ_2^r are the radii of curvature of the reflected wavefront.

The diffraction matrix is diagonal when the incident field is expressed by components parallel and perpendicular to the plane containing the incident ray and the diffracted edge, and the diffracted field is expressed by components parallel and perpendicular to the plane containing the diffracted ray and the edge.

So, to simplify the diffracted field calculation, the following unit vectors are introduced

$$
\hat{\phi}' = -\hat{Z} \times \hat{I}
\tag{2.6}
$$

$$
\hat{\beta}_0' = \hat{\phi}' \times \hat{I}
\tag{2.7}
$$

$$
\hat{\phi} = \hat{Z} \times \hat{D}
\tag{2.8}
$$

and

$$
\hat{\beta}_0 = \hat{\phi} \times \hat{D} \qquad .
\tag{2.9}
$$

The geometry for the three-dimensional wedge diffraction problem is shown in Figure 2.3. The point of diffraction (Q_E) is located where

8
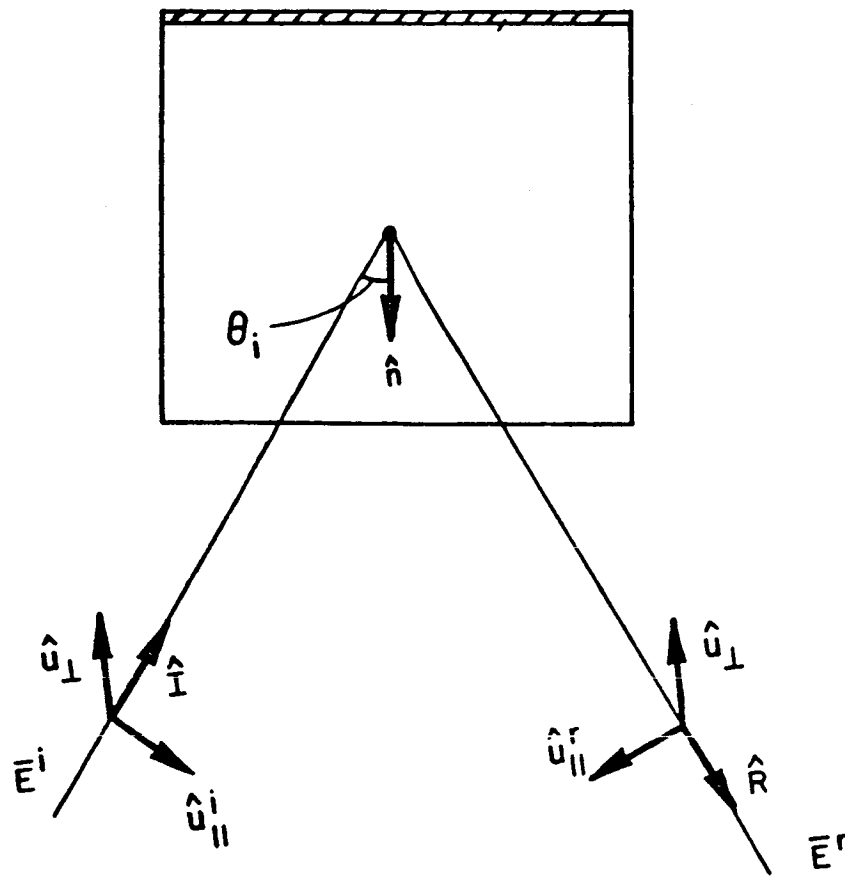
Figure 2.2. Coordinate system used for 3D reflection and diffraction.

9
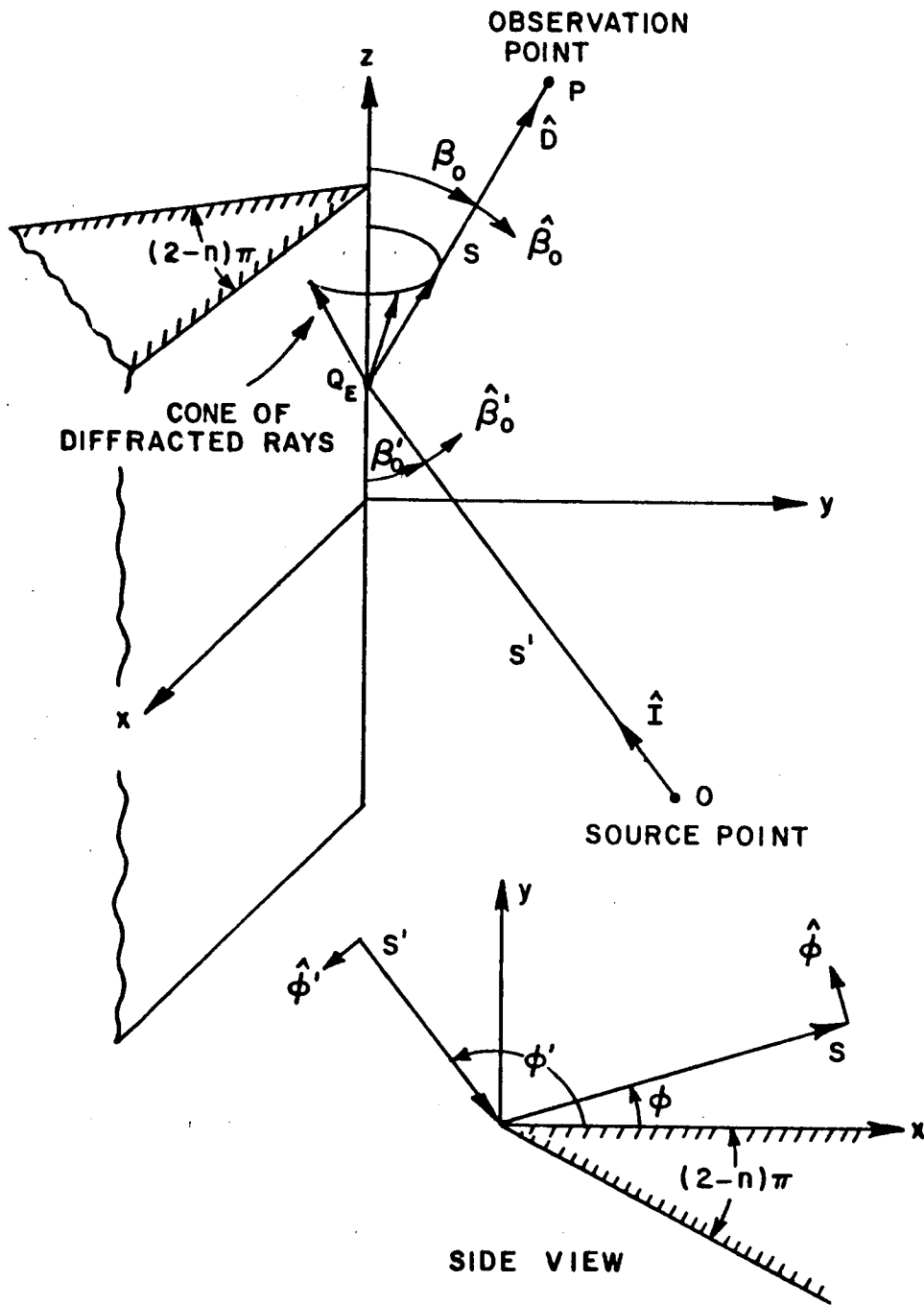
Figure 2.3. Geometry for three-dimensional wedge diffraction problem.

β'_0 equals β_0 (see Figure 2.3). The diffracted field solution is given by

$$\begin{bmatrix} E^d_{\beta_0} \\ E^d_\phi \end{bmatrix} = \begin{bmatrix} -D_s & 0 \\ 0 & -D_h \end{bmatrix} \cdot \begin{bmatrix} E^i_{\beta'_0} \\ E^i_{\phi'} \end{bmatrix} \sqrt{\frac{s'}{s(s+s')}} \; e^{-jks} \qquad (2.10)$$

where

$$D_{s,h}(L,\phi,\phi',\beta_0) = \frac{-e^{-j\pi/4}}{2n\sqrt{2\pi k}\;\sin\beta_0} \left[\cot\left(\frac{\pi+\beta^-}{2n}\right) F(kLa^+(\beta^-)) \right.$$

$$\left. + \cot\left(\frac{\pi-\beta^-}{2n}\right) F(kLa^-(\beta^-)) \mp \left[\cot\left(\frac{\pi+\beta^+}{2n}\right) F(kLa^+(\beta^+)) \right. \right.$$

$$\left. \left. + \cot\left(\frac{\pi-\beta^+}{2n}\right) F(kLa^-(\beta^+)) \right] \right] \qquad (2.11)$$

with

$$F(x) = 2j \left|\sqrt{x}\right| e^{jx} \int_{\left|\sqrt{x}\right|}^\infty e^{-j\tau^2} d\tau \quad , \text{ and} \qquad (2.12)$$

$$a^\pm(\beta) = 2\cos^2\left(\frac{2n\pi N^\pm - (\beta)}{2}\right) \quad . \qquad (2.13)$$

Where $N^\pm$ satisfy the equations:

$$N^+ = \text{INT}\left[\frac{1}{2n} + \frac{\beta}{2\pi n} + .5\right] \qquad (2.14)$$

and

$$N^- = \text{INT}\left[-\frac{1}{2n} + \frac{\beta}{2\pi n} + .5\right] \qquad (2.15)$$

11

with

$$\beta = \beta^{\pm} = \phi \pm \phi' \qquad (2.16)$$

and INT [ ] being the greatest integer value. The magnitude and phase of the transition function $F(x)$ are shown in Figure 2.4. When x is small, $F(x)$ is given by

$$F(x) \sim \left[\sqrt{\pi x} - 2x e^{j\pi/4} - \frac{2}{3} x^2 e^{-j\pi/4} \right] e^{j(\pi/4 + x)} \qquad (2.17)$$

and when x is large one finds that

$$F(x) \sim 1 + \frac{j}{2x} - \frac{3}{4} \frac{1}{x^2} - j \frac{15}{8} \frac{1}{x^3} + \frac{75}{16} \frac{1}{x^4} \quad . \qquad (2.18)$$

If n=2, the wedge becomes a half plane and the form for $D_{s,h}$ reduces such that

$$D_{s,h}(L,\phi,\phi',\beta_0) = \frac{-e^{-j\pi/4}}{2\sqrt{2\pi k} \sin\beta_0} \left[\frac{F(kLa(\beta^-))}{\cos\beta^-/2} \mp \frac{F(kLa(\beta^+))}{\cos\beta^+/2} \right] \qquad (2.19)$$

and

$$L = \frac{ss'}{s+s'} \sin^2\beta_0 \quad . \qquad (2.20)$$

In Equation (2.11), the 2nd and 4th terms are associated with the wedge face along the x axis (Figure 2.3) and the 1st and 3rd with the face at $\phi = n\pi$.
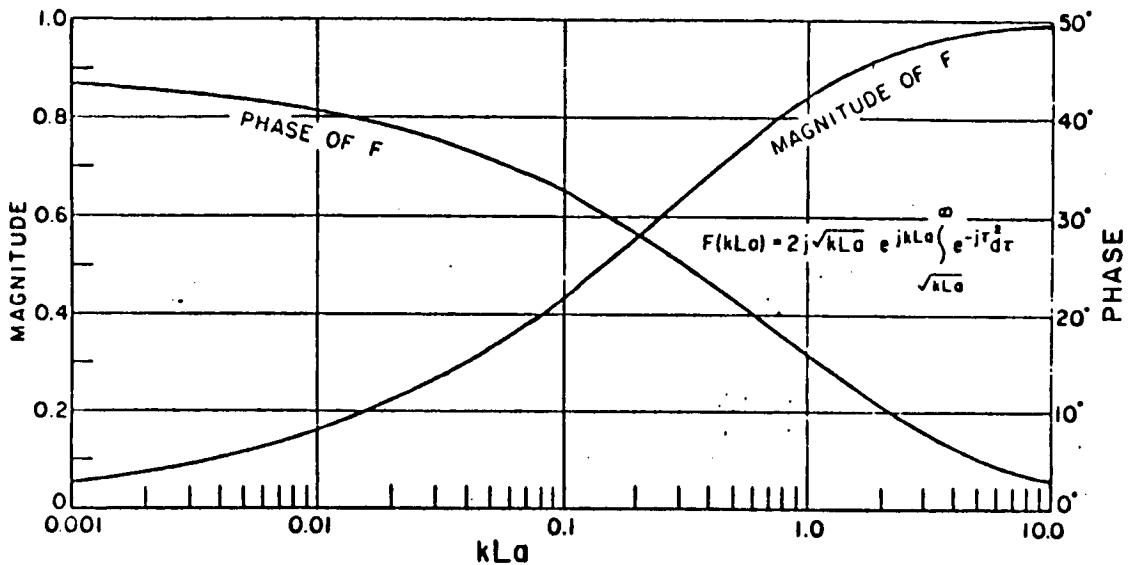
Figure 2.4. Transition function.

C. EQUIVALENT EDGE CURRENTS

The Equivalent Edge Current concept is a method introduced by Ryan and Peters [5] to calculate the field in regions where the edge diffraction solution fails which happens when the edge rays are not present or they converge to a line or point, i.e., a caustic.

Equivalent edge currents are obtained by finding a current that gives the same fields at the observation point as is diffracted to that point by an infinite straight edge which is illustrated in Figure 2.5. So, an Equivalent edge current is a hypothetical line source whose

13
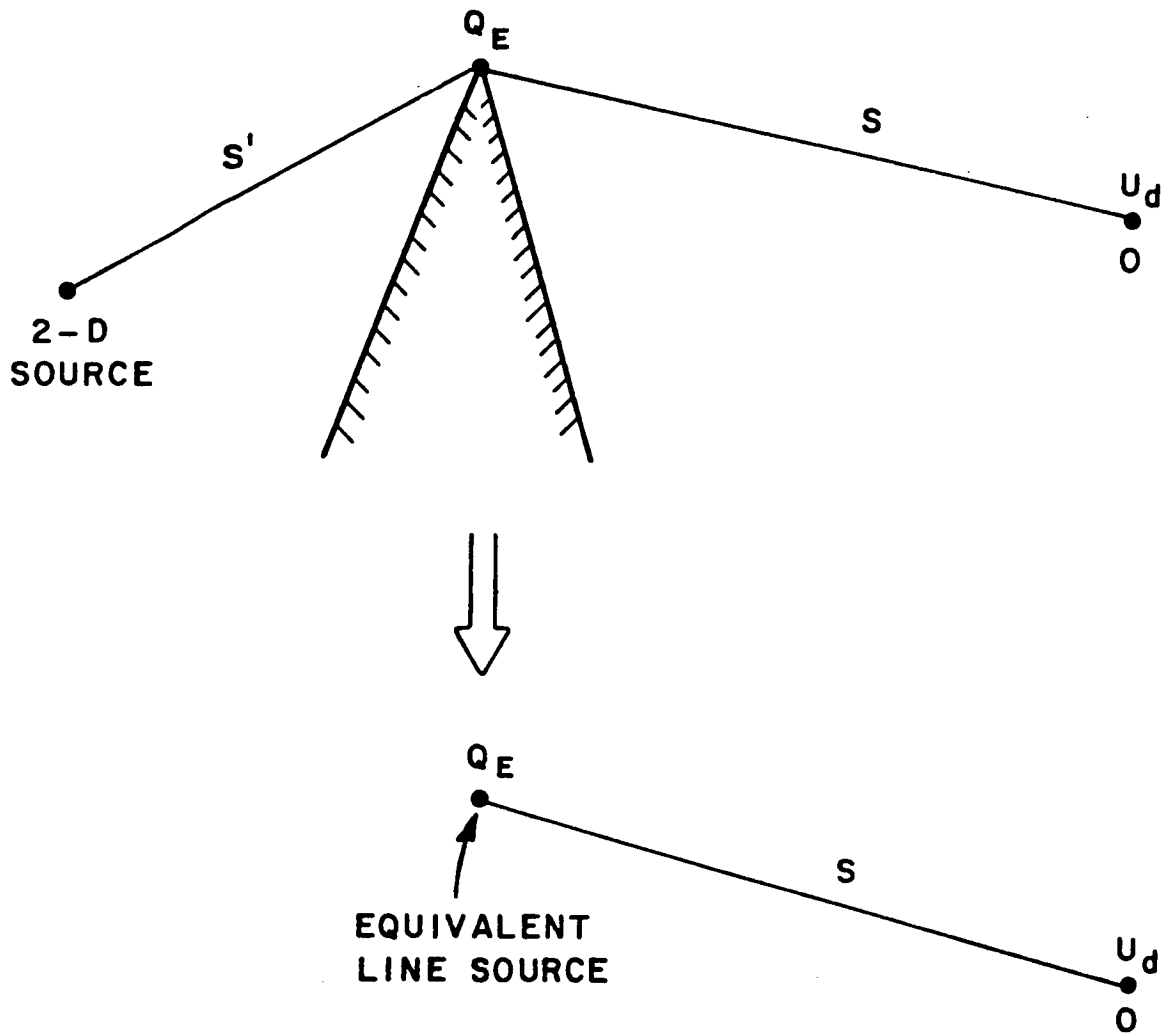
Figure 2.5.   Illustration of equivalent edge current concept.

radiation is calculated using conventional potential theory. One limitation to this method is that locally the edge diffracted fields must have the same cylindrical wave behavior as the infinite line source, namely $\frac{e^{-jks}}{\sqrt{s}}$, where s is the distance from the source to the observation point.

The expressions for the equivalent magnetic and electric line sources are given as follows:

$$
\begin{bmatrix} I^m \\ I^e \end{bmatrix} = \frac{j2}{\begin{bmatrix} Y_0 \\ Z_0 \end{bmatrix} k} \cdot \frac{1}{n} \sin \frac{\pi}{n} \left[\frac{1}{\cos\frac{\pi}{n} - \cos\frac{\phi-\phi'}{n}} \pm \frac{1}{\cos\frac{\pi}{n} - \cos\frac{\phi+\phi'}{n}} \right] \begin{bmatrix} H^i_\| \\ E^i_\| \end{bmatrix} . \tag{2.21}
$$

The parameters, n, ϕ, ϕ', $H^i_\|$, and $E^i_\|$ are defined in the three-dimensional wedge diffraction problem.

Now these currents may be used to evaluate the diffracted fields from a finite edge in the usual formal ways. The vector potential functions are given by

$$
\overline{A} = \frac{1}{4\pi} \int_L \frac{\overline{I^e} e^{-jk|\overline{r}-\overline{r}'|}}{|\overline{r}-\overline{r}'|} \, d\ell' \tag{2.22}
$$

and

$$
\overline{F} = \frac{1}{4\pi} \int_L \frac{\overline{I^m} e^{-jk|\overline{r}-\overline{r}'|}}{|\overline{r}-\overline{r}'|} \, d\ell' \tag{2.23}
$$

where L is the contour of the edge, and of course

$$
\overline{H} = \nabla \times \overline{A} + \frac{1}{j\omega\mu} \nabla \times \nabla \times \overline{F} \tag{2.24}
$$

and

$$\bar{E} = -\nabla \times \bar{F} + \frac{1}{j\omega\epsilon} \nabla \times \nabla \times \bar{A} \quad . \qquad (2.25)$$

The far field can be obtained more directly as

$$\bar{E}^e = -j\omega\mu \, \bar{A}_{trans} \qquad (2.26)$$

and

$$\bar{H}^m = -j\omega\epsilon \, \bar{F}_{trans} \qquad (2.27)$$

where

$\bar{E}^e$ is the electric field from the electric current sources,

$\bar{H}^m$ is the magnetic field from the magnetic current sources, and

H^e and E^m are related to E^e and H^m by the intrinsic impedance of the medium.

Note that the subscript "trans" means the transverse component of the potential function.

D. CORNER DIFFRACTION

The corner diffraction coefficient has been developed by Sitka, Burnside and Chu [5], to calculate the scattered field associated with the termination of a finite length edge. The need for this coefficient can be demonstrated by considering the corner diffraction geometry shown in Figure 2.6. The edge diffraction point Q_E, is located a distance z' from the corner. As the location of the receiver moves in the minus $\hat{z}$
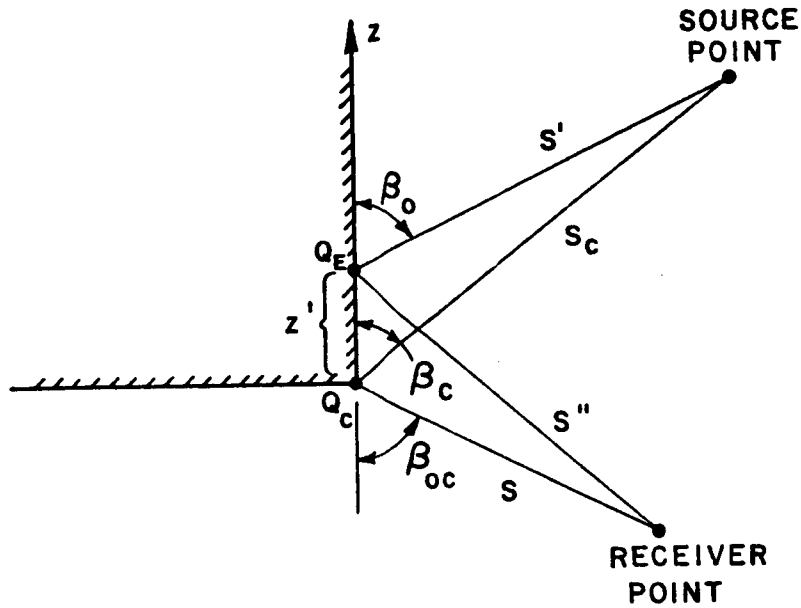
Figure 2.6. Geometry for corner diffraction problem.

direction, the point Q_E moves toward the corner until it falls off the edge in which case no edge diffraction term exists. The corner diffracted field compensates for this discontinuity similar to the way the edge diffracted field compensates for the GO discontinuities.

The corner diffracted fields associated with one corner and one edge in the near field with spherical wave incidence are given by

$$
\begin{vmatrix} E_{\parallel}^c \\ \\ E_{\perp}^c \end{vmatrix} \sim \begin{vmatrix} IZ_0 \\ \\ MY_0 \end{vmatrix} \frac{\sqrt{\sin\beta_c \ \sin\beta_{oc}}}{(\cos\beta_{oc}-\cos\beta_c)} \ F[kL_c a(\pi+\beta_{oc}-\beta_c)] \ \frac{e^{-jks}}{4\pi s} \qquad (2.28)
$$

where

$$\begin{bmatrix} I \\ M \end{bmatrix} = - \begin{bmatrix} E_{\parallel}^i(Q_C) \\ E_{\perp}^i(Q_C) \end{bmatrix} \begin{bmatrix} C_s(Q_E)Y_0 \\ C_h(Q_E)Z_0 \end{bmatrix} \sqrt{\frac{8\pi}{k}} \ e^{-j\pi/4} \qquad (2.29)$$

and

$$C_{s,h}(Q_E) = \frac{-e^{-j\pi/4}}{2\sqrt{2\pi k} \ \sin\beta_0} \left| \frac{F[kLa(\beta^-)]}{\cos\frac{\beta^-}{2}} \left| F\left[\frac{La(\beta^-)/\lambda}{kL_c a(\pi+\beta_{0c}-\beta_c)} \right] \right| \right.$$

$$\mp \frac{F[kLa(\beta^+)]}{\cos\frac{\beta^+}{2}} \left| F\left[\frac{La(\beta^+)/\lambda}{kL_c a(\pi+\beta_{0c}-\beta_c)} \right] \right| \right| . \qquad (2.30)$$

The function $F(x)$ was defined earlier, $a(\beta) = 2\cos^2(\beta/2)$ where
$\beta^{\mp} = \phi \mp \phi'$, and $L = s's'' \sin^2 \beta_0/(s'+s'')$ and $L_c = s_c s/(s_c+s)$ for
spherical wave incidence. The function $C_{s,h}(Q_E)$ is a modified version
of the diffraction coefficient for the half-plane case ($n = 2$). The
modification factor,

$$\left| F\left[\frac{La(\beta)/\lambda}{kL_c a(\pi+\beta_{0c}-\beta_c)} \right] \right| \qquad (2.31)$$

is an empirically derived function that insures that the diffraction
coefficient will not change sign abruptly when it passes through the
shadow boundaries of the edge. There is also a corner diffraction term
associated with the other edge forming the corner and is found in a
similar manner.

18

The corner diffraction coefficient described above is for the corner of a flat plate. When the corner is formed out of a wedge, the corner diffraction coefficient is given by Equations (2.28) and (2.29) with the following modification:

$$
\begin{aligned}
C_{c,h}(Q_E) = \frac{-e^{-j\pi/4}}{2n\sqrt{2\pi k}\,\sin\beta_0} &\left[\cot\left(\frac{\pi+(\beta^-)}{2n}\right)F[kL^{in}a^+(\beta^-)] \cdot \left| F\left[\frac{L^i a^+(\beta^-)/\lambda}{kL_c\quad a(\pi+\beta_{oc}-\beta_c)}\right]\right| \right.\\
&+ \cot\left(\frac{\pi-(\beta^-)}{2n}\right)F[kL^{io}a^-(\beta^-)] \cdot \left| F\left[\frac{L^i a^-(\beta^-)/\lambda}{kL_c\quad a(\pi+\beta_{oc}-\beta_c)}\right]\right| \\
&\mp \left[\cot\left(\frac{\pi+(\beta^+)}{2n}\right)F[kL^{rn}a^+(\beta^+)] \cdot \left| F\left[\frac{L^{rn}a^+(\beta^+)/\lambda}{kL_c\quad a(\pi+\beta_{oc}-\beta_c)}\right]\right| \right. \\
&\left.\left. + \cot\left(\frac{\pi-(\beta^+)}{2n}\right)F[kL^{ro}a^-(\beta^+)] \cdot \left| F\left[\frac{L^{ro}a^-(\beta^+)/\lambda}{kL_c\quad a(\pi+\beta_{oc}-\beta_c)}\right]\right| \right]\right] .
\end{aligned}
$$

$$(2.32)$$

If the corner involves three intersecting edges, as at the corner of a cube, then each of the edges will have a corner diffraction term. The four terms making up Equation (2.32) are associated with the incident and reflection shadow boundaries of the two faces making up the wedge. If one wishes to treat each face of the structure individually, then he can use only the two terms associated with that face. The terms

19

associated with the other face are obtained when that face is considered. Using this approach, one does not have to worry about which edges have already been included in the calculation.

Calculating the diffraction from a tip of a pyramid has been a problem of interest for many years. Unfortunately, an uniform tip diffraction coefficient is still unavailable. An approximate solution, however, can be obtained by using corner diffraction coefficients [7] as described above. The scattering from each edge making up the tip is calculated and then summed with the other edges.

Unfortunately, the present corner diffraction solution has cases where it works much better than others. This occurs because the present solution is heuristically derived from the equivalent current solution. Corner diffraction works well for backscattered fields; however, for some bistatic geometries it becomes discontinuous. An illustration of this was given by Marhefka [8] by considering the backscatter from a 2 wavelength square plate, as shown in the insert of Figure 2.7. The backscattered field is calculated in the principal plane at $\theta=90$ degrees and for conical cuts of $\theta=60$ and 30 degrees with θ polarization. The classic equivalent currents, Michaeli's equivalent currents [9], corner diffraction, and physical theory of diffraction methods are compared. Note that for the principal plane, all the methods produce the same result. For the conical cuts, the methods only differ at levels 35dB below the peak. It is impossible to decide from these first order results which solution is more accurate, since any other methods, such as measurements or moment methods, will contain higher order terms.

20
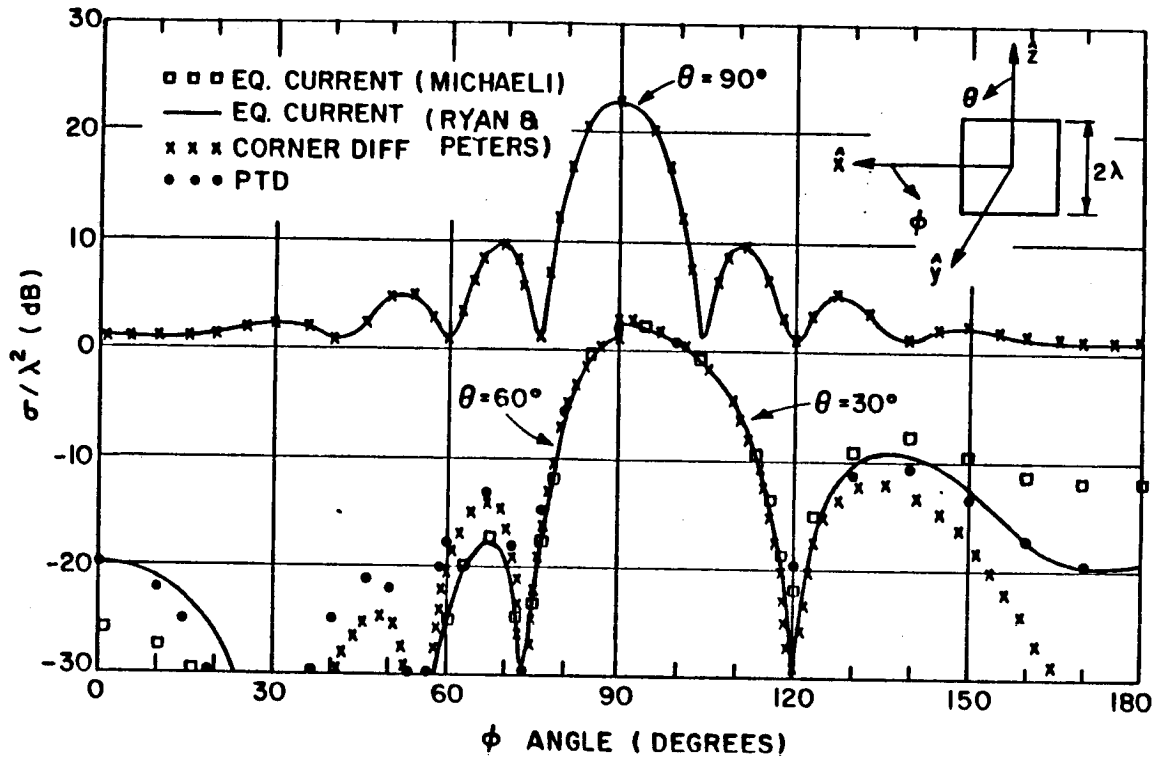
Figure 2.7. Comparison of various methods for the prediction of the
$\hat{\theta}$ polarized backscatter from a plate.

In order to illustrate the bistatic scattering problem the geometry shown in Figure 2.8 is used. Using spherical coordinates, the incident direction is (θ^i=45°, ϕ^i=0°) and the scattered direction is (θ^s,ϕ^s=122°). A pattern is taken letting θ^s sweep from 0 to 360 degrees. The moment method results [10] are shown in Figure 2.9. The results are given in dB with respect to a square wavelength and are shown on a polar plot with 10 dB/division and the outer circle being the peak of the moment method results for that polarization. The results using the classical equivalent currents, corner diffraction, and physical theory of diffraction are shown in Figures 2.10, 2.11, and 2.12, respectively. Each plot is normalized to the same peak as the corresponding moment method results. The nulls in Figures 2.9a and 2.9c at θ=90 and 270 degrees are from higher order effects not included in the asymptotic solutions. Note that the corner diffraction and equivalent current solutions have problems at angles of θ equal to around 60 and 120 degrees. These are the false shadow boundary locations, that is, the angles corresponding to where $\phi+\phi'$ and $\phi-\phi'$ are equal to π. Since the pattern is not in the plane of incidence, however, there should not be a real shadow boundary. The PTD solution does not exhibit the discontinuities that the corner diffraction solution does.

In summary, the various methods agree closely in principal plane calculations; however, their differences become more apparent in the off principal planes. The discontinuities exhibited by the corner diffraction coefficient also occur in the absorber solution in Chapter III.
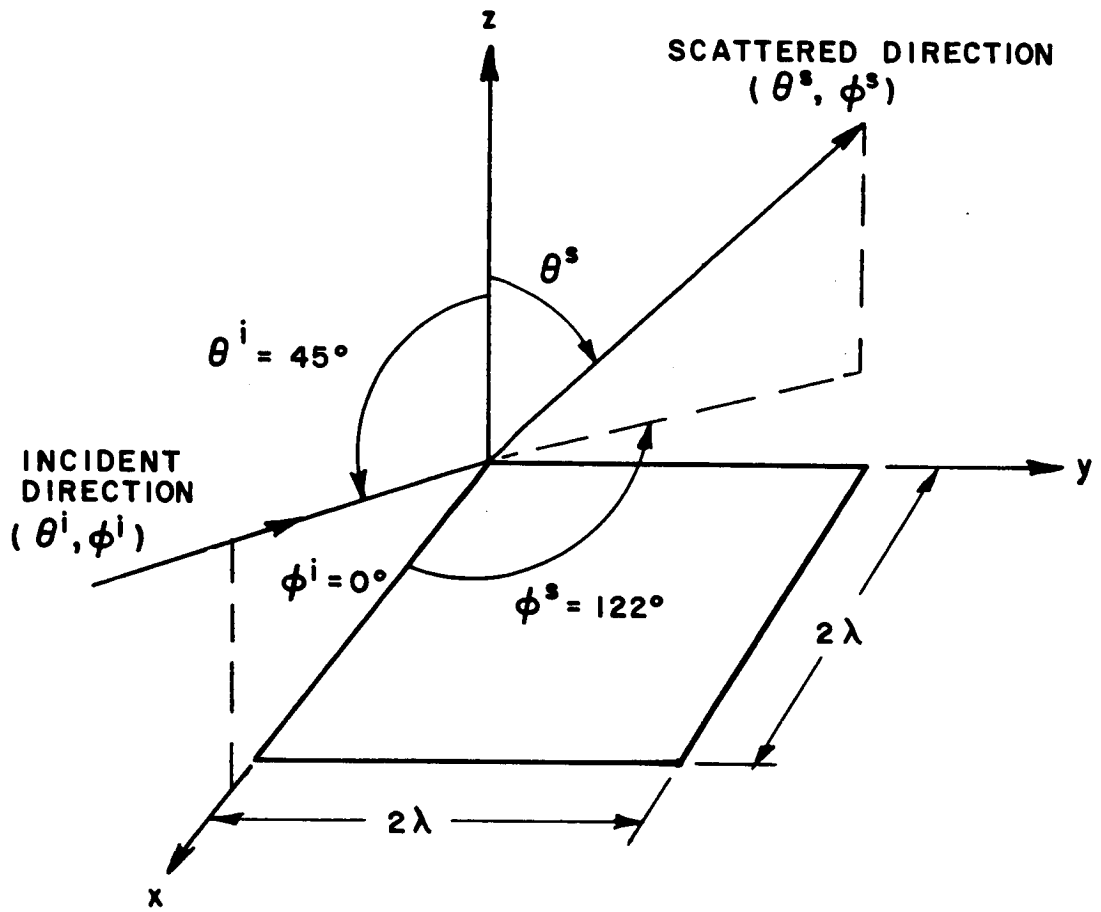
Figure 2.8. Geometry for bistatic scattering from a plate.
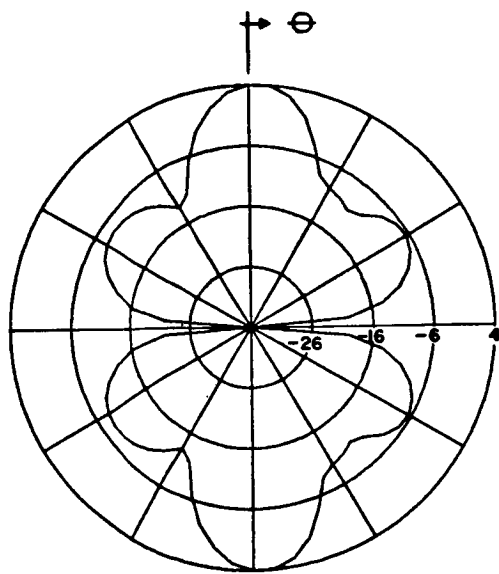
a.) theta-theta
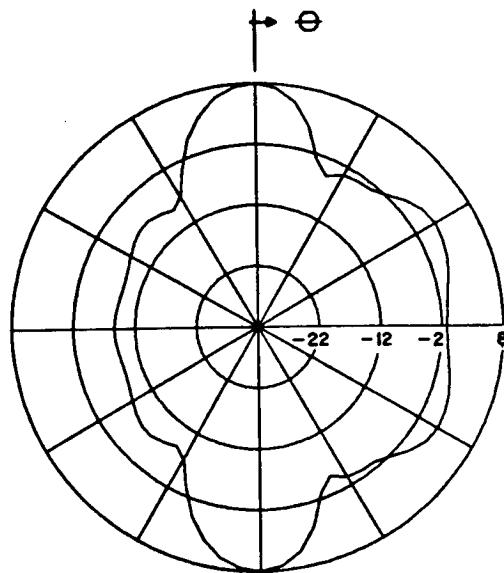
b.) theta-phi
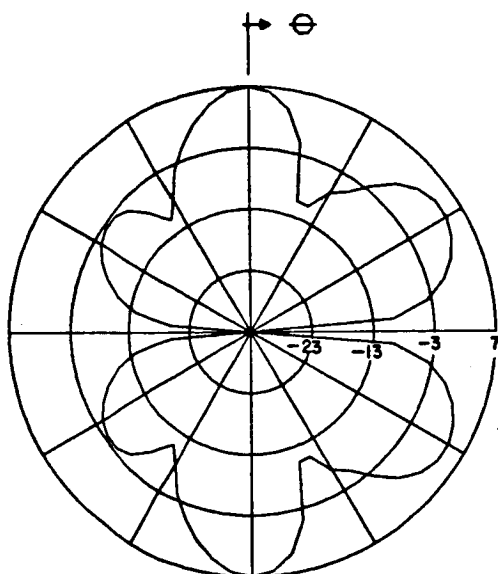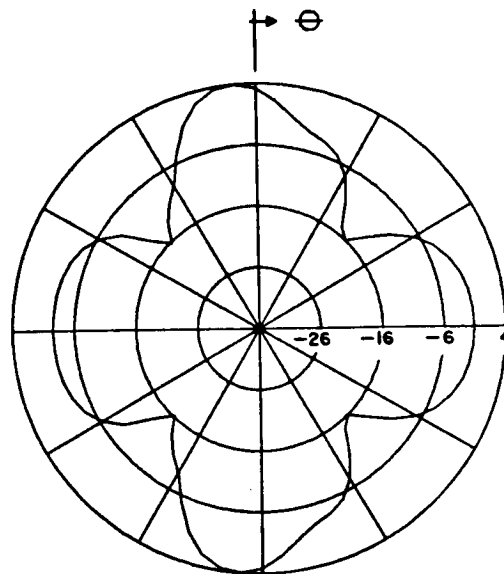
c.) phi-theta

d.) phi-phi

Figure 2.9.   Bistatic scattering from a plate using the method of moments.   (Incident polarization-scattered polarization)

24
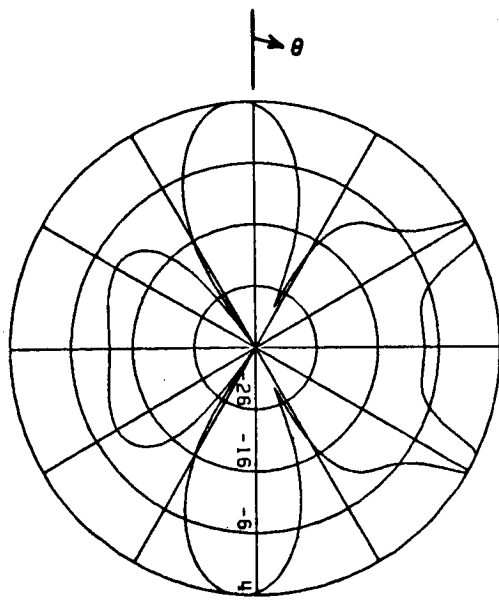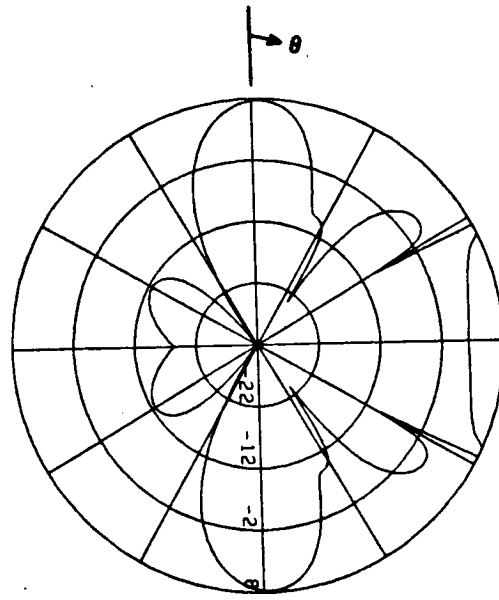
a.) theta-theta
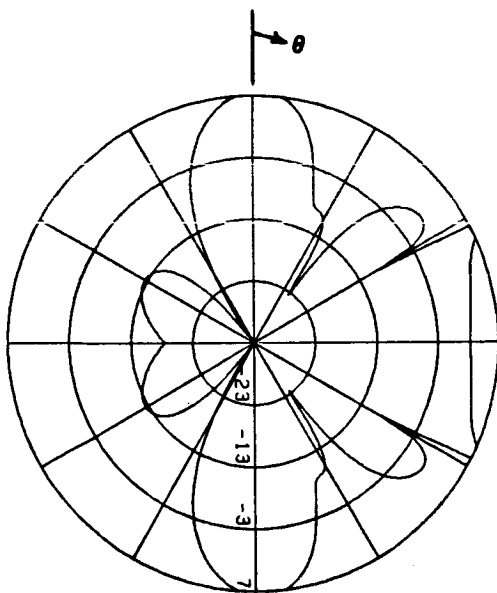
b.) theta-phi
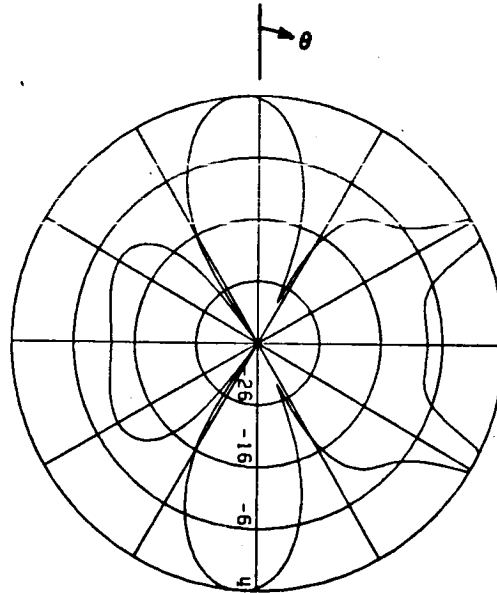
c.) phi-theta

d.) phi-phi

Figure 2.10. Bistatic scattering from a plate using the classical equivalent currents of Ryan and Peters. (Incident polarization-scattered polarization)
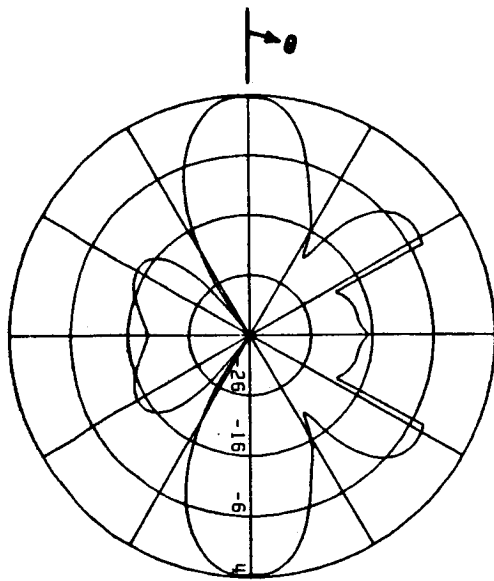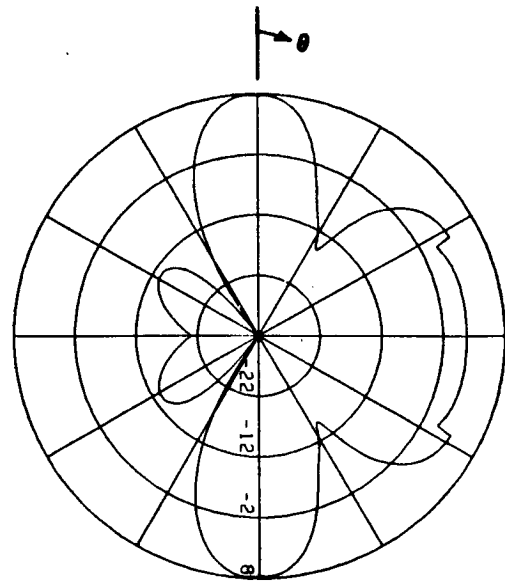
a.) theta-theta
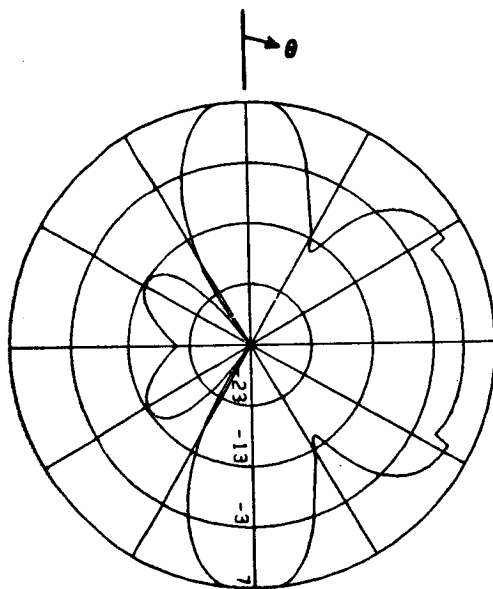
b.) theta-phi
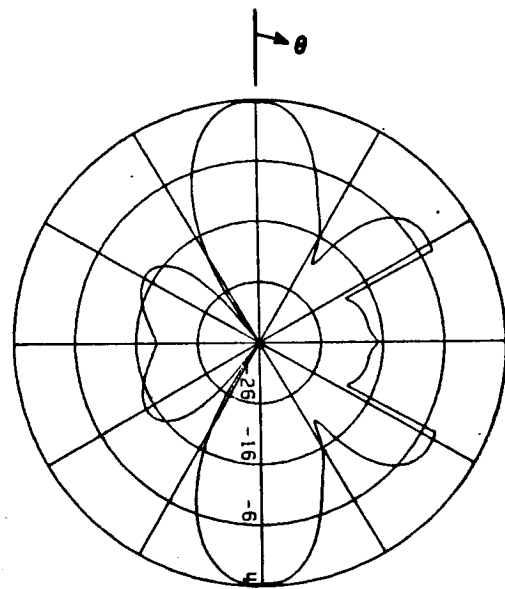
c.) phi-theta

d.) phi-phi

Figure 2.11. Bistatic scattering from a plate using the corner
diffraction method. (Incident polarization-scattered
polarization)
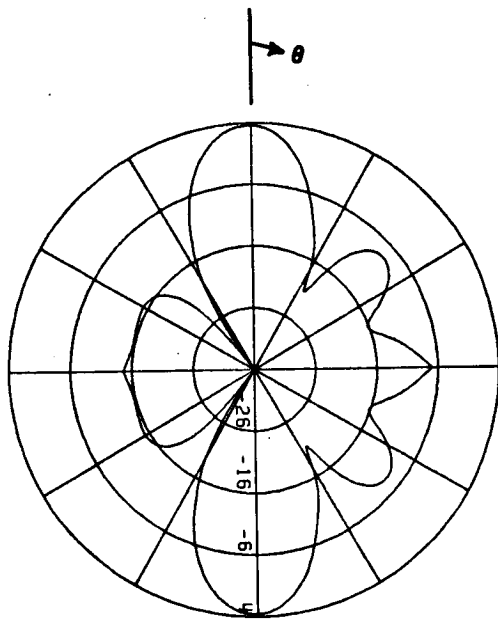
a.) theta-theta
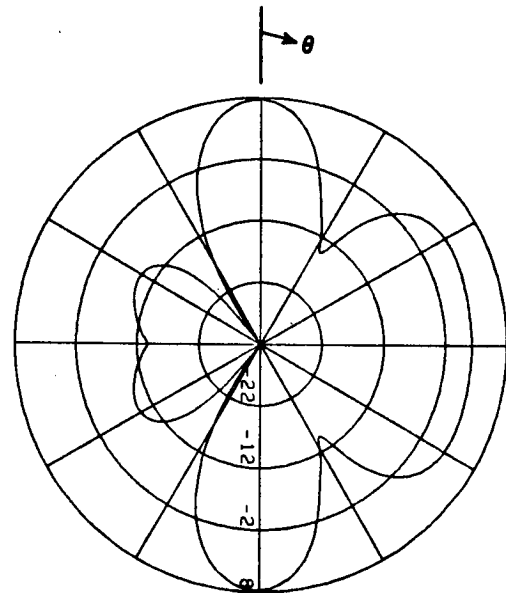
b.) theta-phi
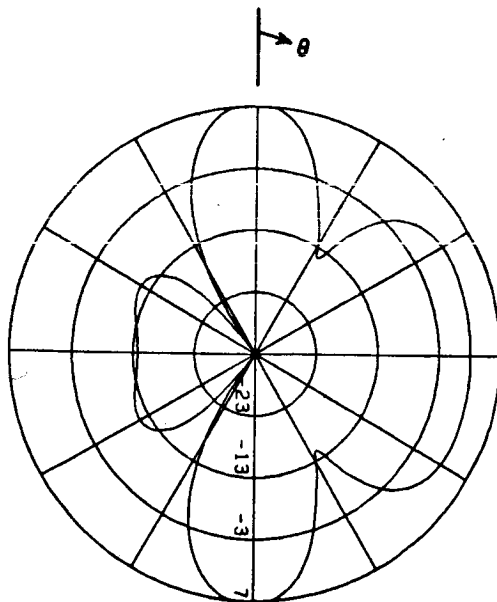
c.) phi-theta
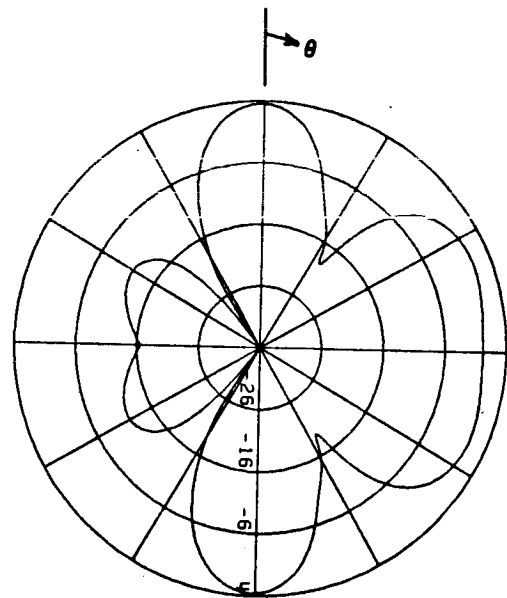
d.) phi-phi

Figure 2.12. Bistatic scattering from a plate using the physical theory of diffraction. (Incident polarization-scattered polarization)

E. REFLECTION AND TRANSMISSION FROM A DIELECTRIC INTERFACE

Consider a plane wave obliquely incident on a dielectric interface with $\mu_1 = \mu_2$ and $\varepsilon_1 \neq \varepsilon_2$ as shown in Figure 2.13. The reflection and transmission coefficients are found by enforcing the boundary conditions for the tangential electric and magnetic fields at the surface. For perpendicular polarization (E-field perpendicular to the z-y plane) one obtains the following expressions:

$$R_\perp = \frac{\cos\theta^i - (\varepsilon_2/\varepsilon_1 - \sin^2\theta^i)^{1/2}}{\cos\theta^i + (\varepsilon_2/\varepsilon_1 - \sin^2\theta^i)^{1/2}} \quad , \quad \text{and} \quad (2.33)$$

$$T_\perp = 1 + R_\perp \quad . \quad (2.34)$$

The expressions for the other polarization (H-field perpendicular to the z-y plane) are

$$R_\| = \frac{(\varepsilon_2/\varepsilon_1)\cos\theta^i - (\varepsilon_2/\varepsilon_1 - \sin^2\theta^i)^{1/2}}{(\varepsilon_2/\varepsilon_1)\cos\theta^i + (\varepsilon_2/\varepsilon_1 - \sin^2\theta^i)^{1/2}} \quad , \quad \text{and} \quad (2.35)$$

$$T_\| = 1 + R_\| \quad . \quad (2.36)$$

For a lossless dielectric all the angles and coefficients are real, however, when ε becomes complex both θ_t and the coefficients can become complex. A method of solving for the real part of θ_t is given by Stratton [11] in his discussion of refraction in a conducting medium. Consider medium 2 only to have complex permittivity, then substituting the negative of the complex permittivity in place of the conductivity in Stratton's solution the following expressions are obtained:
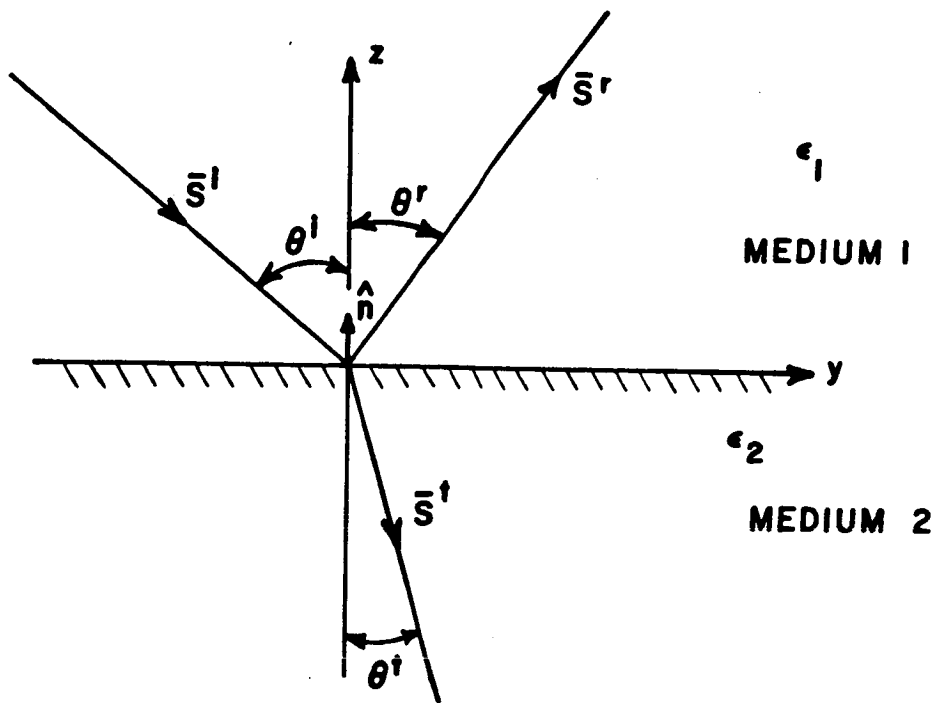
Figure 2.13. Geometry for Fresnel coefficients.

$$\text{Real } \theta_t = \cos^{-1}\left[\frac{q}{\sqrt{q^2 + k_1^2 \sin^2\theta_i}}\right] \qquad (2.37)$$

$$q^2 = \frac{1}{2}\left[\alpha_2^2 - \beta_2^2 - k_1^2 \sin^2\theta_i + \sqrt{4\,\alpha_2^2\,\beta_2^2 + (\alpha_2^2 - \beta_2^2 - k_1^2 \sin^2\theta_i)^2}\right]$$

$$(2.38)$$

where

$$k_2 = w\sqrt{\epsilon_2\mu_2} = \alpha_2 + j\,\beta_2 \qquad \text{and} \qquad k_1 = w\sqrt{\epsilon_1\mu_1} \qquad (2.39)$$

Figure 2.14 shows plots of the magnitude of $R_\parallel$ and $R_\perp$ for $\epsilon_r = 1.5 - j.69$. Note that $R_\parallel$ has a zero at the critical angle when the ϵ_r real, but the complex permittivity eliminates that zero. Notice also that the reflection coefficients approaches unity as the angle of incidence approaches 90 degrees. This happens for all values of ϵ_r; thus, all dielectrics look like conductors as grazing incidence is approached.

F. DIFFRACTION BY A DIELECTRIC WEDGE

The dielectric wedge problem has been the topic of many papers and reports for 30 years because of the difficult nature of the boundary conditions. Some of the different solutions include those by Senior [12], Rawlins [13], Berntsen [14], and Joo, Ra and Shin [15]. Some of the above solutions as well as many that they reference are either very limited or too complicated to be of practical use. Many of these papers show no calculated patterns. Some solutions involve a power series expansion in terms of the inverse of the material's index of refraction.
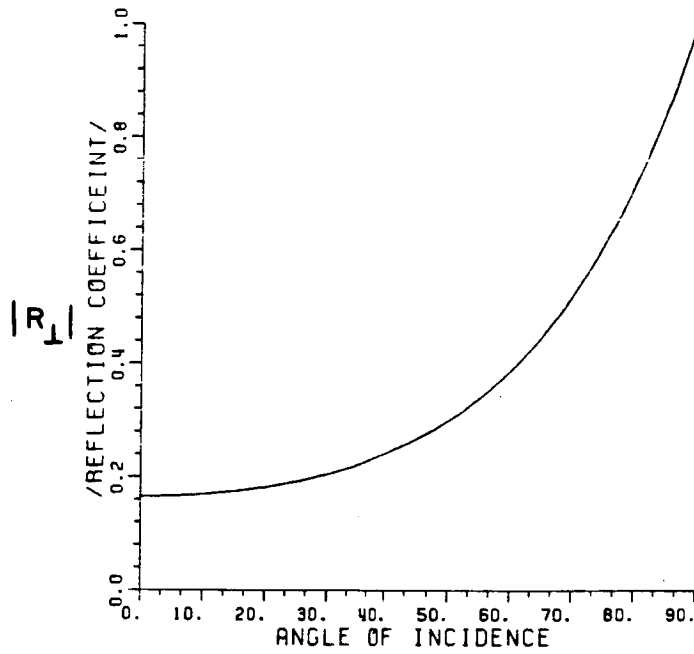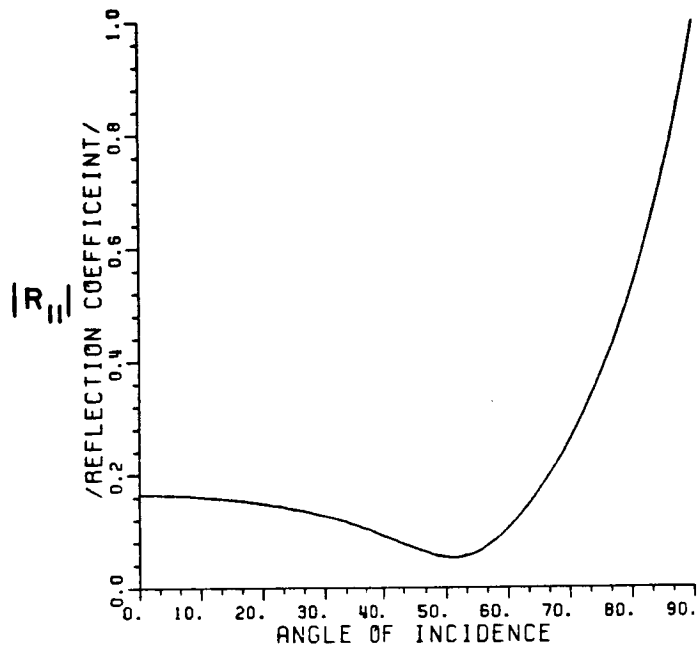
Figure 2.14. Fresnel coefficients at 3 GHz for ϵ_r=1.5-j.69.

These solutions do not converge rapidily when the dielectric constant is close to 1.

Rawlins obtained a Neumann series solution in an implicit form and calculated only the first term in the series for the special case of an E-polarized plane wave diffraction by a right angle wedge. His power series is in terms of (n^2-1) which restricts ϵ_r between 1 to 2 to get a convergent series. Since, the series converges much faster for ϵ_r near 1 compared to values near 2 and closed form expressions are given for only the first term of the series, solutions for ϵ_r close to 1 will be much more accurate than for values close to 2. The incident direction is also restricted to the quadrant opposite the right angle wedge where the transmitted rays are trapped by the wedge.

Rawlins' equations are expressed in terms of incident, reflected, and diffracted rays with programable expressions for each. Thus, Rawlins' solution is limited to a small class of problems but has the advantages that it is easy to calculate and interpret the results. Fortunately, free space absorber material commonly has dielectric constants between 1 and 2, so, Rawlins' solution is used to compare with an UTD solution.

The UTD solution for the perfectly conducting wedge is modified by replacing the reflection coefficient of +1 or -1 with a Fresnel reflection coefficient and reducing the magnitude of the incident shadow boundary by the magnitude of the transmited ray. This technique was developed by Burnside and Burgner [3] and Teran and Burnside [4] for a dielectric slab. The same modification can be used for a wedge;

32

however, the results are only verified for a right angle wedge with an incident ray coming from the quadrant opposite the dielectric.

Three different methods of determining the reflection are considered. In method 1, the reflection coefficient is found from the angle between the incident ray and the surface normal. This incident angle is used in Equations (2.33) through (2.36) of the previous section to arrive at a reflection coefficient. The reflection coefficient is thus calculated separately for each face of the wedge. The modified diffraction coefficient is shown below:

$$
D_{s,h}(L,\phi,\phi',\beta_0) = \frac{-e^{-j\pi/4}}{2n\sqrt{2\pi k}\ \sin\beta_0}
$$

$$
\left[\begin{bmatrix} 1-T_\parallel^N \\ 1-T_\perp^N \end{bmatrix} \cot\left(\frac{\pi+\beta^-}{2n}\right) F(kLa^+(\beta^-)) + \begin{bmatrix} 1-T_\parallel^0 \\ 1-T_\perp^0 \end{bmatrix} \cot\left(\frac{\pi-\beta^-}{2n}\right) F(kLa^-(\beta^-)) \right.
$$

$$
\left. + \begin{bmatrix} R_\parallel^N \\ R_\perp^N \end{bmatrix} \cot\left(\frac{\pi+\beta^+}{2n}\right) F(kLa^+(\beta^+)) + \begin{bmatrix} R_\parallel^0 \\ R_\perp^0 \end{bmatrix} \cot\left(\frac{\pi-\beta^+}{2n}\right) F(kLa^-(\beta^+)) \right]
$$

$$
(2.40)
$$

with the superscript on R and T specifing which wedge face. In this form the reflection and transmission coefficients depend only on the incident angle, the wedge angle, and ε_r. They are independent of the scattered angle.

When the reflection coefficients are determined in this manner, reciprocity is not satisfied as there is no dependence on scattered angle and there is a change with incident angle.

The second method is chosen to satisfy reciprocity. The reflection coefficient is determined by dividing the angle between the incident and scattered directions by 2 and using it as the incident angle in Equations (2.33) through (2.36) of the previous section. Using this method the reflection coefficient is dependent on both the incident and scattered directions but is independent of the wedge angle. The diffraction coefficient equation for method 2 is identical to method 1 except the superscripts on R and T are not needed since the same reflection coefficient is used for both wedge faces.

The final method uses the same reflection coefficient as method 2 but the transmission coefficient is taken as unity which eliminates the terms associated with the incident shadow boundries. The reasoning behind this method is that the incident shadow boundary is not as abrupt as the reflection shadow boundary because energy can pass through the tip of the wedge. This would make the scattered energy associated with the incident shadow boundary less. Setting the transmission coefficients equal to unity is then assuming the effects from the reflection shadow boundary will dominate the return.

Calculated results for bistatic scattering of a plane wave with E-field polarized in the direction of the edge are shown in Figures 2.15 thru 2.20. Comparisons between UTD results and Rawlins are made for all three methods at two different incident angles at 50 wavelengths from

34
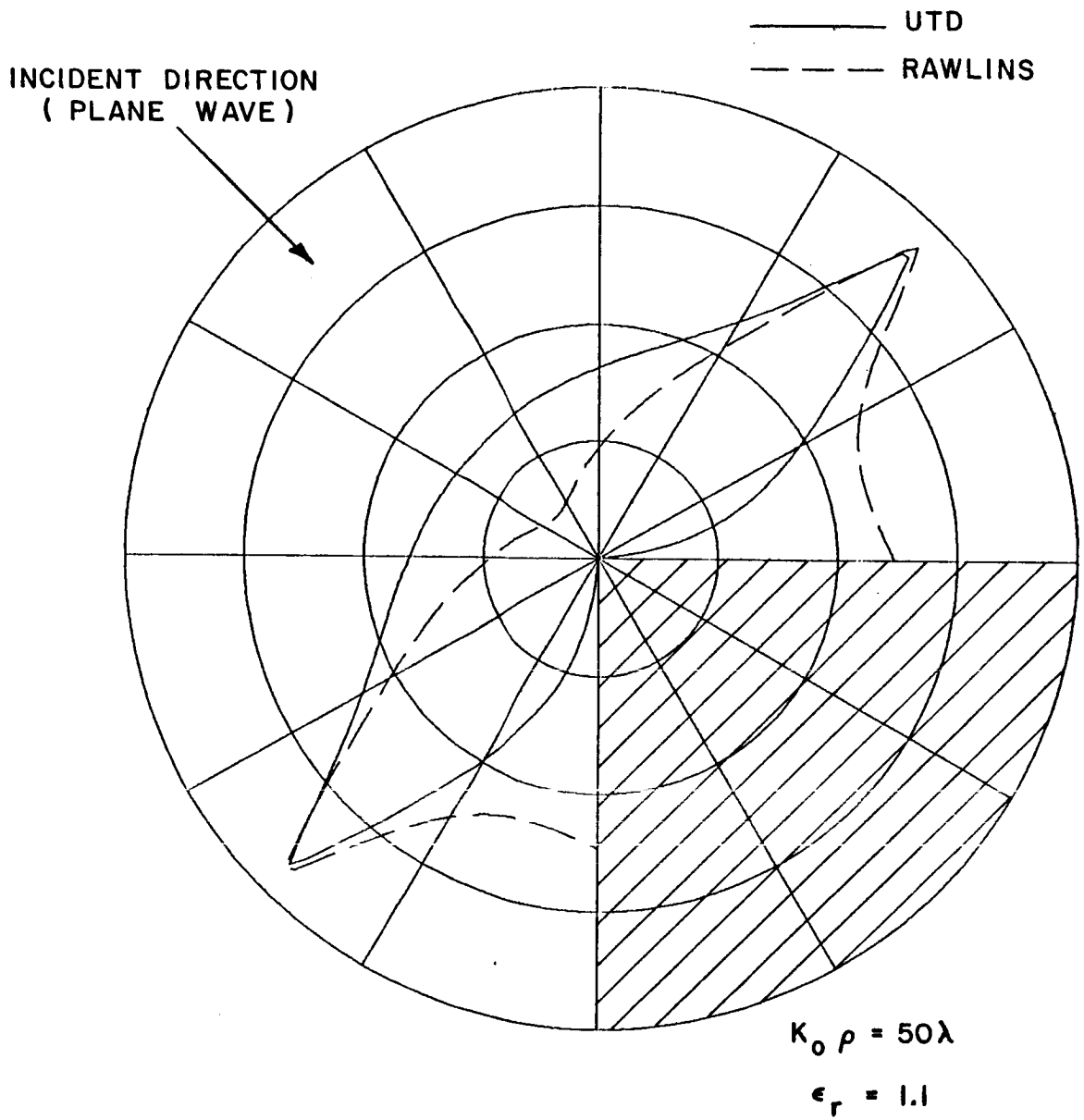
Figure 2.15. Diffraction of an E-polarized plane wave by a right angle dielectric wedge, using method 1.

INCIDENT DIRECTION
PLANE WAVE

——————— UTD
— — — — RAWLINS

$K_o \, \rho = 50 \lambda$

$\epsilon_r = 1.1$
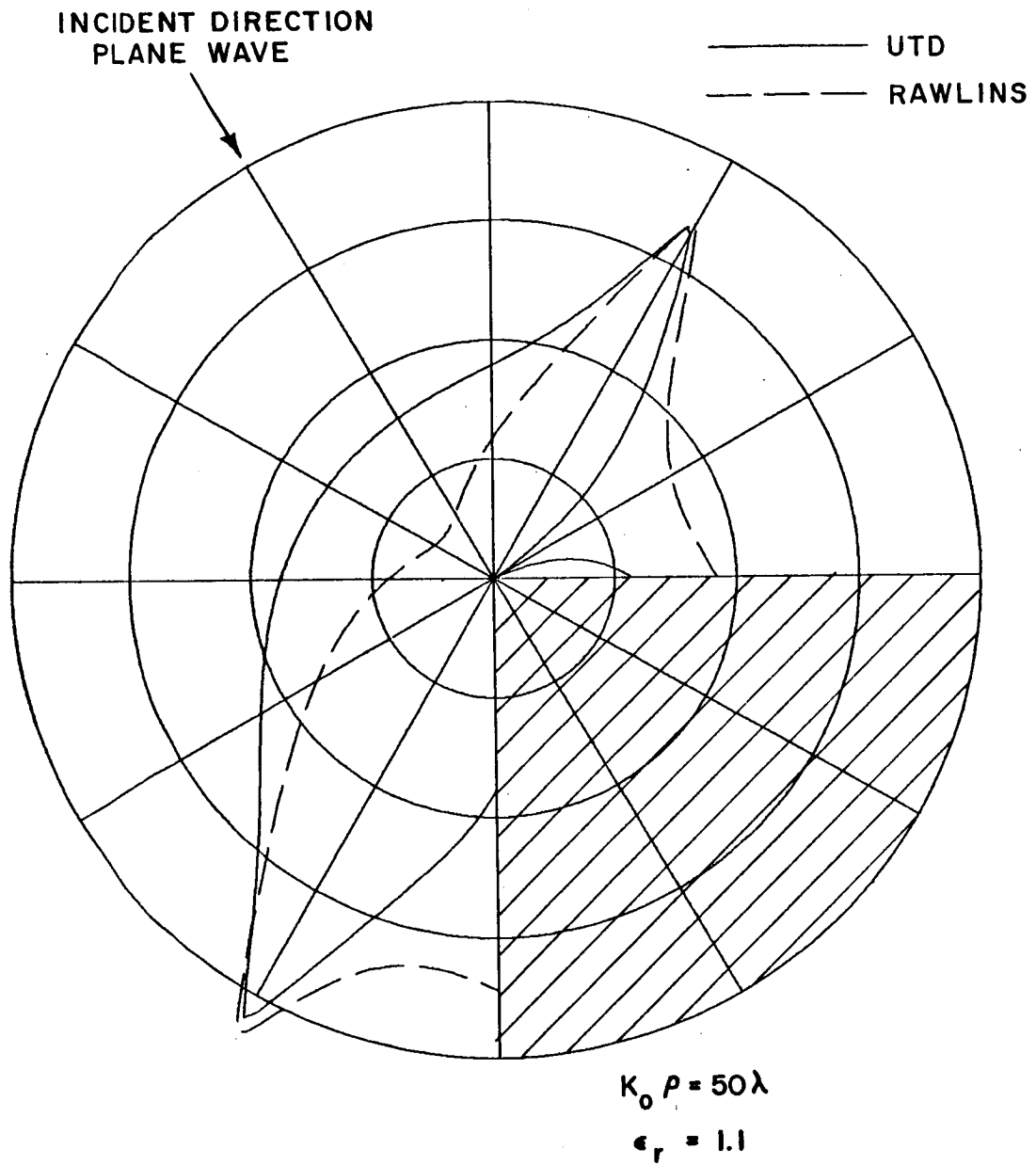
Figure 2.16. Diffraction of an E-polarized plane wave by a right angle
dielectric wedge, using method 1.
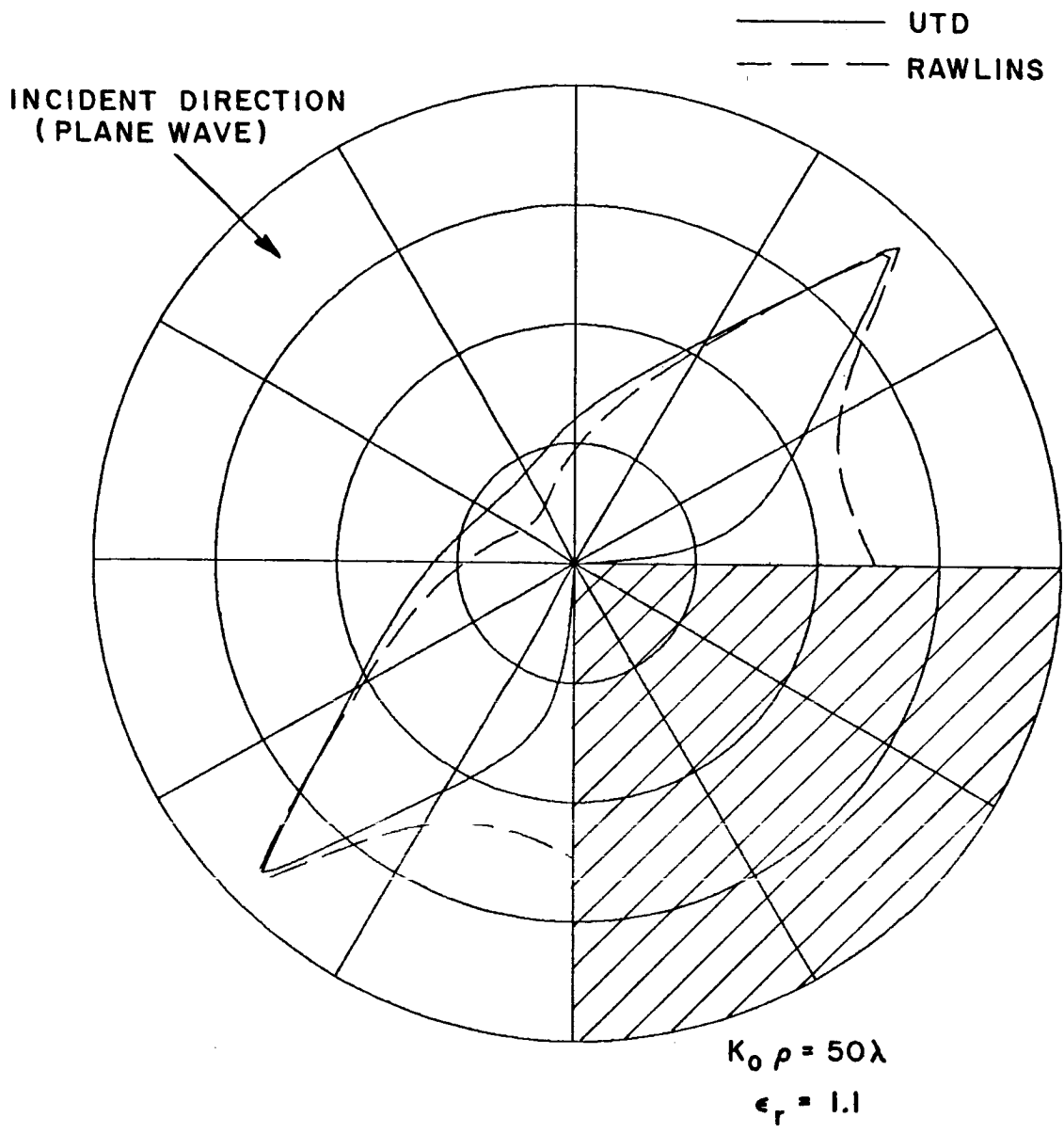
Figure 2.17. Diffraction of an E-polarized plane wave by a right angle dielectric wedge, using method 2.
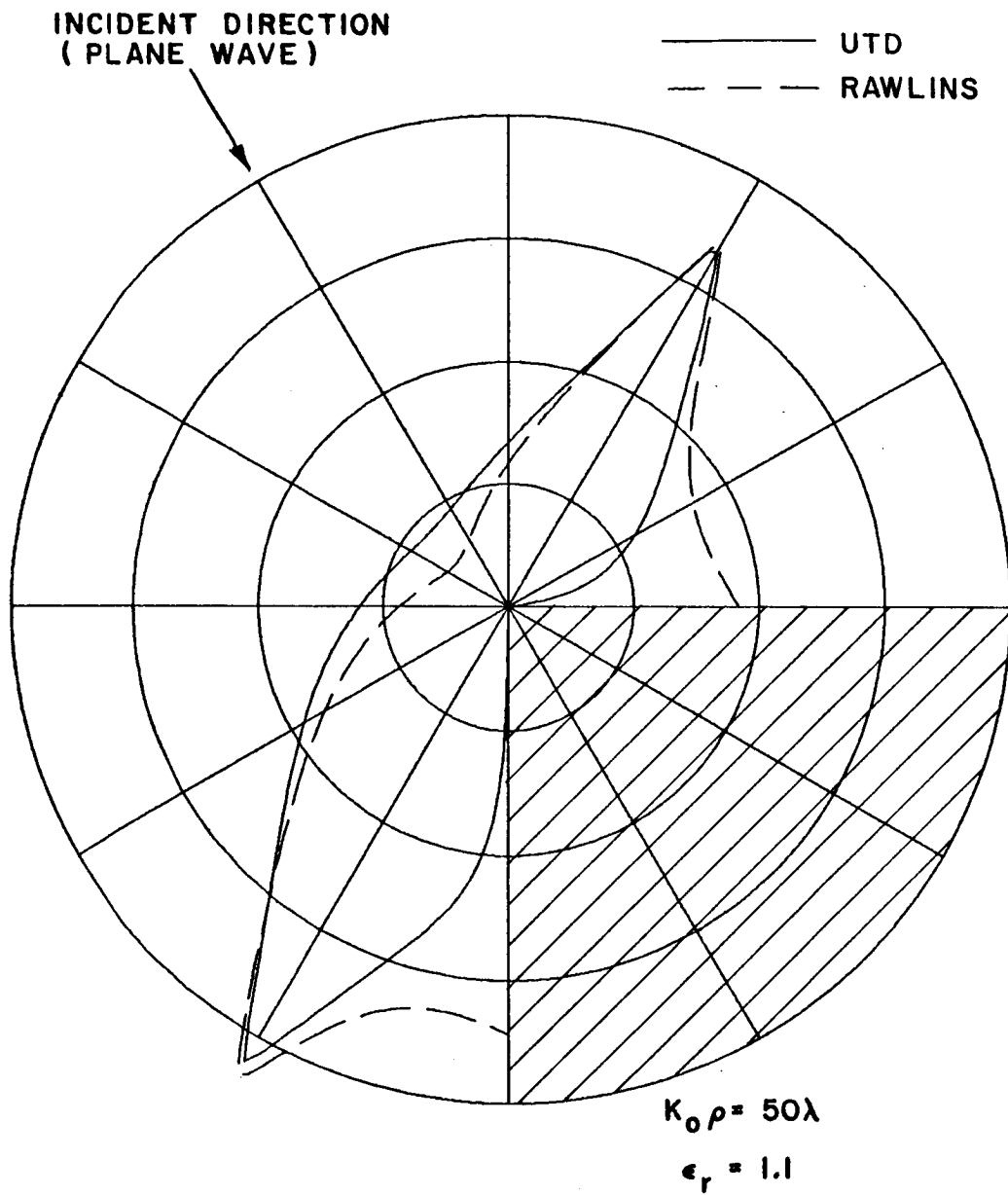
Figure 2.18. Diffraction of an E-polarized plane wave by a right angle dielectric wedge, using method 2.

38
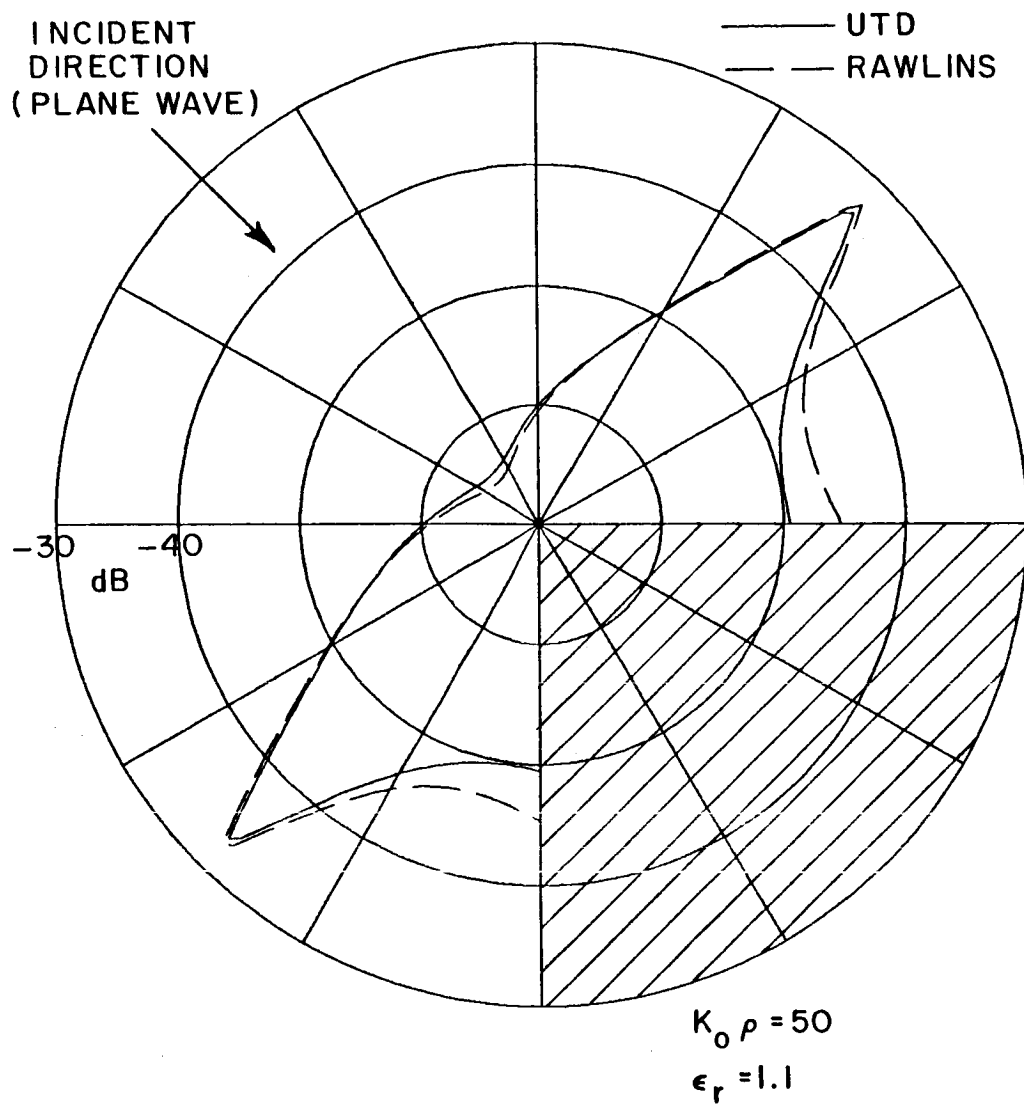
Figure 2.19. Diffraction of an E-polarized plane wave by a right angle dielectric wedge, using method 3.
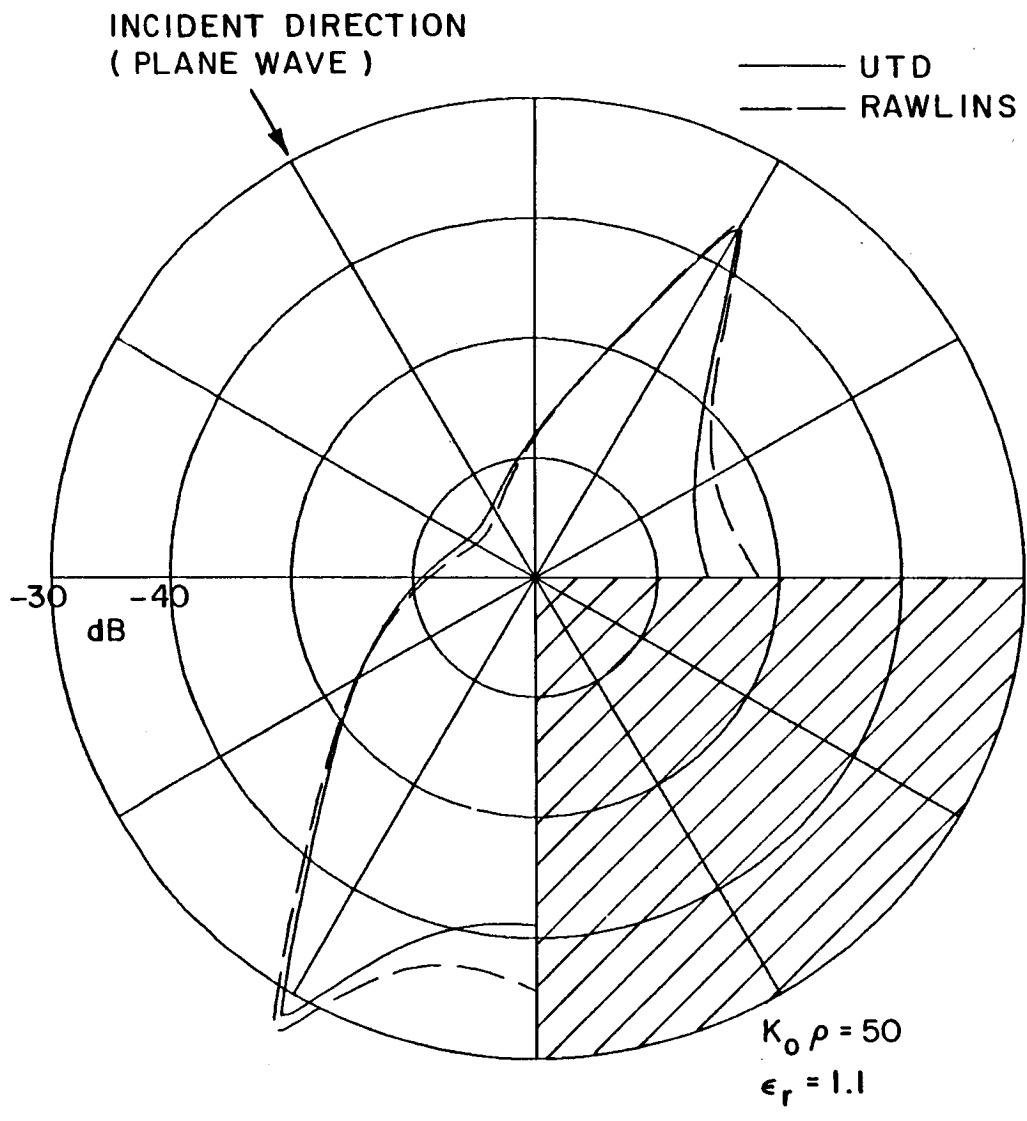
Figure 2.20. Diffraction of an E-polarized plane wave by a right angle dielectric wedge, using method 3.

the wedge. Figures 2.15 and 2.16 show the results for method 1, Figures 2.17 and 2.18 show results for method 2, and Figures 2.19 and 2.20 show the results for Method 3. The dielectric constant of the material is chosen close to one (ε_r=1.1) since Rawlins solution is more accurate at values of ε_r close to 1 as mentioned previously.

All methods agree near the reflection shadow boundries but show considerable differences in other regions. Rawlins' solution disagrees greatest with the UTD solutions in the regions near the dielectric and at backscatter. Since Rawlins' solution uses the correct boundary conditions and the UTD solution is a modification of the conducting wedge results, one suspects Rawlins' results to be the more accurate near the dielectric. Method 3 shows the best agreement with Rawlins' results near the dielectric and in the backscattered region.

At the lower reflection shadow boundary in Figures 2.16, 2.18, and 2.20 Rawlins' reflection coefficient, which is the first term of the Fresnel coefficients when expanded to the order (n^2-1), disagrees with the UTD solution, which uses the correct reflection coefficients, making the UTD solution more accurate at the shadow boundries.

The disagreement between the methods is much greater for parallel polarization than for perpendicular. Measurements of parallel polarization can be used to verify which method should be used. Chapter 4 reports the results of backscattered measurements from wedge absorbers. These measurements show identical wedge-on backscatter for both polarizations. Method 3 predicts identical backscatter for both

polarizations, while for the case measured, Methods 1 and 2 predicted more than a 10 dB difference. Method 3, thus, appears superior for backscatter measurements but for bistatic measurements the comparisons with Rawlins solution show Method 2 may be better for some cases. Nevertheless, based on the measurements done and the comparisons with Rawlins' solution Method 3 is chosen for use in the next chapters to calculate scattering from absorber pyramids and wedges.

Finally, Figure 2.21 shows diffracted field calculations for both polarizations and $\varepsilon_r=1.45-j.58$, using Method 3. This value of ε_r corresponds with the absorber values of ε_r covered in the next chapter. The H-polarized plane wave case is lower than the E-polarized case because of the smaller reflection coefficient. At backscatter they are the same because the normal incidence reflection coefficients are used here and they are identical.
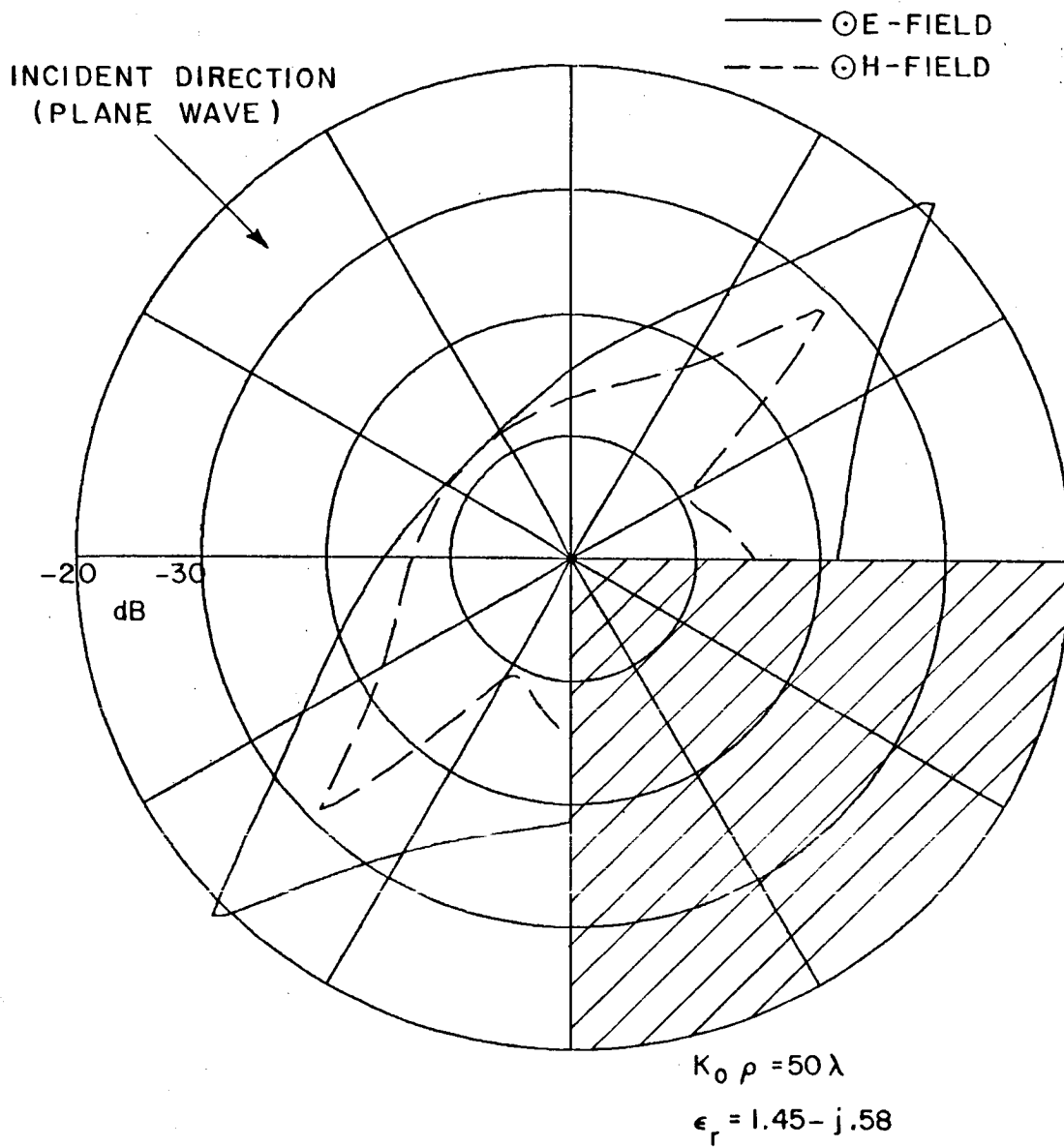
Figure 2.21. Diffraction of both an E and H-polarized plane wave by a right angle dielectric wedge with $\varepsilon_r=1.45-j.58$, using Method 3.

43

CHAPTER III

MODELING OF SCATTERING FROM ABSORBERS

A. INTRODUCTION

Pyramid absorbers have been in use for many years; yet, there have been few high frequency attempts to calculate their scattering properties. This is probably due to a combination of the following reasons. 1) A tip is difficult to analyze, 2) the material is penetrable and somewhat inhomogeneous, 3) there has not been much need for better absorber until recently, and 4) accurate measurements to compare with calculations are difficult to obtain.

Bucci and Franceschetti [16] and Serin [17] made some early attempts to calculate scattering from wedge shaped absorber by using ray tracing. They, however, limited there analysis to reflected rays which dominate the scattering for only some geometries and materials.

In this chapter the material properties of present day absorber are first considered followed by methods for calculating the scattering contribution from transmitted, reflected, and diffracted fields. These high frequency contributions when summed give a model for absorber scattering.

Only high frequency methods are considered in this chapter. When the absorber pyramids are smaller than a wavelength a transmission line model can be used as discussed in Chapter VI.

44

Absorbers from four different manufactureres were measured during this study. Because only a small number of samples were tested, which may not accurately represent a given company's line of abosrbers, they are designated as Company A, B, C, and D.

B. PROPERTIES OF MATERIAL

In the past various materials have been used in the manufacturing of microwave absorbers, including horse hairs, rubber, and foams. Today, carbon impregnated urethane foam is in widespread use, but development of other absorbing materials, with the present emphasis on objects with small scattering signatures, may replace the urethane foam. Urethane foam is also difficult to make fire retardant and absorbing at the same time.

The absorber presently used in the ElectroScience Laboratory anechoic chamber is made from carbon impregnated urethane foam with a protective layer of paint and some type of fire retardant added during the carbon impregnating. King, Shimabukuro, and Wong [18] reported the paint layer raises the reflection coefficient on some absorber at 94 GHz. At least one of the absorber companies suggests using half painted pyramids for frequencies above 30 GHz. The paint effects of Company D's and Company B's absorber were studied between 6 and 18 GHz on the compact range by measuring unpainted and painted pieces of absorber. In this frequency range the painted absorber performed as well as the unpainted.

Values for the absorber permittivity at various frequencies, as reported by a product engineer at one of the absorber companies, are shown in Table 3.1. The region below 1 GHz has widely changing permittivity so no values are given.

Some absorbers, 24" and taller, have lower permittivities because a lower concentration of carbon is used to impregnate them. The real part is only slightly reduced since it is mostly due to the foam. The imaginary part drops considerably with less carbon.

The skin depth is especially significant in the 1 GHz region. For frequencies at or above 3 GHz, the skin depth is sufficiently small so that most of the energy entering the absorber is lost to heat as most absorber has between 3" and 6" of absorber backing.

C. TRANSMITTED RAY PATHS

One of the great difficulties in applying high frequency solutions to penetrable bodies is tracing all the multiple ray paths. Calculating the shadow boundary effects associated with these ray paths also poses a major problem. Fortunately, the absorber material's high loss attenuates the transmitted rays which suggests the use of the techniques developed in the previous chapter to analyze the material scattering.

Consider the case of nose-on incidence on a wedge with an interior angle of 14 degrees and $\varepsilon_r = 1.5 - j.69$ as shown in Figure 3.1. Upon striking one face of the wedge, the incident ray is split into reflected

TABLE 3.1

TYPICAL ABSORBER MATERIAL PROPERTIES

$$\epsilon = \epsilon_0 \left(\epsilon_r' - j\epsilon_r'' \right)$$

$$\mu = \mu_0$$

$$\delta = -\tan^{-1} \frac{\epsilon_r''}{\epsilon_r'}$$

$$\text{SKIN DEPTH} = \frac{1}{K''}$$

FREQUENCY	ϵ_r'	ϵ_r''	δ	SKIN DEPTH
1 GHz	3.0	.59	-11.13^0	11.1"
3 GHz	1.5	.69	-24.7^0	2.3"
10 GHz	1.45	.58	-21.8^0	1.4"
100 GHz	1.3	.03	-1.3^0	1.45"

Figure 3.1. Various ray paths for nose-on incidence.

and transmitted rays. The reflected ray paths will be treated in the next section so that leaves the transmitted ray. Using Equation (2.37), the real part of the transmitted angle is found to be 49 degrees. The transmitted ray then passes through the pyramid and arrives at the far side of the absorber where it undergoes total internal reflection because the incident angle has exceeded the critical angle of 50.6 degrees for the dielectric-air boundary. The transmitted ray is, thus, trapped and pushed towards the base of the absorber. The 2" skin depth would cause this ray to be significantly attenuated before it could travel to the back of the absorber, be reflected, travel up the base and be re-launched air.

The transmitted ray can escape from the absorber if the incident angle is less than 14 degrees, as shown in Figure 3.2. If there were a row of wedges this transmitted-transmitted ray would then be trapped by the next wedge in line. So, if the two way path through the base of the absorber has enough attenuation to prevent rays from leaving the absorber, the transmitted ray contribution to scattering from the pyramid is assumed to be zero.

D. REFLECTED TERMS

Many different reflected ray paths are possible with the periodic pyramid shape and these paths change with different transmit-receive
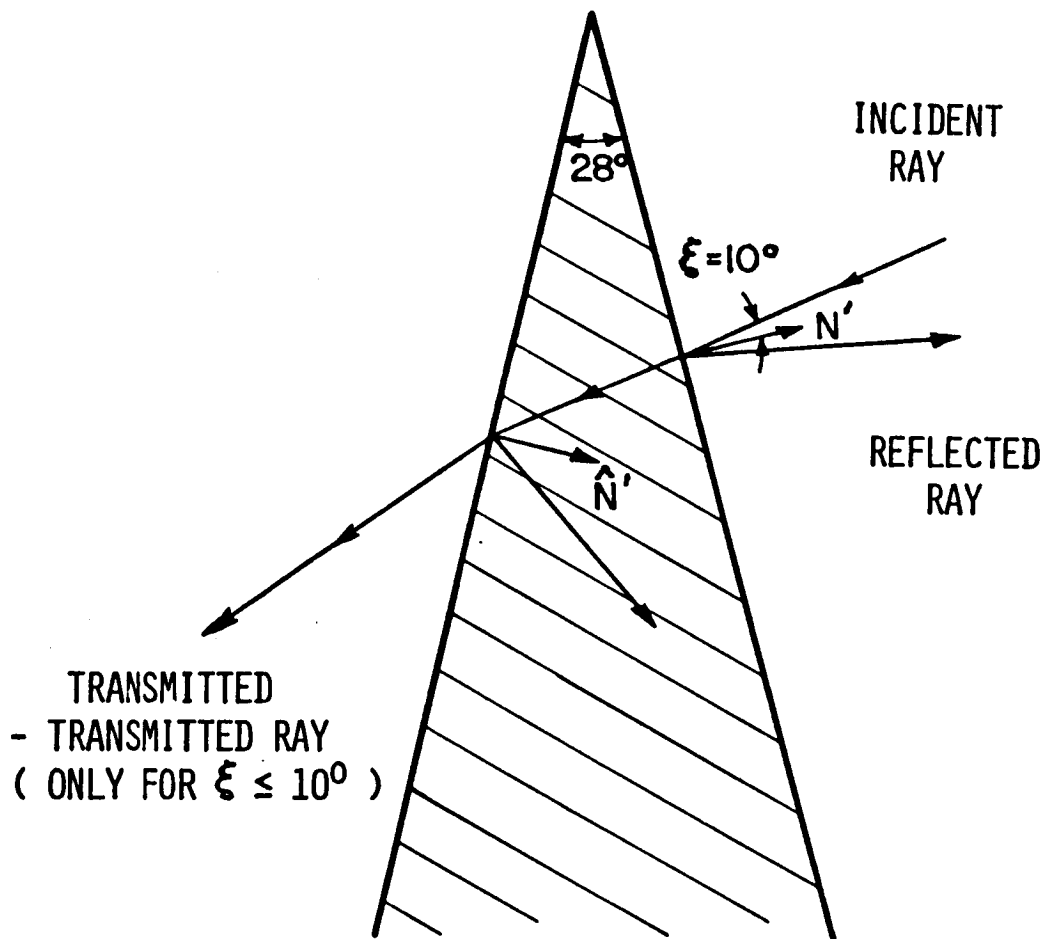
Figure 3.2. Transmitted field ray paths for 10° incidence.

angles. The dominant paths also change with different incident-scattered directions. With the sides of the pyramids being straight the reflected fields will remain as plane waves if the incident field is a plane wave.

Consider first, the case of nose-on backscatter from an $\alpha=21$ degrees pyramid such as shown in Figure 3.3. (Note: In the side view shown, the $\alpha=21$ degrees pyramid appears as about a 22 degree wedge.) An incident ray striking the left surface of the right pyramid is reflected towards the left pyramid. This ray then reflects off the left pyramid back towards the right pyramid. The ray continues to move toward the base of the pyramid until after the fourth bounce where it starts heading back towards the pyramid tips. After a total of eight reflections the ray is heading back in the direction of the incident ray. The magnitude of the multiple reflected ray is found by multipling the Fresnel reflection coefficient of each bounce together to get a total reflection coefficient. The total reflection coefficient for different values of ε_r are shown in Table 3.2 for both polarizations. Notice that with eight bounces the reflection coefficient is highly dependent on the polarization and material properties.

To find the reflected field contribution in the backscattered direction, the fields are found in the plane of the pyramid tips (shown dashed on Figure 3.3) and then an aperture integration is performed.
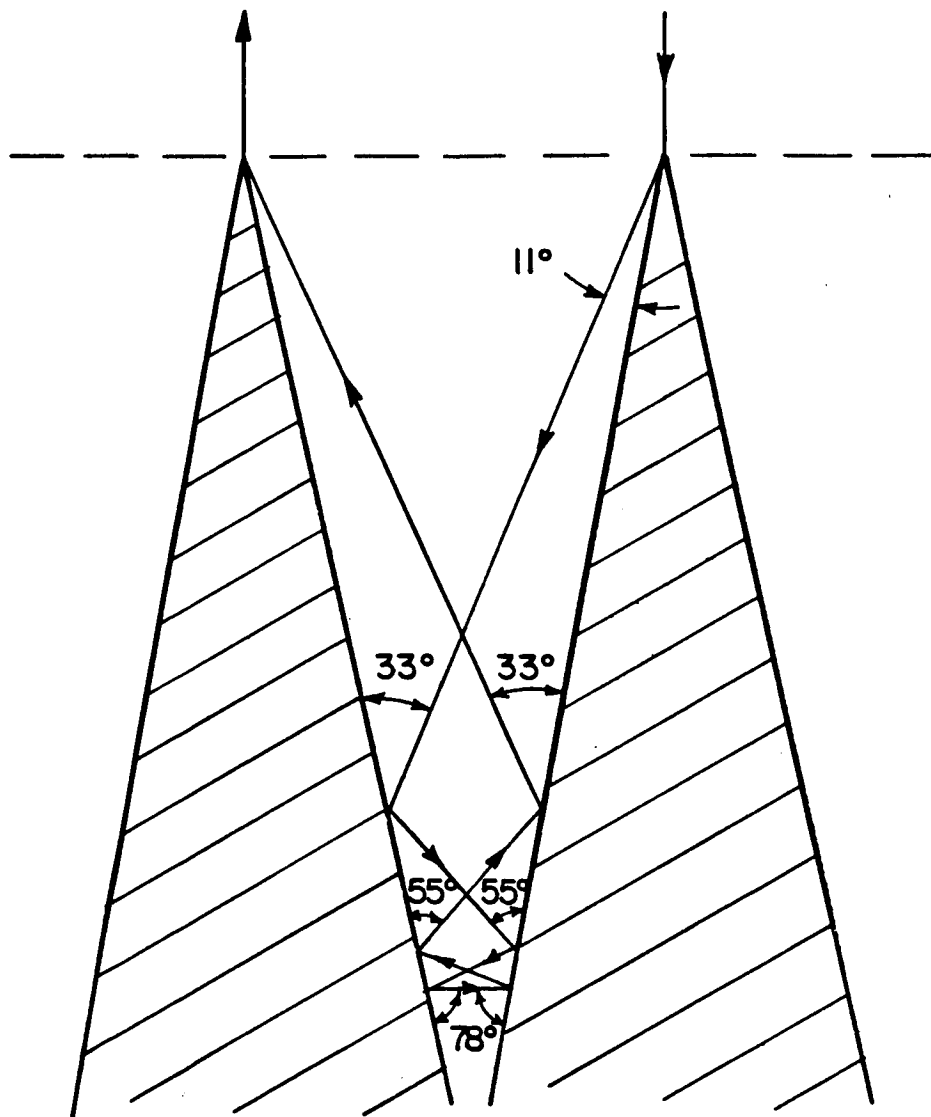
Figure 3.3. Reflected field ray paths for nose-on incidence.

TABLE 3.2

E REFLECTED / E INCIDENT
FOR NOSE-ON BACKSCATTER FROM α=21° ABSORBER

	$\perp$	II
3 GHZ (ϵ_R = 1.5 - J.69)	.000235 (-72 DB)	1.7×10^{-6}
10 GHZ (ϵ_R = 1.45 - J.58)	.000128 (-78 DB)	7×10^{-7}
(ϵ_R = 1.3 - J.29)	.0001 (-100 DB)	3.3×10^{-8}

Consider next the case of 45 degree incidence on an α=28 degree pyramid as shown in Figure 3.4. This represents a much more difficult ray tracing problem than for nose-on incidence because of the many different paths for the reflected fields. The paths with the fewest bounces and the largest areas will be the dominant terms since each bounce causes attenuation.

A three bounce path exists from a ray hitting near the top of the pyramid as shown on the right side of Figure 3.4. After the third reflection the ray leaves at an angle of 145 degrees. Notice that the three bounce ray just misses reflecting off the tip of the next pyramid. If the incident ray strikes a little further down the pyramid, as shown in the left side of Figure 3.4, then the ray will bounce a fourth time and be launched at an angle of 65 degrees.

To find the reflected field contribution to the scattered field an aperture integration method is used once again. The dashed line in Figure 3.4, represents the plane over which the integration is performed. A top view of the pyramids in Figure 3.4 is shown in Figure 3.5. The areas where the reflected paths, described above, intersect the aperture over which the integration is done, are shaded.

Other reflected paths include a 6 bounce path for incident rays hitting the top or bottom faces of the pyramids near the valleys as shown in Figure 3.5. The six bounce path's small launch area combined with the greater number of bounces make it insignificant compared to the other terms. Some other paths exist that tend to circle around the pyramids; however, they are very difficult to trace since they have many bounces and small launch areas.
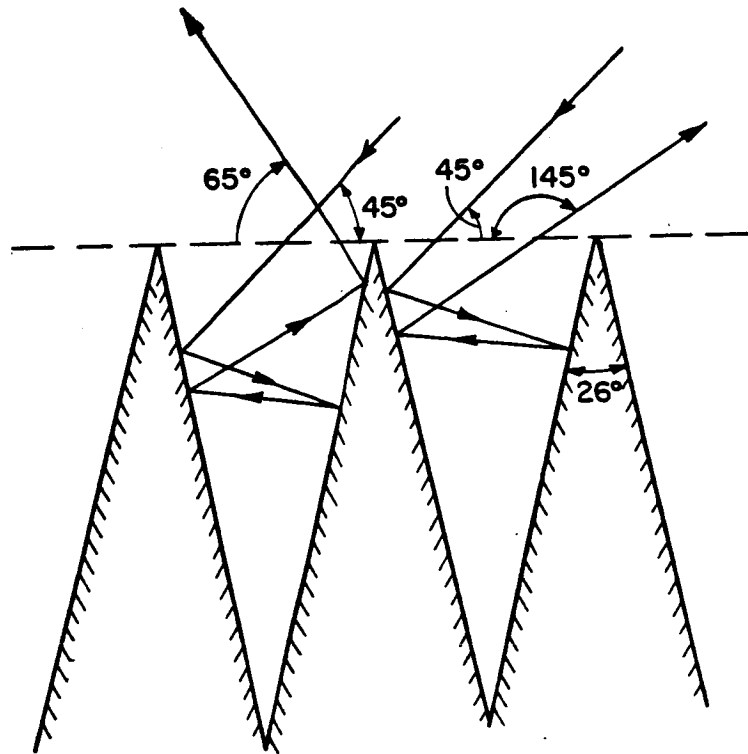
Figure 3.4. Dominant reflected field ray paths for 45° incidence.
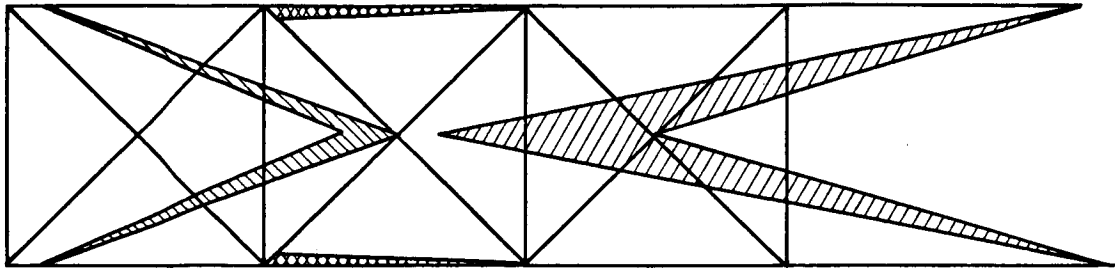
▨	4 BOUNCES LAUNCH ANGLE OF 65°
▨	3 BOUNCES LAUNCH ANGLE OF 145°
▨	6 BOUNCES

Figure 3.5. Top view of pyramids shown in Figure 3.4. The shaded areas indicate where the reflected paths intersect the plane indicated by the dashed line in Figure 3.4.

56

This ray tracing approach to the reflected field contribution is a high frequency solution with an additional assumption that the absorber is not acting as a waveguide below cutoff at the bases. As the reflected wave travels toward the base of the pyramids the cutoff frequency of the waveguide would get higher. When the frequency becomes less than the cutoff frequency, the energy would tend to get transferred into the absorber. For the case of 45 degree incidence, in the second example of this section, the rays do not travel very far down the pyramid. This would be a problem, however, in the nose on incidence case as the reflected rays travel close to the base.

E. TIP DIFFRACTION

The method of calculating tip diffraction described in Chapter II-D combined with the dielectric modifications described in Section F of that same chapter are used to find the scattered field from the tip of the pyramid absorber. The modified corner diffraction coefficient is given by

$$C_{s,h}(Q_E) = \frac{-e^{-j\pi/4}}{2n\sqrt{2\pi k}\,\sin\beta_0}$$

$$
\left[\cot\left(\frac{\pi+(\beta^-)}{2n}\right)F[kLa^+(\beta^-)]\cdot\left|F\left[\frac{La^+(\beta^-)/\lambda}{kL_c a(\pi+\beta_{0C}-\beta_C)}\right]\right| \right]\cdot\begin{bmatrix}1-T_{\parallel}^N\\[4pt]1-T_{\perp}^N\end{bmatrix}
$$

$$
+\begin{bmatrix}1-T_{\parallel}^0\\[4pt]1-T_{\perp}^0\end{bmatrix}\cot\left(\frac{\pi-(\beta^-)}{2n}\right)F[kLa^-(\beta^-)]\cdot\left|F\left[\frac{La^-(\beta^-)/\lambda}{kL_c a(\pi+\beta_{0C}-\beta_C)}\right]\right|
$$

$$
+\begin{bmatrix}R_{\parallel}^N\\[4pt]R_{\perp}^N\end{bmatrix}\cot\left(\frac{\pi+(\beta^+)}{2n}\right)F[kLa^+(\beta^+)]\cdot\left|F\left[\frac{La^+(\beta^+)/\lambda}{kL_c a(\pi+\beta_{0C}-\beta_C)}\right]\right|
$$

$$
+\begin{bmatrix}R_{\parallel}^0\\[4pt]R_{\perp}^0\end{bmatrix}\cot\left(\frac{\pi-(\beta^+)}{2n}\right)F[kLa^-(\beta^+)]\cdot\left|F\left[\frac{La^-(\beta^+)/\lambda}{kL_c a(\pi+\beta_{0C}-\beta_C)}\right]\right|\;\cdot
$$

(3.1)

Consider the pyramid geometry shown at the top of Figure 3.6. The absorber tip of square cross section and angular dimension α is oriented symmetrically about the negative z-axis with its apex at the origin. The radar direction (i.e., the angle of incidence and reflection for the backscattered field) is specified by the spherical coordinates θ and ϕ.

58

Consequently, $\theta=0$ degrees represents nose-on incidence for the absorber pyramid and $\phi=0$ degrees specifies a plane of incidence broadside to one of the pyramid faces, while $\phi=45$ degrees specifies a plane of incidence passing through an edge of the pyramid.

The corner diffraction equation is used four times, once for each edge termination. In the far field, the terms involving F[kLa] are equal to unity so they drop out. The value for n is found from the wedge angle (WA) which is given by

$$WA = (2-n)*\pi \qquad\qquad (3.2)$$

with the relationship between WA and α given by

$$WA = 2 \sin^{-1} \sqrt{\frac{1-\cos\alpha}{1+\cos\alpha}} \qquad . \qquad\qquad (3.3)$$

The reflection and transmission coefficients are found using Method 3 described in Chapter II-F. Using this method the backscatter return is independent of polarization so only one polarization is shown in the figures.

Figure 3.6 shows the backscattered field from tip diffraction of an $\alpha=21$ degree pyramid as a function of theta for the $\phi=0$ and 45 degree plane of incidence at 10 GHz. The cross-polarized return is zero because of the symmetry at $\phi=0$ degrees. Notice in the $\phi=0$ degrees plot a spike occurs at about 80 degrees which corresponds to being broadside to the top face of the pyramid. This singularity occurs because only the scattered field from the tip is being calculated; thus, the model is for an infinite pyramid. To eliminate the singularity, the contribution
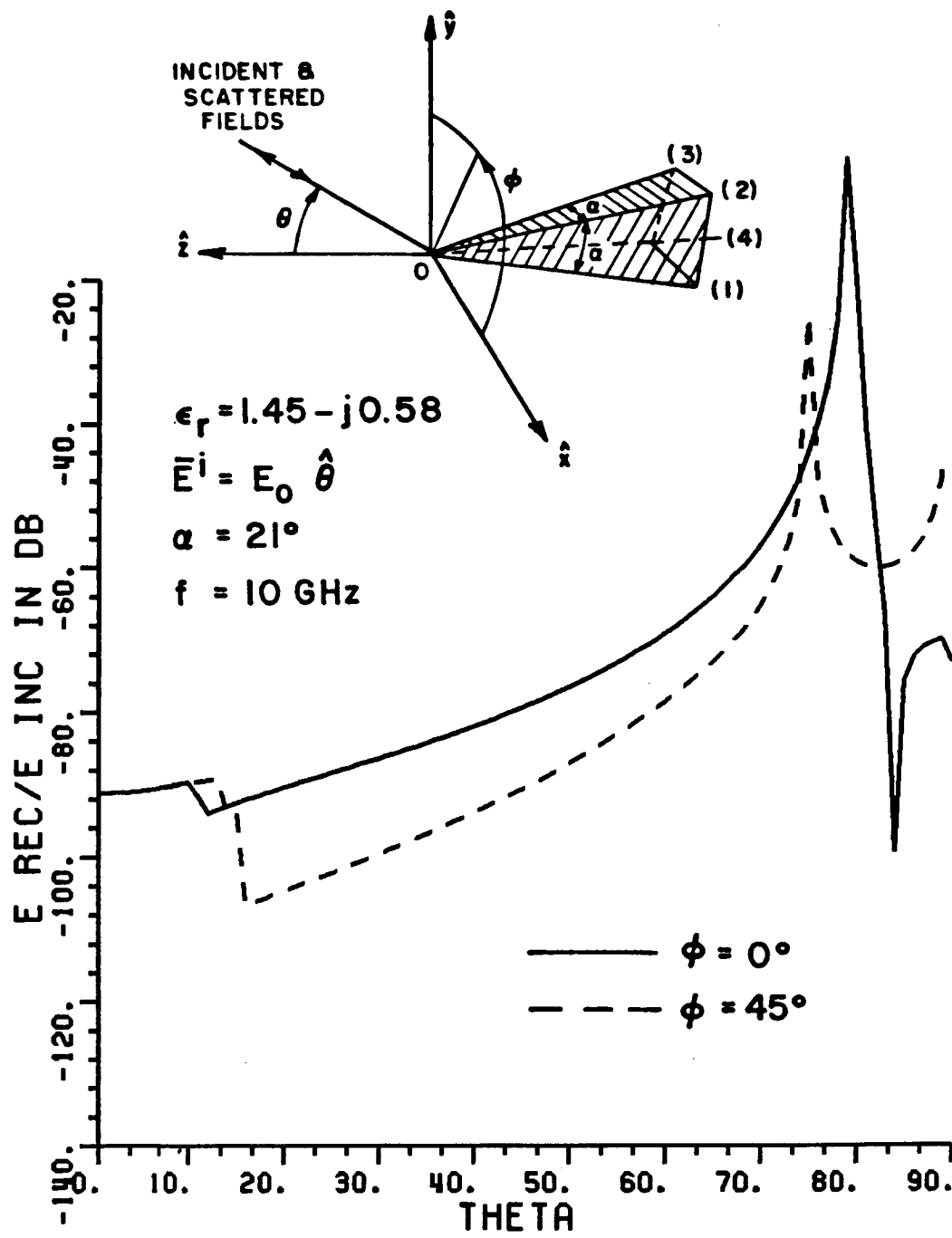
Figure 3.6. Backscatter from one pyramid tip as a function of theta.

from the base of the pyramid could be added to the tip contribution giving the correct broadside backscatter. In the ϕ=45 degrees plot the spike occurs at about 75 degrees which corresponds to being broadside to one of the edges of the pyramid.

A discontinuity in the ϕ=0 degrees plot occurs at about 10 degrees. This discontinuity is caused by the lower face of the pyramid passing from the lit region into the shadow region. The ϕ=45 degree plot shows a discontinuity at about 13 degrees which corresponds with the back two faces of the pyramid passing from the lit to shadow region.

Figure 3.6 shows a lower maximum tip contribution for the rotated case. This does not represent much advantage to the user since pyramid absorber should not be used when the backscattered return near grazing incidence is of concern because wedge or convoluted surface absorbers offer much lower return. Away from nose-on incidence this calculation shows some improvement in the results for the rotated absorber case. The greatest improvement in the rotated results is for θ between 20 and 30 degrees. As mentioned previously, the results in the regions near the discontinuities are suspect.

(Note: some of the plots have a two step jump instead of one which is due to one edge of pyramid passing into the shadow region slightly before another from the small offsets build into the program to avoid singularities.)

Figure 3.7 shows the backscattered field from tip diffraction off an α=26 degree pyramid at 10GHz. Notice that there are a few minor changes between the α=21 degrees plot and this one. First, the α=21
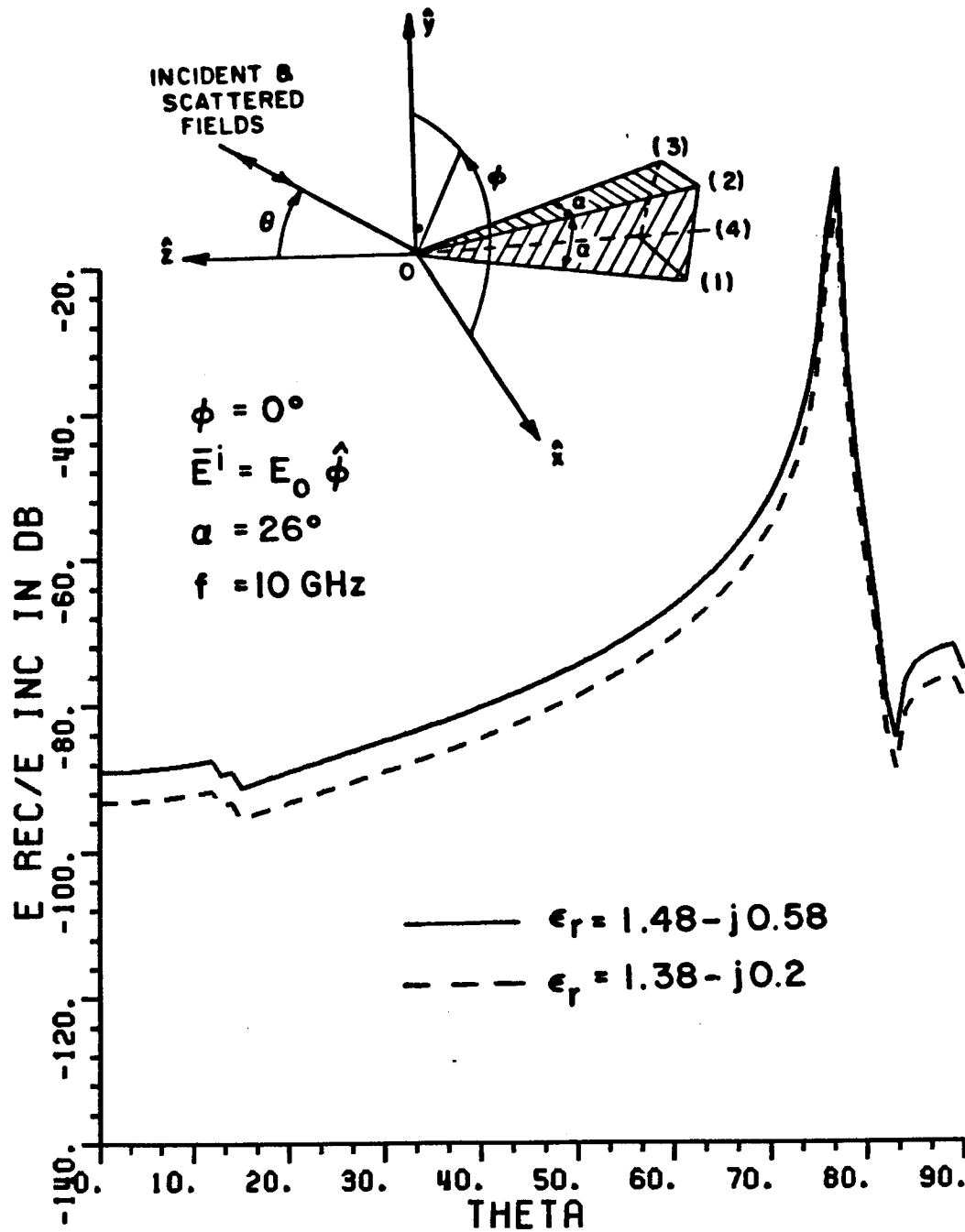
Figure 3.7. Backscatter from one pyramid tip as a function of theta.

degree plot is shifted down about 2 dB from the α=26 degrees plot in the tip on region. This represents a very marginal improvment for a narrower pyramid. However, if α is decreased to 10 degrees the plot moves down about 7 dB as shown in Figure 3.8. Second, the singularity at broadside and the discontinuity at the shadowing angles move slightly.

Figure 3.7 also shows the effect of changing the dielectric constant of the material. As mentioned previously, reducing the amount of carbon used in the doping process, the dielectric constant can be reduced. Company D reports a value of ε_r=1.38 -j.2 at 10 GHz as being a lightly doped value so it is used for comparisons. (Note: The real part of epsilon drops only slightly compared to the drop in the imaginary part. The low loss for this value of ε makes it impractical for short absorbers but not for tall ones.) The backscattered field near nose-on incidence is about 4 dB less for the lower value of ε.

Since the pyramid is assumed to be infinite. changing the frequency does not change the shape of the tip diffraction plots but only shifts the plot up or down depending on the frequencies change. The tip contribution is inversely proportional to frequency.

To find the RCS of a pyramid tip in dB relative to a square meter from the graphs, simply add 11 dB. The 11 dB comes from the factor 4π in the RCS equation.

Figure 3.9 shows the geometry and a plot of bistatic scattered field from an α=26 degree pyramid at 10 GHz with θ^i=45 degrees and θ^s sweeping from 0 to 90 degrees. There are three discontinuities shown in the plot. The first, at about 13 degrees, is associated with the front

63

Y-axis: E REC/E INC IN DB, with values -20., -40., -60., -80., -100., -120., -140.

X-axis: THETA, with values 0., 10., 20., 30., 40., 50., 60., 70., 80., 90.

Diagram label: INCIDENT & SCATTERED FIELDS

$\phi = 0°$

$\bar{E}^i = E_0\, \hat{\theta}$

$\epsilon_r = 1.45 - j\,0.58$

$f = 10\,GHz$

Legend:

—— $\alpha = 21°$

– – – $\alpha = 10°$
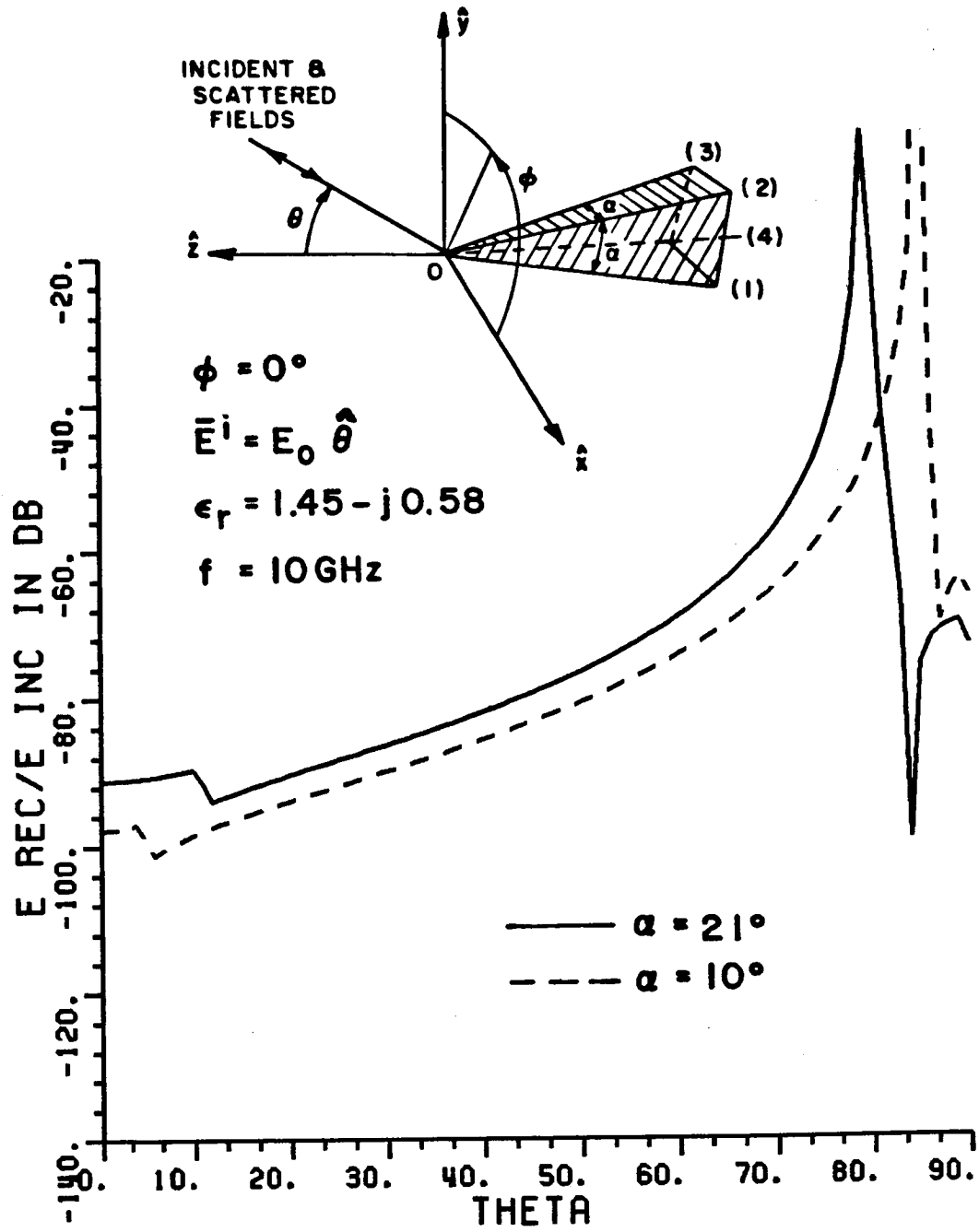
Figure 3.8. Backscatter from one pyramid tip as function of theta.

64

face of the pyramid becoming shadowed at the receiver. The second jump, at about $\theta^S=29$ degrees, corresponds to passing through the reflected shadow boundaries of edges 1 and 4. The jump at about 55 degrees correspondes to passing through the reflection shadow boundaries of edges 2 and 3. Even though the pattern is not along the cone of diffracted rays the corner diffraction coefficient gives a false discontinuity. This problem with the corner diffraction is demonstrated in Chapter II-D.

The results for $\hat{\theta}$ polarized E field are shown in Figure 3.10 and are similar to the $\hat{\phi}$ polarized results except for theta less than 20 degrees.

F. BASE DIFFRACTION

The contribution from the base of the pyramid is calculated using the corner diffraction method described in the previous section. However, for the case of nose-on backscatter a caustic of the edge diffracted rays causes the corner diffraction to be singular. This caustic is only for the edges connecting the four base points and not for the edges connecting the base to the tip. So, corner diffraction is used for the edges running from the base to the tip and an equivalent current solution is used for the base to base edges.
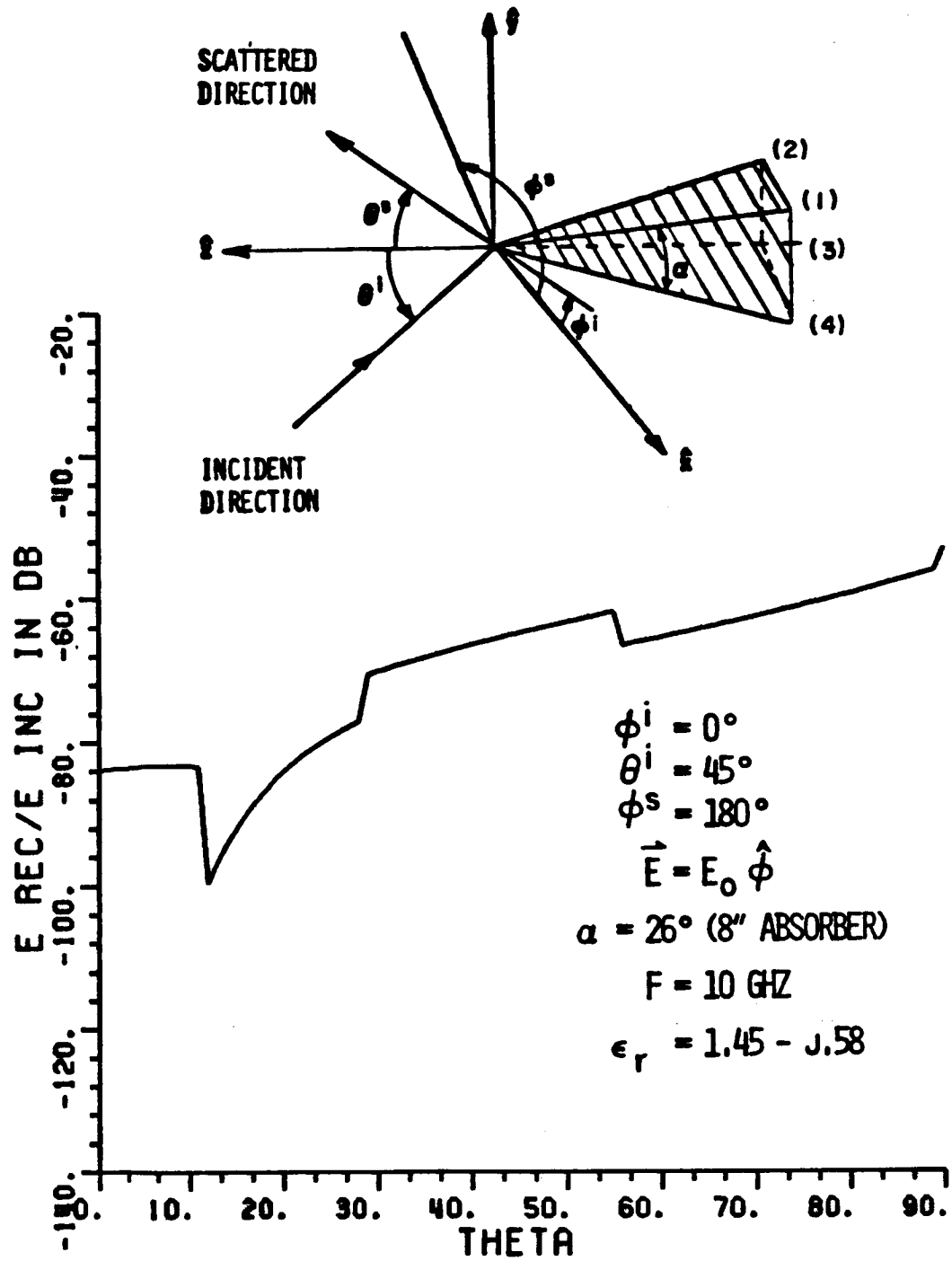
Figure 3.9. Bistatic scattering from α=26° absorber ($\hat{\phi}$ polarized).

Figure 3.10. Bistatic scattering from α=26° absorber (θ̂ polarized).

The equivalent edge current solution of Chapter III-C is modified to include the effects of the dielectric. The modified 4 term equivalent current equation is given by

$$
\begin{bmatrix} I^m \\ I^e \end{bmatrix} = \frac{j}{\begin{bmatrix} Y_0 \\ Z_0 \end{bmatrix}} \cdot \frac{1}{kn} \left\{ \begin{bmatrix} R^1_{\parallel} \\ R^1_{\perp} \end{bmatrix} \cot \left[\frac{\pi + (\phi - \phi')}{2n} \right] \right.
$$

$$
+ \begin{bmatrix} R^2_{\parallel} \\ R^2_{\perp} \end{bmatrix} \cot \left[\frac{\pi - (\phi - \phi')}{2n} \right] + \begin{bmatrix} R^3_{\parallel} \\ R^3_{\perp} \end{bmatrix} \cot \left[\frac{\pi + (\phi + \phi')}{2n} \right]
$$

$$
+ \begin{bmatrix} R^4_{\parallel} \\ R^4_{\perp} \end{bmatrix} \cot \left[\frac{\pi - (\phi + \phi')}{2n} \right] \right\} \cdot \begin{bmatrix} H^i_{\parallel} \\ E^i_{\parallel} \end{bmatrix} \qquad \qquad (3.4)
$$

The above equation uses four sets of equivalent reflection coefficients. For the case of an exterior wedge, (n>1) terms one and two have a value of one minus the transmission coefficient. For an interior wedge there are 4 sets of reflection coefficients each associated with a ray path. The reflection coefficients are dependent on both the incident angle and dielectric constant.

The method of finding these reflection coefficients is best illustrated by an example. Consider an interior wedge of 70 degrees as shown in Figure 3.11. With n=.388 the cotangent terms in Equation (3.4) become singular at the following 4 locations:
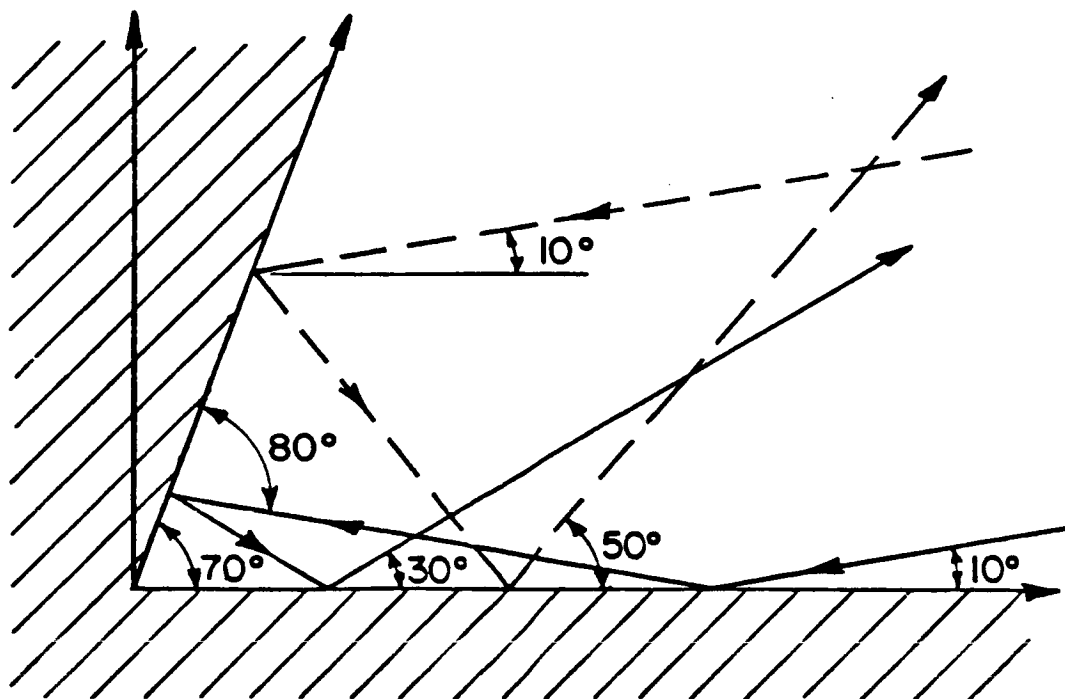
Figure 3.11. Reflected paths for a 70° interior wedge.

69

1) $\phi - \phi' = 40°$

2) $\phi' - \phi = 40°$

3) $\phi + \phi' = 100°$

4) $\phi + \phi' = 40°$ $\quad$.

$$(3.5)$$

Now, if the incident angle is chosen as 10 degrees the two ray paths are shown in Figure 3.11. Consider the ray path that strikes the horizontal face of the wedge first. It bounces 3 times and then is launched at an angle of 30 degrees. In this case, $\phi+\phi'=40$ degrees so this path corespondes to the fourth set of reflection coefficients. Thus, R^4 is the reflection coefficient at 10 degrees times that at 80 degrees times that at 30 degrees. The other path shown strikes the 70 degree face first, is reflected 2 times and then is launched at an angle of 50 degrees. This path corespondes to R^1 since $\phi-\phi'=40$ degrees. R^1 is then the reflection coefficient at 60 degrees times that at 50 degrees.

The other two reflection coefficients, R^2 and R^3 do not have ray paths associated with them for 10 degree incidence so a value of zero is used for these terms.

CHAPTER IV

EXPERIMENTAL MEASUREMENTS AND COMPARISON WITH CALCULATIONS

A. INTRODUCTION

This chapter reports the results of measurements taken on absorbers and compares them with calculations. The method of calculating wall scattering from the single pyramid model of the previous chapter is covered in Section B. Section C covers the results of backscatter measurements on pyramid absorber done using a compact range, while, Section D covers the bistatic measurements of an pyramid absorber wall. Finally, Section E covers the backscatter from wedge absorber. The measurements are all calibrated against a sphere and are reported in terms of an effective scattering (in dB) which is found using Equation (5.3) relative to a square centimeter.

The absorber measured is specified by the manufacturer and the overall height of the product. The 8" products have 6" pyramids, 2" bases, and 64 pyramids per piece. The 12" products have 10" pyramids, 2" bases, and 36 pyramids per piece.

B. CALCULATING WALL SCATTERING USING ABSORBER MODEL

Previous measurements of absorber scattering from the sidewalls of the ElectroScience Lab's anechoic chamber showed the wall acts as a

71

highly dispersive material [19] such that the specular return was no larger than the return at non-specular angles. This effect may be caused by a number of factors some of which are listed here. First, the manufacturing of the absorber involves impregnating the foam with carbon in a solution. The absorber is placed tips up so that the carbon concentration will be slightly greater towards the bottom of the absorber. This also gives a non-uniform effect. Second, the tips of the absorber are not of uniform height some tips may even be broken off. pyramids do not tend to be completely straight as some may be bent in one way or another. Larger pyramids or ones placed in a fixed spot tend to sag due to gravity. Fourth, the different 2' x 2' pieces are somewhat unevenly placed on the wall. Whatever the reason, the net effect is the absorber tends to act very dispersive.

When considering only a section of an infinite wall hit by an incident plane wave, the scattered field will be a summation of the scattering from each of the pyramids in the highlighted area such that

$$\vec{E}^s_{Tot} = \sum_{m=1}^{N} \vec{E}^s_m \qquad (4.1)$$

where N is the number of pyramids. The effective scattering of the wall would then be

$$\sigma_{wall} = 10 \log 4\pi \, r^2 \left| \frac{\vec{E}^s_{Tot}}{\vec{E}^i} \right|^2 . \qquad (4.2)$$

If the pyramids are considered to have a random phase shift associated with them ($\tilde{\theta}$ having uniform distribution over $[0,2\pi]$) the expected value of the RCS can be found from the well known expression

$$\text{EXPECTED VALUE} \left[\left| \sum_{m=1}^{N} A_m e^{j\tilde{\theta}_m} \right|^2 \right] = \sum_{m+1}^{N} A_m^2 \quad . \tag{4.3}$$

With an incident plane wave all Am's are equal so the effective scattering of the highlighted wall section is then

$$\sigma_{wall} = 10 \log 4\pi r^2 \left| \frac{\vec{E}_1^s}{\vec{E}_i} \right|^2 + 10 \log N \tag{4.4}$$

where E_1^s is the scattered field field from one pyramid and N is the number of pyramids being highlighted.

To further investigate the adding in power effects, pieces of absorber from different companies where placed on a mount in the target zone of a compact range. Nose-on backscatter frequency domain data was taken from 6 to 18 GHz and then Fourier transformed to get a time domain result. The maximum peak-to-peak voltage of the time domain plot was measured at the location of the tips. This voltage squared for different manufacturers absorber are shown in Figures 4.1, 4.2, and 4.3. The 8" absorber has 64 tips per 2' x 2' piece of absorber while the 12" has 36 tips. More than one data point indicates measurements on different pieces or in the case of four pieces, a different arrangement of the same four pieces.

73
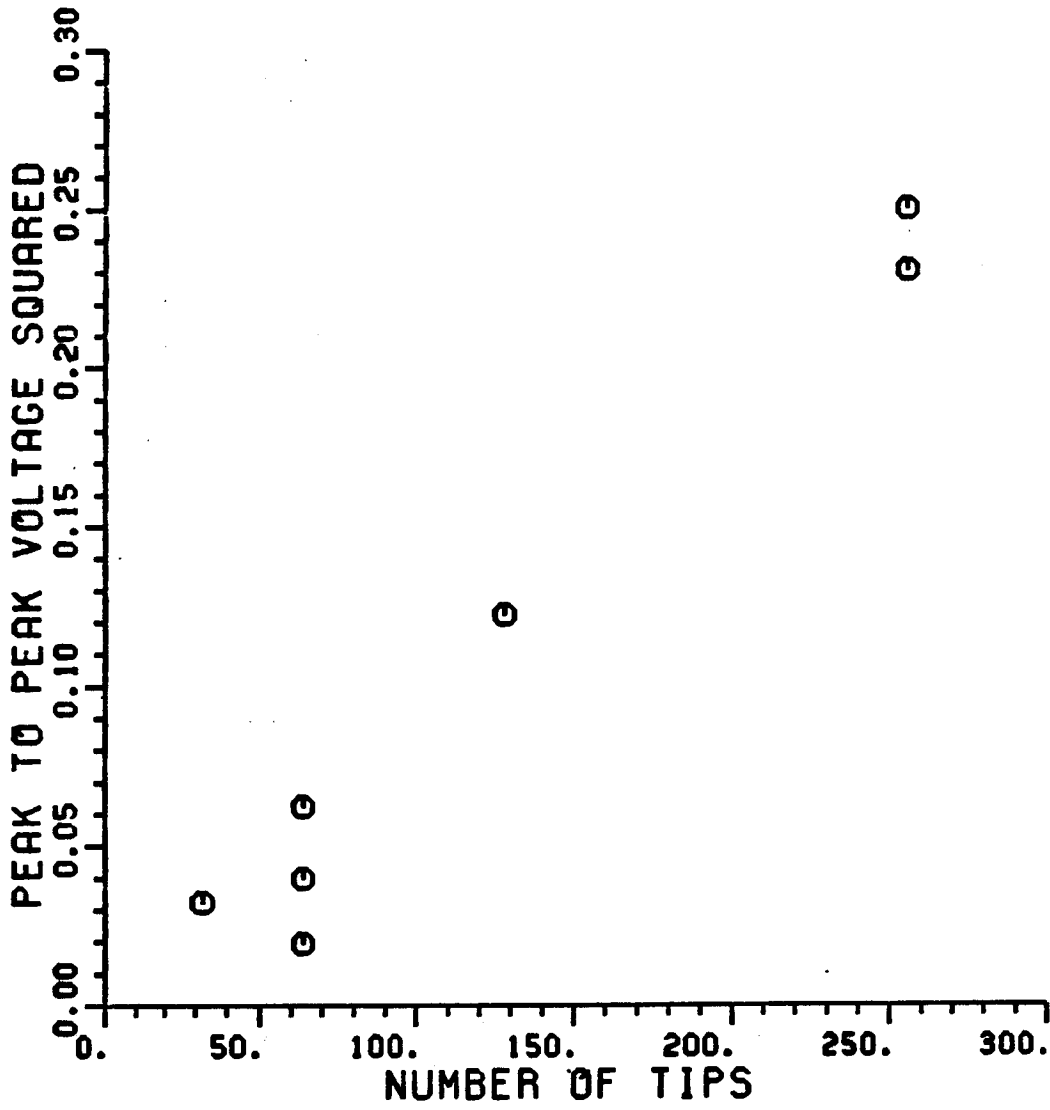
Figure 4.1. Peak-to-peak voltage squared versus number of tips for Company A's 8" absorber.
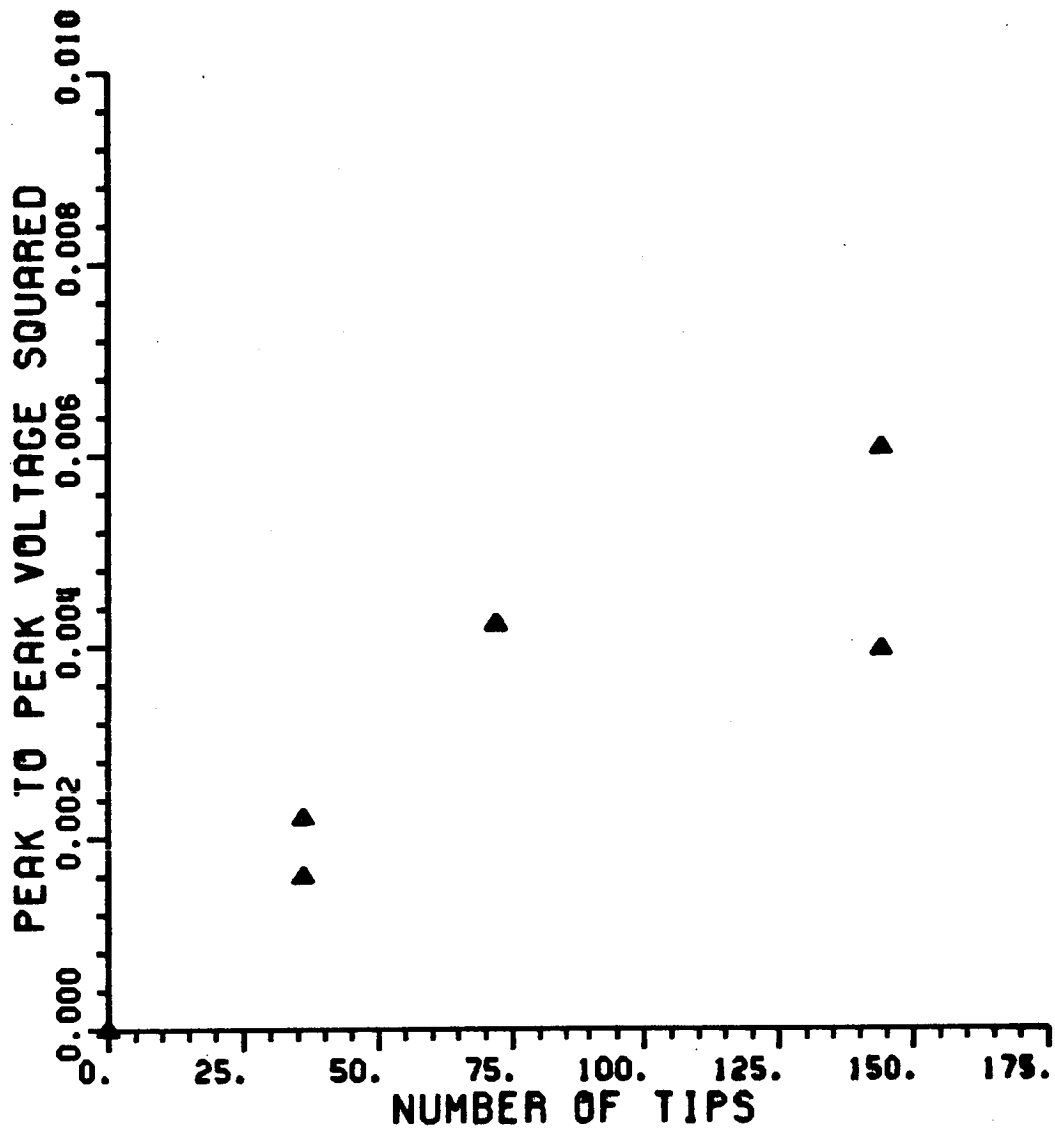
Figure 4.2. Peak-to-peak voltage squared versus number of tips for Company C's 12" absorber.
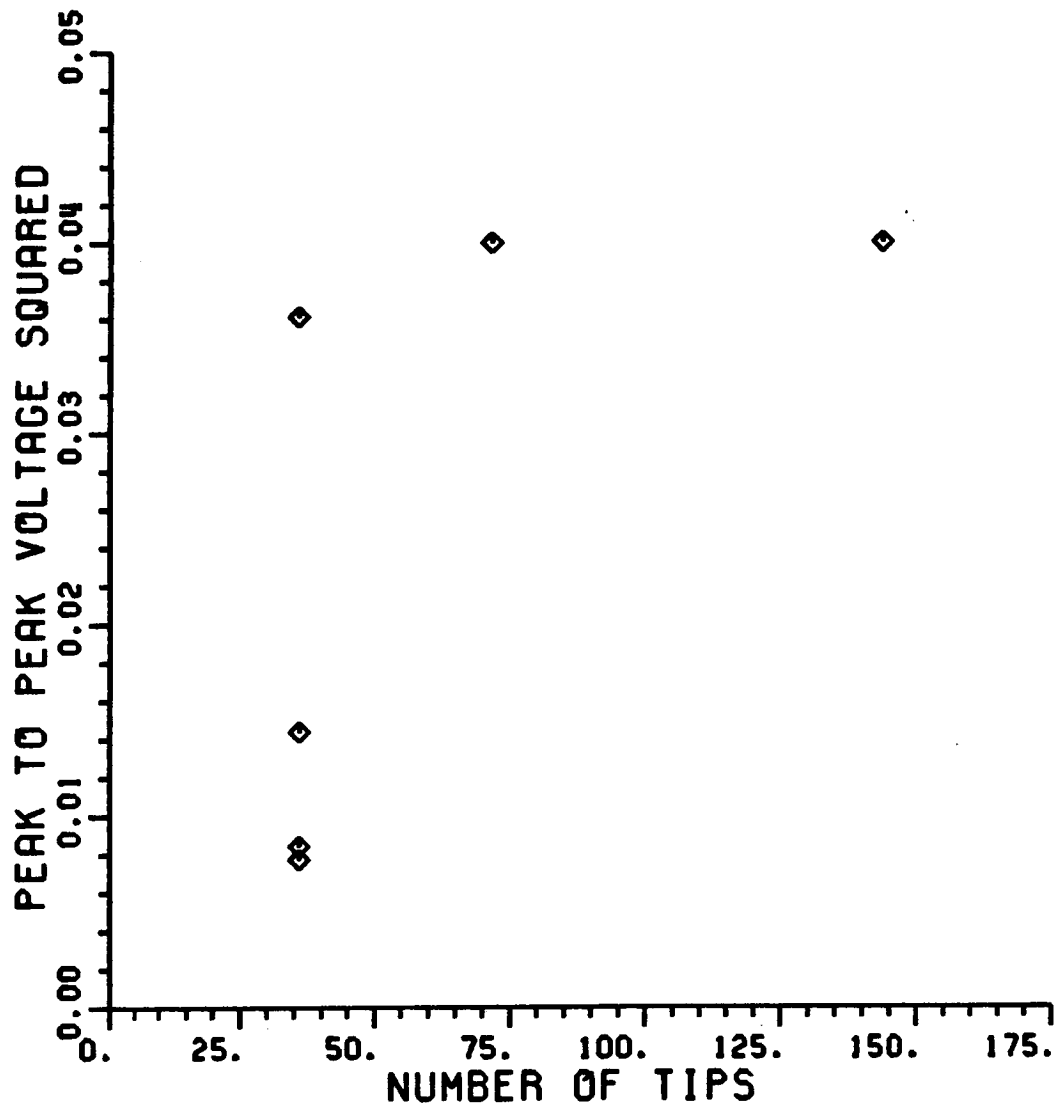
Figure 4.3. Peak-to-peak voltage squared versus number of tips for Company D's 12" absorber.

A straight line plot indicates adding in power while a parabolic curve opening upward indicates adding in phase. Figure 4.1 shows a straighter line than figures 4.2 and 4.3. There are a number of contributing factors to these results. 1) Company A's absorber is at least 8 years old, thus, more worn, contributing to the adding in power effect while the other absorbers are new. 2) The larger number of tips with the 8" absorber gives better assurance that the actual values are close to the expected value (central limit theorem). 3) Company C's absorber appears to be acting better than adding in phase. This may be because the tips on one piece may be adding in phase while the tips from piece to piece are adding in power. 4) One piece of Company D's absorber gave a much larger return than the other three pieces and the bad piece was used in both the 72 and 144 tip measurements. This one bad piece dominated the return for the 72 tip result and maybe even the 144 tip result.

Comparing the peak-to-peak voltage response assumes the adding in power effects are independent of frequency, which is a high frequency approximation. As the frequency gets lower the minor differences in position and dielectric constant will become less significant and this approximation will break down. To investigate this effect the height of the tips from pieces of Company C's 12" pyramids were measured using a surveying scope. The height of the tips differed by as much as 1 cm on the same piece! The corner and edge pyramids tended to be shorter than the pyramids in the middle which is probably

related to their manufacturing technique. To get a measure of the height difference, each pyramid height (d_n) was put into the following summation:

$$\text{SUMMATION OF RETURNS} = \sum_{n=1}^{36} e^{-2jkd_n} \qquad . \qquad (4.5)$$

The magnitude of the sum versus frequency for two different pieces of absorber appear in Figure 4.4. A value of 36 indicates phase addition is required, whereas, a value of 6 indicates power addition should be used. It is clearly seen that near 2 GHz the height difference is negligible but not at higher frequencies. The pyramid heights were measured with near perfect alignment which is not easily done with range measurements. Nevertheless, if the pyramid's returns are assumed to add in phase instead of power, the 10log N term in Equation (4.4) changes to 20log N. The values from Figure 4.4 could also be used to model an effect between adding in power or phase.

C. BACKSCATTER FROM PYRAMID ABSORBERS

The backscattter field from various pieces of absorber were measured by mounting them in the target zone of the ElectroScience Lab's compact range. The backscattered field was measured over the frequency range 6 to 18 GHz in 10 MHz increments. A hardware window with 90db isolation is centered around the target region to gate out unwanted returns. The frequency domain data is windowed using a Kaiser-Bessel window, then Fourier transformed to get a bandlimited time domain response.
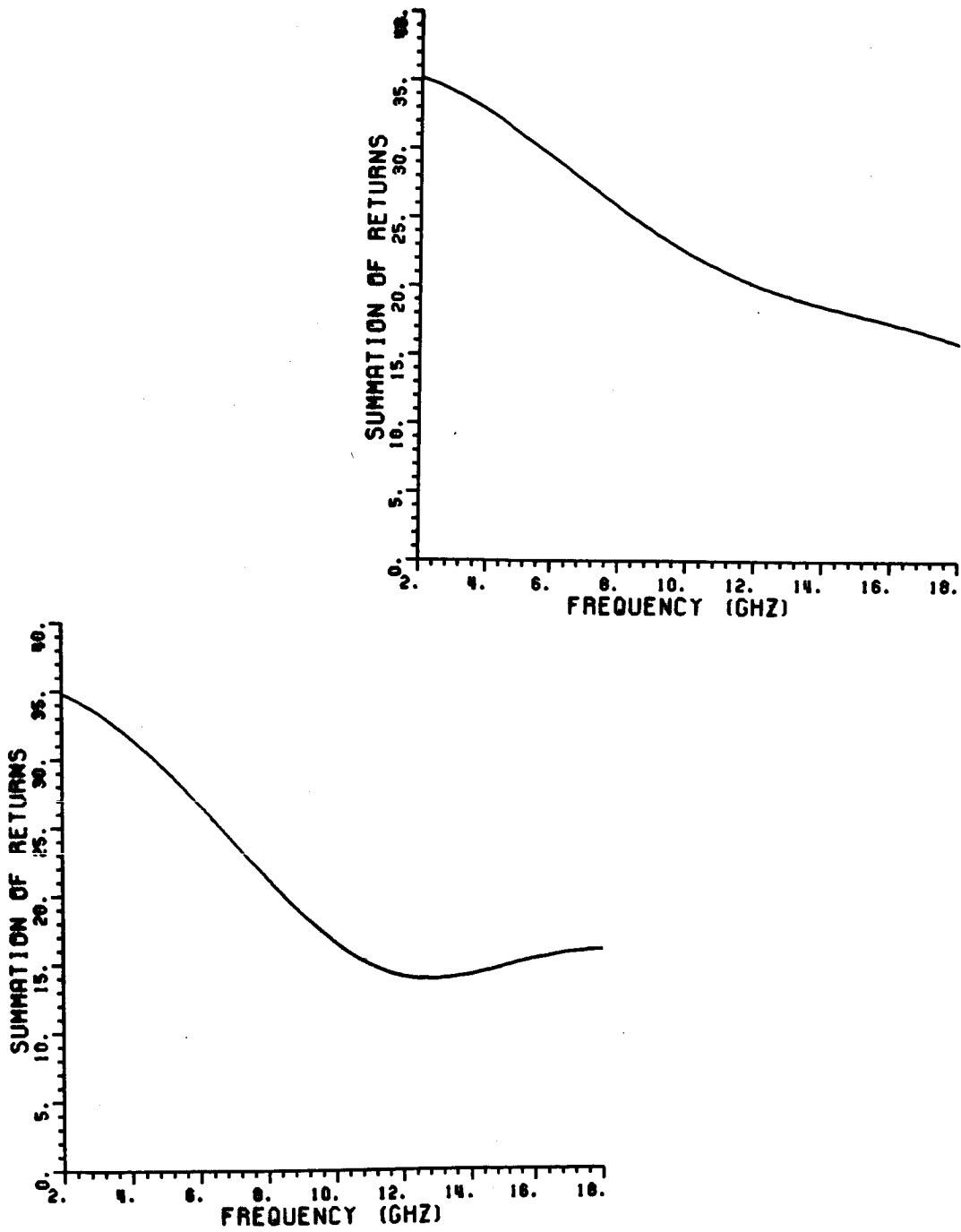
Figure 4.4. Summation of scattering from 2 different pieces of Company C's 12" absorber at different frequencies.

Figures 4.5 and 4.6 show the time and frequency domain results, respectively, for the nose-on backscatter from one 2'X 2' piece (36 pyramids) of Company B's 12" absorber. (Measured data from eight other pieces of this type appear in Chapter V). The arrival time for the contribution from the high frequency mechanisms, due to geometry, are marked. The valleys mark indicates the arrival time for both the base diffraction and multiple reflections off the pyramid faces while the back mark indicates terms coming from the back end of the absorber. Energy passing all the way through the absorber base (2" depth) and striking the wood behind the absorber would arrive slightly after the back mark. The absorber has a skin depth of around 2" in this frequency range so this return should be small. The return in the region between the tip and base returns can not be assigned to any of the high frequency mechanisms analyzed but may be due to irregularities in the dielectric constant or multiple diffracted terms not considered. These returns tend to not be consistent from one piece to the next with both the level and position changing. Also, the level of these returns for some manufactureres are much higher than for others. The valleys of the pyramids around the outside of this piece were higher so the return just before the valleys may be from these pyramids. The return anticipating the tips may be due to the processing done to generate the time domain plot from the band limited frequency data. Ten pieces of this type of absorber were tested with results varying about +/-3 dB from this one. This piece represents neither the best nor worst piece. However, this return does represent one of the better separations between the tip and other returns.

Figure 4.5. Band limited time domain response of a 2'x2' piece of
Company B's 12" pyramid absorber with nose-on oncidence.

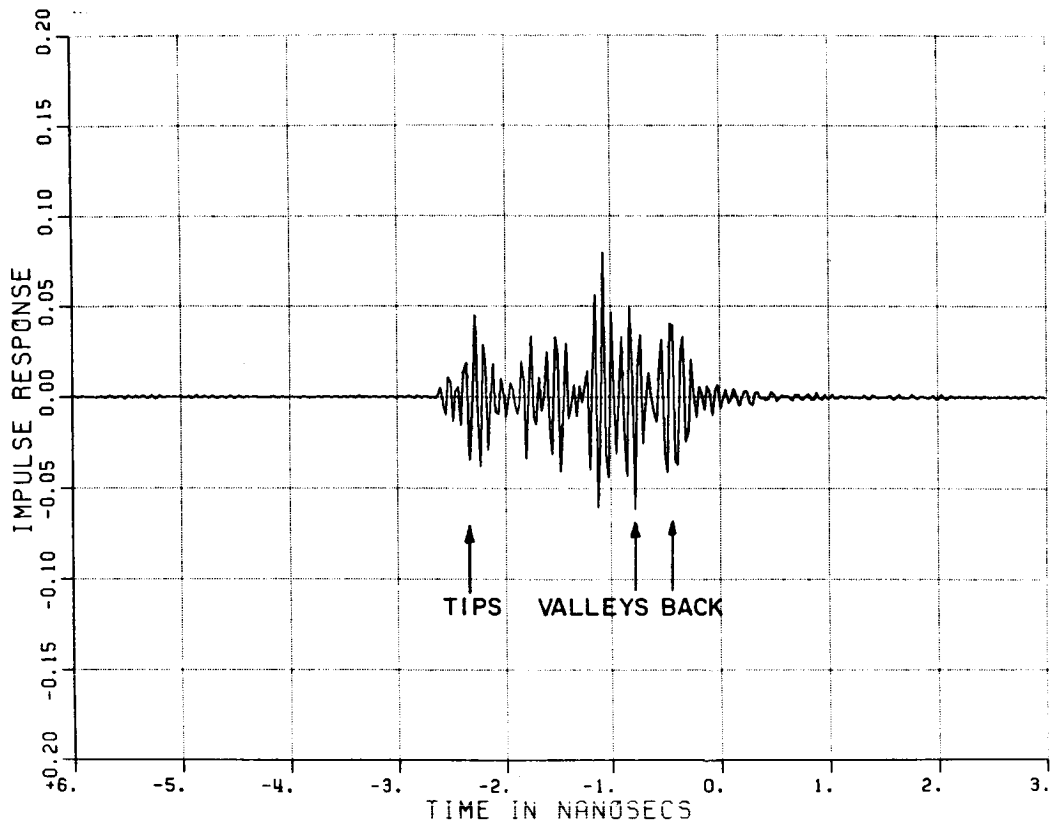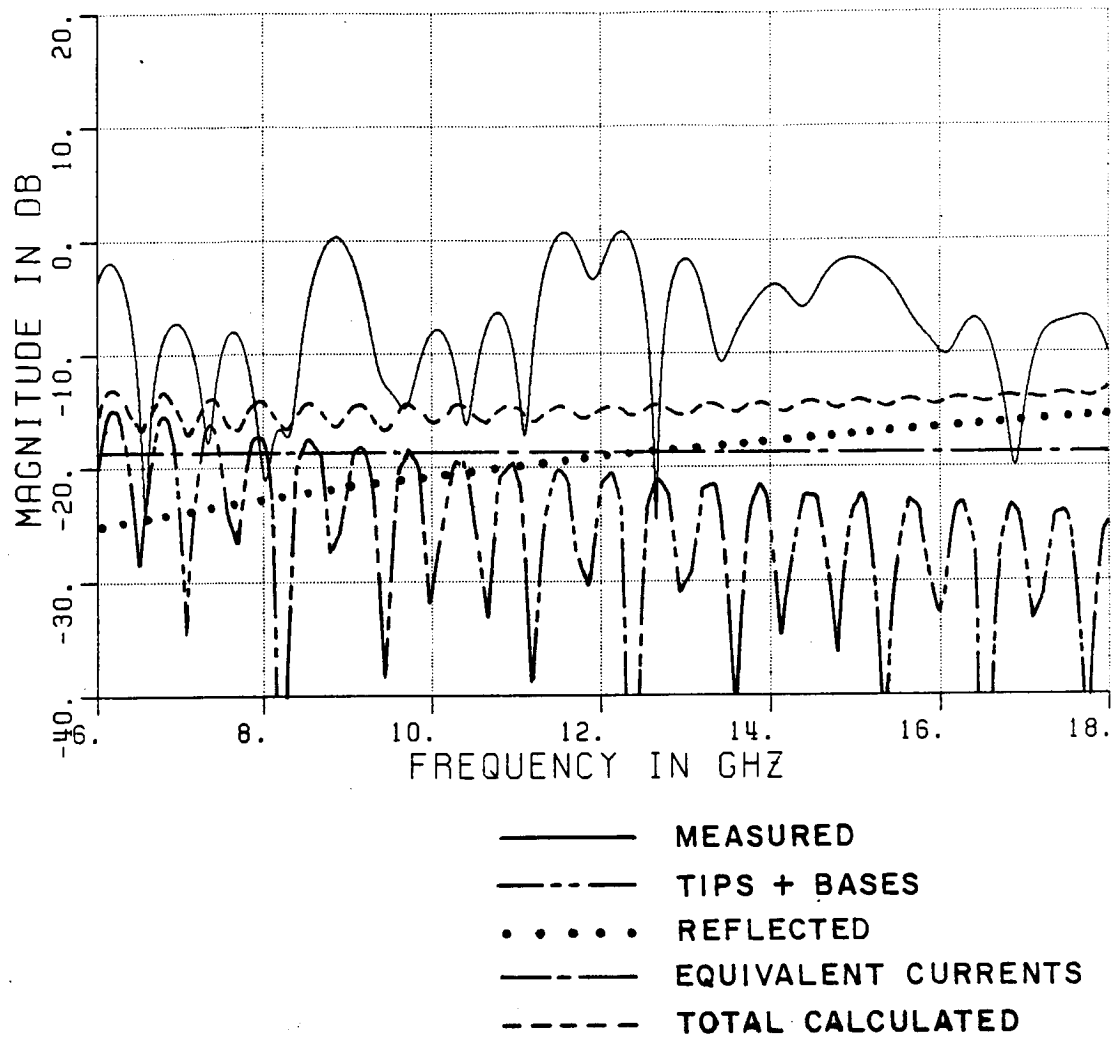Figure 4.6. Calculated and measured nose-on RCS of 1 sample of Company
B's 12" pyramid absorber.

The frequency domain plots show calculated returns for the different mechanisms described in the previous chapter. A summation curve is also shown that assumes the tips and bases add in phase according to physical separation while the reflected terms add incoherently with the other terms.

By windowing the time domain plot of Figure 4.5, the return from the tips can be separated from the other returns. An inverse Fourier transform then gives the return from the tips as a function of frequency. This is shown in Figure 4.7 along with calculated results assuming the tips add coherently and incoherently. The measured results are between the calculated curves.

With a larger mounting structure, the scattering from 4 pieces of the same absorber was measured. Using the same procedure as for a single piece, the tip contribution is found and compared with calculated results in Figure 4.8. The measured results from 4 pieces of absorber tend to agree closer with the incoherent calculations than for the single piece case.

The scattering from a single tip was measured by cutting apart a larger piece. The time domain plot appears in Figure 4.9 and the corresponding frequency data is compared with a calculated result in Figure 4.10. The calculated results are below the measured results near 18 GHz which may be due to system limitations. The calculated results are below -80 dBSM!

The scattering from a 15 piece section of absorber was measured by rolling a movable wall section into the compact range target area. The
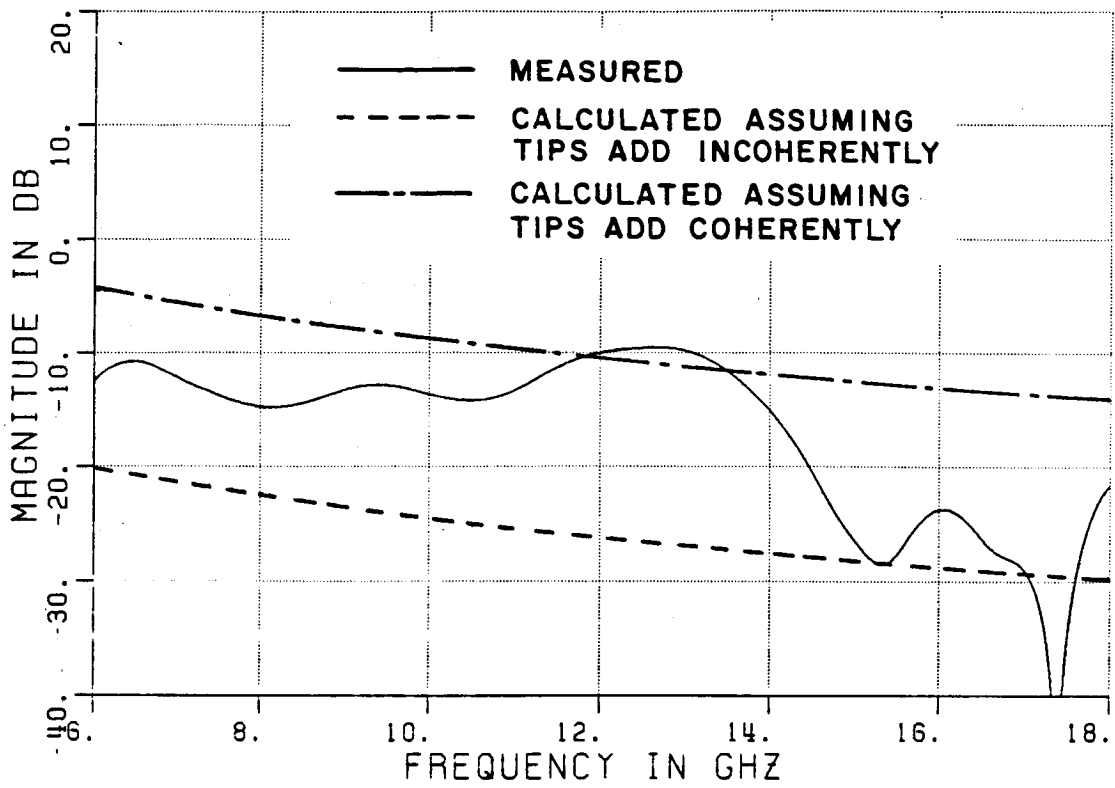
Figure 4.7. Calculated and measured nose-on RCS from the tips of one piece of Company B's 12" absorber pyramids.

C - 2
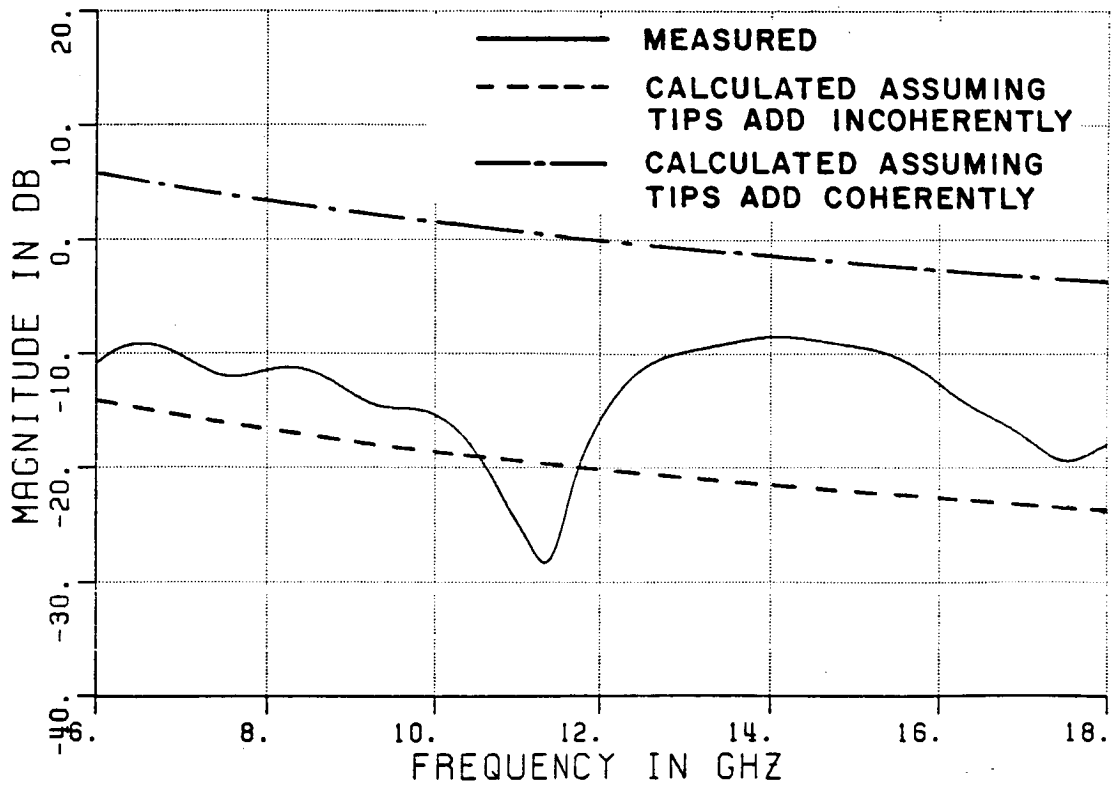
Figure 4.9. Calculated and measured nose-on RCS from the tips of 4 pieces of Company B's 12" absorber.
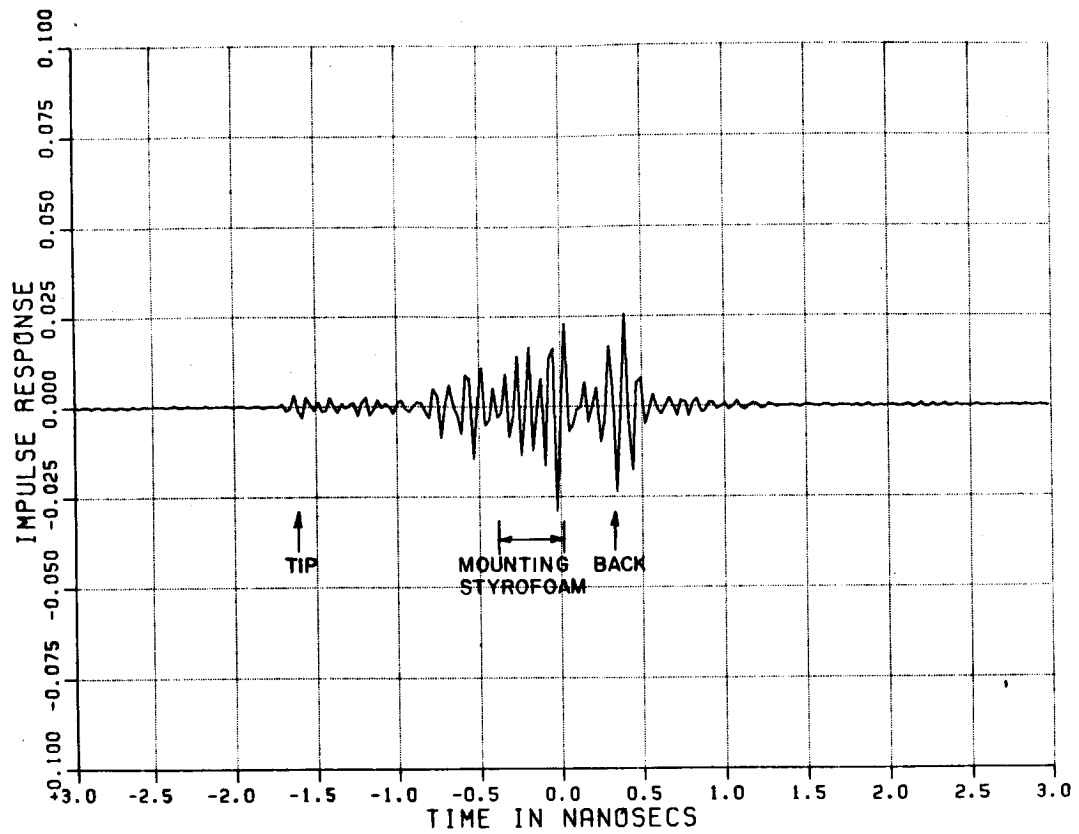
Figure 4.9. Band limited time domain repsonse from 1 tip of Company D's pyramid absorber.
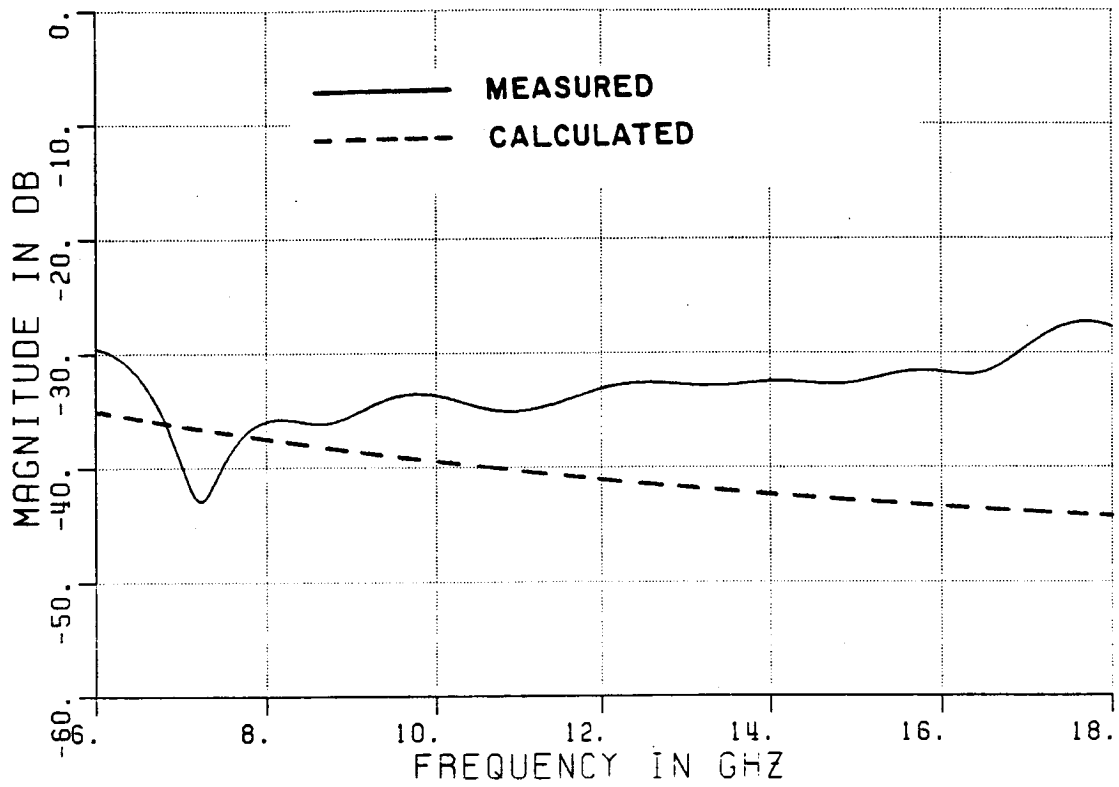
Figure 4.10. Calculated and measured nose-on RCS from the tip of a single pyramid.

MAGNITUDE IN DB

FREQUENCY IN GHZ
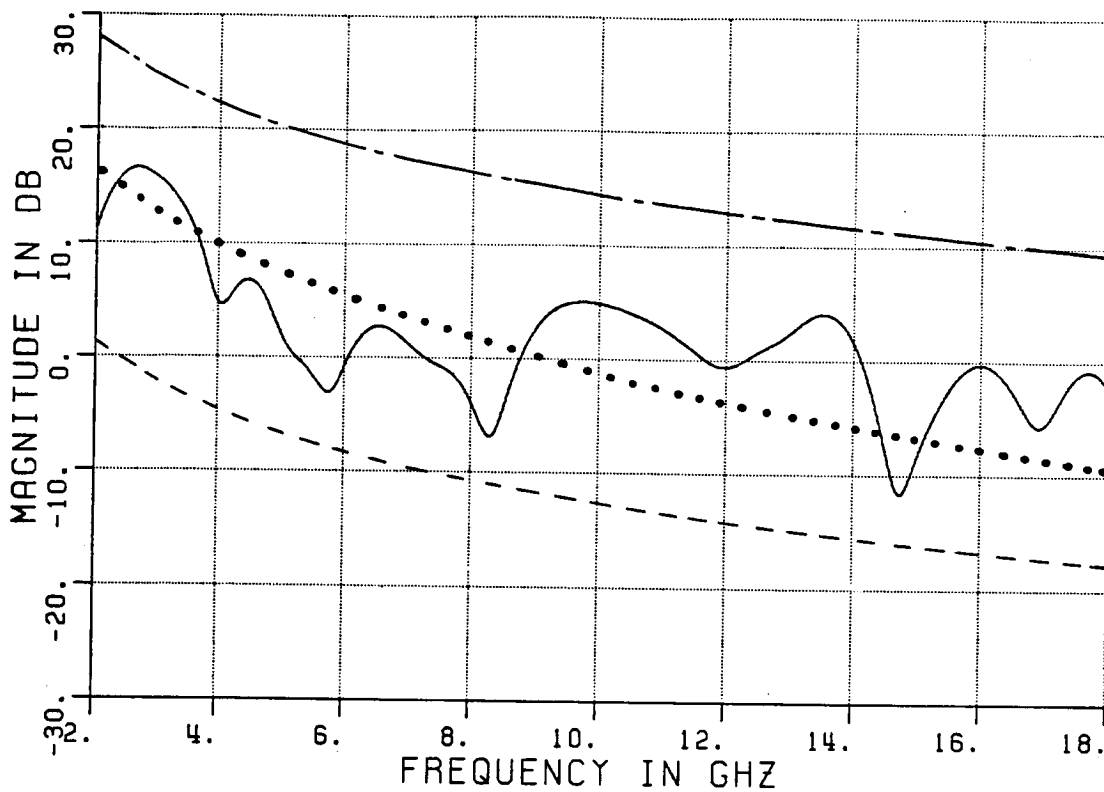
———— MEASURED

————— CALCULATED ASSUMING
TIPS ADD INCOHERENTLY

—·—— CALCULATED ASSUMING
TIPS ADD COHERENTLY

· · · · · CALCULATED ASSUMING
TIPS ADD ACCORDING
TO FIGURE 4.4a

Figure 4.11. Calculated and measured return from the tips of 15 pieces
of Company B's 12" absorber.

scattering from the tips are compared with calculated results in Figure 4.11. The calculated results include a coherent, an incoherent, and a curve assuming the tips from each piece of absorber add according to Figure 4.4a. Note that this last result assumes the scatter from different pieces are still considered to be incoherent because the tips on the same piece tend to add in phase more than the tips from different pieces. The third calculated curve follows the measured values much better than the first two.

The backscatter for different incident angles was measured for different theta angles where theta is defined in Figure 4.12. The time domain response from 4 pieces of Company B's 12" absorber for $\theta=0$, 15, 30, 45, 60, and 70 degrees and vertical polarization are shown in Figures 4.13 through 4.18, respectively. The coresponding plots for horizontal polarization are shown in Figures 4.19 through 4.24, respectively. The large spike at the beginning of these plots is from the front face of the first absorber piece as shown in Figure 4.12.

These plots show a low backscatter level except for the $\theta=60$ and 70 degrees. At this point the incident direction is nearly normal to the pyramid faces, giving a large return. The return at $\theta=75$ degrees was also measured, though not shown, and was off the scale. The return from each of the 24 columns of pyramids can be seen in Figures 4.18 and 4.24.

A number of outside sources plus the calculations done in Figure 3.6 indicate some difference in the backscatter by rotating the absorber 45 degrees. (As mentioned before, Figure 3.6 is just the tip
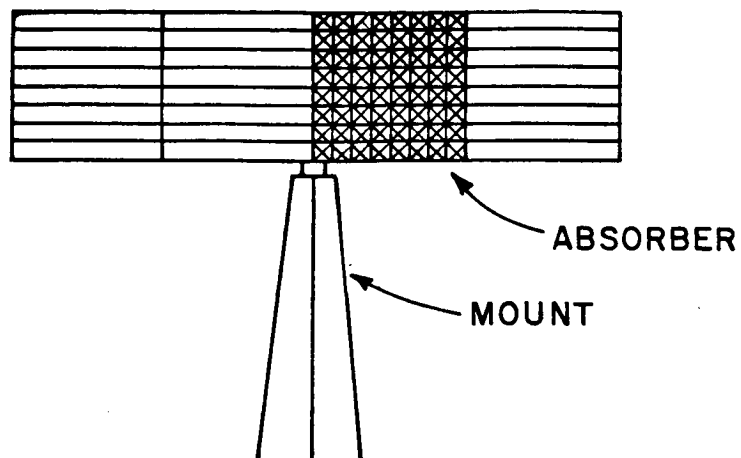
(a)
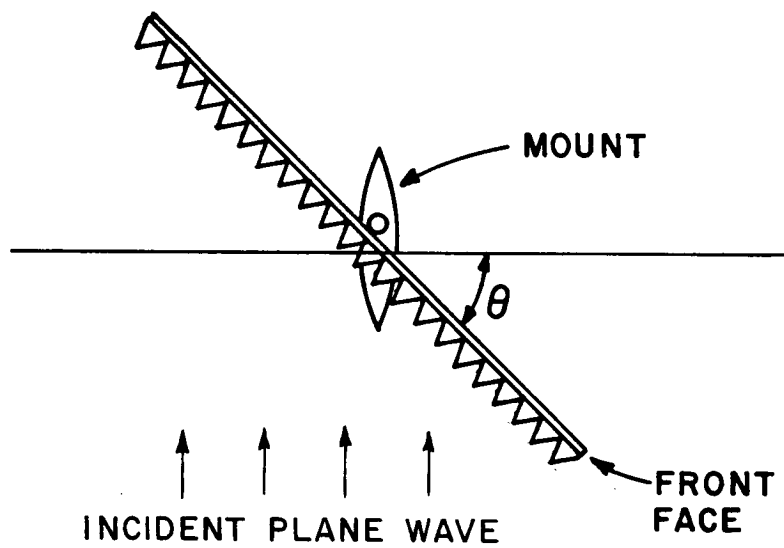
(b)

Figure 4.12. Mounting structure for 4 piece absorber measurements with a) front view, and b) top view.
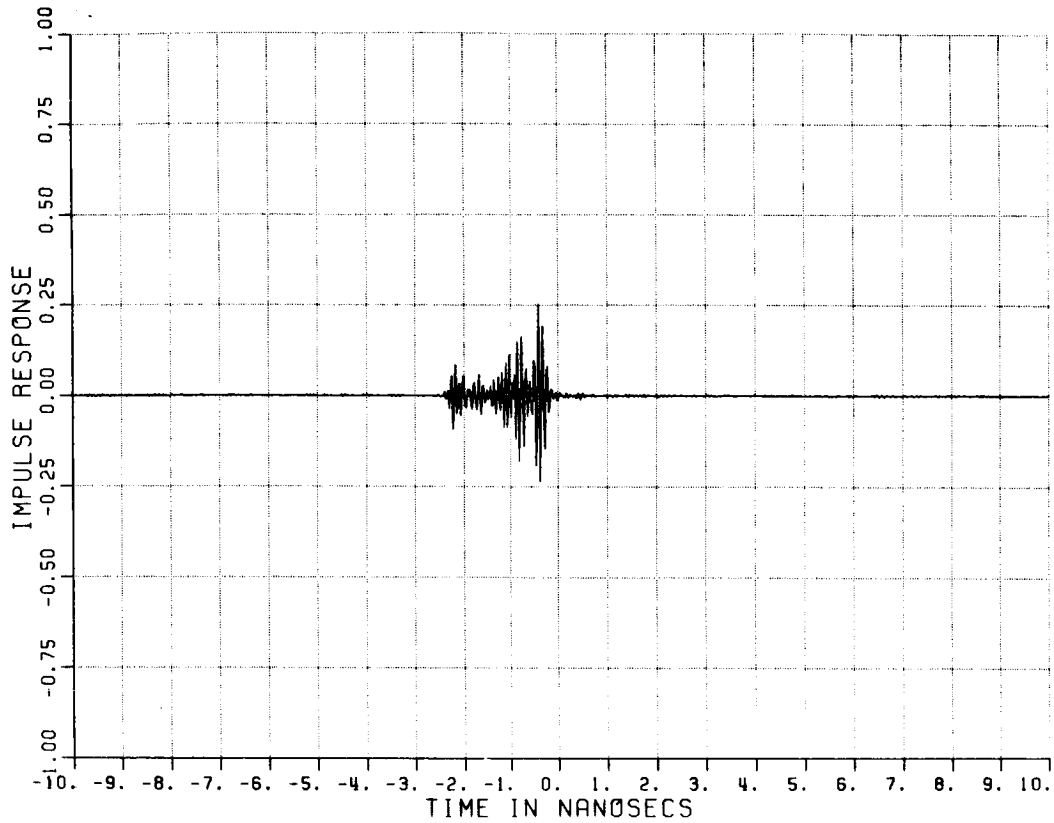
Figure 4.13. Time domain response from 12" pyramids with θ=0° and
vertical polarization.
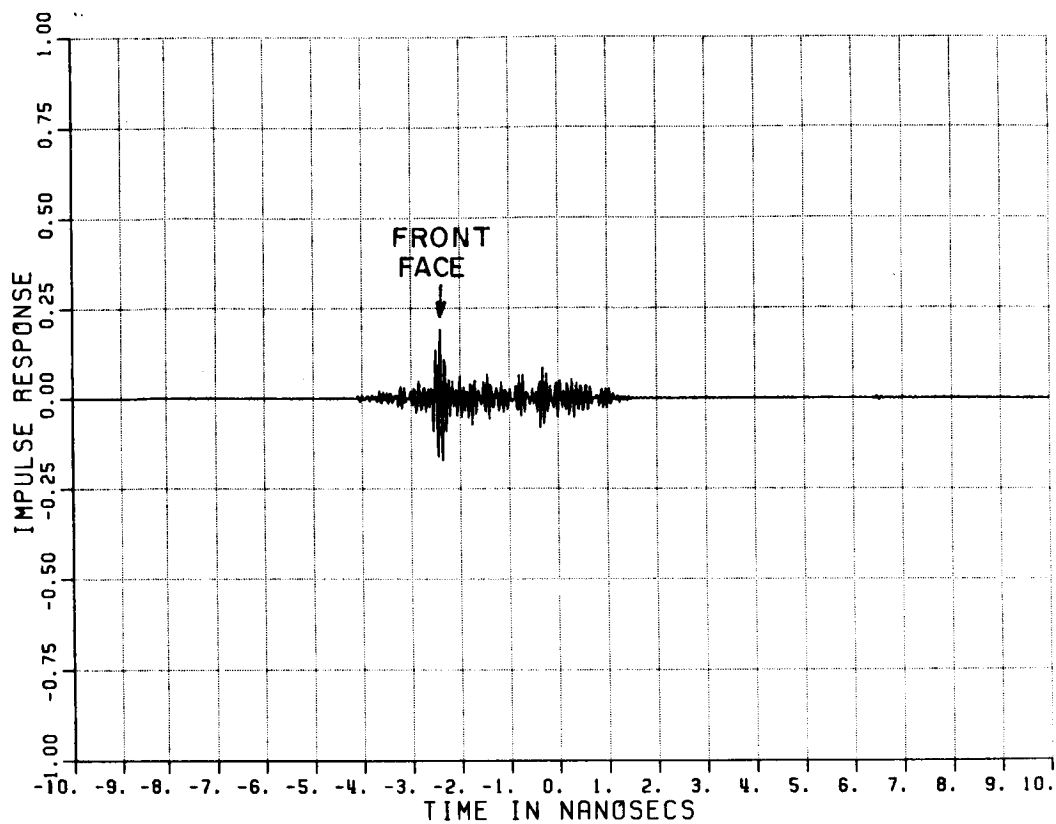
Figure 4.14. Time domain response from 12" pyramids with θ=15° and vertical polarization.
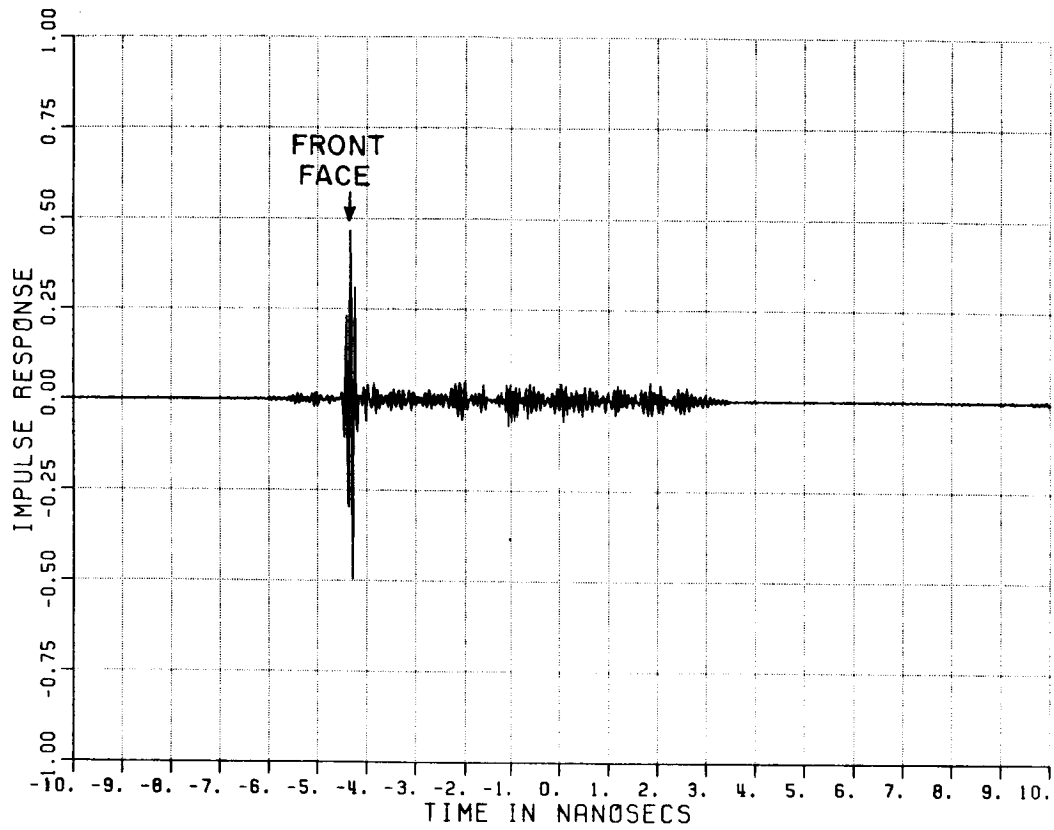
Figure 4.15. Time domain response from 12" pyramids with θ=30° and vertical polarization.
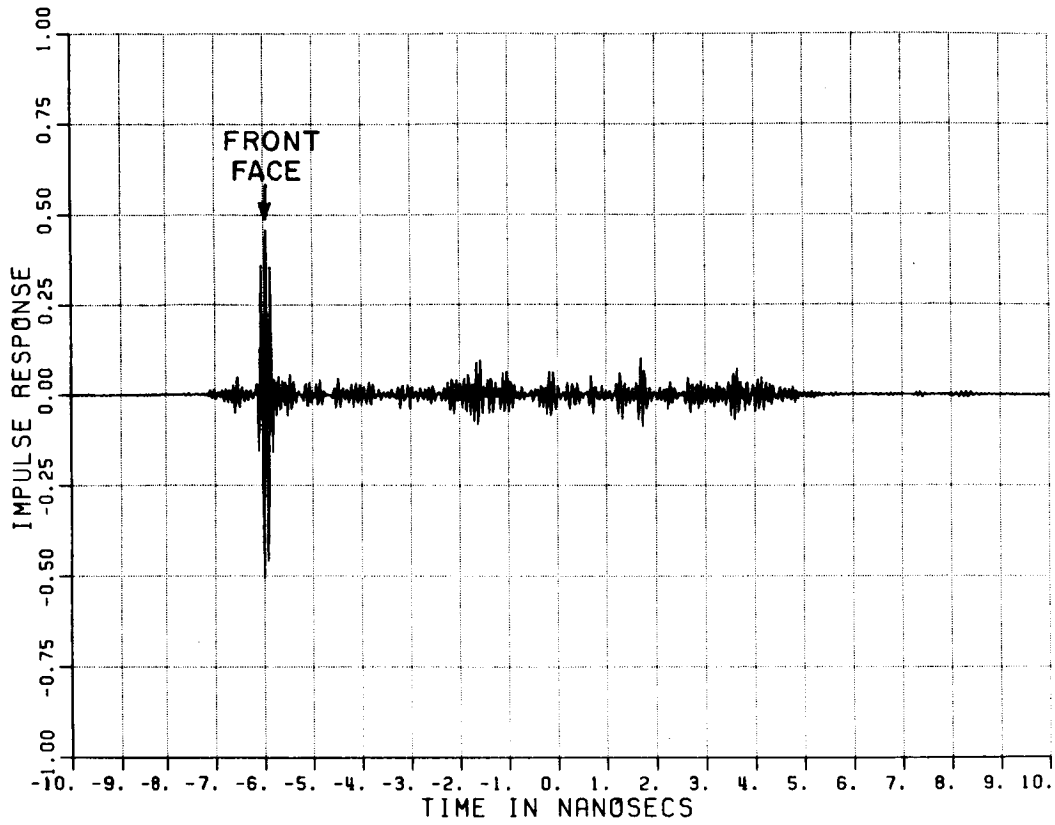
Figure 4.16. Time domain response from 12" pyramids with θ=45° and vertical polarization.

Figure 4.17. Time domain response from 12" pyramids with θ=60° and vertical polarization.

Figure 4.18. Time domain response from 12" pyramids with θ=70° and vertical polarization.

Figure 4.19. Time domain response from 12" pyramids with θ=0° and horizontal polarization.

Figure 4.20. Time domain response from 12" pyramids with θ=15° and horizontal polarization.

98

Figure 4.21. Time domain response from 12" pyramids with θ=30° and horizontal polarization.

Figure 4.22.   Time domain response from 12" pyramids with θ=45° and horizontal polarization.

100

Figure 4.23. Time domain response from 12" pyramids with θ=60° and horizontal polarization.

101

Figure 4.24. Time domain response from 12" pyramids with θ=70° and horizontal polarization.

102

contribution and the greatest improvement in the rotated case is near the discontinuity where the solution is most suspect.) Rotated pieces of absorber were measured using the geometry shown in Figure 4.25. The time domain response for θ = 0, 15, 30, 45, 60, and 70 degrees and vertical polarization are shown in Figures 4.26 through 4.31. The coresponding plots for horizontal polarization are shown in Figures 4.32 through 4.37.

Notice there is no leading spike from the beginning of the absorber as there was in the unrotated case. This is because the leading front face was turned as shown in Figure 4.25 compared to 4.12. The over all scattering level appears unchanged from the unrotated case for these measurements. However, this measurement used different top and bottom edges for the rotated case than the unrotated. A second set of measurements on an extended absorber wall where the edge effects are eliminated should be used to confirm these measurements.

D. BISTATIC SCATTER FROM AN ABSORBER COATED WALL

The measurement of scattering from Company A's 8" absorber was done using the experimental set-up shown in Figure 4.38. A pair of three foot diameter parabolic dish antennas with broadband TEM horn feeds at their focii were used to illuminate a patch of wall at an incident angle of 45 degrees. The receiver was placed between 30 degrees and 120 degrees at different locations as shown.

ABSORBER PIECE ROTATED 45°

1/2 PIECE OF ABSORBER ROTATED 45°
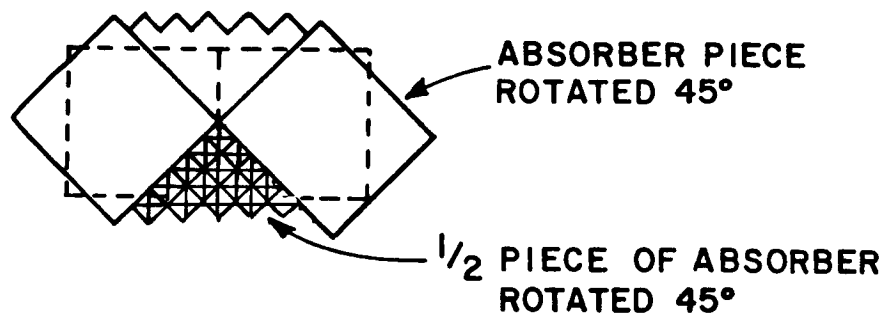
Figure 4.25. Mounting positions for rotated absorber pieces.
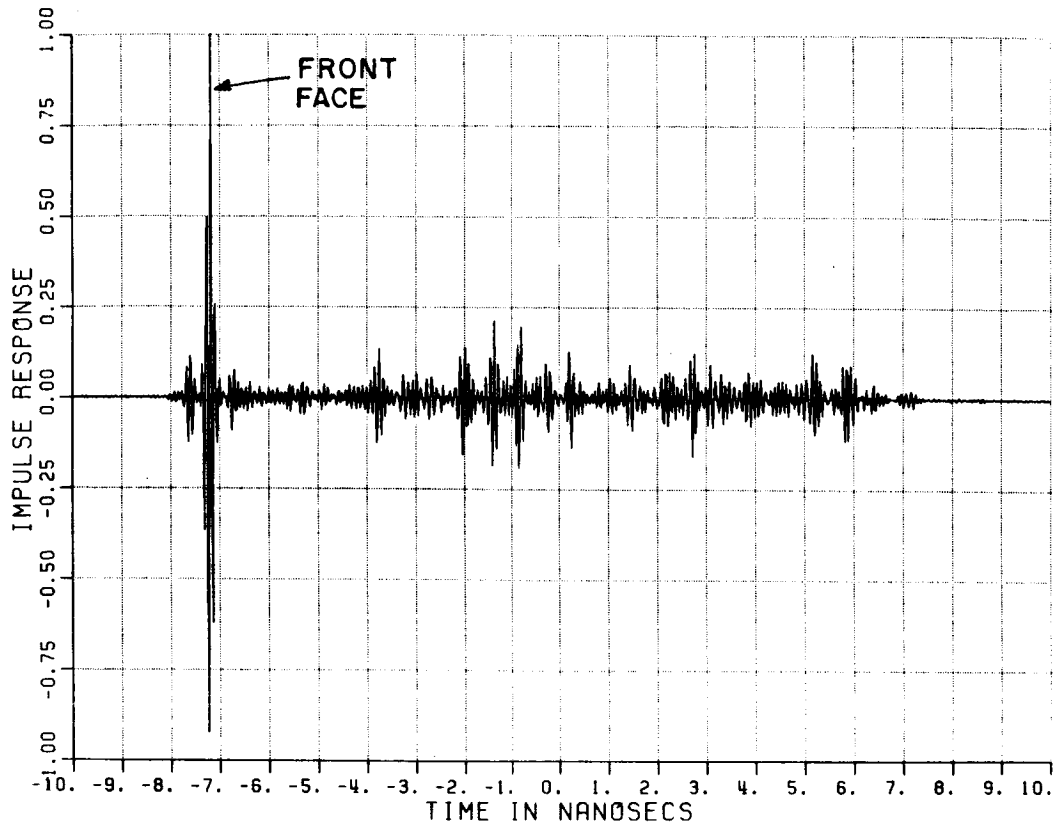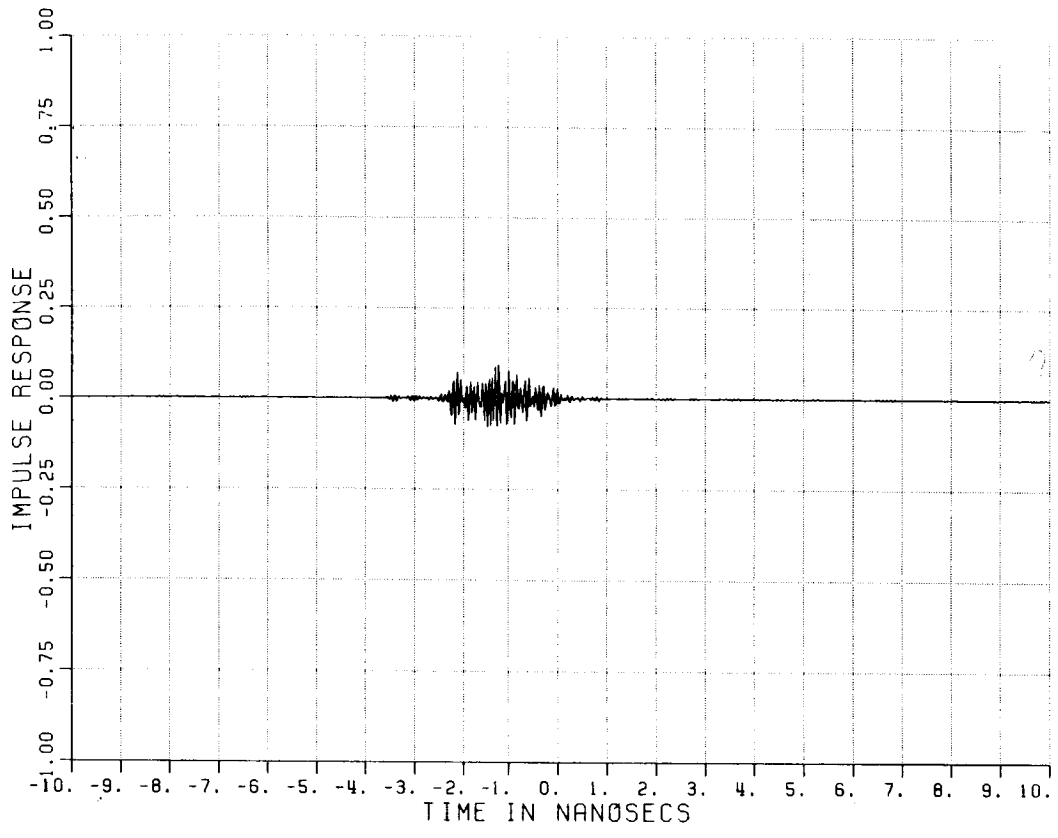
Figure 4.26. Time domain response from rotated 12" pyramids with θ=0° and vertical polarization.
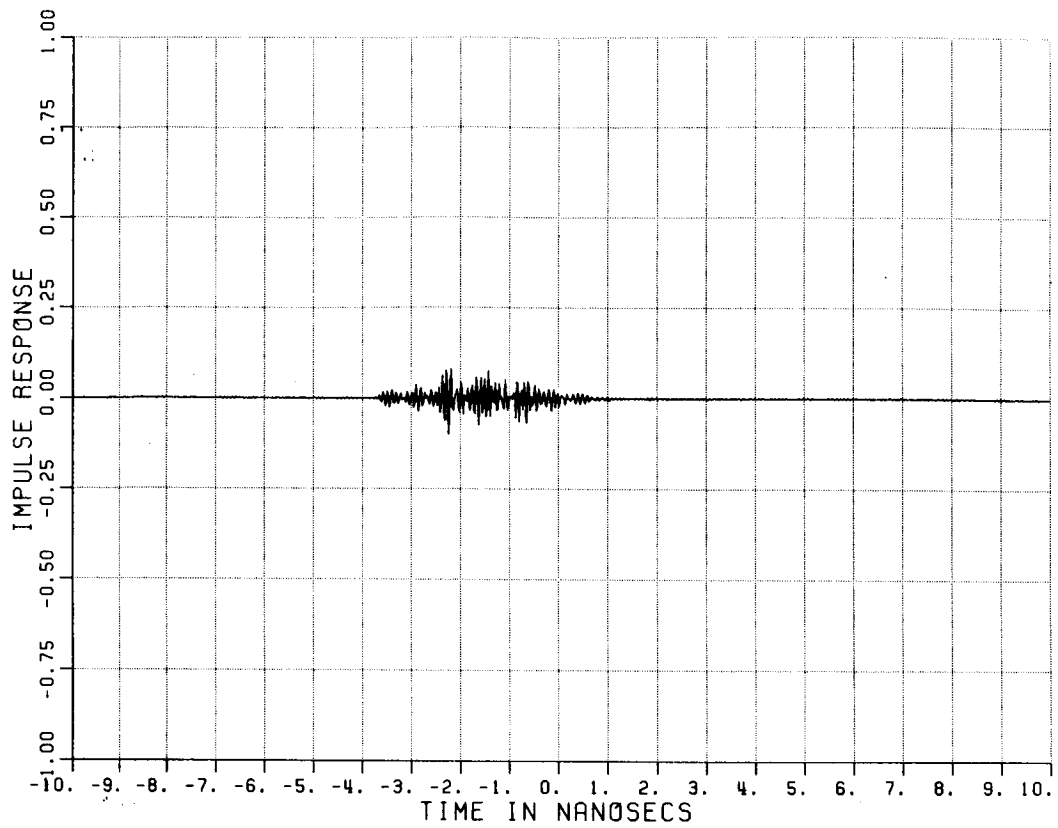
Figure 4.27. Time domain response from rotated 12" pyramids with θ=15° and vertical polarization.

106
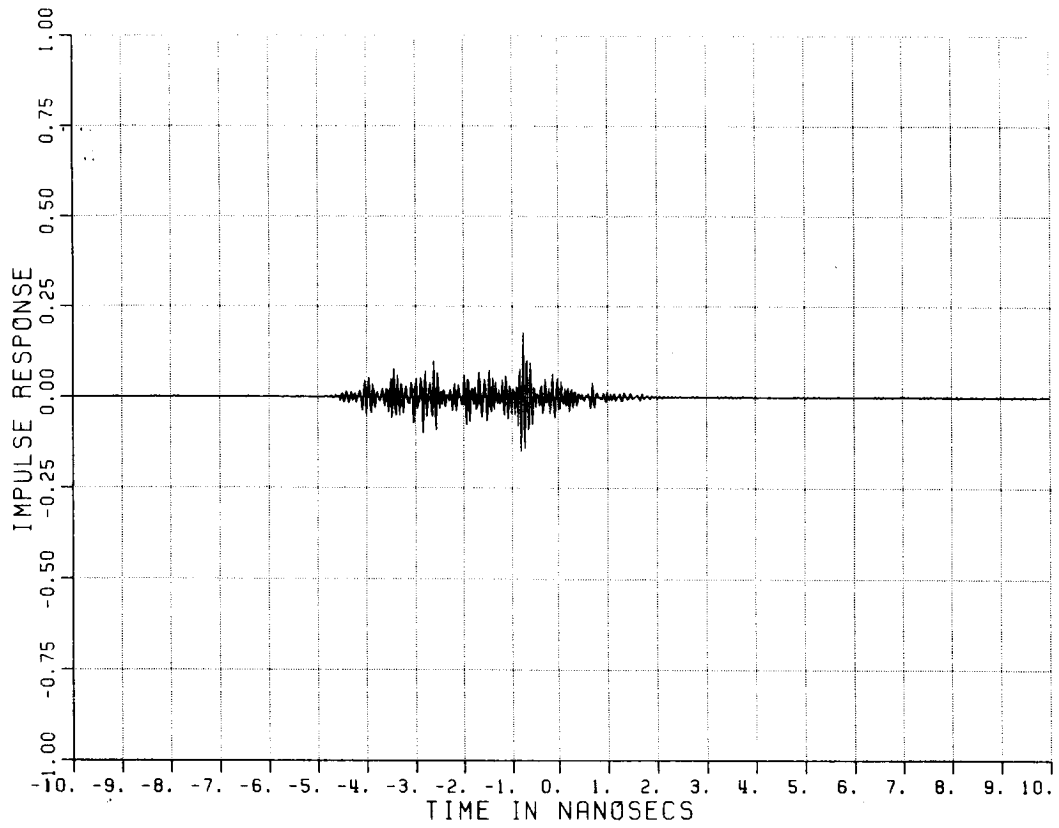
Figure 4.28. Time domain response from rotated 12" pyramids with θ=30° and vertical polarization.
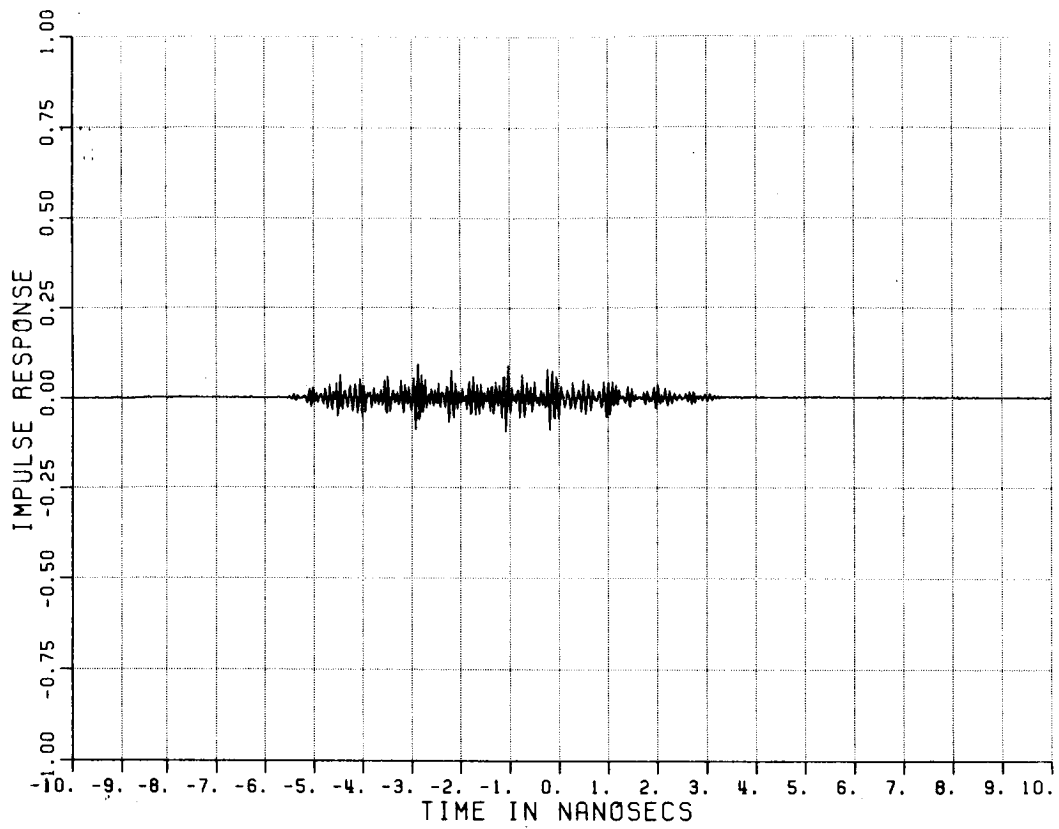
Figure 4.29. Time domain response from rotated 12" pyramids with θ=45° and vertical polarization.

108
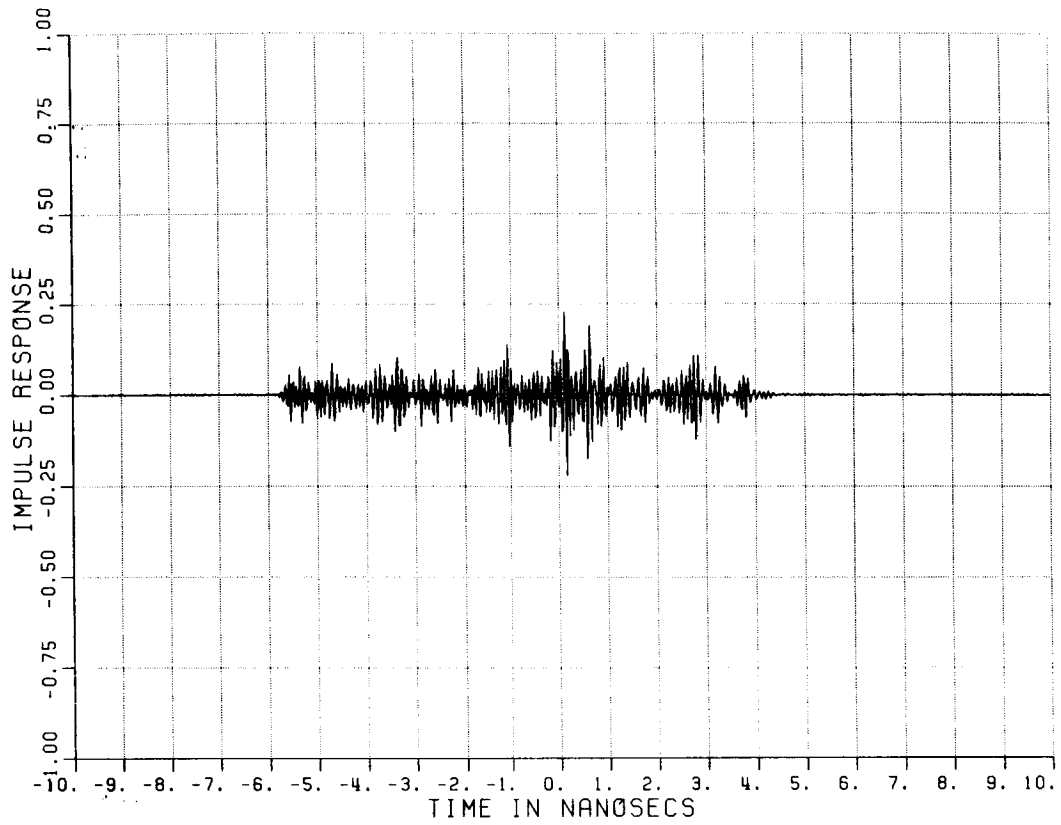
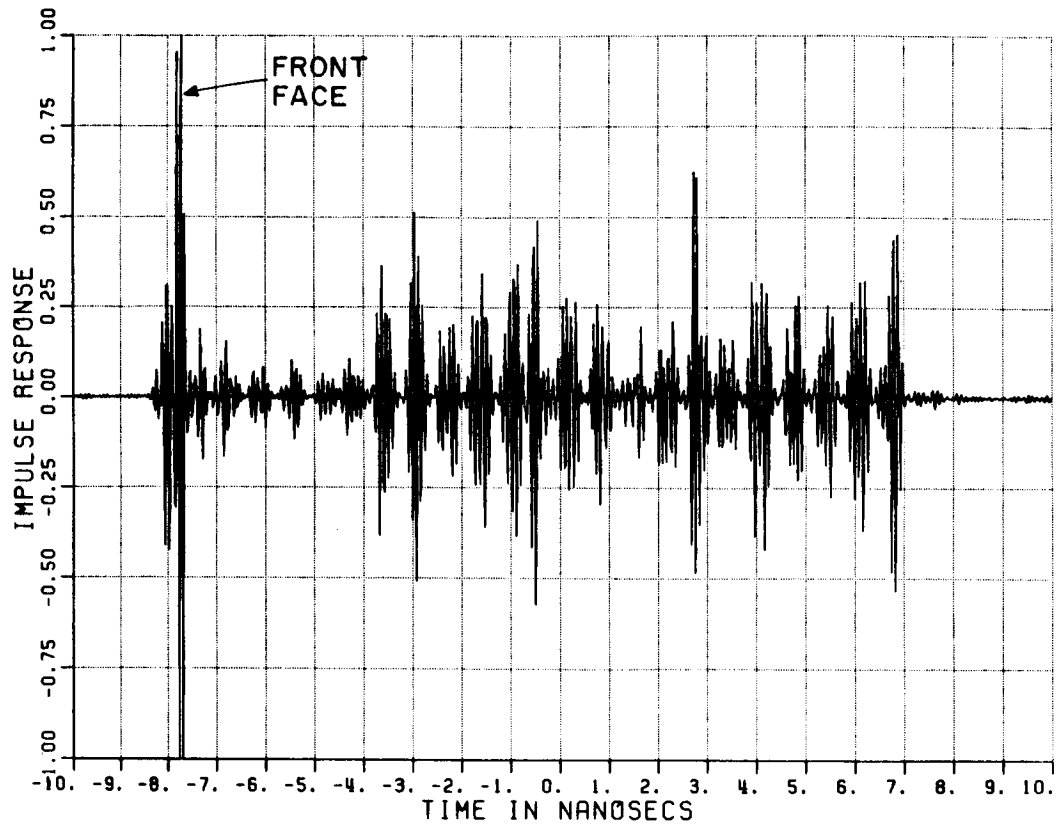Figure 4.30. Time domain response from rotated 12" pyramids with θ=60° and vertical polarization.
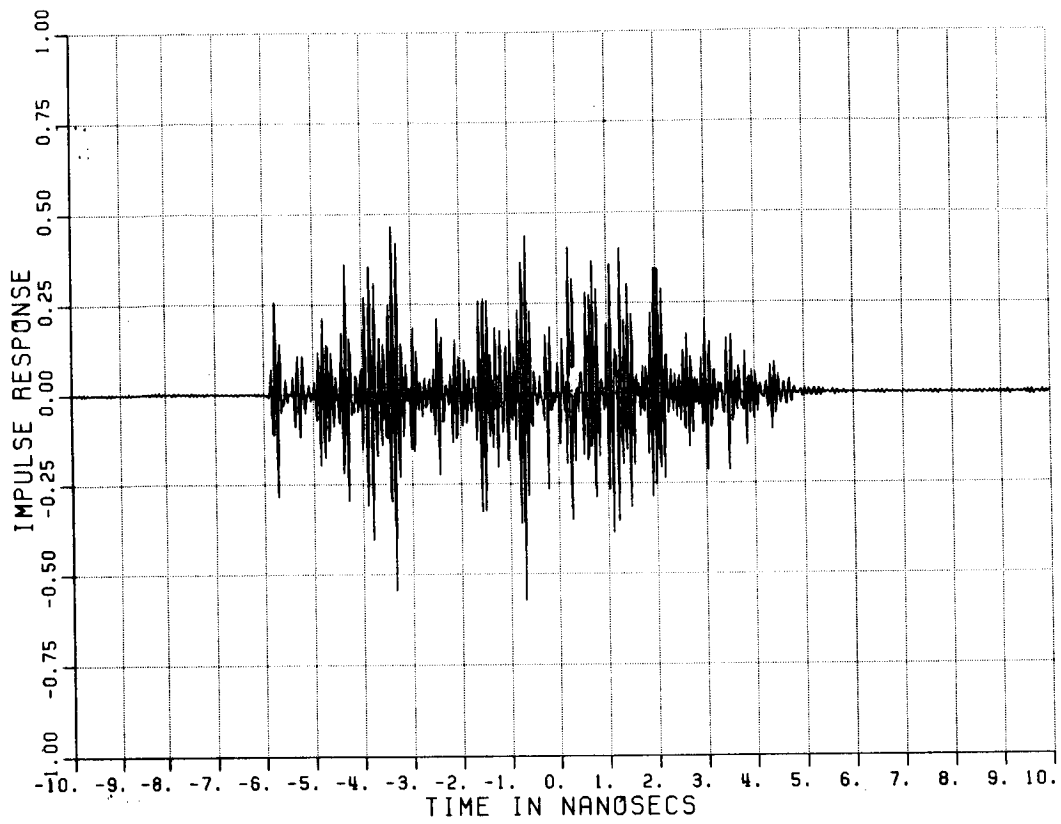
Figure 4.31. Time domain response from rotated 12" pyramids with θ=70° and vertical polarization.

110
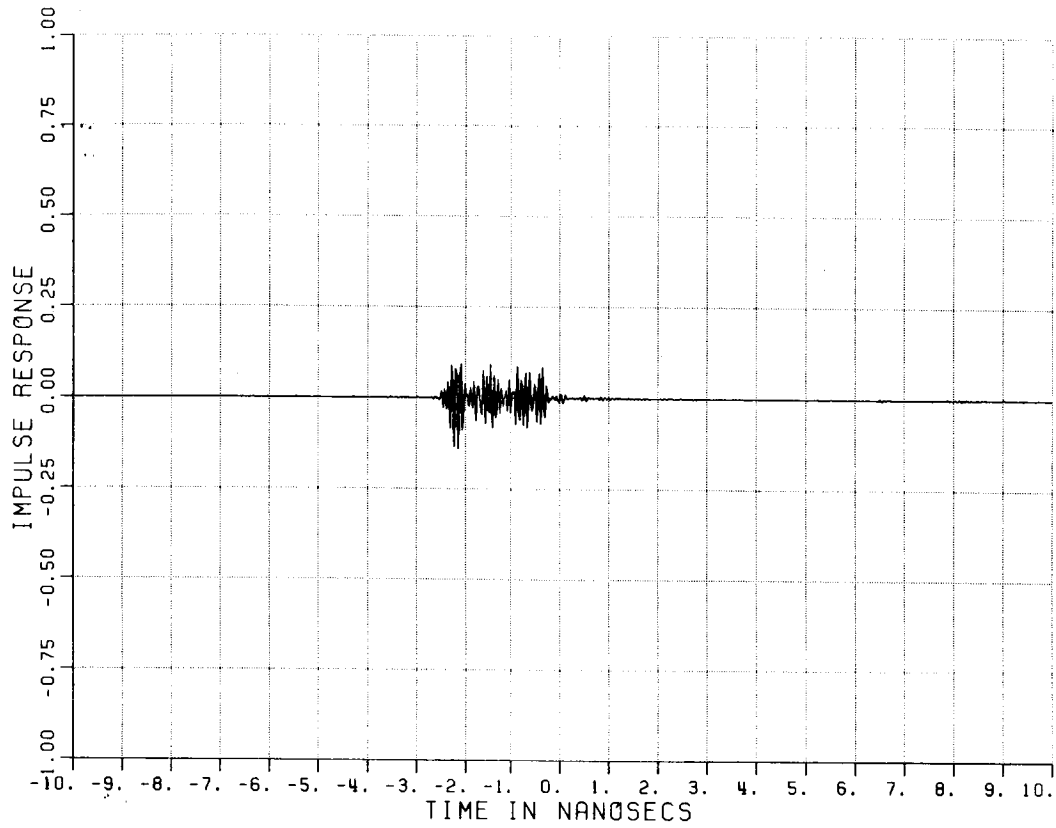
Figure 4.32. Time domain response from rotated 12" pyramids with θ=0°
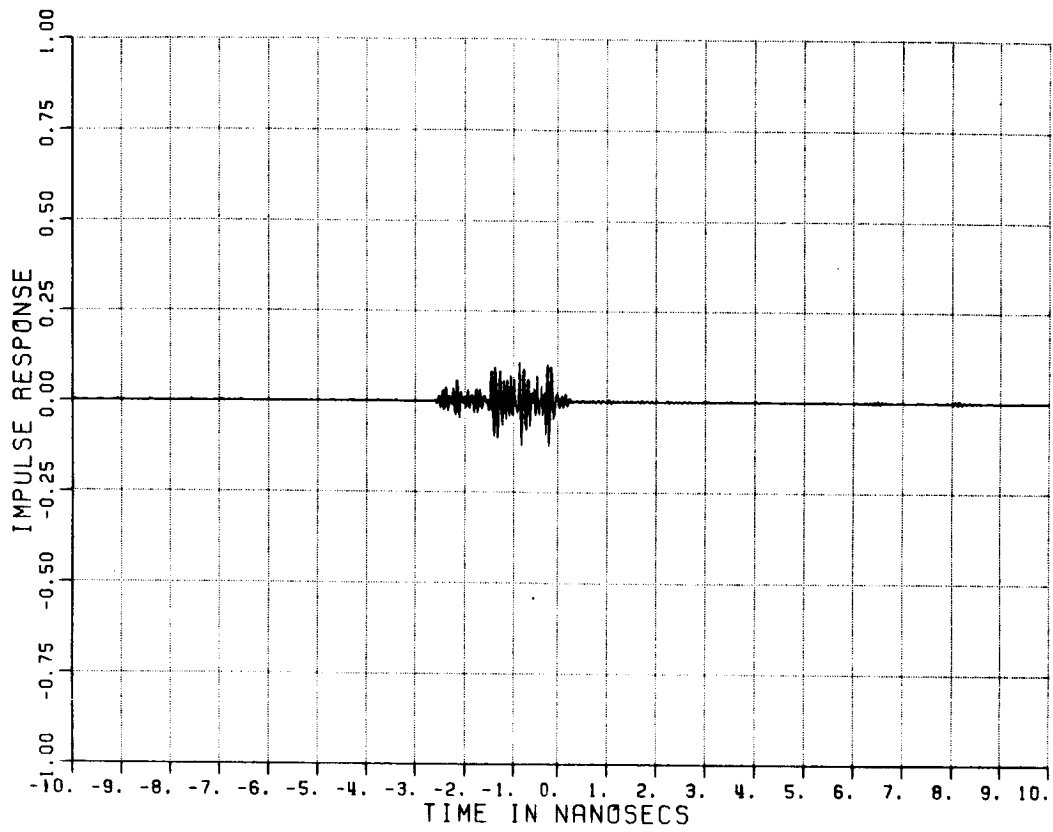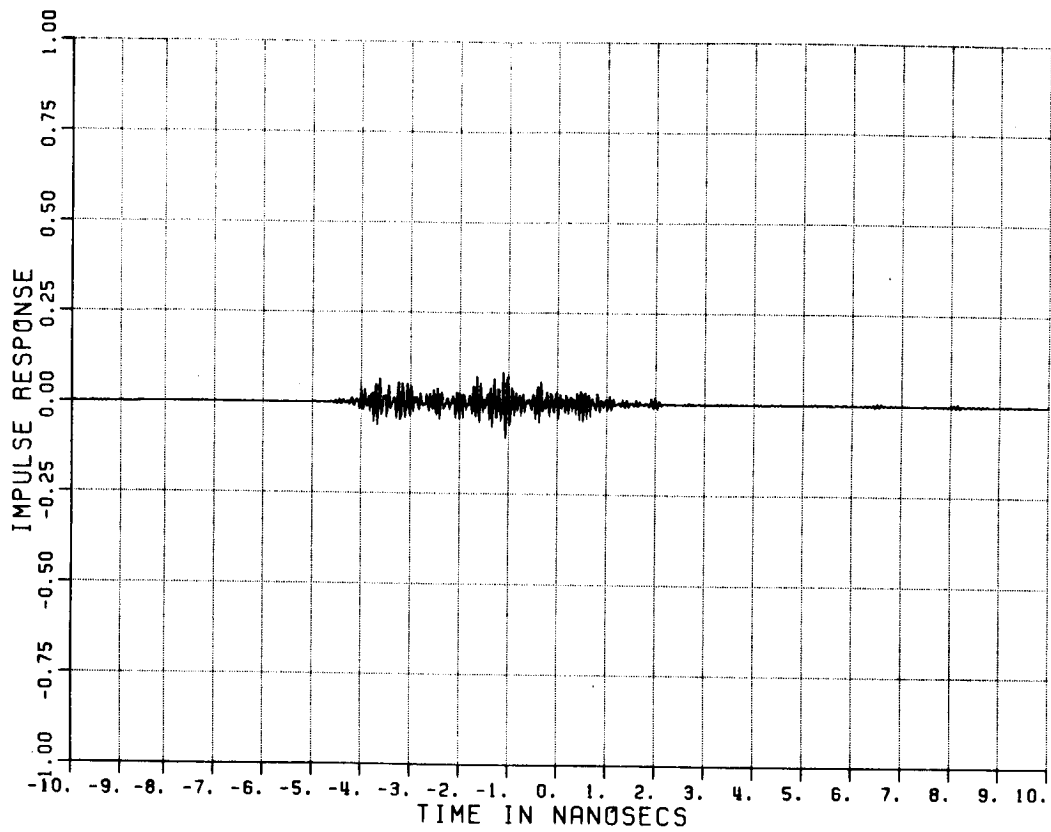and horizontal polarization.

111
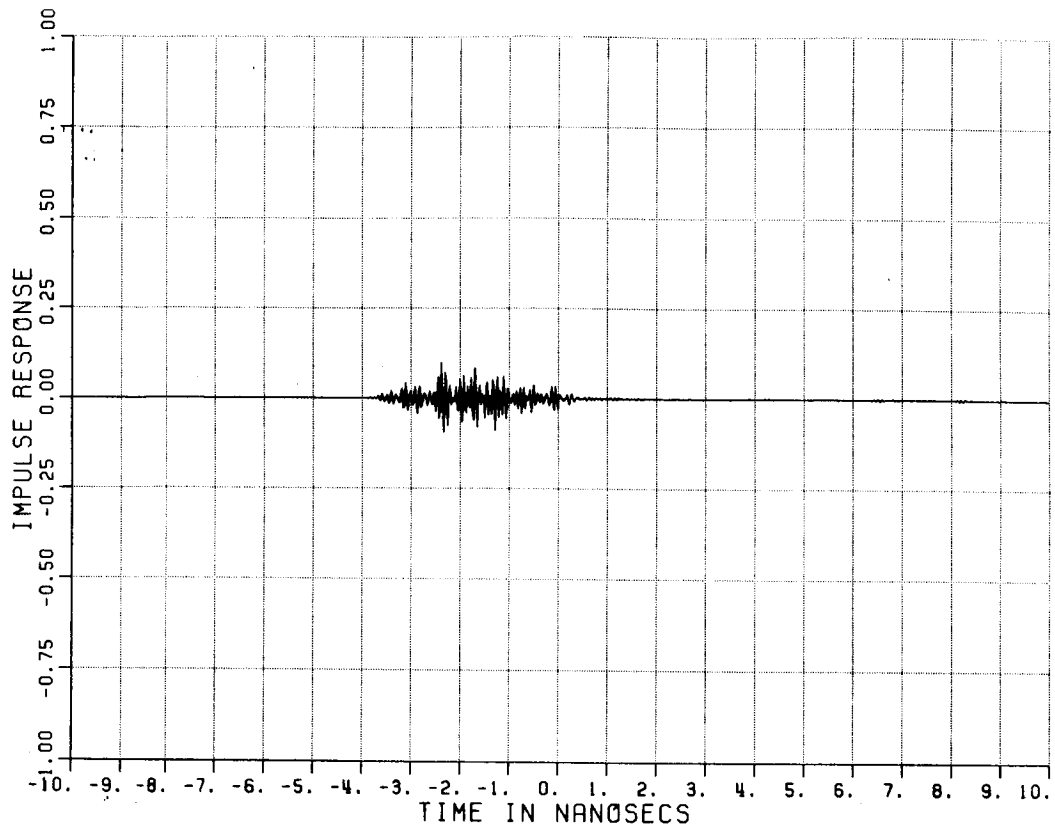
Figure 4.33. Time domain response from rotated 12" pyramids with θ=15° and horizontal polarization.
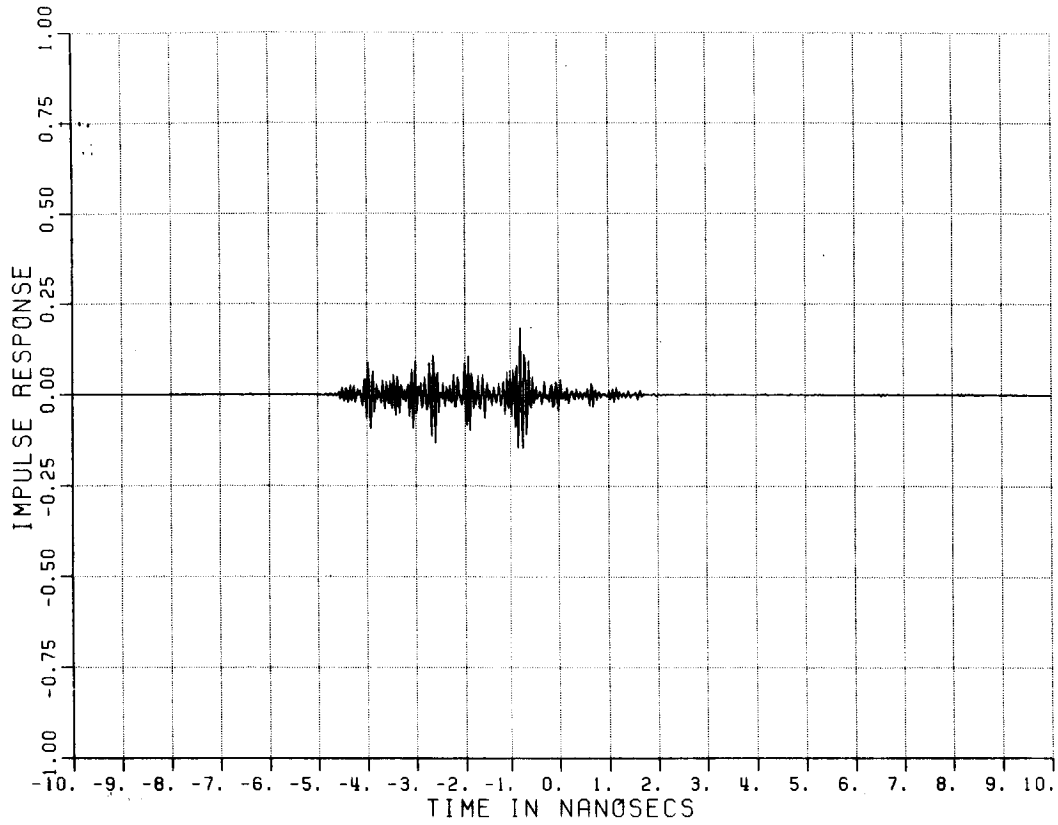
Figure 4.34. Time domain response from rotated 12" pyramids with θ=30° and horizontal polarization.
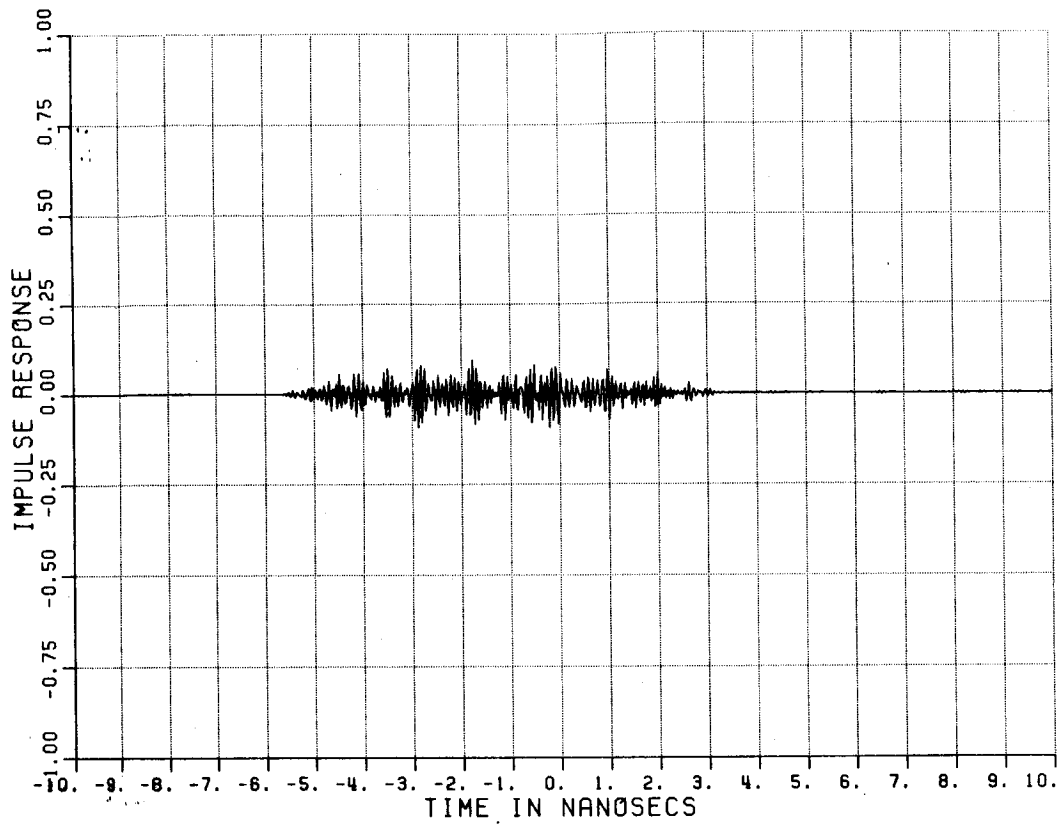
Figure 4.35. Time domain response from rotated 12" pyramids with θ=45° and horizontal polarization.
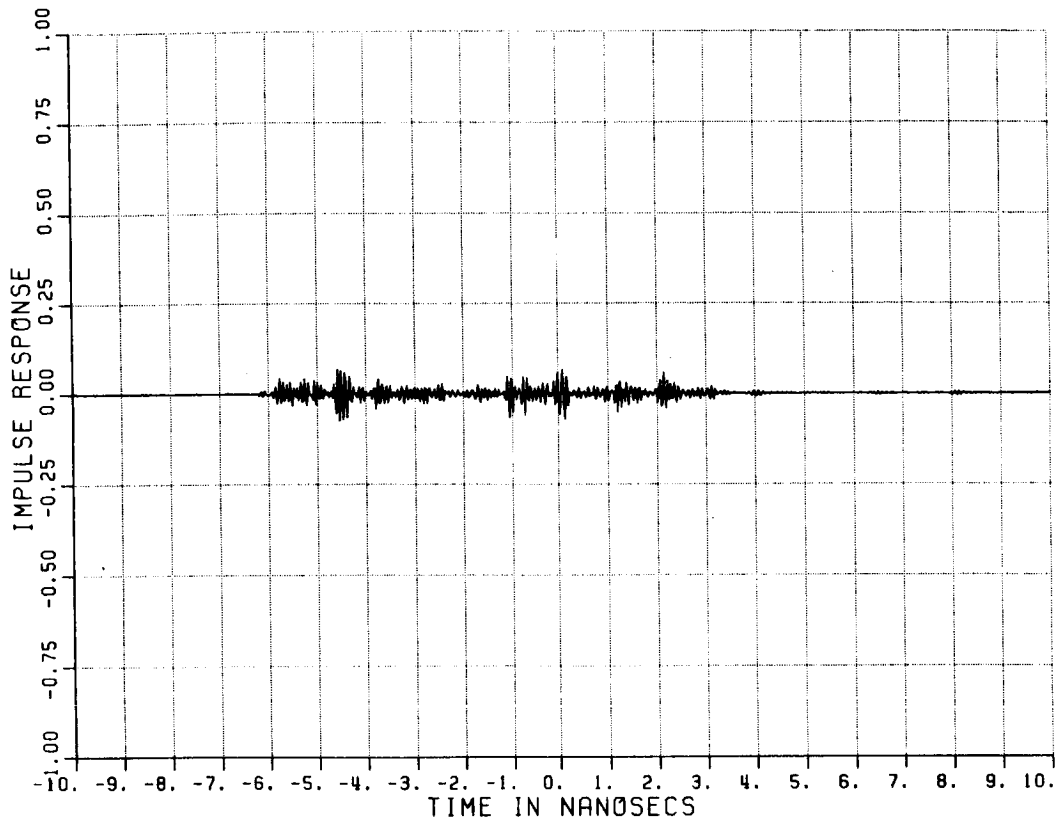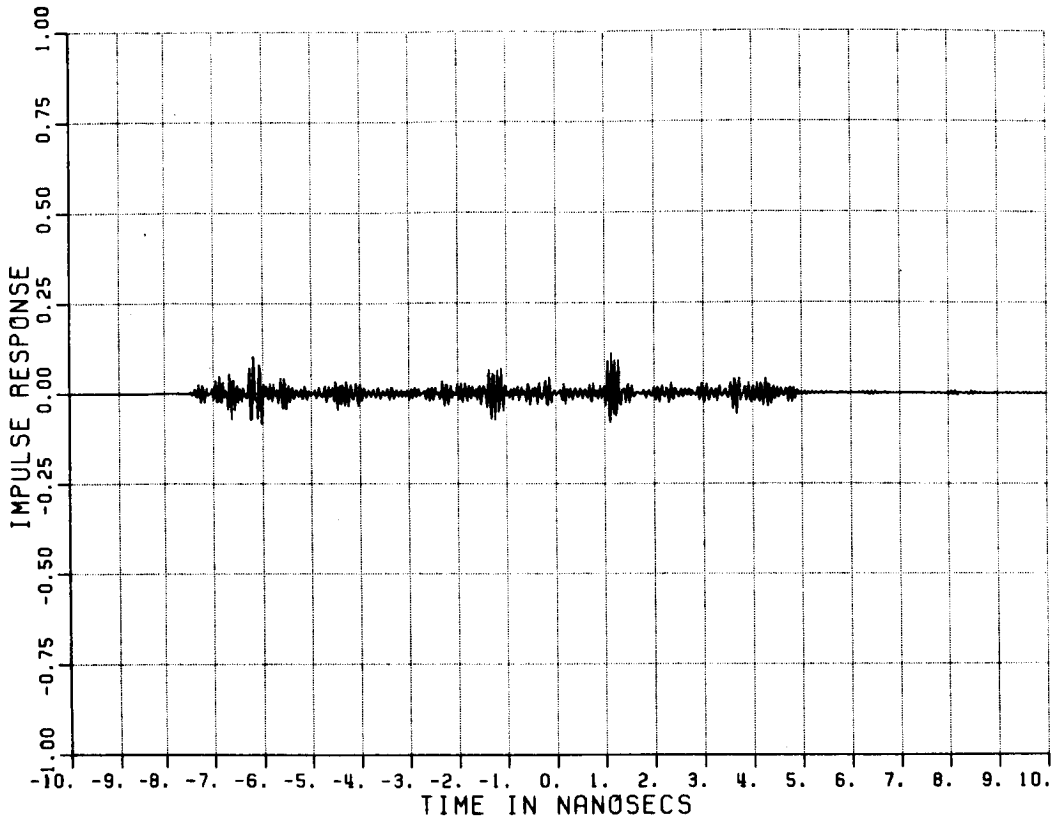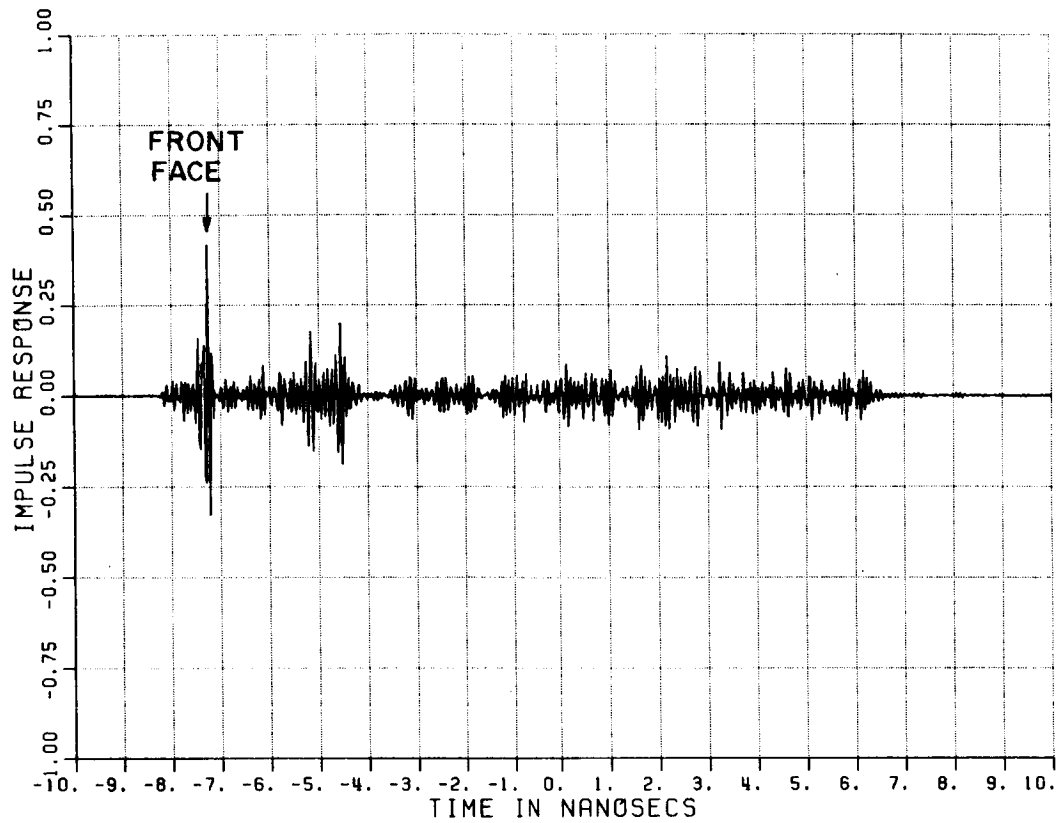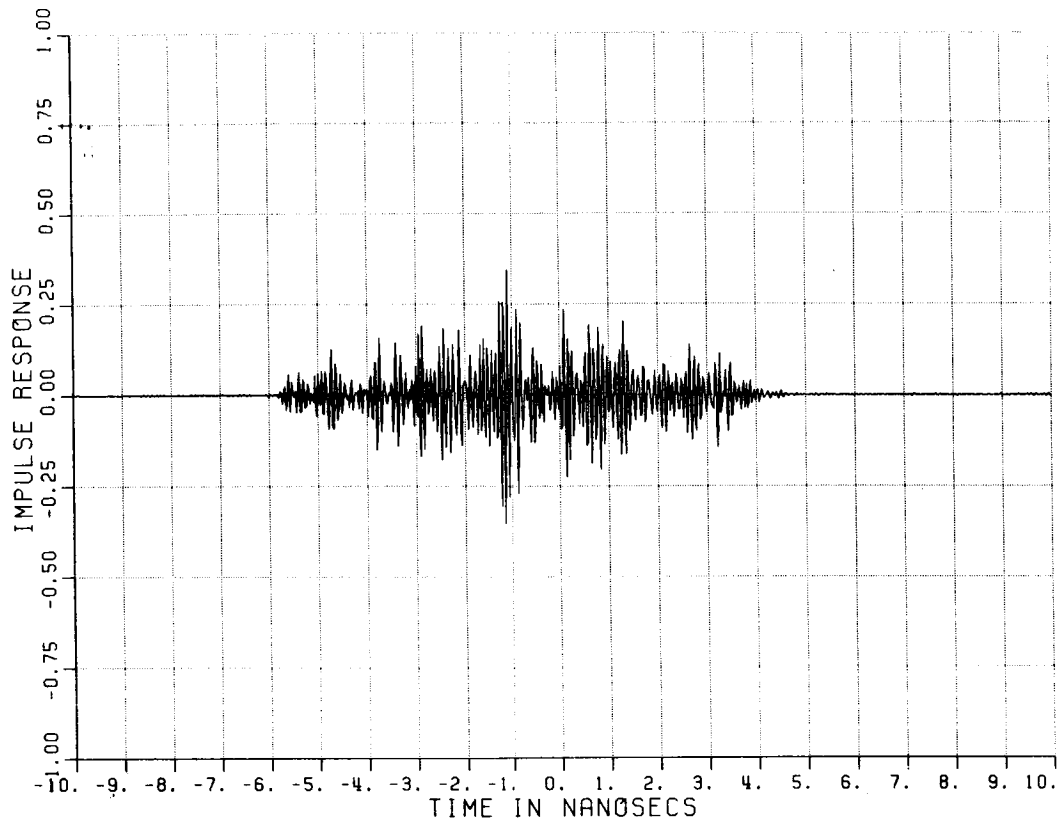
Figure 4.36. Time domain response from rotated 12" pyramids with θ=60° and horizontal polarization.

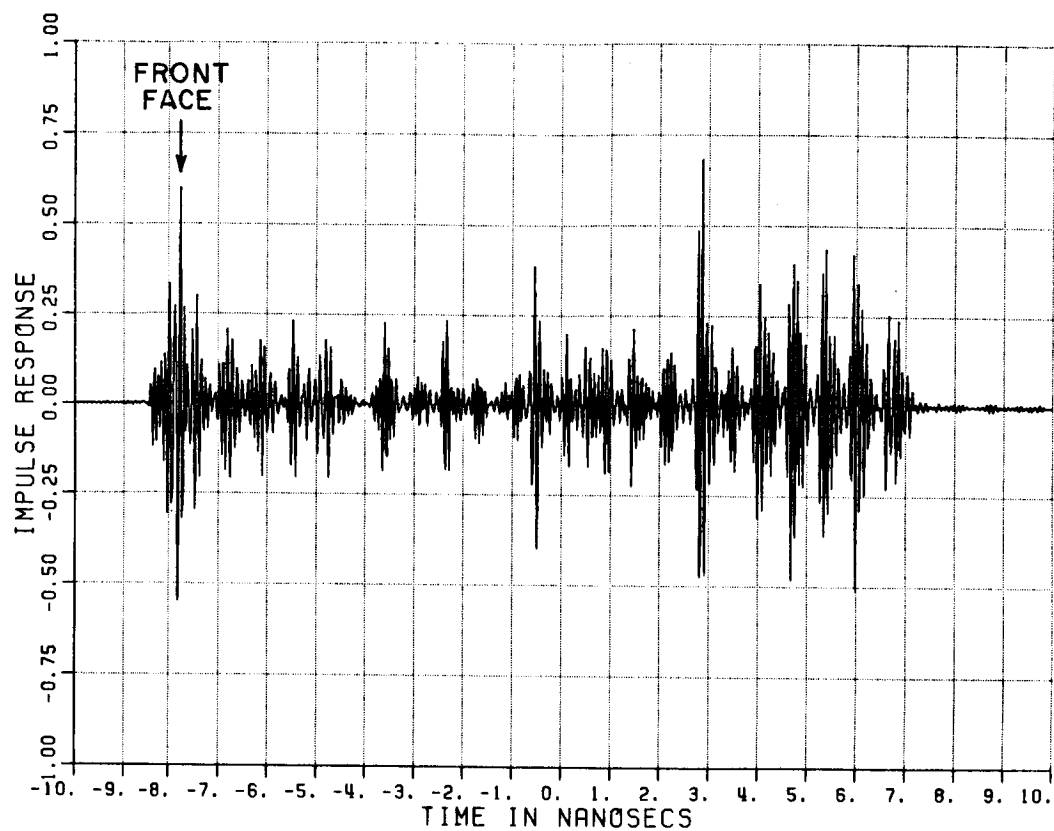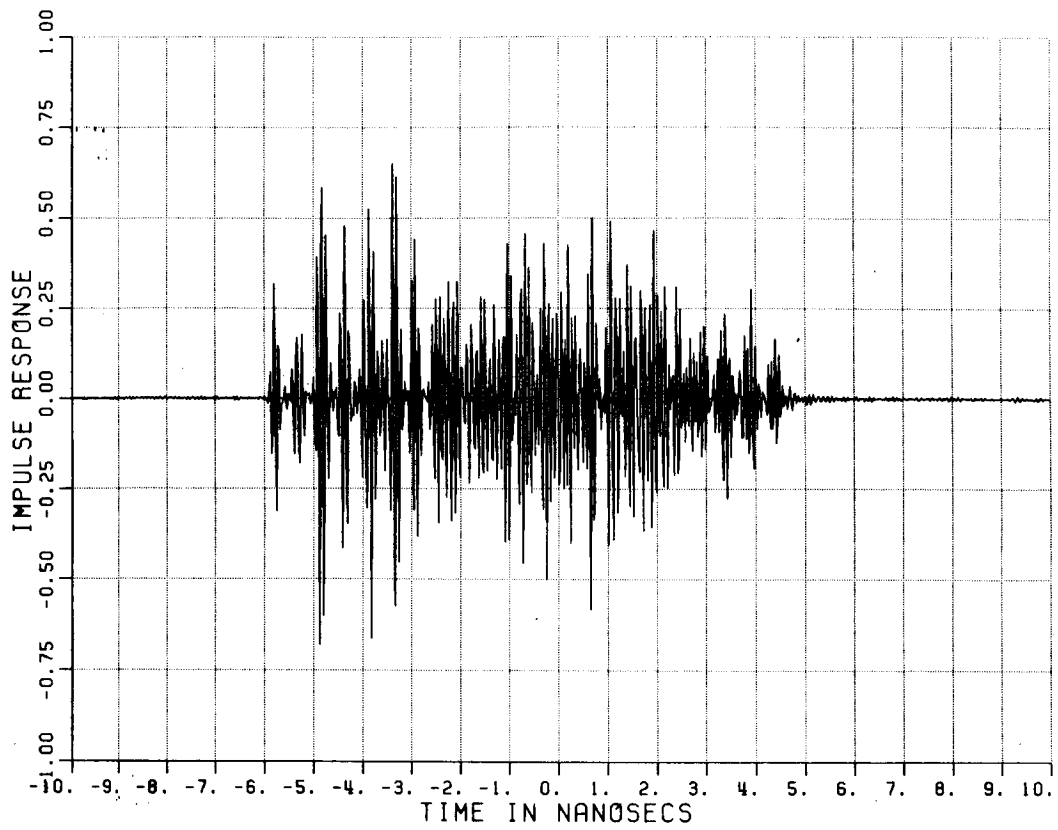Figure 4.37. Time domain response from rotated 12" pyramids with θ=70°
and horizontal polarization.

116
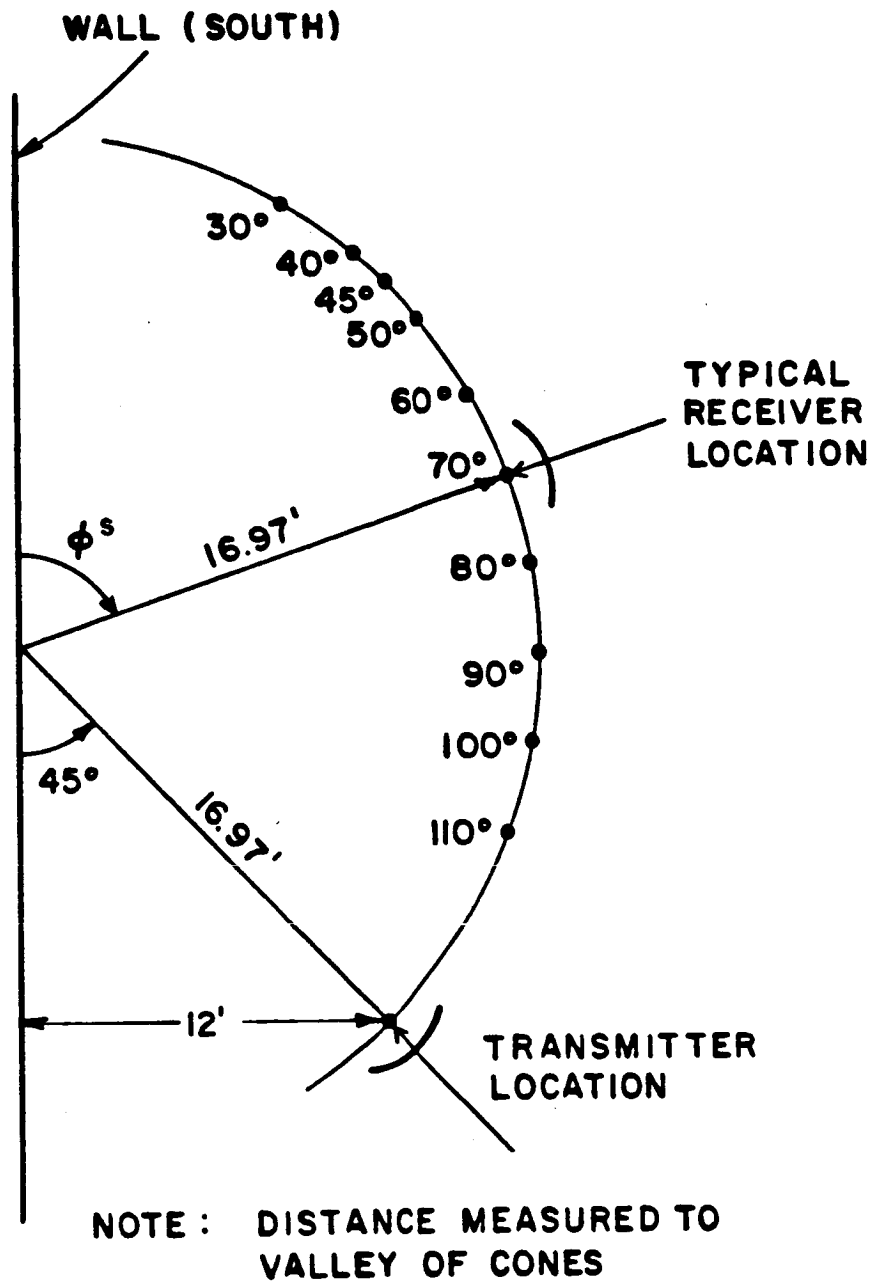
Figure 4.38. Top view of geometry for absorber wall measurements with 3 foot parabolic dishes.

A stepped CW radar system was connected to these antennas, with software gating set to center the response of the wall in the window. A set of data covering frequencies 2 to 18 GHz was measured for the wall, the wall plus a styrofoam column with a calibration sphere on top, and the wall plus column. The wall measurements were then calibrated against the sphere measurements.

The calibration procedure is not ideal in this case because the desired target (absorber wall) is not removed during the calibration measurement. So, the calibration sphere is not at the same location as the target and any sphere-wall effects are not subtracted out. Fortunately, the sphere return is much greater than the wall return and the sphere-wall effects. The sphere was placed about 1/2" from the pyramid tips to minimize the error from the sphere not being at the same location as the absorber.

Another set of measurements was required to determine the energy incident on each tip. For this, the sphere was moved both horizontally and vertically and the return measured. About 40 tips fall within the halfpower beamwidth for 45 degree incidence. This corresponds to about the same area as the dish dimensions projected onto the wall. (This occurs because the wall is in the near field of the antenna.)

The bandlimited time domain plots for ϕ^S=90, 70, 45, and 30 degrees, are shown is Figures 4.39, 4.41, 4.43 and 4.45 respectively. The coresponding frequency domain results of this experiment in terms of effective scattering are given in Figures 4.40, 4.42, 4.44 and 4.46. The calculated arrival time for tip and base scattering from the pyramids in the main beam are shown on each plot. Since ϕ^S=45 degrees

118
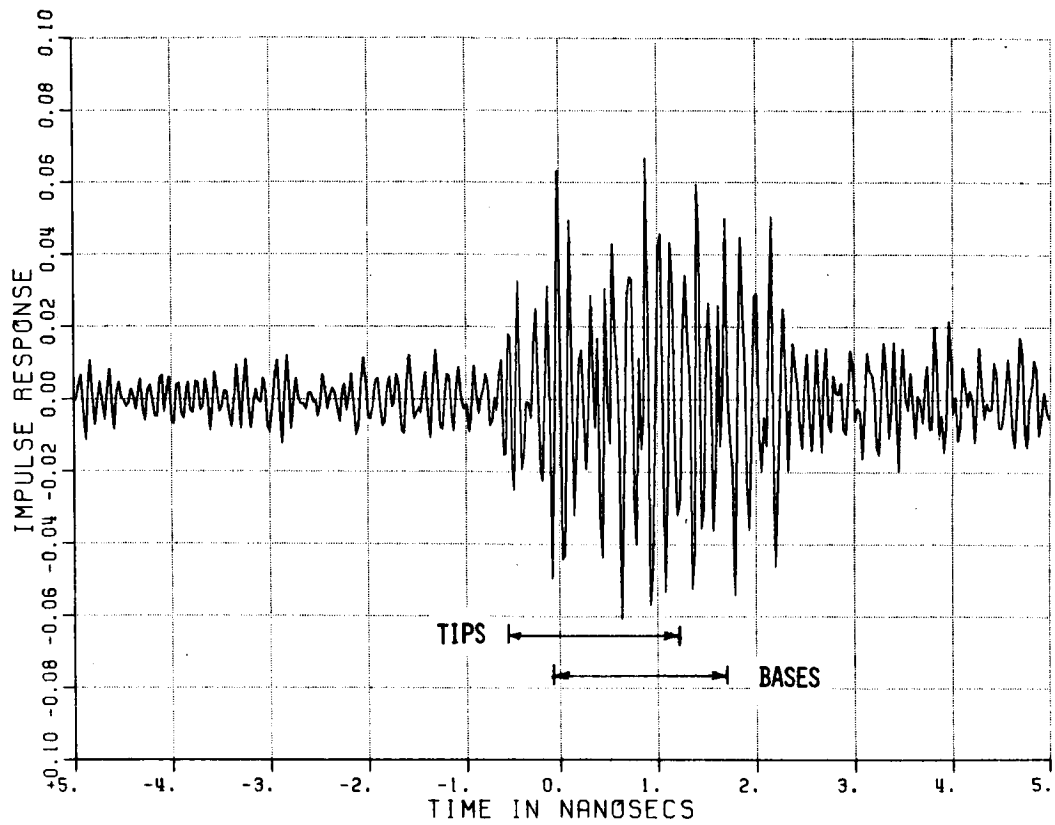
Figure 4.39. Bistatic time domain response of an absorber wall of 8"
pyramids with $\theta^i=45°$, $\phi^S=90°$, and vertical polarization.

119
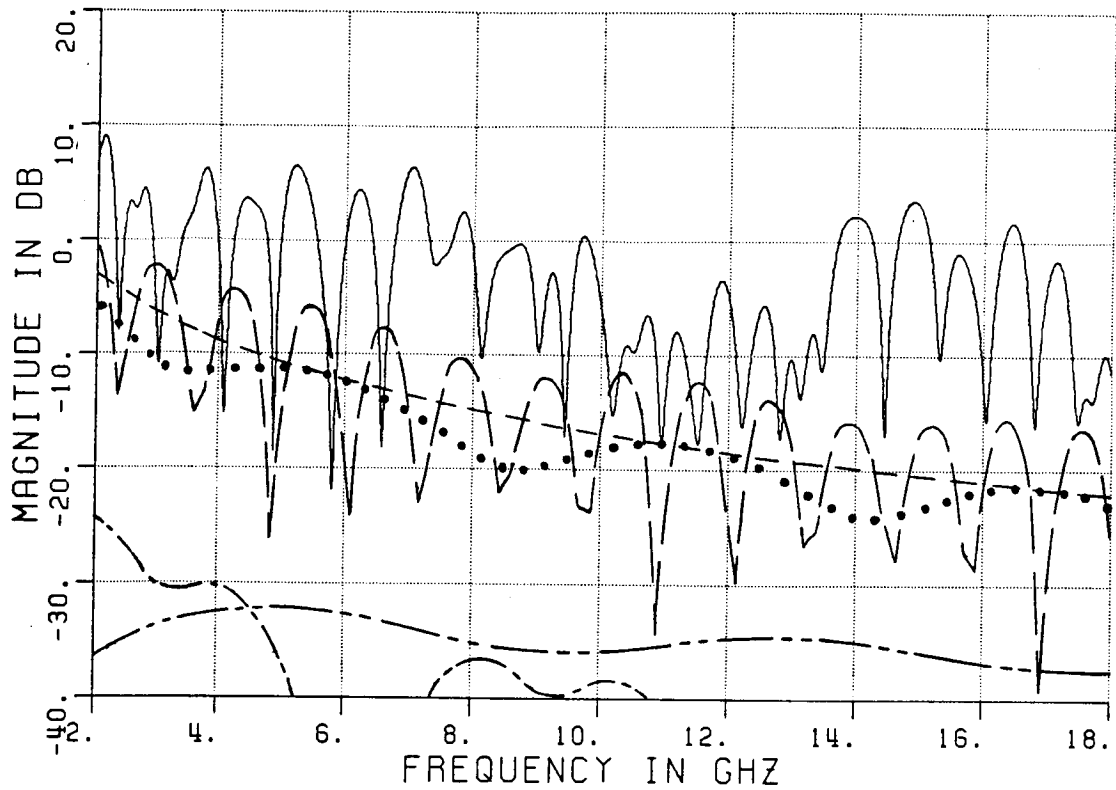
- ──────── MEASURED
- ── ── ──TIPS
- • • • • • BASES
- ──·──·── REFLECTED 140°
- ──···── REFLECTED 65°
- ── ──── TIPS + BASES

Figure 4.40. Measured and calculated bistatic scatter from an absorber wall of 8" pyramids with $\theta^i=45°$, $\phi^S=90°$, and vertical polarization.

120
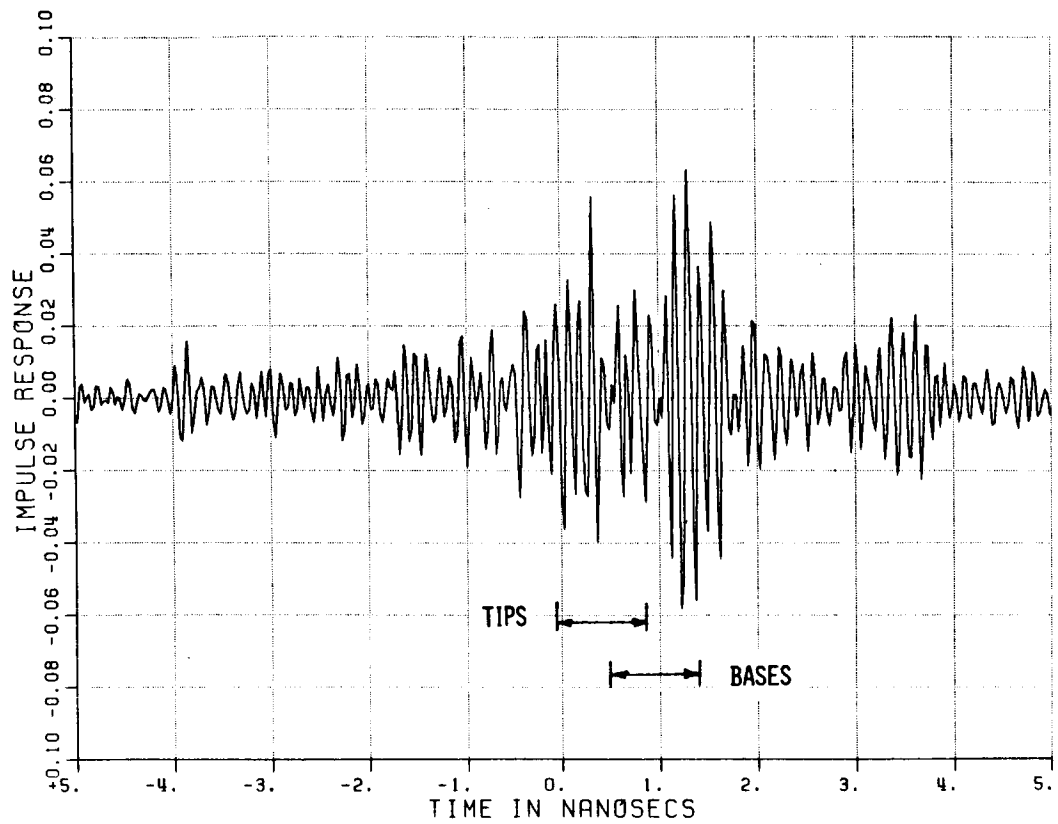
Figure 4.41. Bistatic time domain response of an absorber wall of 8' pyramids with $\theta^i=45°$, $\phi^S=70°$, and vertical polarization.

121

Figure 4.42. Measured and calculated bistatic scatter from an absorber wall of 8" pyramids with $\theta^i=45°$, $\phi^s=70°$, and vertical polarization.
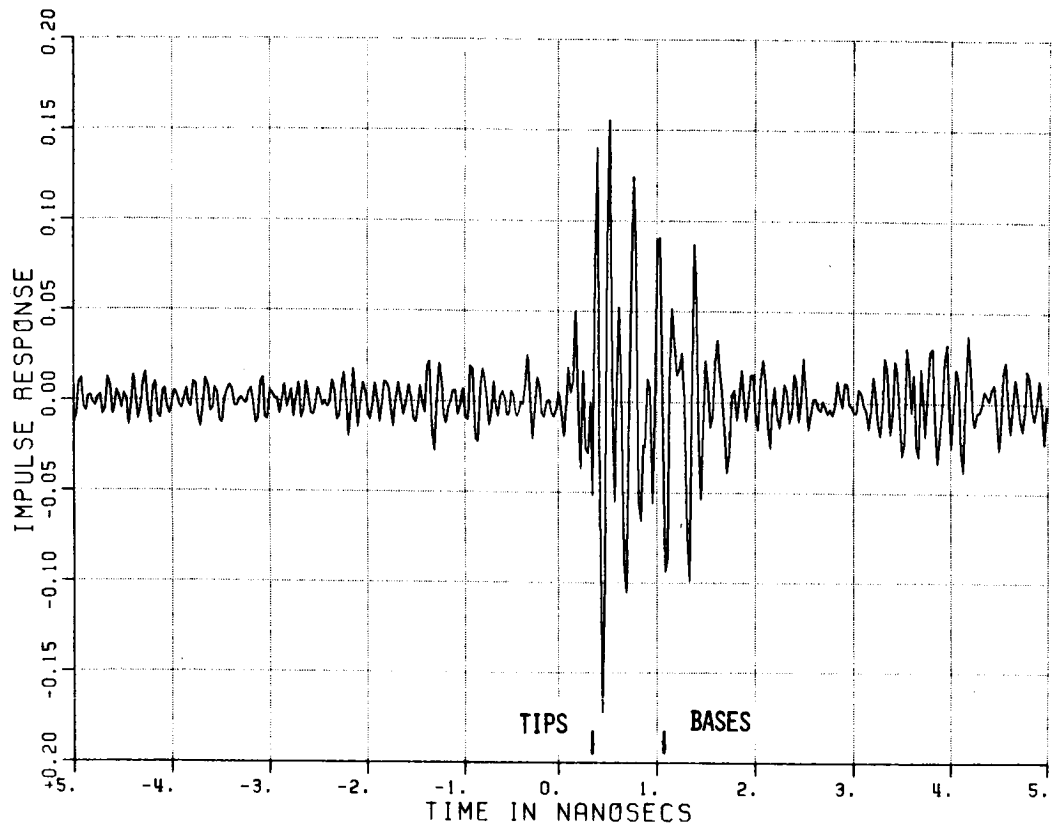
Figure 4.43. Bistatic time domain rsponse of an absorber wall of 8" pyramids with $\theta^i=45°$, $\phi^S=45°$, and vertical polarization.

123

Figure 4.44. Measured and calculated bistatic scatter from an absorber wall of 8" pyramids with $\theta^i=45°$, $\phi^S=45°$, and vertical polarization.
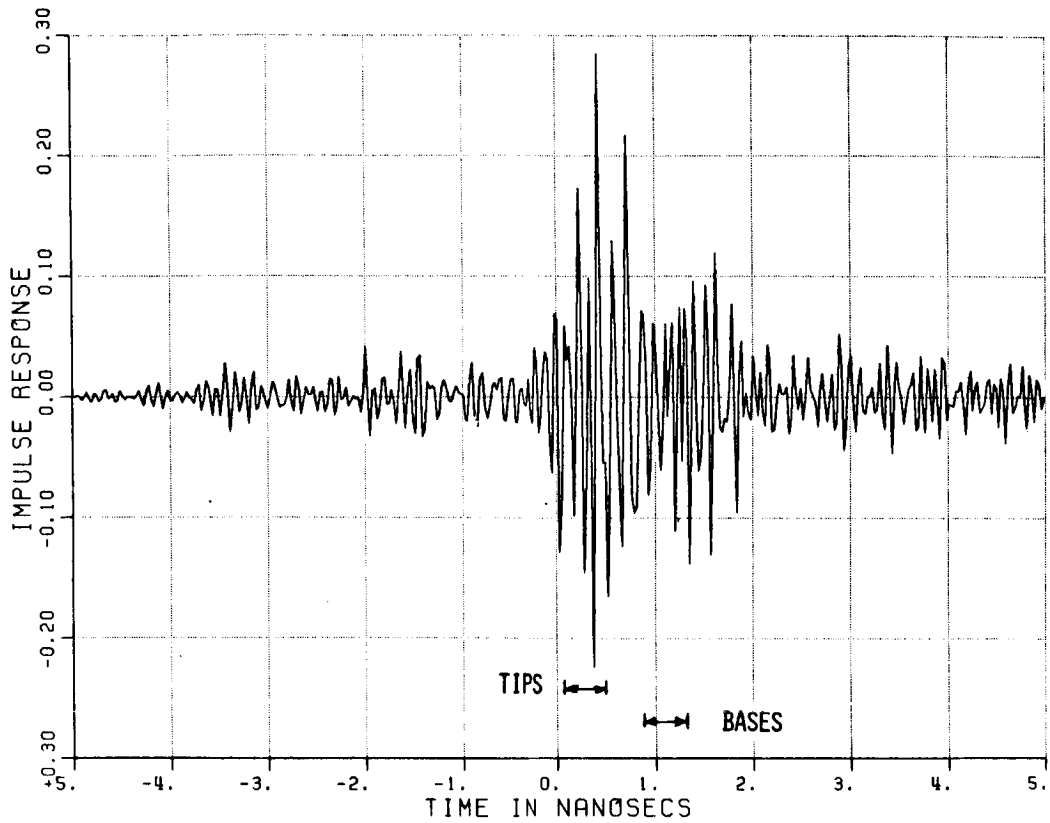
Figure 4.45. Bistatic time domain response of an absorber wall of 8" pyramids with $\theta^i=45°$, $\phi^S=30°$ and vertical polarization.
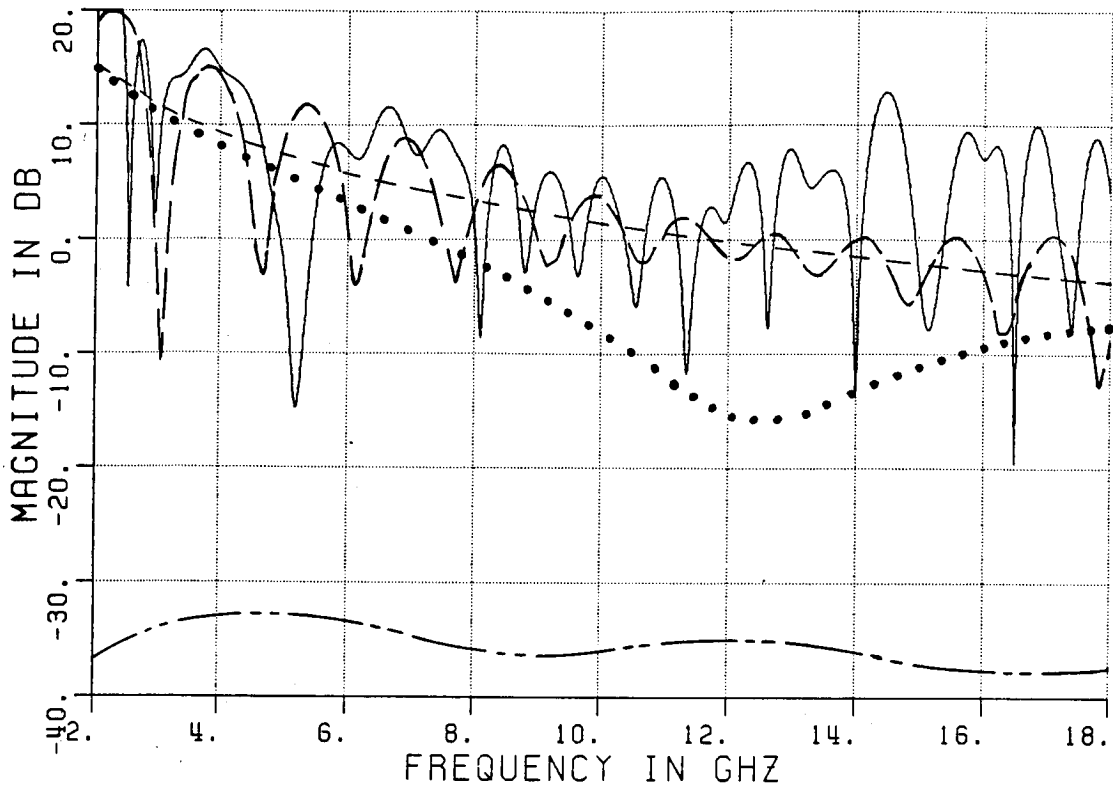
Figure 4.46. Measured and calculated bistatic scatter from an absorber wall of 8" pyramids with $\theta^i = 45°$, $\phi^s = 30°$, and vertical polarization.

is the specular angle all the tip contributions should arrive at the same time as well as the base contributions.

The frequency domain plots show both measured and calculated results. The reflected 140 and 65 degree cases refer to the reflected terms worked out in the example in Chapter III-D. The magnitude of the reflected terms for some of the angles are off the bottom of the scale so those plots show no reflected terms. The tips + bases term shows the summation of the individual tips and bases terms. The tips and bases adding in and out of phase cause the interference pattern. Since the back wall calculations of the previous section show the insignificance of the equivalent current solution compared to the other contributions it is not calculated for this case.

The ϕ^S=90 degrees plot shows fairly good agreement between the tip+ base term and the measured results. The reflected terms are well below the level of the other terms. The reflected 65 degrees term is much stronger than at ϕ^S=70 degrees, especially above 10 GHz. The ϕ^S=70 degree case shows less agreement than the ϕ^S=90 degree one.

At ϕ^S=45 degrees, the calculated plot shows the tip terms equaling the base ones while the time domain plot shows the tips stronger than the base terms. The calculated pattern results do not account for shadowing of the bases by adjacent pyramids. The tips plus bases plot is indeed higher than the measured results while the tips plot passes closer to the measured results.

The ϕ^S=30 degrees case shows the same effect except here the bases have a much weaker return than the tips at the higher frequencies, so the shadowing effect is not as clear. Note that the bistatically

127

scattered field is not concentrated at the 45 degree scatter angle which indicates that the absorber is a random scatter. If the absorber scatters coherently, then the scattered field must maximize at 45 degrees.

E. BACKSCATTER FROM WEDGE ABSORBER

Backscatter measurements of Company C's 8" wedge absorber (6" tall wedge plus 2" thick backing) were taken using a compact range. Four pieces of 2' by 2' absorber were mounted in a horizontal row a shown in Figure 4.12 with the wedges running horizontal. To reduce the junction effects between the pieces, they were glued together to form 8' long continuous wedges. The backscatter was measured for various theta angles as defined in Figure 4.12.

The time domain responses for both polarizations with $\theta=0$ degrees, generated from a 6 to 18 GHz frequency sweep, are shown in Figures 4.47 and 4.48. The expected arrival time for the returns from the wedge tips, valleys, and back edge of the absorber are indicated on each figure. In both polarizations the wedge tip contribution dominates the return and there is little polarization dependence. The lack of polarization dependence is considerably different from that of a conducting wedge where the wedge return is much stronger for the E field parallel to the edge than for perpendicular.

The calculated and measured frequency data for vertical and horizontal cases appear in Figures 4.49 and 4.50, respectively. The plots shown include the total measured results and the measured results

128

Figure 4.47. Time domain response from 8" wedges with θ=0° and vertical polarization.
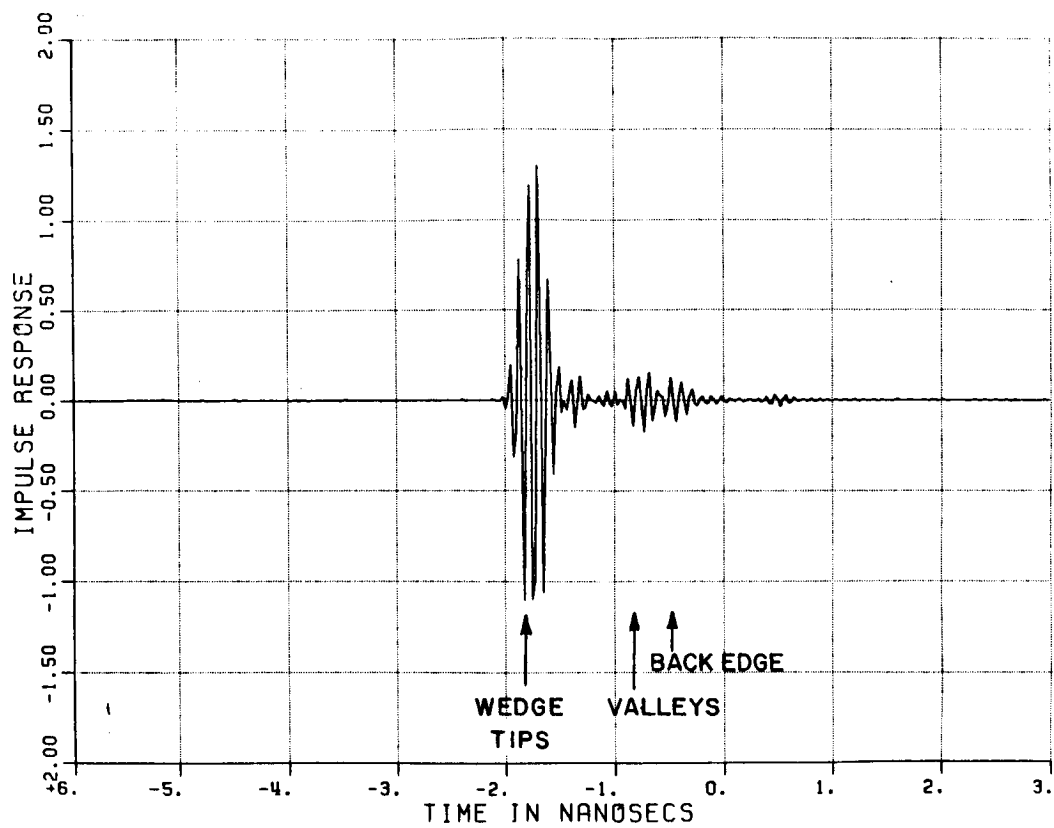
Figure 4.48. Time domain response from 8" wedges with θ=0° and horizontal polarizaiton.

130
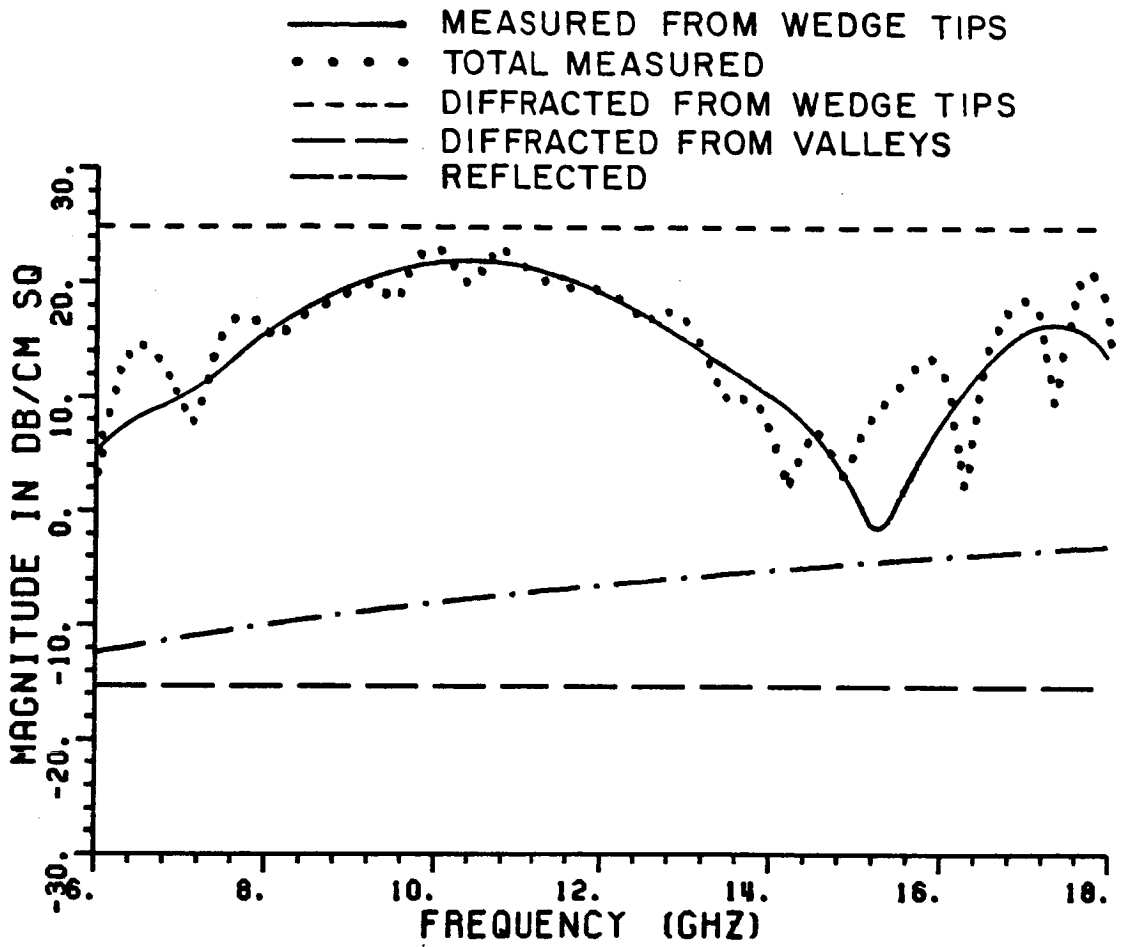
Figure 4.49. Calculated and measured backscatter from four pieces of wedge absorber with vertical polarization.
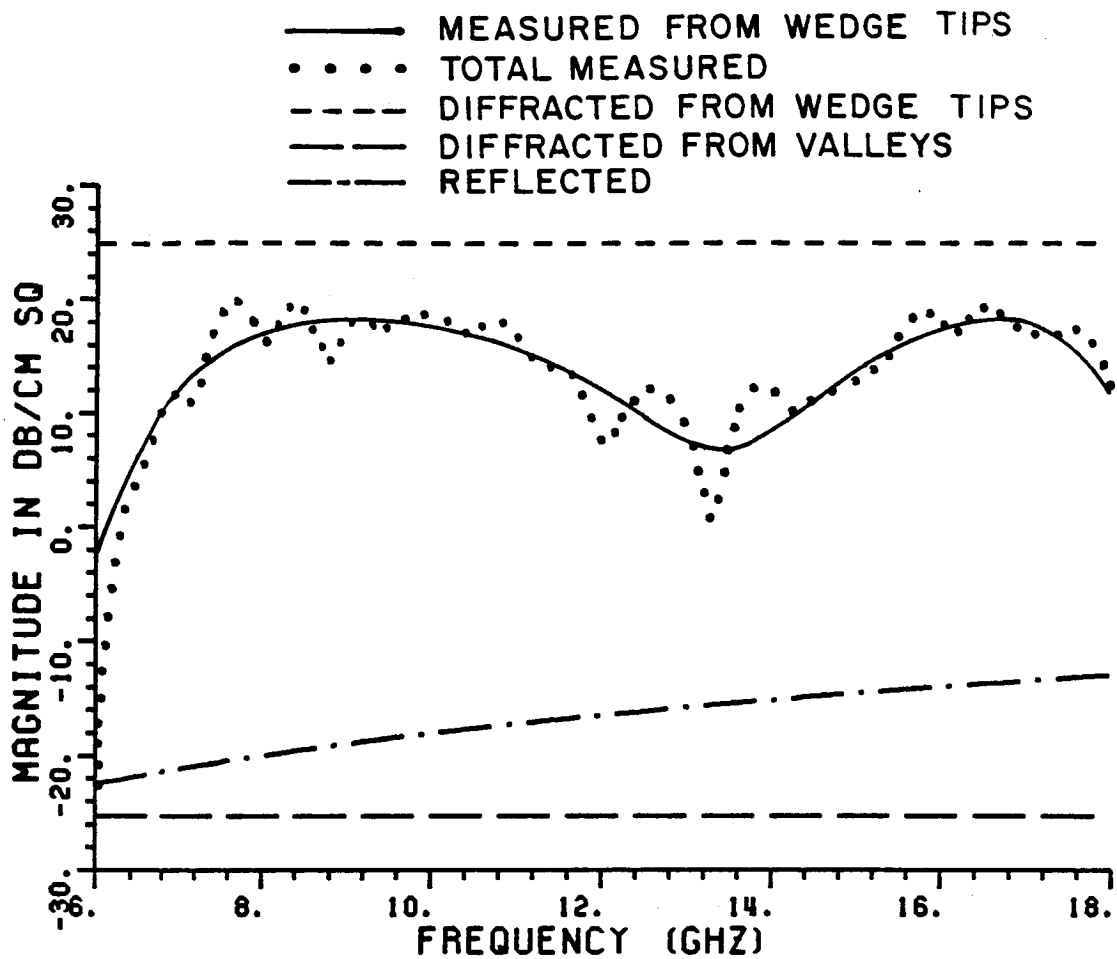
Figure 4.50. Calculated and measured backscatter from four pieces of wedge absorber with horizontal polarization.

from just the wedge tips with the other contributions software gated out. The calculated returns include the contribution from the wedge tips and valleys found using an equivalent current solution and a reflected contribution found from an aperture integration approach. The calculated wedge diffraction shows polarization independence but predicts a stronger return than what was measured.

The calculated return assumes that each 2' long section of wedge tip adds incoherently with the others, in other words, each 8' long row is considered as 4 incoherent scatters and each row is considered incoherent from the other rows. These assumptions are based on the pyramid absorber results of adding incoherently from piece to piece. The calculated return, also, assumes the wedges are perpendicular to the incident direction which is perfect alignment.

The calculated results from the wedge tips show no frequency dependence while the calculated results are showing some oscillation. This may be due to slight differences in position and some of the wedges being bent. The calculated return also appears about 10 dB higher than the measured results. This may be partly due to the alignment since the backscatter wedge tips return drops very radpidly away from perpendicular incidence as demonstrated in the next set of figures.

Figures 4.51 through 4.60 show the backscatter time domain response for angles of θ=15, 30, 45, 60, and 70 degrees for both polarizations. The large early return on each plot comes from the front face of the absorber as mentioned previously and shown in Figure 4.12. This return should not considered as part of the wedge return since it would not exist in absorber wall measurements. For angles of θ=45 degrees and

133

larger, the arrival time for the wedge contribution from each piece is indicated. The junctions between pieces does not seem to be giving consistently larger returns than from the wedge. This indicates that with the wedges glued together the junctions between pieces does not adversely affect the wedge performance. (Note: The wedges were glued together because the wedges on one piece of absorber did not line up with the wedges on adjacent pieces because of differences in height and position on each piece. Glueing the pieces together smooths the transistions from one piece to the next.)

Notice that the backscatter return from the wedges drops off very quickly with incident angle. The measured results at $\theta=15$ degree are more than 25 dB below those at $\theta=0$ degrees. The model used in this report predicts a return from the beginning and end of the wedge only with theta not equal to 0 degrees, so, the small return is expected.

The wedge backscatter at theta greater than 15 degrees compares very favorably against the pyramid measurements from Section C of this chapter. These measurments demonstrate the usefulness of wedge absorbers in areas where grazing or close to grazing on the material is a major concern.

If away from normal incidence the major portion of the incident energy striking the wedge is not being backscattered then where is it going? It seems unlikely that all the energy is being absorbed so the logical assumption is the energy is scattering in the specular direction. This hypothesis has not been tested in this study. A bistatic measurement of a long strip or wall of wedge absorber is needed.
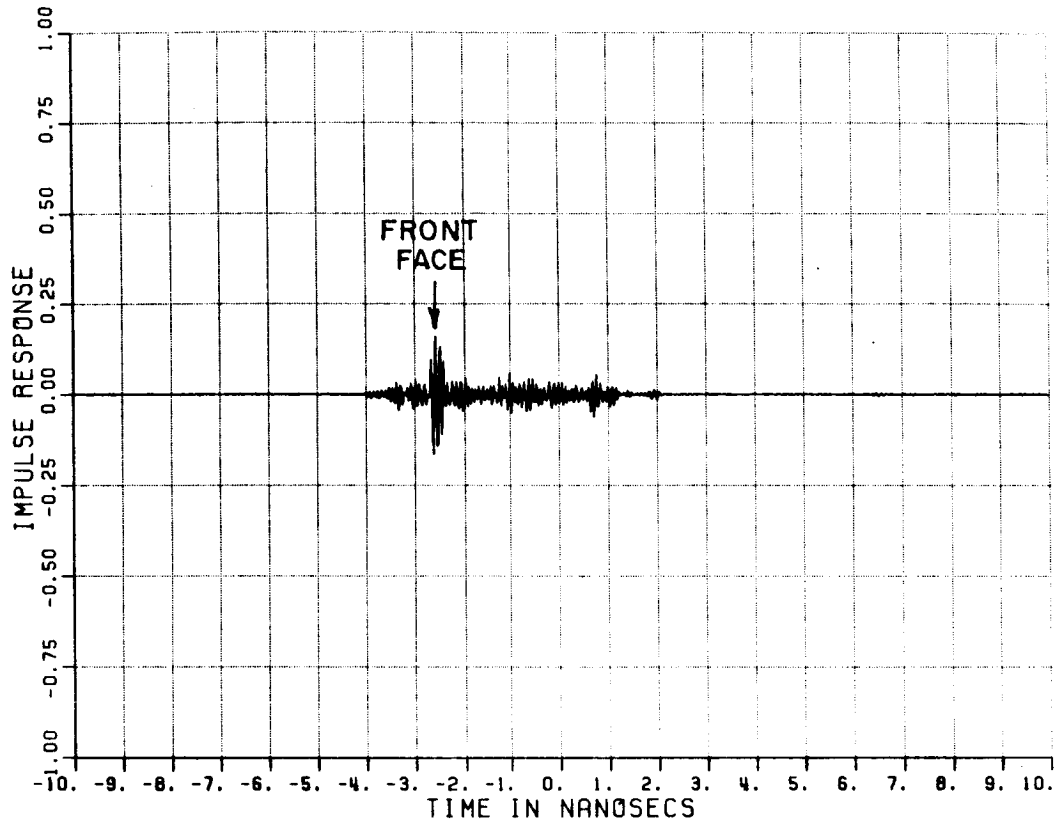
Figure 4.51. Time domain response from 8" wedges with θ=15° and vertical polarization.
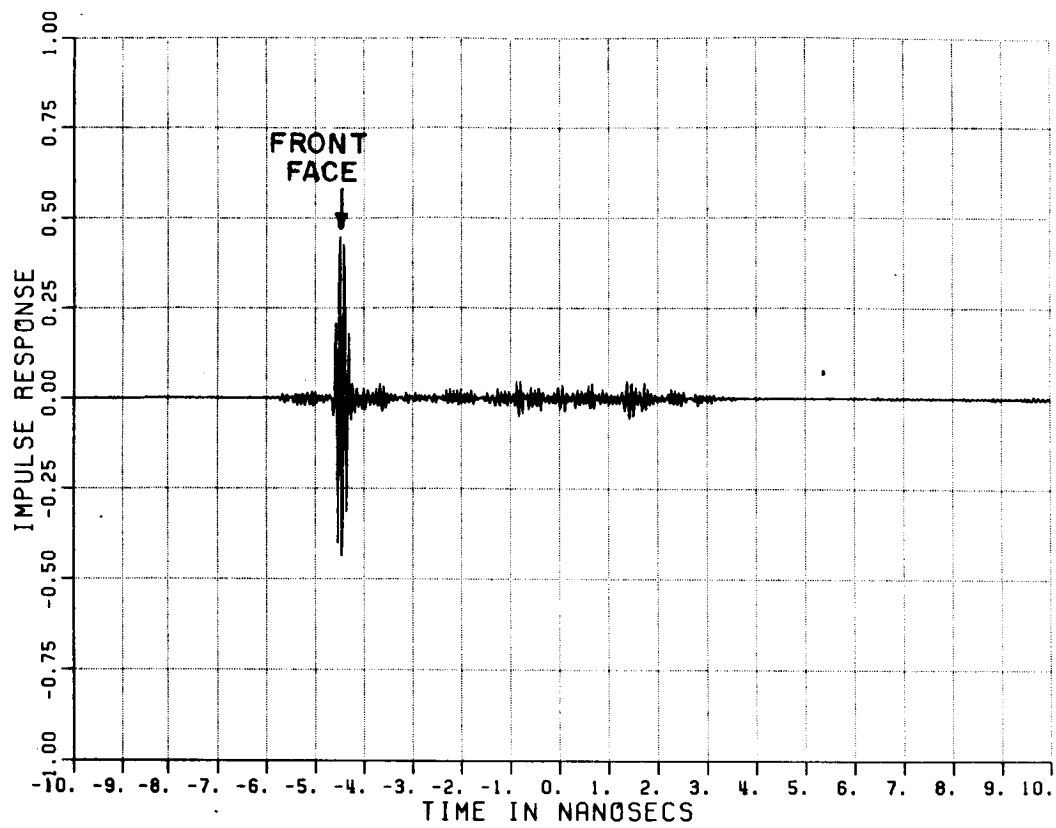
Figure 4.52. Time domain response from 8" wedges with θ=30° and vertical polarization.
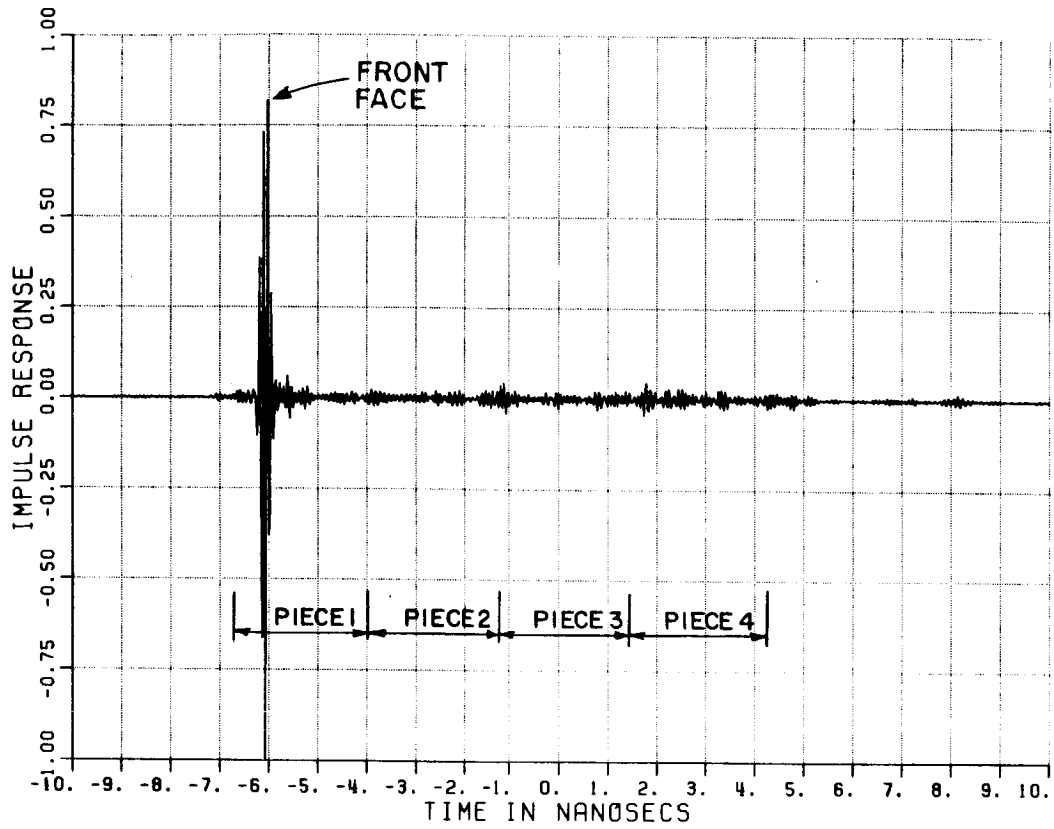
Figure 4.53. Time domain response from 8" wedges with θ=45° and vertical polarization.

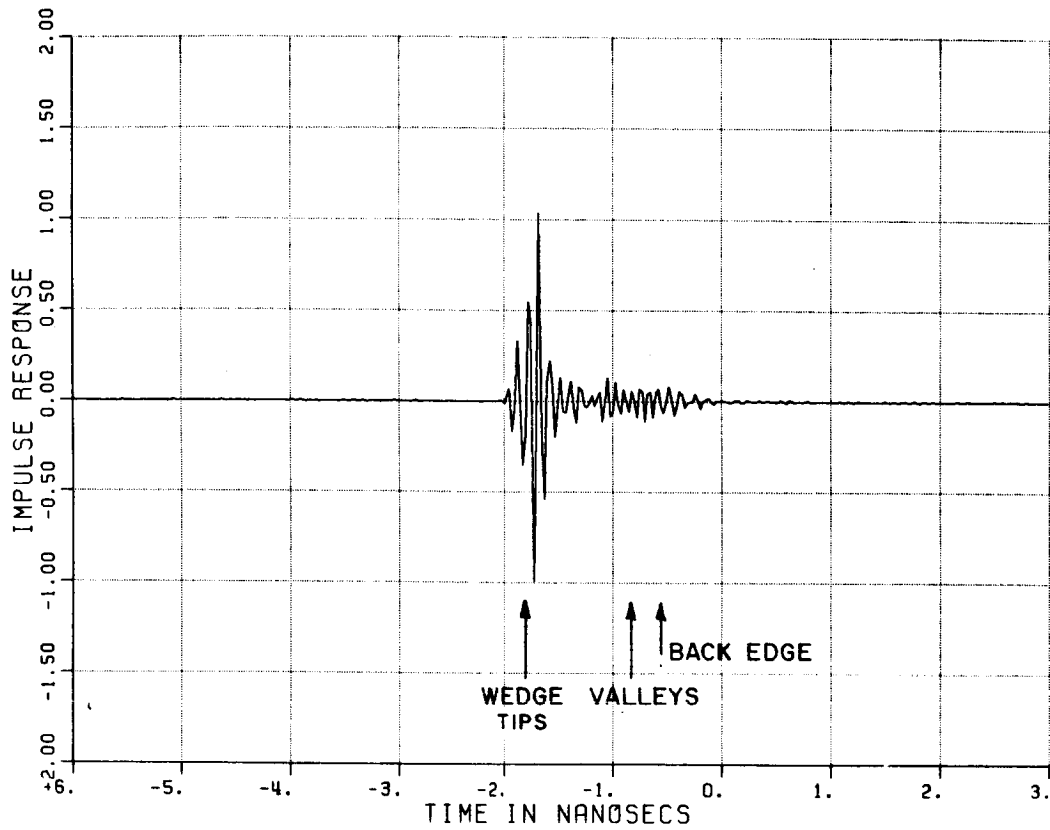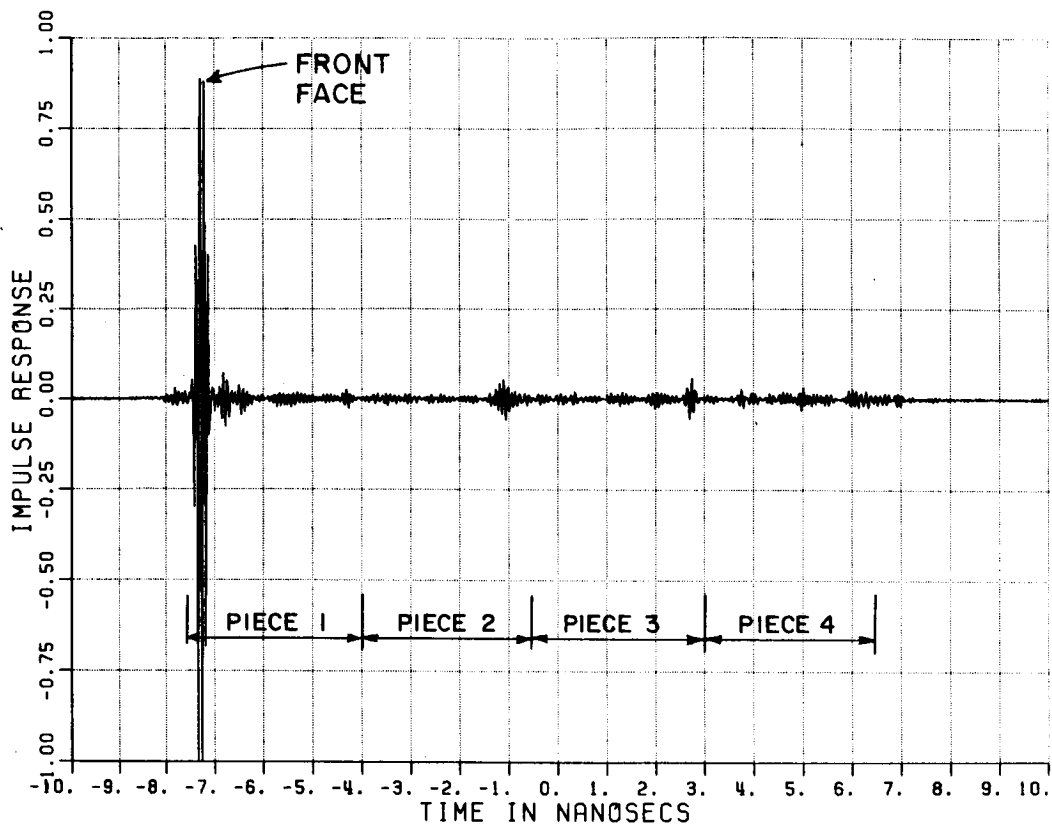Figure 4.54. Time domain response from 8" wedges with θ=60° and vertical polarization.

138
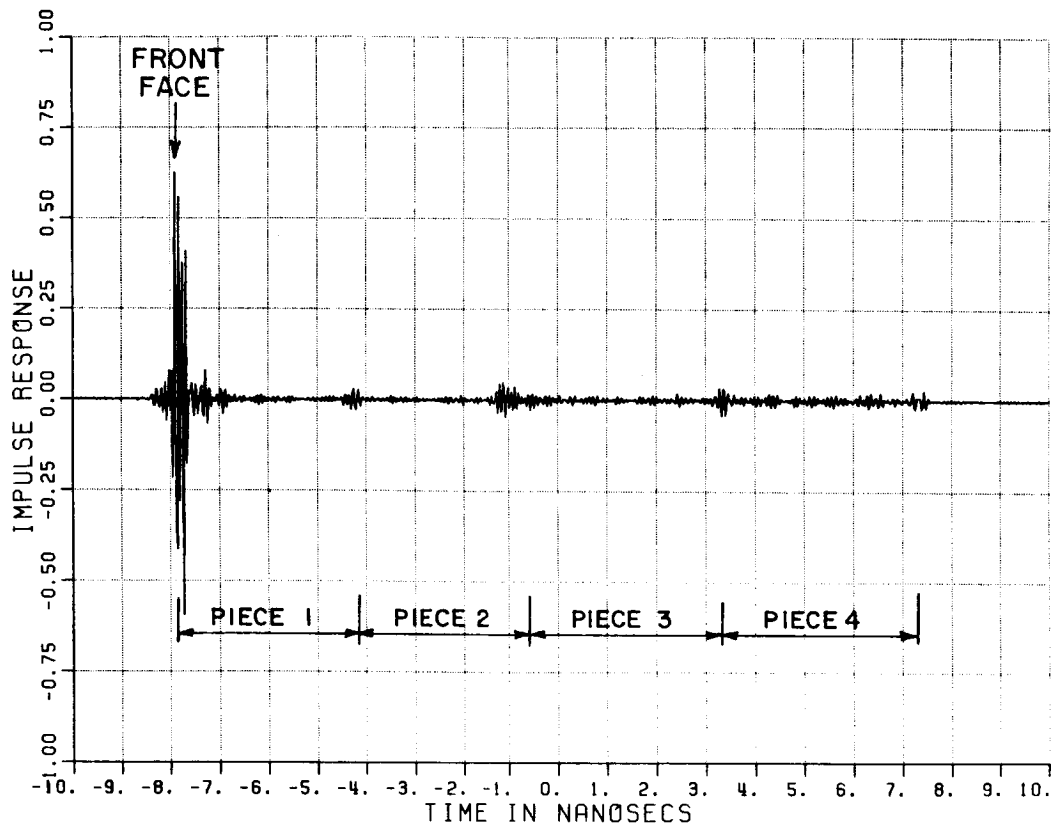
Figure 4.55. Time domain response from 8" wedges with θ=70° and vertical polarization.
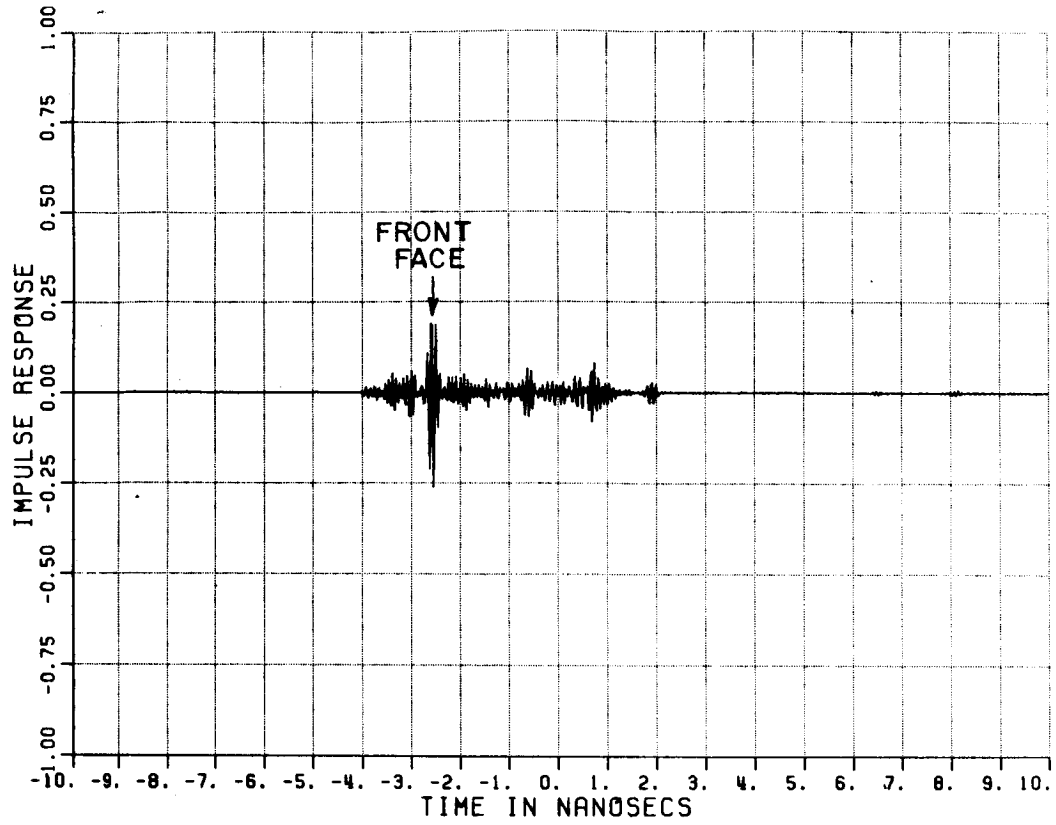
Figure 4.56. Time domain response from 8" wedges with θ=15° and horizontal polarization.
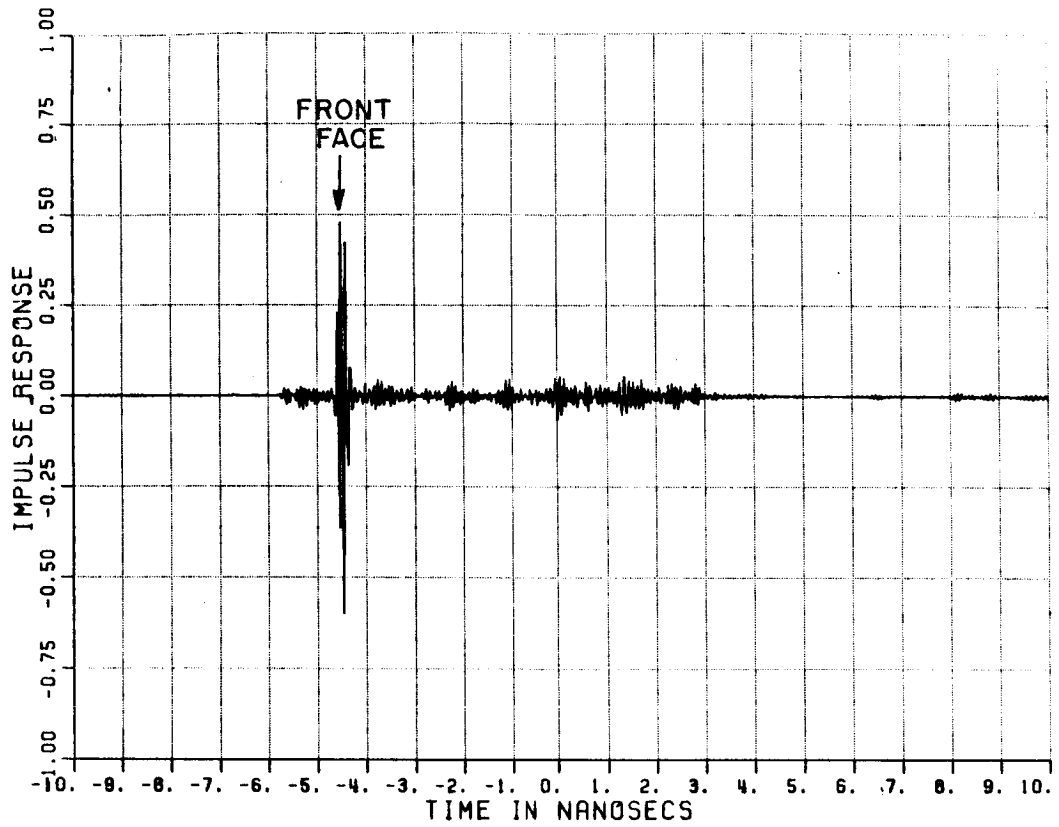
Figure 4.57. Time domain response from 8" wedges with θ=30° and horizontal polarization.
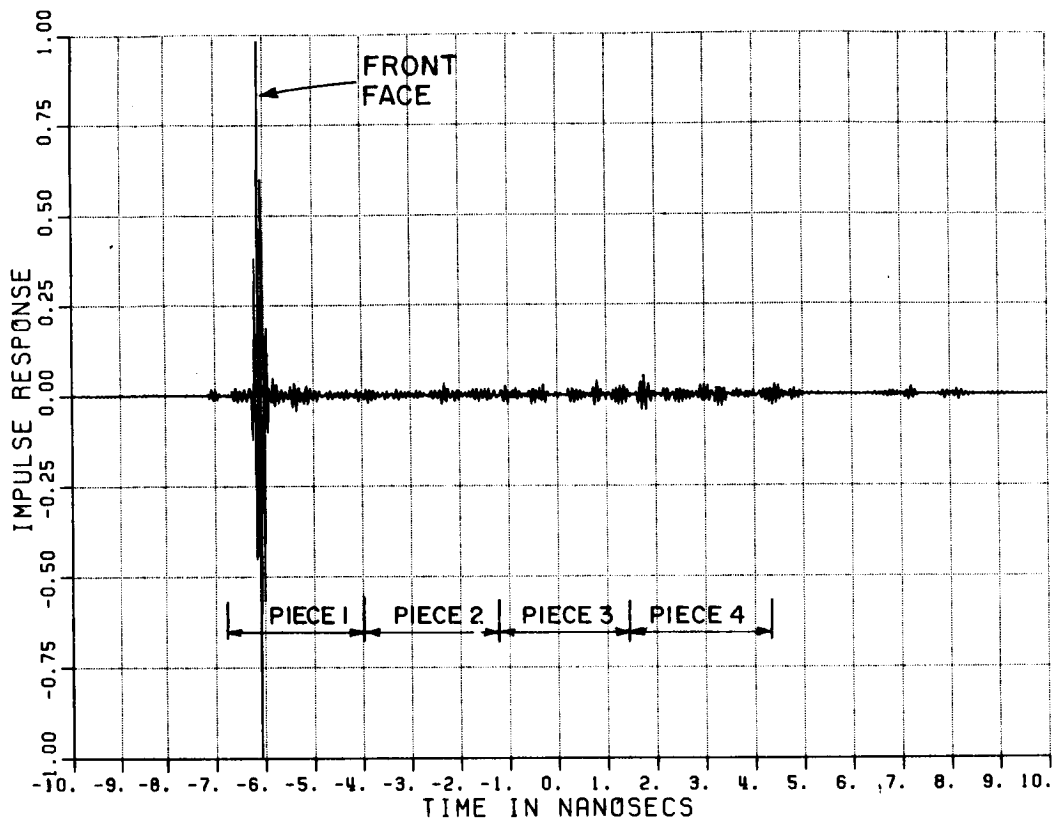
Figure 4.58. Time domain response from 8" wedges with θ=45° and horizontal polarization.
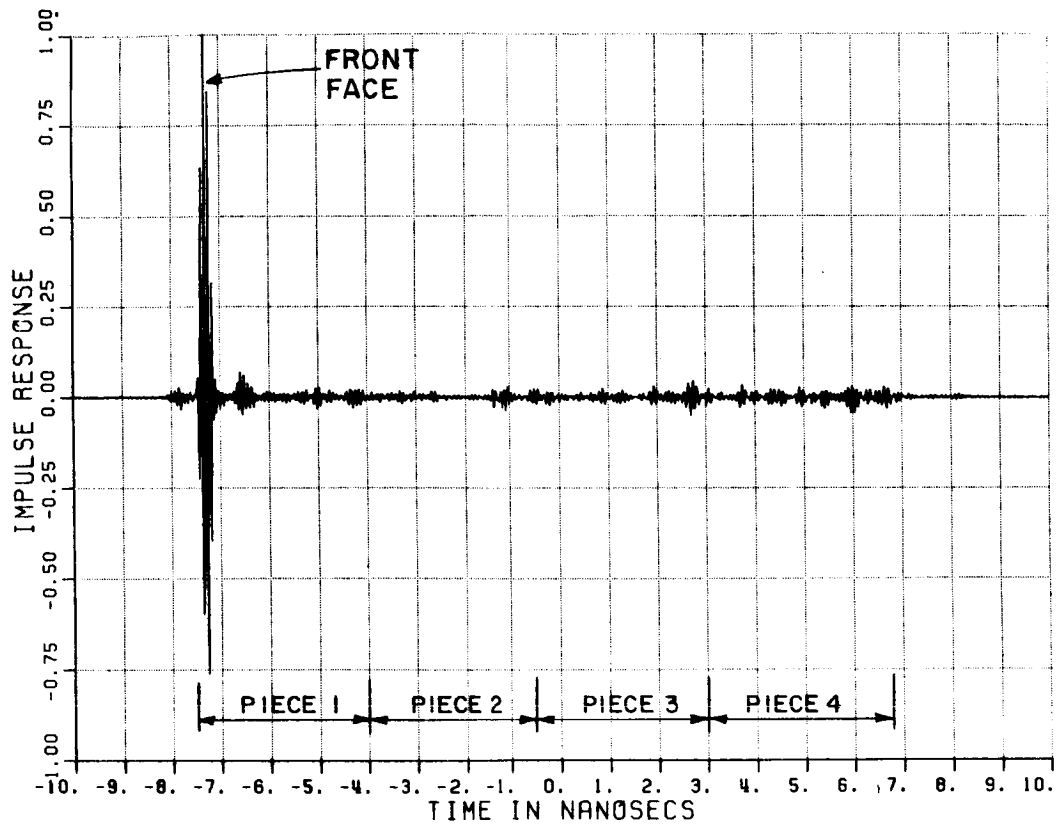
Figure 4.59. Time domain response from 8" wedges with θ=60° and horizontal polarization.
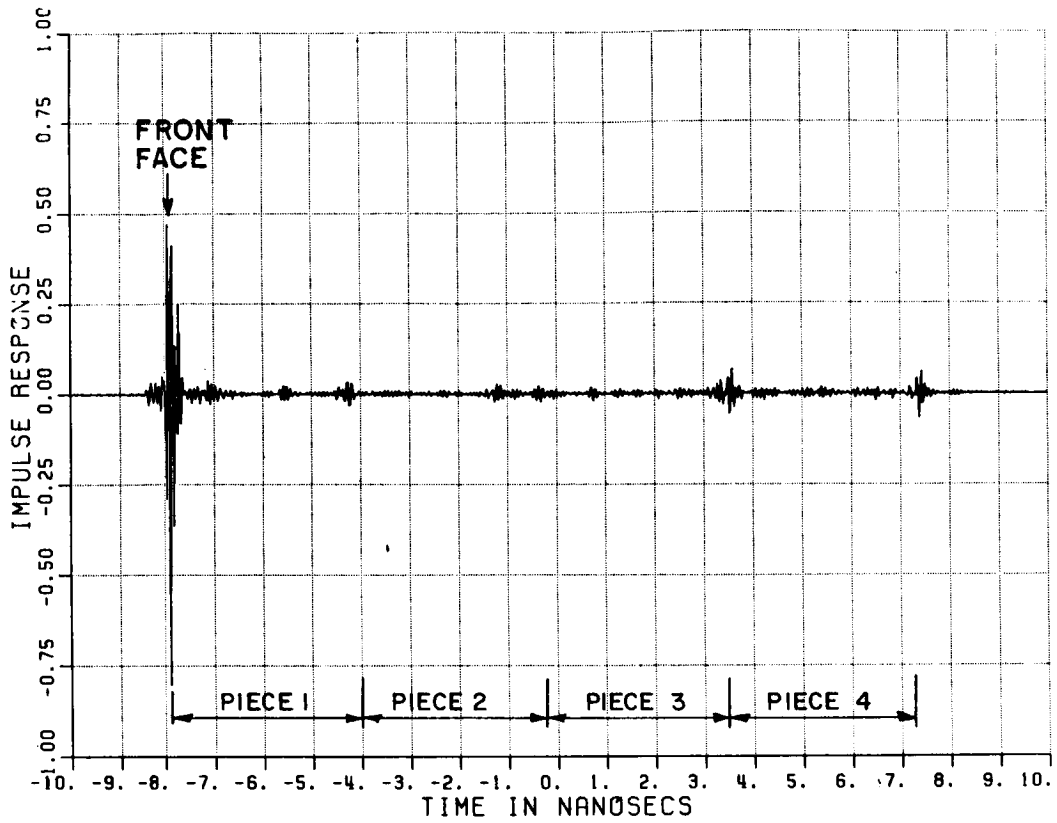
Figure 4.60. Time domain response from 8" wedges with θ=70° and horizontal polarization.

144

CHAPTER V

MEASUREMENT PROCEDURES FOR FREE SPACE ABSORBERS

A. INTRODUCTION

The accurate measurement of good absorbing materials poses a difficult problem by definition since a perfect absorber would absorb all of the incident energy. The low scattered level from an imperfect absorber can be masked by larger erroneous returns which have to be carefully avoided. For example, measuring the scattering from a single piece of 2' x 2' perfect absorber in a compact range target zone will result in a backscattered field from the hole in the incident field as seen in the diffraction coefficients. Even with a reflection coefficient of zero a return is caused from the edge effects.

Possible ways to avoid edge effects include attempting to subtract out the edge effects by using the premise that the edge effects will increase proportional to the circumference while the absorber return would increase proportional to the area. This method sounds good but has the problem that absorber tends to scatter energy incoherently, as was shown in the previous chapter, such that the scattered power is proportional to the area rather than the square of the area making it inseparable from the edge returns. The edge effects could be reduced by

mounting the absorber on a special mount. One possible mount is suggested and shown in Figure 5.1. The discontinuity in the incident field is reduced by adding more absorber behind the piece under test and sloping the sides at the same angle as the pyramids. The edge effects are thus reduced for normal incidence on the pyramids but would remain a problem for wide bistatic and backscattered angles. A conducting plate placed behind the absorber tests for energy passing all the way through the absorber and then back out. Wedge type absorber requires a slightly different mounting structure to terminate the ends of the wedges.

The edge effects can be best avoided by either taking measurements such that a time domain plot can be generated or by measuring an extended wall. The edge effects can be time gated out in the first method and the second method tends to avoid illumination of the edges which diffract.

However, measuring the scattering from an absorber wall introduces a number of additional problems mainly with calibration. Usually, the measurement system is calibrated by comparing against a calibrated standard target of the same type as the target. Consequently, to find the specular reflection coefficient, calibration is done against a conducting plate; whereas, to find reflectivity, calibration should be against a wall of known reflectivity. Unfortunately, no calibrated diffusely scattering walls are available.

This chapter discusses these problems, derives calibration equations for measuring reflectivity, and gives guidelines for measuring free space absorber materials.

ABSORBER UNDER TESTING

MOUNTING STRUCTURE

CONDUCTING PLATE TO TEST PENETRATION THROUGH ABSORBER
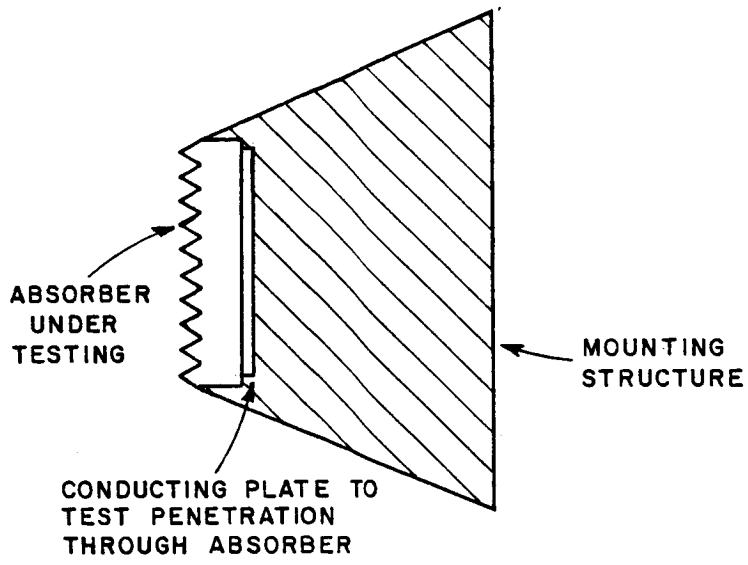
(a) SIDE VIEW
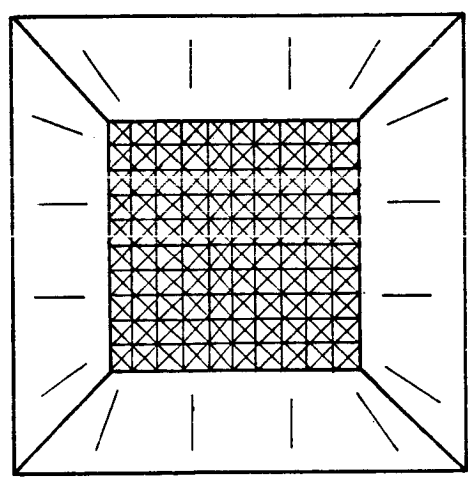
(b) FRONT VIEW

Figure 5.1. Mounting structure to reduce edge effects.

147

B. REFLECTION COEFFICIENT

Most manufacturers specify free space absorbers in terms of a reflection coefficient for a 2' X 2' piece measured with a standardized set up. The procedure involves comparing the far field return from a 2' X 2' absorber section to the return from a conducting plate of the same size as the absorber. Only specular angles can use this method of calibration since the conducting plate theoretically has a reflection coefficient of unity for specular angles and zero for non-specular angles. The plate calibration requires very accurate plate alignment for maximum return. With this method receiver dynamic range may also be a problem.

A standard size is needed because the reflection coefficient tends to decrease as the area increases because of the adding in power effects of the absorber versus adding in phase effects for a plate. The adding in power effects are, of course, a function of frequency. As seen in the measurements and calculations of the previous Chapter, at 2 GHz the 12" absorbers display considerably more adding in phase effects than at 10 or 18 GHz. At frequencies lower than those measured the reflection coefficient will start to become independent of area. Since the reflection coefficient changes with area it is also a function of the illumination even with plate calibration so a standard size with a standard illumination is used to give meaning to specified reflectivities.

Measuring a small piece of absorber has the disadvantage that edge effects can limit how good of absorber can be measured. Approximate values for the lowest measurable reflection coefficient for untreated edges can be easily found using the diffraction solutions described in Chapter II. For a treated edge lower values may be obtainable depending on the edge termination.

Consider the broadside RCS of a 2' X 2' conducting plate at 6 GHz. The high frequency RCS of a conducting plate is $4\pi A^2/\lambda^2$ giving a value of 29 dBSM. (Note that dBSM represents a dB relative to a square meter.) For a perfectly absorbing plate (reflection coefficient of zero) the broadside RCS is calculated from the diffraction coefficients in Chapter II to be -10dB. Thus, even though the material is perfect, a measurement of a 2' X 2' piece yields an apparent reflection coefficient of r^2=-39dB. This simply results from the measurement errors associated with the experimental procedure and represents a lower limit for measurable reflection coefficient for this example. One of the absorber companies lists the reflection coefficient of their 8" and 12" pyramid absorbers as -40 dB using this measurement method which may be the edge effects rather than the reflection coefficient.

The actual edge effects can differ from this example for pyramidal free space absorber because the edge termination is not as abrupt as the flat plate. This probably reduces the edge diffracted field allowing for accurate measurement of lower reflection coefficients. The use of time domain responses where some edge effects can be software gated out also should lower the measureable reflection coefficient.

The edge effect is experimentally demonstrated in the time domain plot shown in Figure 5.2 for a 2' X 2' piece of 12" pyramid absorber at normal incidence measured on a compact range. The time domain plot was generated from frequency data taken between 6 and 18 Ghz at 10 Mhz increments. The return from the pyramid tips, valleys, and the back edge of the absorber are marked. The dominant return here is the back edge of the absorber. The return from energy entering the absorber, traveling through the absorber to the back then coming back out the front would arrive at about the same time as the the edge effects. (The propagation constant being slightly higher in the absorber which would delay the return some.) This term is measured in extended wall measurements and found to be smaller than the pyramid response so in Figure 5.2 the return is attributed to edge effects.

C. REFLECTIVITY

The bistatic pyramid measurements in Chapter IV showed that the reflected power displays predominantly diffuse behavior with little evidence of a specular component. Consequently, the absorber does not act as a reflecting surface but like a diffuse one. A perfectly diffuse surface (also called Lambert scatter) has the property that the scattered energy is proportional to cos (θ) where θ is the angle of propagation relative to the scatter surface normal. (For a Lambert
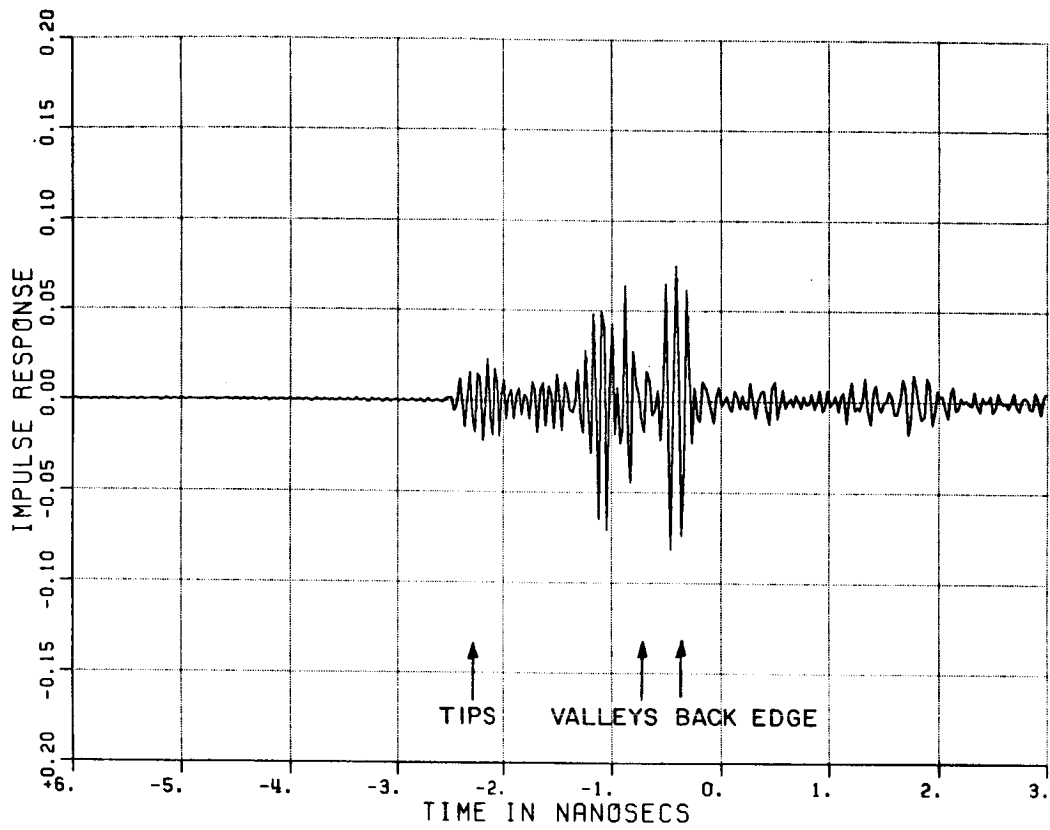
Figure 5.2. Time domain response of backscatter from 1 piece of Company C's 12" pyramid absorber.

151

scatterer the radiation in a given direction is proportional to the projection of the illuminated surface area onto a plane normal to the direction of propagation. In other words, the illuminated area appears to be of uniform brightness when viewed from any angle, but the apparent size of the illuminated area or projected area decreases as cos θ.) The Chapter IV bistatic measurements also showed that the reflectivity is a function of angle since the reflected power increases as the receiver moves closer to the wall even though the projected area is decreasing. Thus the reflected energy per unit solid angle as given by Swarner, et al. [19] is

$$P_\Omega = C \cdot S_D \cdot \rho^2 \cdot W_A \cdot \cos(\theta_i) \qquad (5.1)$$

where S_D is the incident power density, ρ^2 is the reflectivity, W_A is the illuminated wall area, and C is a proportionality constant. Since for a flat wall, the constant C can be evaluated by integrating over a hemisphere ($2 \cdot \pi$ steradians) yielding a value of $1/\pi$ for C.

Since for pyramidal absorbers reflectivity is function of both the incident and receive angles the equation becomes

$$P_\Omega = \frac{S_D \cdot \rho^2(\theta_i, \theta_r) \cdot W_A \cdot \cos(\theta_i)}{\pi} . \qquad (5.2)$$

Using a diffuse scattering model for absorber has the advantage that the reflectivity should be independent of the area measured in the frequency range studied. Disadvantages of measuring reflectivity include difficulties in calibration since no standardized diffuse wall is available. The equations for calibrating reflectivity measurements against a sphere are derived in Section E of this Chapter.

152

D. EFFECTIVE SCATTERING

The measurements of scattering shown in Chapter IV for the 8-inch pyramid absorber are presented in terms of effective scattering of the wall, where the effective scattering is defined as the RCS of a conventional far-field small target scatterer which would produce the same return as that from the wall for a particular test configuration. The effecting scattering was found by

$$\text{Effective Scattering} = 10\log 4\pi \cdot |E_{cal}|^2$$

where E_{cal} is defined in Equations (5.3). Unfortunately, the effective scattering is, also, not an unique property of the absorber coated wall but includes parameters of the measurement system.

Effective scattering is easier to measure directly than reflectivity since calibration is done against a sphere. The reflectivity can be found using the equations derived in the next section.

E. CALIBRATION EQUATIONS

The usual procedure for calibrating a system involves measuring the return from both an unknown target as well as a known one so that the system parameters such as wavelength, gains and distances need not be known. The calibrated scattered field of the unknown target is then found by taking a ratio such as the following one reported by Walton and Young [20]:

$$E_{cal}(\text{target}) = \frac{E_R(\text{target}) \cdot \text{EXACT (sphere)}}{E_R \text{ (sphere)}} \tag{5.3}$$

153

where EXACT(sphere) is the calculated return from the sphere, and E_R (target) and E_R (sphere) represent the scattered E-field from just the target and just the sphere, respectively. Both terms, thus, assume some background subtraction or nulling so that they contain just the scattering contribution from the sphere or target. This equation also assumes the unknown target satisfies the same type of scattering model as the sphere. For example, from the radar range equation both targets must be in the far field of the antenna and the antenna in the far field of both targets; in other words, both sphere and unknown target are far-field small-target scatterers. A more detailed description of different scattering models is given by Swarner et al. [19].

Similarly, the reflection coefficient (Γ) of an unknown target can be found by calibrating against a plate of the same size as follows.

$$\Gamma \text{ (target) } = \frac{\Gamma \text{ (plate) } \cdot E_R \text{ (target)}}{E_R \text{ (plate)}} \qquad (5.4)$$

where E_R (target) and E_R (plate) represent the scattered electric field from just the target and just the sphere respectively and $\Gamma = \pm 1$ depending on the geometry for the conducting plate. If the edges of the target and plate are not illuminated this equation is theoreticaly sound. However if the edges are illuminated this equation makes the erroneous assumption that the edge effects of the target compared to the plate are always proportional to Γ. This equation should still work well if the edge effects are small compared to the specular return. This is true for a conducting plate but is not necessarily true for good absorbers.

If the plate calibration is difficult because of dynamic range or
alignment problems the reflection coefficient of the target can also be
easily found by calibrating against a sphere return by the following
equation provided the target and sphere are both small-target
scatterer such that

$$\Gamma \text{ (target)} = \frac{E_R \text{ (target)} \cdot EXACT \text{ (sphere)} \cdot \Gamma \text{ (plate)}}{E_R \text{ (sphere)} \cdot CALCULATED \text{ (plate)}} \qquad (5.5)$$

A Moment Method solution can be used to calculate the scattered E-field
from a plate but for most practical applications the plate size will be
greater than a wavelength so a high frequency solution can be used to
get an approximate value.

If the calibrated scattered field of the target is already known
then Γ of the target is found simply from

$$\Gamma \text{ (target)} = \frac{E_{cal}\text{(target)} \cdot \Gamma \text{ (plate)}}{CALCULATED \text{ (plate)}} \qquad (5.6)$$

This equation shows the reflection coefficient can be easily found
from E_{cal}; however, difficulties in calibration arise when measuring the
reflectivity . The calibration, ideally would be compared to a
calibrated diffuse target. Since none exists the obvious alternatives
include using a conducting plate or sphere. The conducting plate is
only useful at specular angles and this has dynamic range problems so
calibration against a sphere seems more appropriate.

The calibration equations are developed, first, for an extended
wall measured in the near field of high gain antennas considering the
ideal case of uniform illumination in the main beam and zero outside;
then, modifications are given to correct for the non-ideal case and for
conventional RCS measurement techniques.

155

The calculation of reflectivity from the calibrated scattered E-field can be found by first considering the near field target illumination as shown in Figure 5.3. Using the near field assumption for a high gain antenna of a collimated beam and uniform illumination, the power density at a target plane is given by

$$S_D = \frac{P_T \cdot \eta_T}{A_{PH}} \tag{5.7}$$

where P_T is the transmitted power, η_T is the transmitting antenna efficiency and A_{PH} represents the physical aperture of the transmitting antenna. From antenna theory the relationship between the gain and effective aperture (A_e) of an antenna is given by

$$A_e = \frac{G \cdot \lambda^2}{4\pi} \tag{5.8}$$

where λ is the wavelength. Incorporating the antenna efficiency gives the following equation for the physical aperture:

$$A_{PH} = \frac{A_e}{\eta} = \frac{G \cdot \lambda^2}{4\pi \cdot \eta} \quad . \tag{5.9}$$

Substituting for A_{PH} gives the power density at the target plane as

$$S_D = \frac{4\pi \cdot P_T \cdot \eta_T^2}{G_T \cdot \lambda^2} \quad . \tag{5.10}$$

Note that the power density is inversely proportional to antenna gain and independent of range while in the familiar far field result the power density is proportional to antenna gain and inversely proportional to the square of the range. The inverse relationship with antenna gain for the near field case results from the transmitted power being spread

156
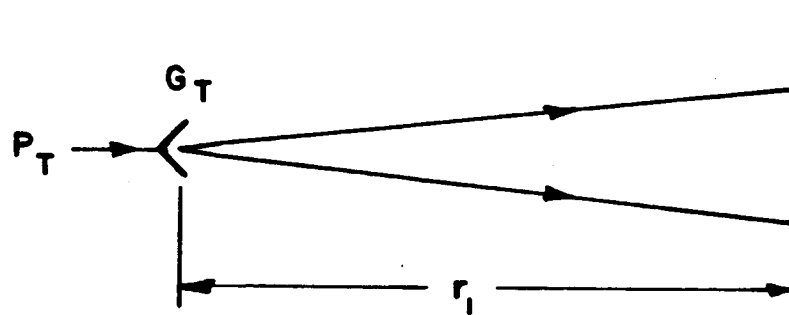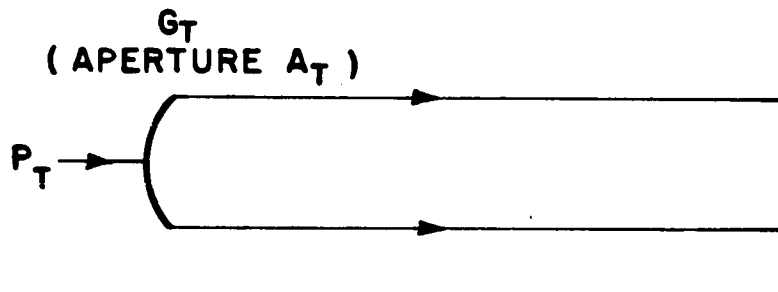
(a) FAR FIELD

(b) NEAR FIELD

Figure 5.3. Target illumination geometry.

over a greater area as gain is increased since the antenna aperture increases linearly with gain. The range independence results from the collimated beam assumption for the near field of a high gain antenna.

Next consider the scattered power from both a small target and a wall. The echo area for a small target is defined as

$$\sigma = \frac{4\pi \cdot [\text{Reflected Power per Unit Solid Angle}]}{[\text{Incident Power per Unit area}]} = \frac{4\pi \cdot P_\Omega}{S_D} \qquad (5.11)$$

Consequently, the power reflected (at angle θ) per unit solid angle is given by

$$P_\Omega = \frac{S_D \cdot \sigma}{4\pi} \quad . \qquad (5.12)$$

The equation for the power reflected per unit solid angle of a diffuse wall was given in Section C of this chapter as

$$P_\Omega = \frac{S_D \cdot \rho^2(\theta_i, \theta_r) \cdot W_A \cdot \cos(\theta_i)}{\pi} \quad . \qquad (5.13)$$

Next the received power is determined by the amount of power incident upon the receiving aperture. For the near field case rays corresponding to scattered power are received only if they are both incident upon the receiving aperture and essentially parallel to the axis of the receiving antenna. This is illustrated in Figure 5.4.

If the wall surface is a diffuse scatter, each incremental element with surface area (dS) will scatter rays over the complete half space as indicated by typical rays 1 through 8 as shown in Figure 5.4. Only rays within the angle of acceptance, or beam width, (B_r), of the receiving antenna will be received. Thus for near field (high gain) models, the
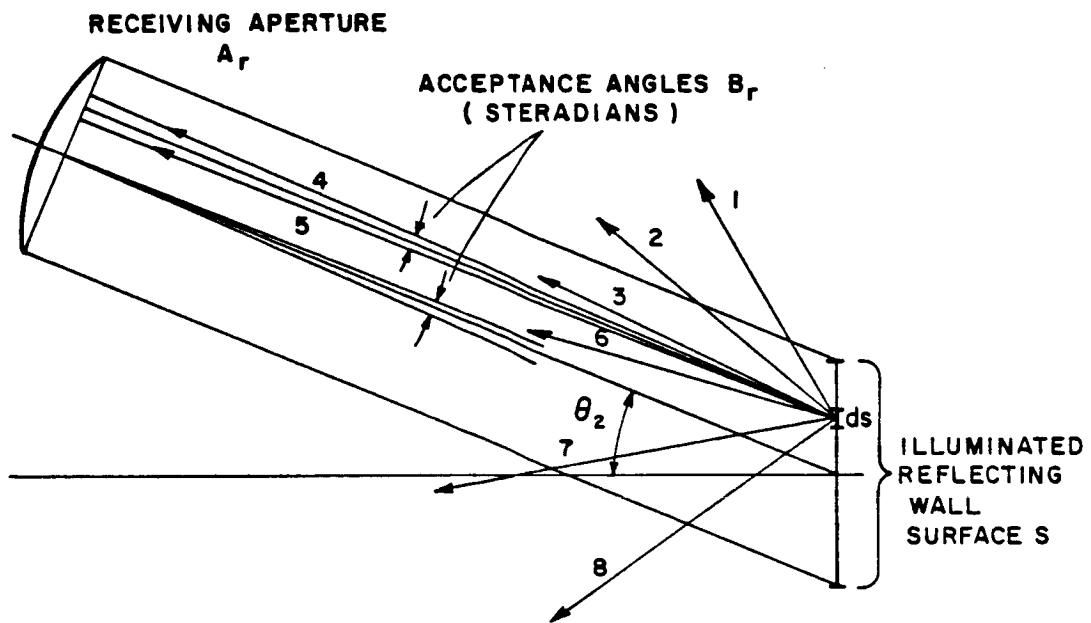
Figure 5.4. Near field receiving antenna geometry.

received power is directly proportional to receiving antenna beam width. But, beam width is inversely proportional to gain (and effective aperture) so the received power is inversely proportional to antenna gain.

For a small target return, the beams of both the transmitting and receiving antennas encompass the target; consequently, any ray reflected toward the receiver which satisfies the acceptance angle criterion will also be incident upon the aperture. The received power is therefore given by

$$P_R = P_\Omega \cdot \eta_R \cdot B_r = \frac{S_D \cdot \eta_R \cdot B_r \cdot \sigma}{4\pi} \qquad (5.14)$$

where S_D is the given by Equation (5.10), η_R is the receiving antenna efficiency, and B_r is the angular beam of the receiving antenna which is given by [19]

$$B_r = \frac{4\pi \cdot \eta_R}{G_R} \cdot \qquad (5.15)$$

Substituting Equations (5.15) and (5.10) into (5.14) gives the following result

$$\frac{P_R}{P_T} = \frac{4\pi \cdot \eta_T^2 \cdot \eta_R^2 \cdot \sigma}{G_T \cdot G_R \cdot \lambda^2} \cdot \qquad (5.16)$$

The power received from a diffusely scattering plane wall extending beyond the limits of both the transmitting and receiving beams is given by

$$P_R = P_\Omega \cdot \eta_R \cdot B_r = \frac{S_D \cdot W_A \cdot \rho^2 \cdot B_r \cdot \cos(\theta_r)}{\pi} \qquad (5.17)$$

160

where S_D is the actual power density in the plane of the wall and W_A is the corresponding wall area common to both the transmitting and receiving antenna beams.

Since Equation (5.10) for S_D was derived for normal incidence to get the power density in the plane of the wall the equation is modified such that

$$S_D = \frac{4\pi \cdot P_T \cdot \eta_T^2 \ \cos(\theta_i)}{G_T \cdot \lambda^2} \qquad (5.18)$$

Substituting this result into the previous equation gives

$$P_R = \frac{16\pi \cdot P_T \cdot \eta_T^2 \cdot \eta_R^2}{G_T \cdot G_R \cdot \lambda^2} \cdot \rho^2 \cdot W_A \cdot \cos(\theta_i) \cdot \cos(\theta_r) \quad . \qquad (5.19)$$

If the projection of the transmitting beam onto the wall falls entirely within that of the receiving beam, then W_A is chosen as the area of the wall illuminated by the transmitter such that

$$W_A = \frac{A_{PH}}{\cos(\theta_i)} = \frac{G_T \cdot \lambda^2}{4\pi \cdot \eta_T \cdot \cos(\theta_i)} \quad . \qquad (5.20)$$

Substituting this into the previous equation one obtains that [19]

$$P_R = \frac{4 \cdot \eta_T \cdot \eta_R^2 \cdot P_T \cdot \rho^2 \cdot \cos(\theta_r)}{G_R} \quad . \qquad (5.21)$$

If the projection of the receiving beam onto the wall falls entirely within the transmitting beam then W_A is chosen as the area of the wall within the receiver field of view such that

161

$$W_A = \frac{A_{PH}}{\cos(\theta_r)} = \frac{G_R \cdot \lambda^2}{4\pi \cdot \eta_R \cdot \cos(\theta_r)} \quad . \tag{5.22}$$

The corresponding received power is given by [19]

$$P_R = \frac{4 \cdot \eta_T^2 \cdot \eta_R \cdot P_T \cdot \rho^2 \cdot \cos(\theta_i)}{G_T} \quad . \tag{5.23}$$

The final step in deriving the calibration equation for a diffuse wall calibrated against a sphere is to divide the the power received from the wall, Equation (5.23), by the power received from a sphere, Equation (5.18), and solve for reflectivity to get

$$\rho^2 = \frac{P_R(\text{target}) \cdot \pi \cdot \eta_T \cdot \text{Exact RCS (sphere)}}{P_R(\text{sphere}) \cdot G_T \cdot \lambda^2 \cdot \cos(\theta_r)} \tag{5.24}$$

if the transmitting antenna beam is small than the receiving beam. If the receiving beam is smaller than the transmitting beam, then one obtains

$$\rho^2 = \frac{P_R(\text{target}) \cdot \pi \cdot \eta_R \cdot \text{Exact RCS (sphere)}}{P_R(\text{sphere}) \cdot G_R \cdot \lambda^2 \cdot \cos(\theta_i)} \tag{5.25}$$

It appears that this method of calibration using a sphere of known cross section is not particularly useful for finding the reflectivity since it is still necessary to know antenna gains, efficiencies, angles, and wavelength; however, using Equation (5.9) for physical aperture Equation (5.24) can be simplified to give

$$\rho^2 = \frac{P_R(\text{target}) \cdot \text{EXACT RCS (sphere)}}{4 \cdot A_{PH_T} \cdot \cos(\theta_r) \cdot P_R(\text{sphere})} \tag{5.26}$$

162

and Equation (5.25) can be simplified to give

$$\rho^2 = \frac{P_R(\text{target}) \cdot \text{EXACT RCS (sphere)}}{4 \cdot A_{PH_R} \cdot \cos(\theta_r) \cdot P_R(\text{sphere})} \tag{5.27}$$

So the reflectivity can be expressed in terms of the received power, the antenna's physical aperture and one angle.

Now consider the case of non-uniform illumination but still in the near field of a collimated beam antenna. A pattern factor replaces the A_{PH} as shown below:

$$\rho^2 = \frac{P_R(\text{target}) \cdot \text{EXACT RCS (sphere)}}{4 \cdot \iint \text{Pat}_T \cdot \text{Pat}_R \, dS \cdot \cos(\theta_i) \cdot \cos(\theta_r) \cdot P_R(\text{sphere})} \tag{5.28}$$

where dS is the surface of the absorber and Pat_T and Pat_R are the normalized projected pattern of the transmitting and receiving antennas onto the absorber. The surface integration is done over the entire wall. Pat_T and Pat_R can be measured separately or together as discussed in the next section.

Even though the derivation of this equation was done only for a near field measurement with high gain antennas it can be shown that the same equation will result assuming conventional far field measurements with the assumption that the edge effects are small or can be gated out and the integration is only over the targets area.

F. MEASUREMENT GUIDELINES

The desired properties of the absorber and its quality determine which types of measurements are applicable. For backscatter, conventional RCS measurements or high gain antenna measurements of an extended wall are useful. Since compact ranges are designed for backscatter measurements, they are difficult to use for bistatic measurements. Also, for bistatic measurements near specular angles, the edge effects are difficult to separate from the pyramid returns making an extended wall measurement necessary.

For conventional far field and compact range measurements away from normal incidence more than one piece wide needs to be measured because the absorber's front face exhibits very strong returns especially close to grazing angles. The front face return may be software gated out but some of the absorber return will be lost as well. Edge treatment such as shown in Figure 5.1 moves the return forward in time. Also, close to grazing incidence the mounting structure behind the absorber is more exposed. Thus, the mounting structure should not be close to the absorbers edges.

Even though the conventional far field RCS measurements have these limitations, the measurements can be useful for a number of reasons. First, set up of a single piece of absorber is much quicker than for a wall. Second, a wide variety of absorber can be measured since only a few of each kind are needed. Third, the specular return gives a good indication of dispersiveness or how well the material adds incoherently.

Also, measuring a single piece eliminates the effects of gaps between absorber placed on a wall and can give an indication of the differences from one piece to the next. Finally, using a frequency sweep to generate a time domain response, the pyramid tip and valley contributions can be separated in time from the edge effects. (The contribution from energy passing through the absorber hitting the base and then coming back out arrives at about the same time as the edge effects making them inseparable. This term requires an extended wall measurement. This mechanism has been found smaller than the other returns for the absorbers measured in this study.) Thus, all these factors make measuring a single piece of absorber a useful tool.

When measuring a single piece of absorber, more than one piece should be measured because the scattering level varies between pieces. To demonstrate this the time and corresonding frequency domain data from 8 different pieces of company B's 12" pyramid absorber are shown in Figures 5.5 through 5.20. All of these pieces were new, having arrived from the manufacturer only a few days before being measured. Rotating a piece 180° did not change the scattering significantly; however, a 90° rotation can make a piece look significantly different.

Extended wall measurements are useful for backscatter as well as bistatic measurements. The antennas must be placed such that the direct transmitter to receiver signal can be hardware gated out; otherwise, the absorber return is lost even with background subtraction. The distance the antennas are from the wall can be changed slightly so the direct signal can be gated out. This changing of distance should have little

effect on the results since the measurements are in the near field of a collimated beam antenna which is assumed to have a pattern which is independent of range. This restriction poses the greatest problem when trying to measure forward scatter near grazing incidence as a very large wall is needed to take the measurement.

The only extended wall measurement considered is the near field collimated beam system because of the following reasons. First, getting an accurate measurement of reflectivity from a non-collimated beam antenna is impossible because the energy would strike the wall at a wide range of angles. For example, the incident energy from a horn antenna would hit the wall at different incident angles and reflectivity changes for different angles. Also the path length changes give amplitude and phase changes. The horn measurement of an absorber wall does not give an accurate value for reflectivity but it can be an useful tool to analyze chamber effects such as interactions between walls and target. Second, a far-field model can not be accurately applied to an extended wall since the scatter size increases with range so that the receiving antenna can never be in the far field of the scatter.

Calibration for the far field measurements can be made against a sphere or plate though a sphere is preferable as discussed in the previous section. For the extended wall measurements a sphere should be used. When calibrating an extended wall against a sphere the projected pattern of the transmitting and receiving antennas on the wall appear in the equations. These patterns can be measured simultanously by placing the transmitting and receiving antennas in the desired position to

166

measure the wall. With the wall preferably removed, a sphere is used to probe the fields at the wall. The scattered field from the sphere is measured as it is moved around on the wall. Normalizing the results to the maximum return, gives the value of $Pat_T \cdot Pat_R$ at each point on the wall. Using pattern multiplication, positions on two perpendicular axis gives an approximate pattern. This measurement has the disadvantage that it depends on the position of both the transmitting and receiving antennas.

The antenna patterns can also be measured separately so that the positions of the antennas can be moved. A field probe or a sphere measures the field across the face of each antenna at about the same distance as the wall on a plane parallel to the antennas aperture. The pattern is then projected onto the surface of the absorber to do the surface integral.

A number of additional experiments were done that were not reported in Chapter IV because of poor signal to noise ratios. The low signal levels involved with measuring absorbers make background subtraction essential and most of the experiments not reported were done without background subtraction.
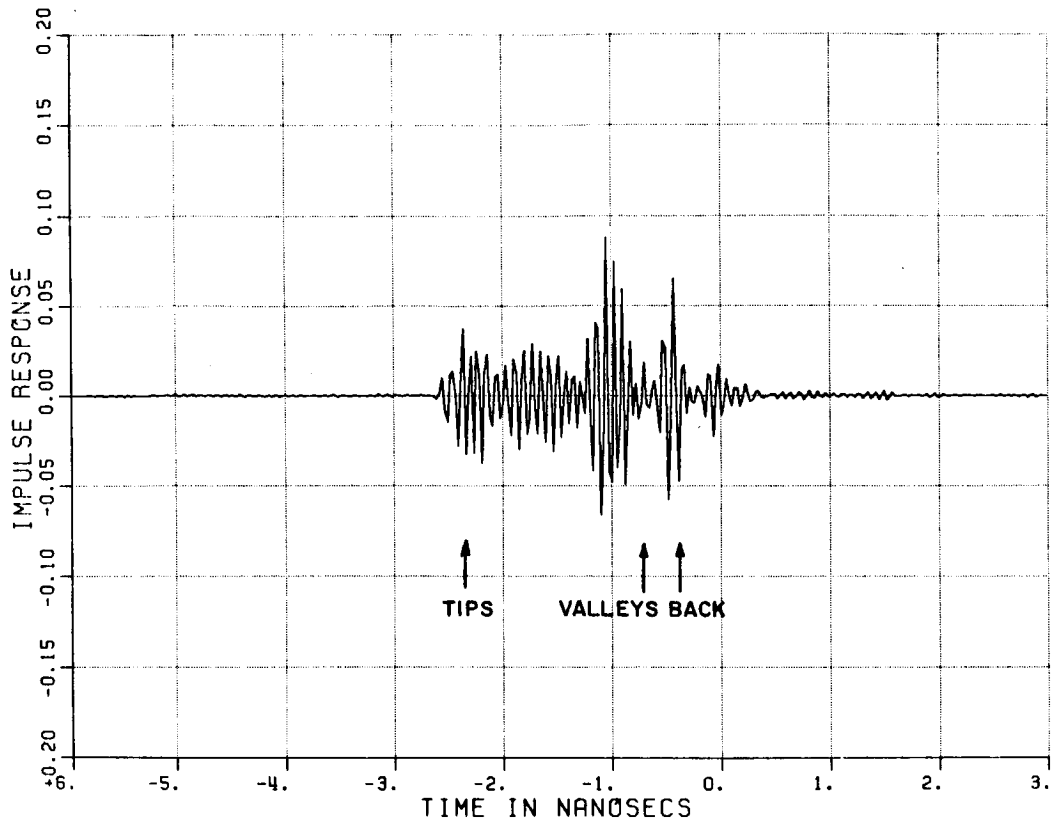
Figure 5.5. Band limited time domain response of 1 sample of Company B's 12" pyramid absorber with nose-on incidence.
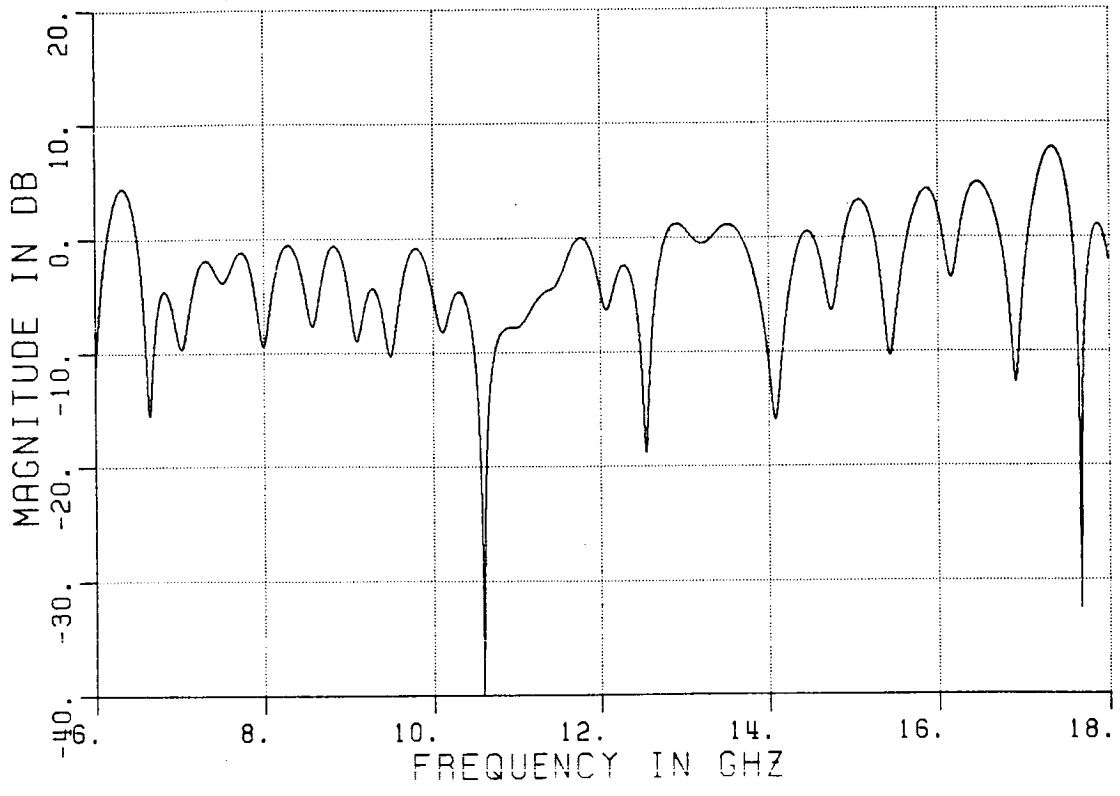
168

Figure 5.6. Measured nose-on RCS of 1 sample of Company B's 12"
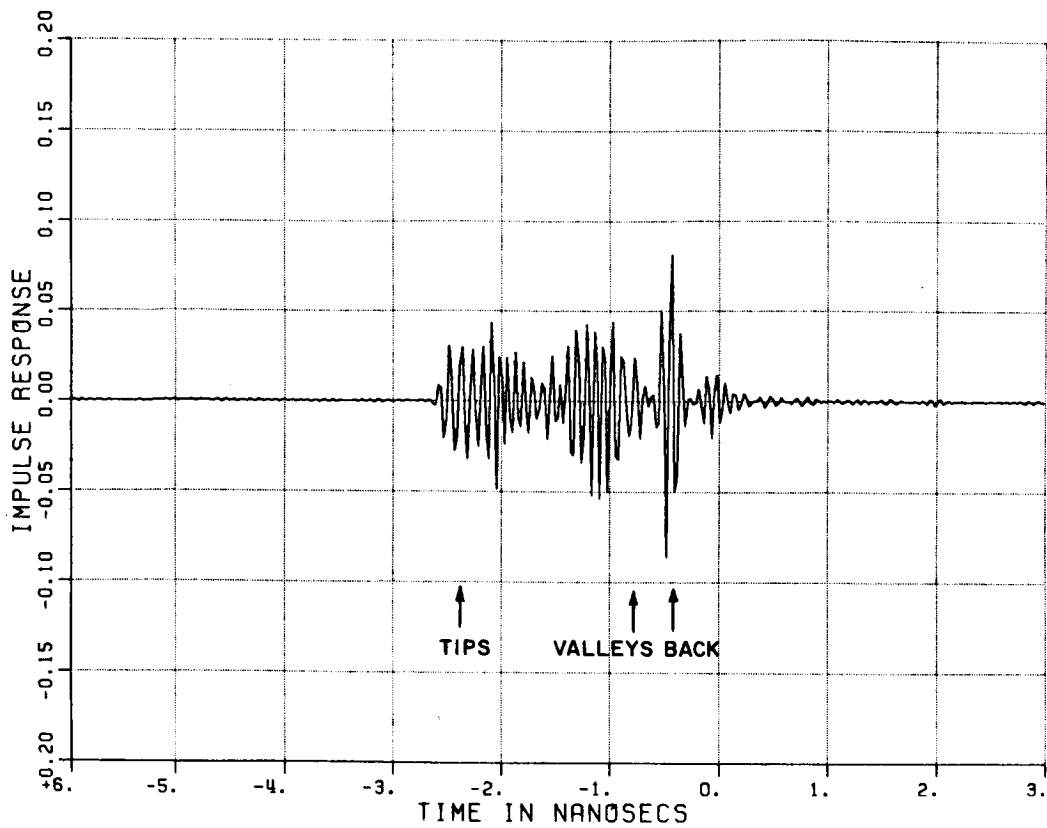pyramid absorber with nose-on incidence.

Figure 5.7. Band limited time domain response of 1 sample of Company
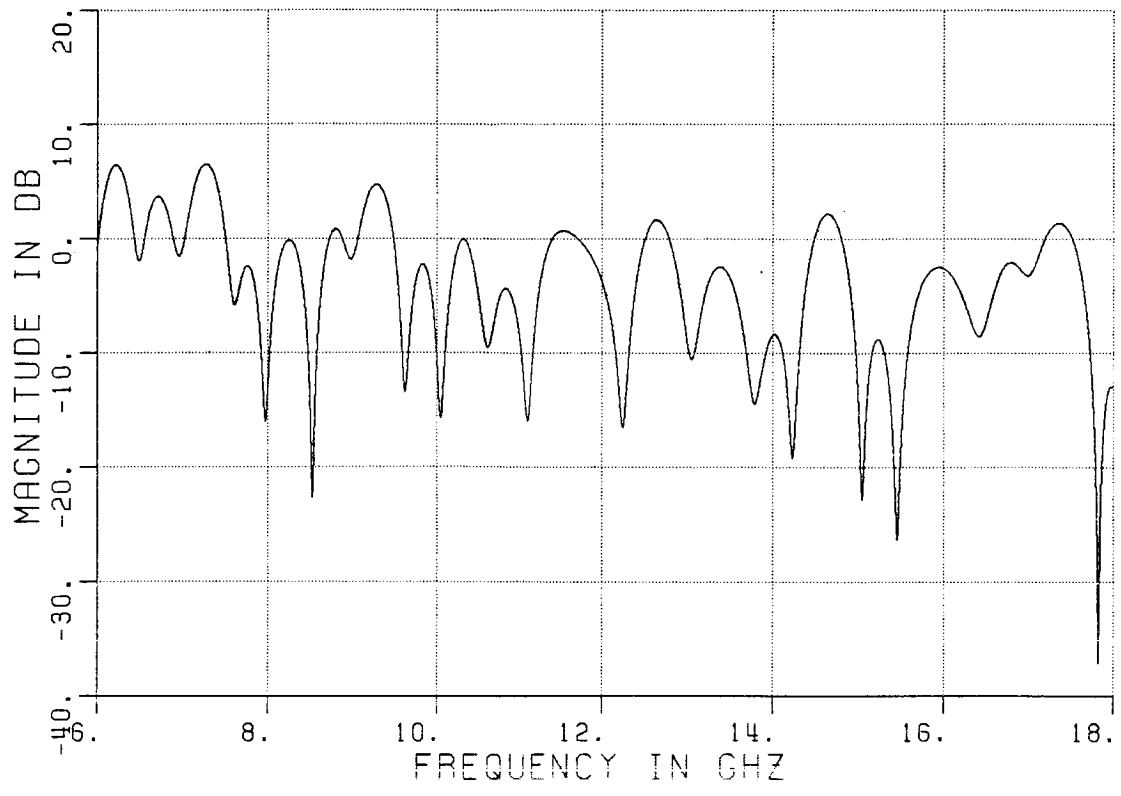B's 12" pyramid absorber with nose-on incidence.

170

Figure 5.8. Measured nose-on RCS of 1 sample of Company B's 12"
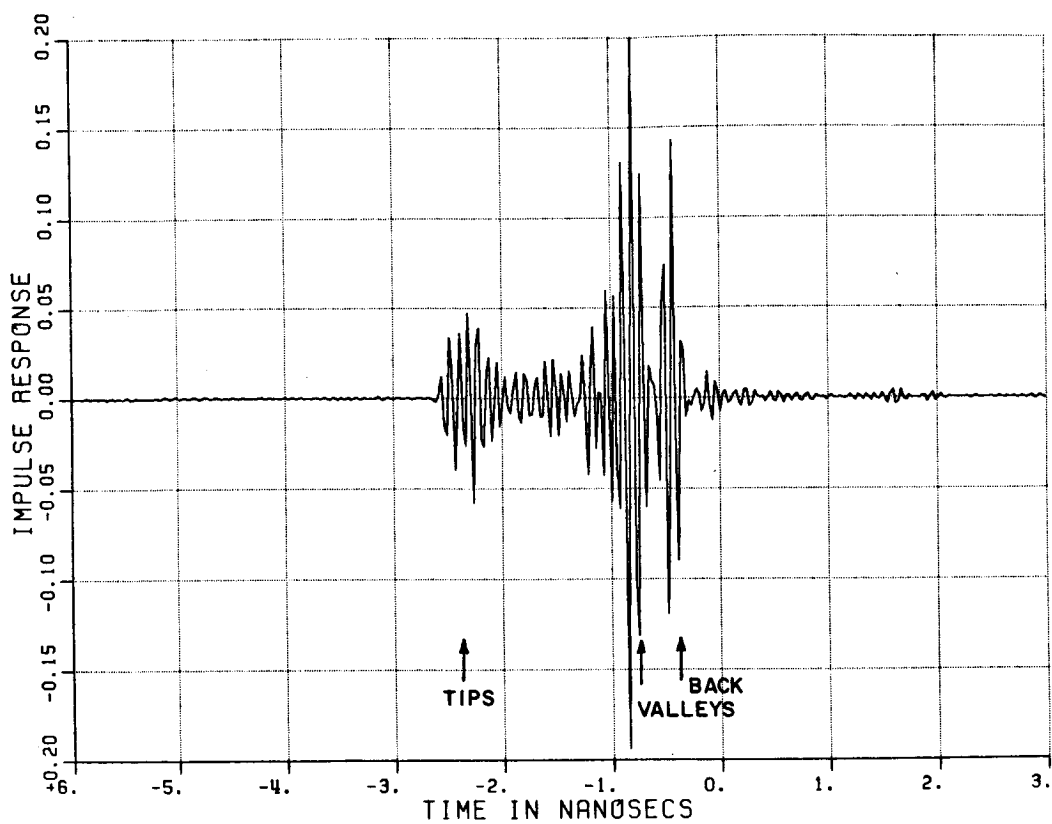pyramid absorber with nose-on incidence.

Figure 5.9. Band limited time domain response of 1 sample of Company B's 12" pyramid absorber with nose-on incidence.
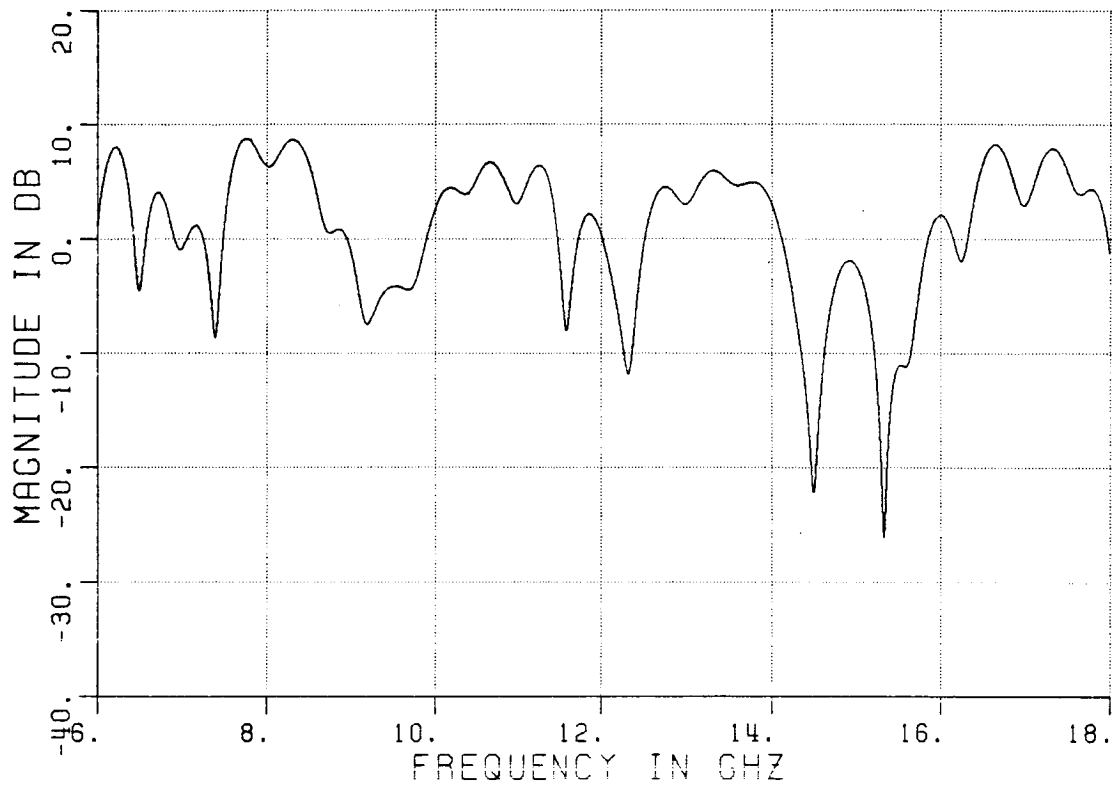
172

Figure 5.10. Measured nose-on RCS of 1 sample of Company B's 12"
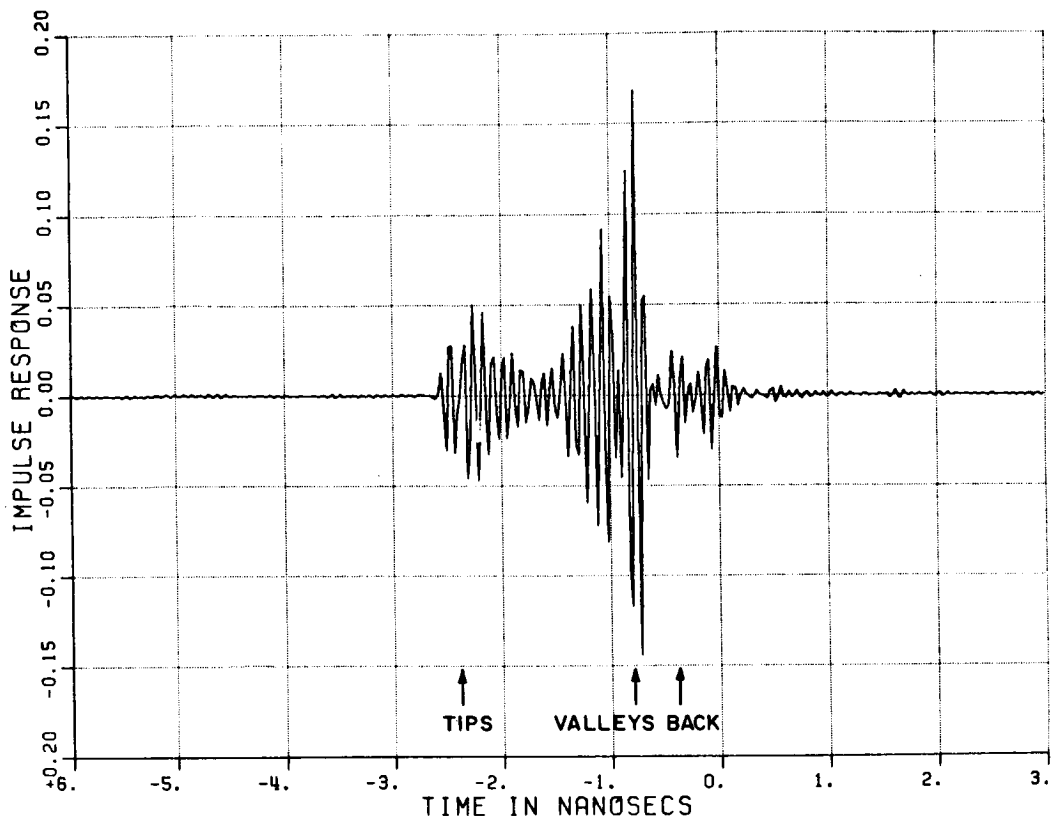pyramid absorber with nose-on incidence.

Figure 5.11. Band limited time domain response of 1 sample of Company B's 12" pyramid absorber with nose-on incidence.

174

Figure 5.12. Measured nose-on RCS of 1 sample of Company B's 12"
pyramid absorber with nose-on incidence.

175

Figure 5.13. Band limited time domain response of 1 sample of Company
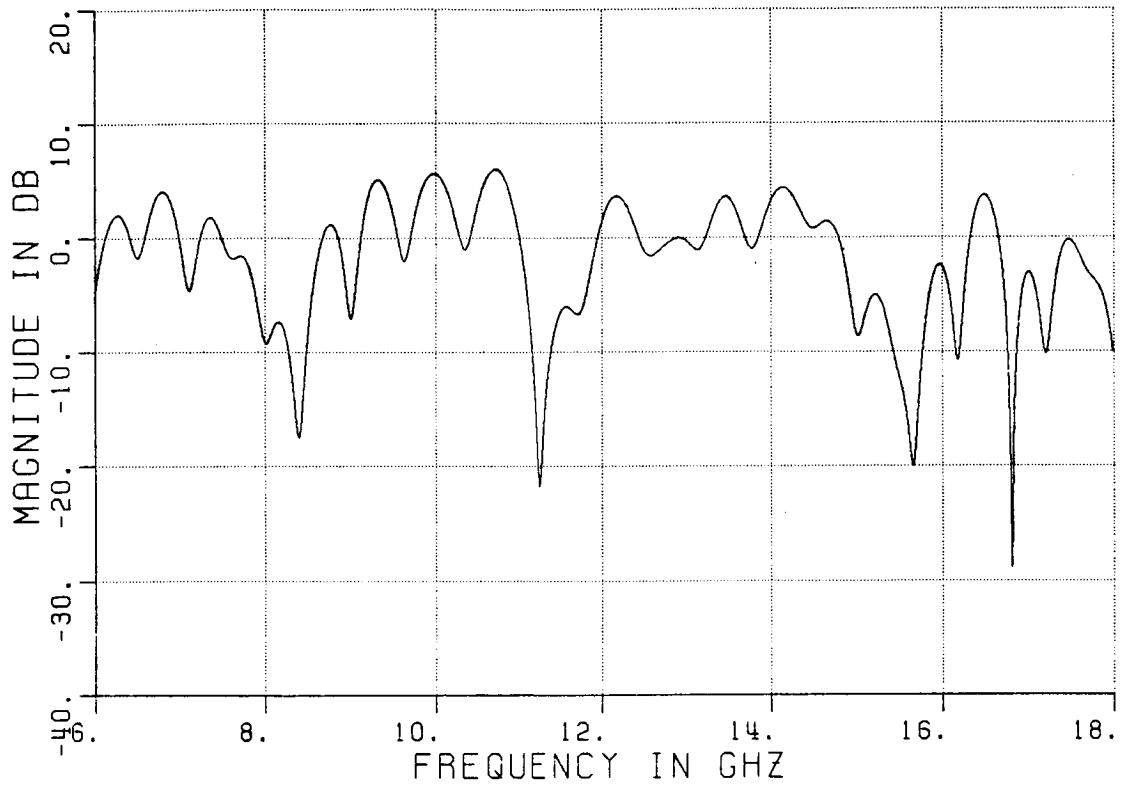B's 12" pyramid absorber with nose-on incidence.

176

Figure 5.14. Measured nose-on RCS of 1 sample of Company B's 12"
pyramid absorber with nose-on incidence.

Figure 5.15. Band limited time domain response of 1 sample of Company
B's 12" pyramid absorber with nose-on incidence.

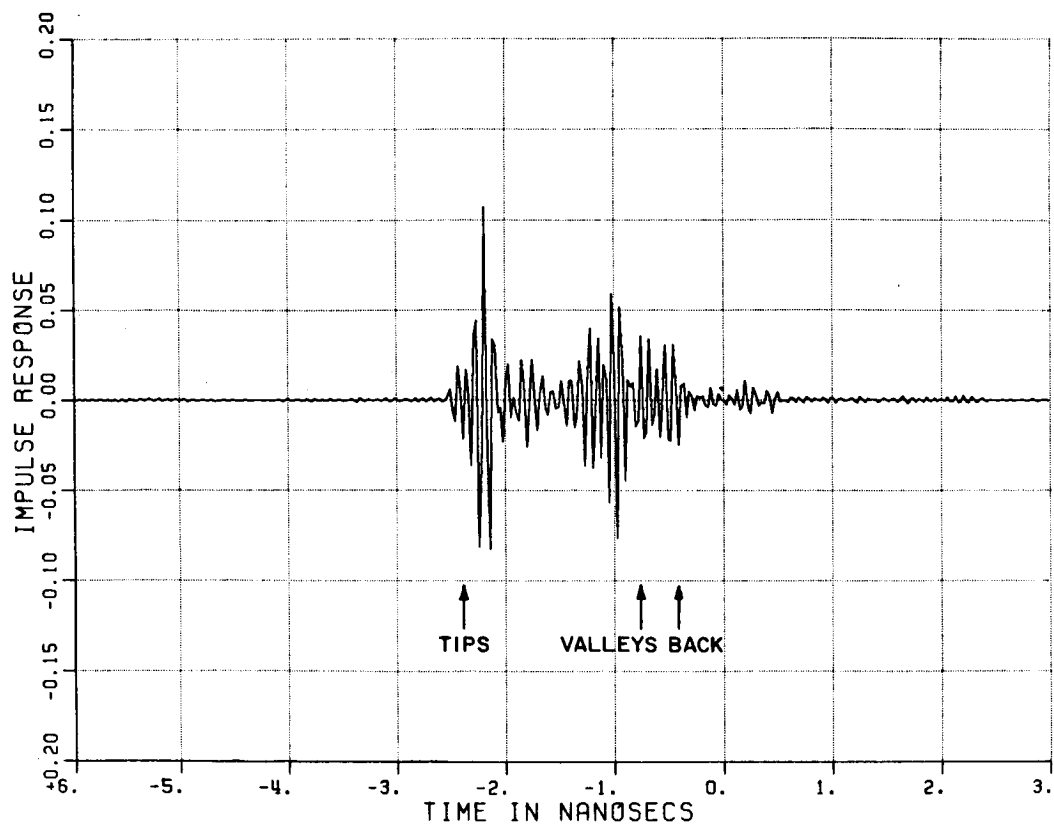Figure 5.16. Measured nose-on RCS of 1 sample of Company B's 12" pyramid absorber with nose-on incidence.

179

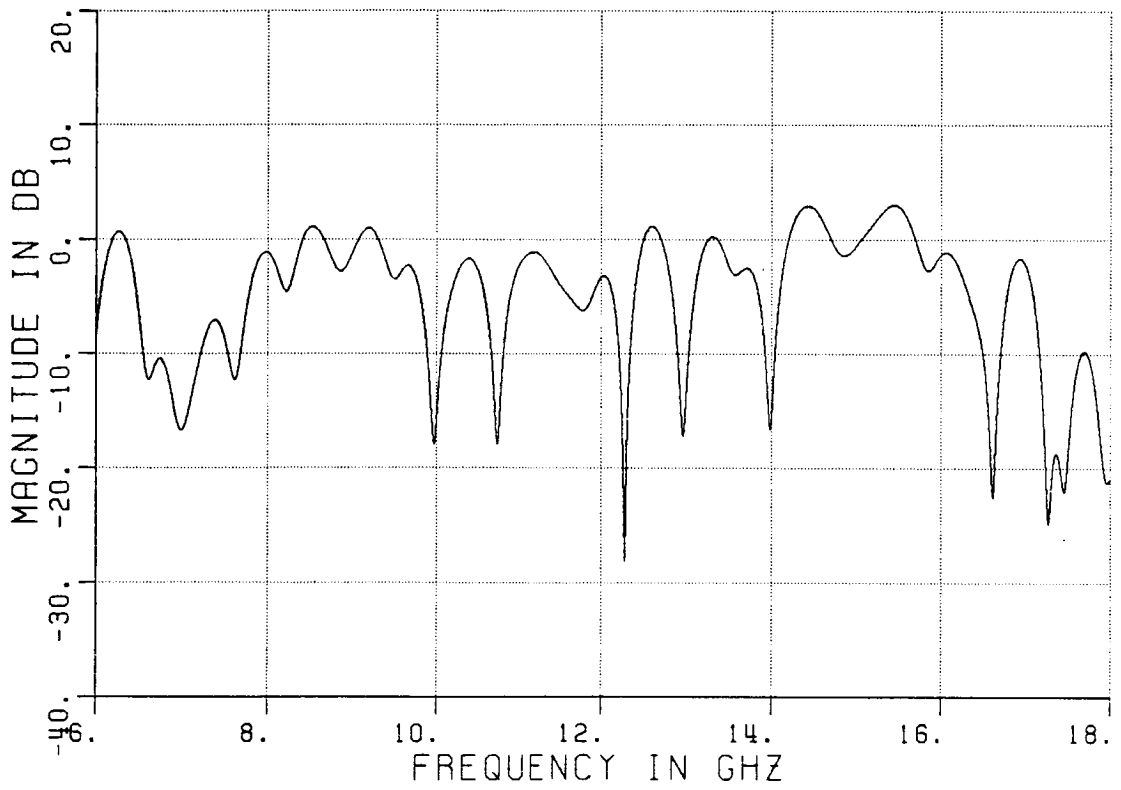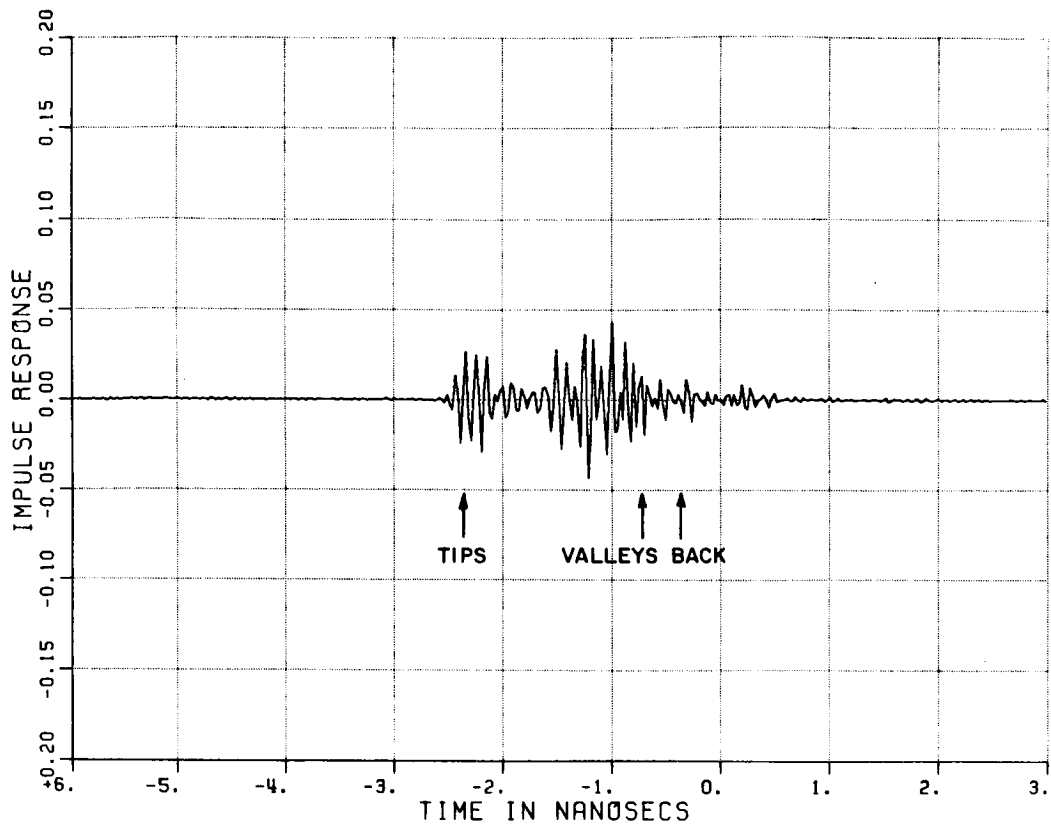Figure 5.17. Band limited time domain response of 1 sample of Company B's 12" pyramid absorber with nose-on incidence.

Figure 5.18. Measured nose-on RCS of 1 sample of Company B's 12"
pyramid absorber with nose-on incidence.

C-3

Figure 5.19. Band limited time domain response of 1 sample of Company
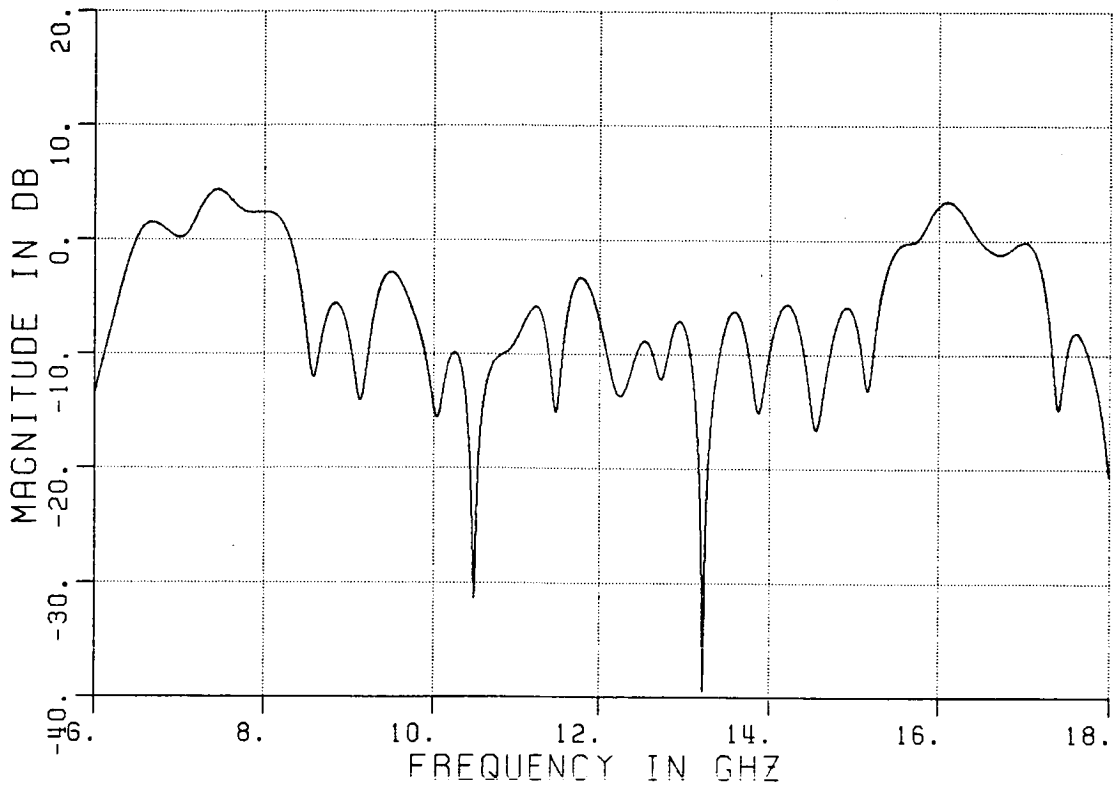B's 12" pyramid absorber with nose-on incidence.

182

Figure 5.20.   Measured nose-on RCS of 1 sample of Company B's 12"
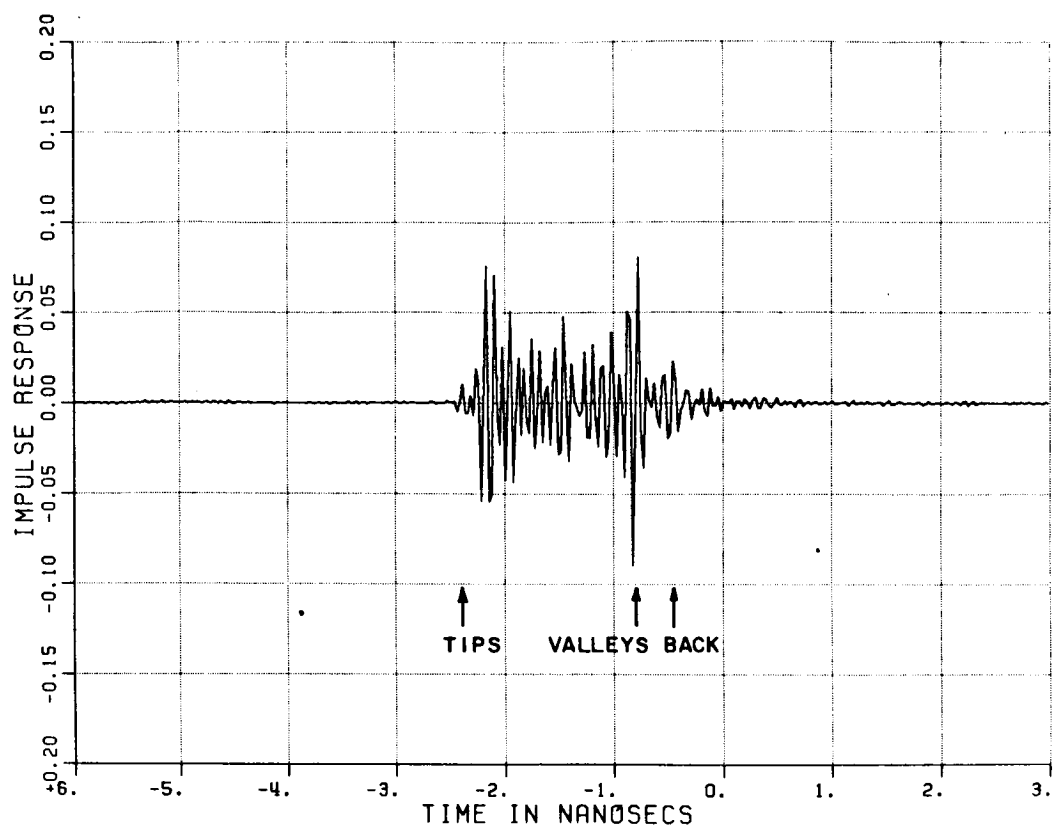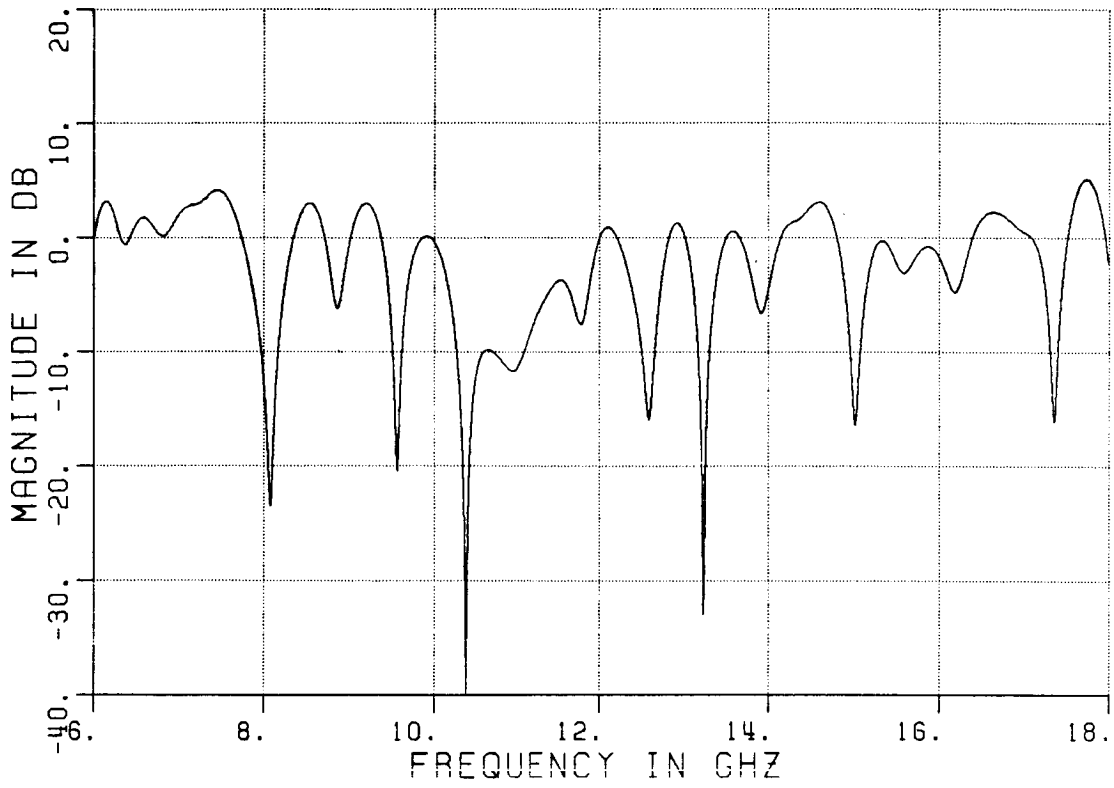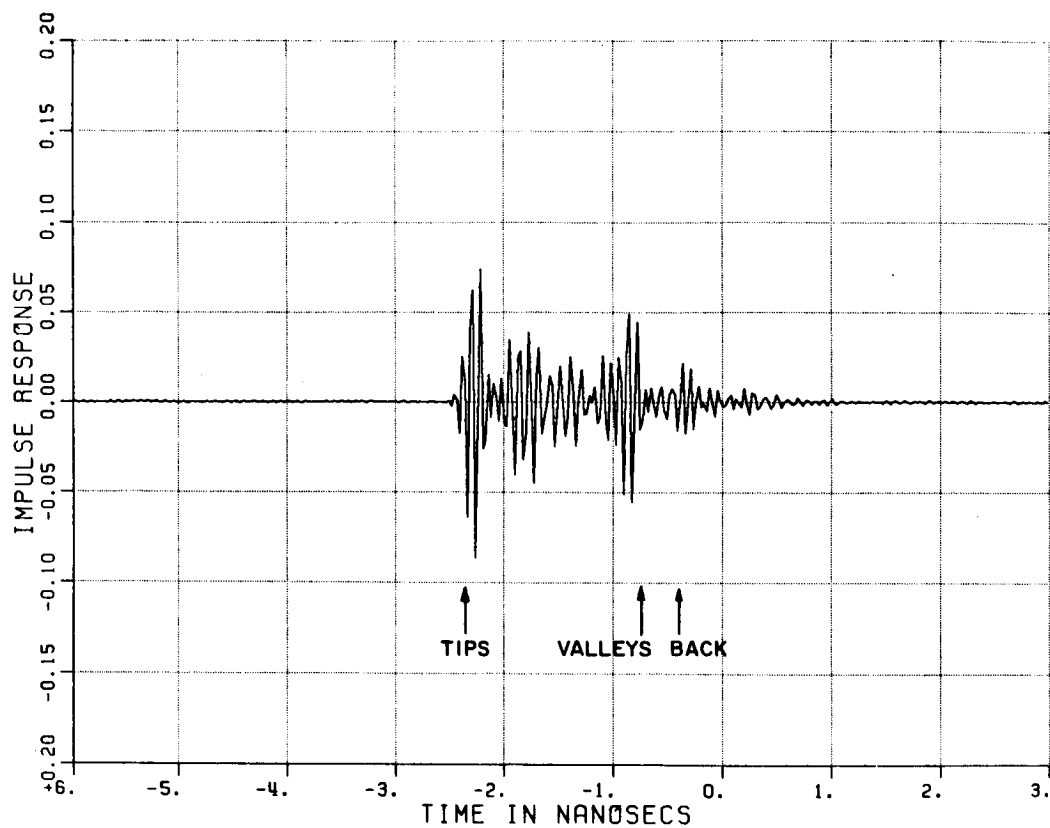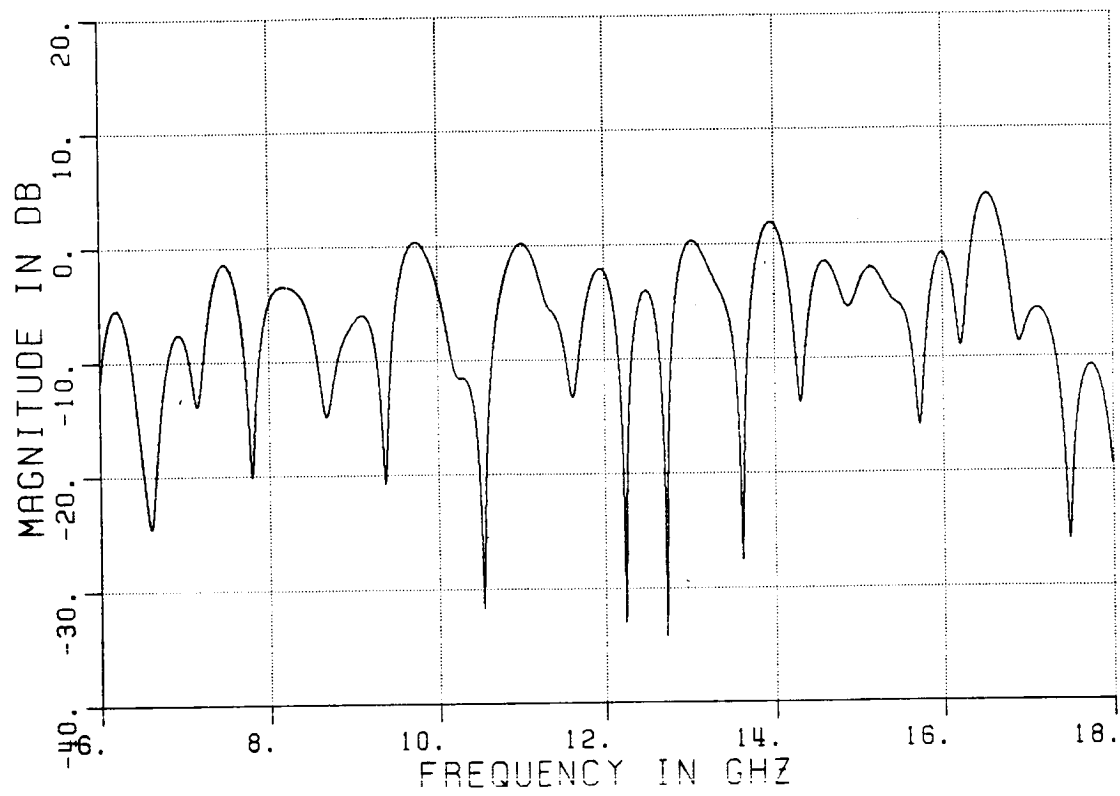pyramid absorber with nose-on incidence.

CHAPTER VI

NEW ABSORBER DESIGN

A. INTRODUCTION

There are two basic electric properties desired of free space absorbers. First, to have a reflection coefficient of zero over a wide range of frequencies, and second, to be lossy so the energy entering the absorber is dissipated. The design of absorber involves how to best satisfy these properties at the same time. Assuming a wide band reflection coefficient of zero is unobtainable, the question of how to minimize the reflection coefficient is considered.

In this chapter both low and high frequency methods of analysis are considered to try to improve the design of the pyramid absorber now commonly used. The scattering from these alternate designs are shown in Section D.

B. IMPEDANCE MATCHING APPROACH

From a low frequency perspective, a transmission line analogy is used to model the system. Consider the graph of impedance versus distance as shown in Figure 6.1 where region 1 represents free space with impedance (Z_0) and region 3 represents the absorber material with impedance (Z_1). Region 2 represents the transition region where the
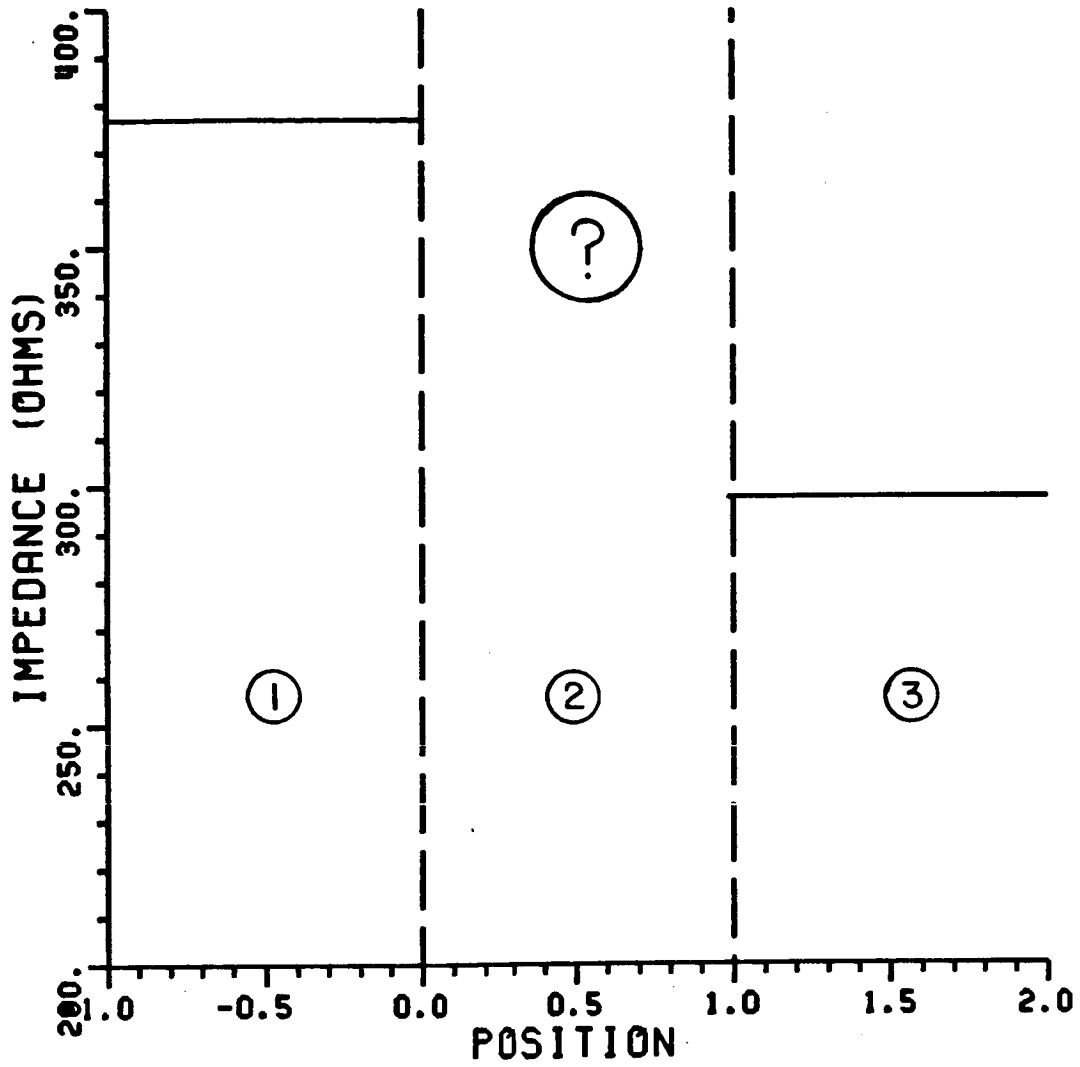
Figure 6.1. Transmission line anology to make transition from region 1 to 3.

impedance is chosen to minimize the reflection coefficient if a signal is incident from region 1. Now what impedance should be chosen in the transition region to minimize reflections between regions 1, 2, and 3?

A first guess is a linear taper between Z_0 and Z_1. A mathematical solution for the resulting non linear differential equations in region 2 can be found in terms of Airy functions. The linear taper solution has a discontinuity in slope at both the leading and trailing edges that result in strong reflections. This is verified by considering that a wedge absorber represents an almost linear taper between free space and the impedance of the dielectric.

The actual impedance in the transition region is found by assuming the net admittance associated with a particular location is weighted according to the area of the absorber material compared to the area of free space as given by Knott [21]. The equation for this is

$$Y = \frac{Y_0 \cdot (A_0 - A) + G \cdot A}{A_0} \qquad (6.1)$$

where Y is the net admittance, Y_0 is the admittance of free space, G is the conductance of a thin slice of the absorber, A_0 is the base area, and A is the absorber area as shown in Figure 6.2. Equation (6.1) makes the assumption that the fields are uniform at each horizontal cut. This, of ourse, is not entirely true but can be considered a rough approximation.

Letting h be the height of the pyramid and z be the position of the slice inward from the tip as shown in Figure 6.2, one obtains that

$$Y = \left(1 - \frac{z}{h}\right)^2 \cdot Y_0 + \left(\frac{z}{h}\right)^2 \cdot G \qquad (6.2)$$
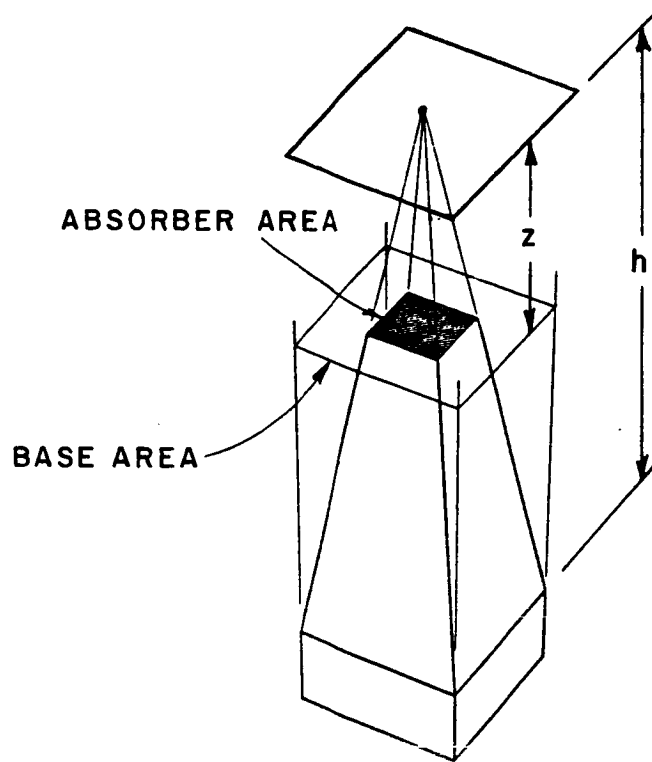
186

Figure 6.2. Geometry for calculating the impedance taper along a dielectric pyramid.

for a pyramid shaped absorber and

$$Y = \left(1-\frac{z}{h}\right) \cdot Y_0 + \left(\frac{z}{h}\right) \cdot G \qquad\qquad (6.3)$$

for the wedge.

Knott [21] says, "Presumably, the conductivity of the carbon-loaded absorber is high enough that G is sensibly the value of the metal backing plate." From the skin depth of the material and the measurments reported in the previous chapters the incident energy is mostly lost due to heat before reaching the back of the absorber so whatever object is placed behind the absorber should have no effect on the scattering. Because of this the conductance should be just the conductance of the absorber material which is given by

$$G = \sqrt{\epsilon_r} \cdot Y_0 \qquad . \qquad\qquad (6.4)$$

Letting the absorber material have a value of $\epsilon_r = 1.6$ and a height of 1 unit, the impedance taper for the wedge is calculated as shown in Figure 6.3. Considering the measured results from a wedge compared to a pyramid one concludes that the linear taper is not optimum without working out the mathematics. The strongest contribution comes from the tip region because of the discontinuity in slope. The second strongest return comes from the valleys because of the second slope discontinuity. The valley contribution is not as strong as the tips because of the attenuation occuring in the signal. So the leading transition region appears to be the more important.
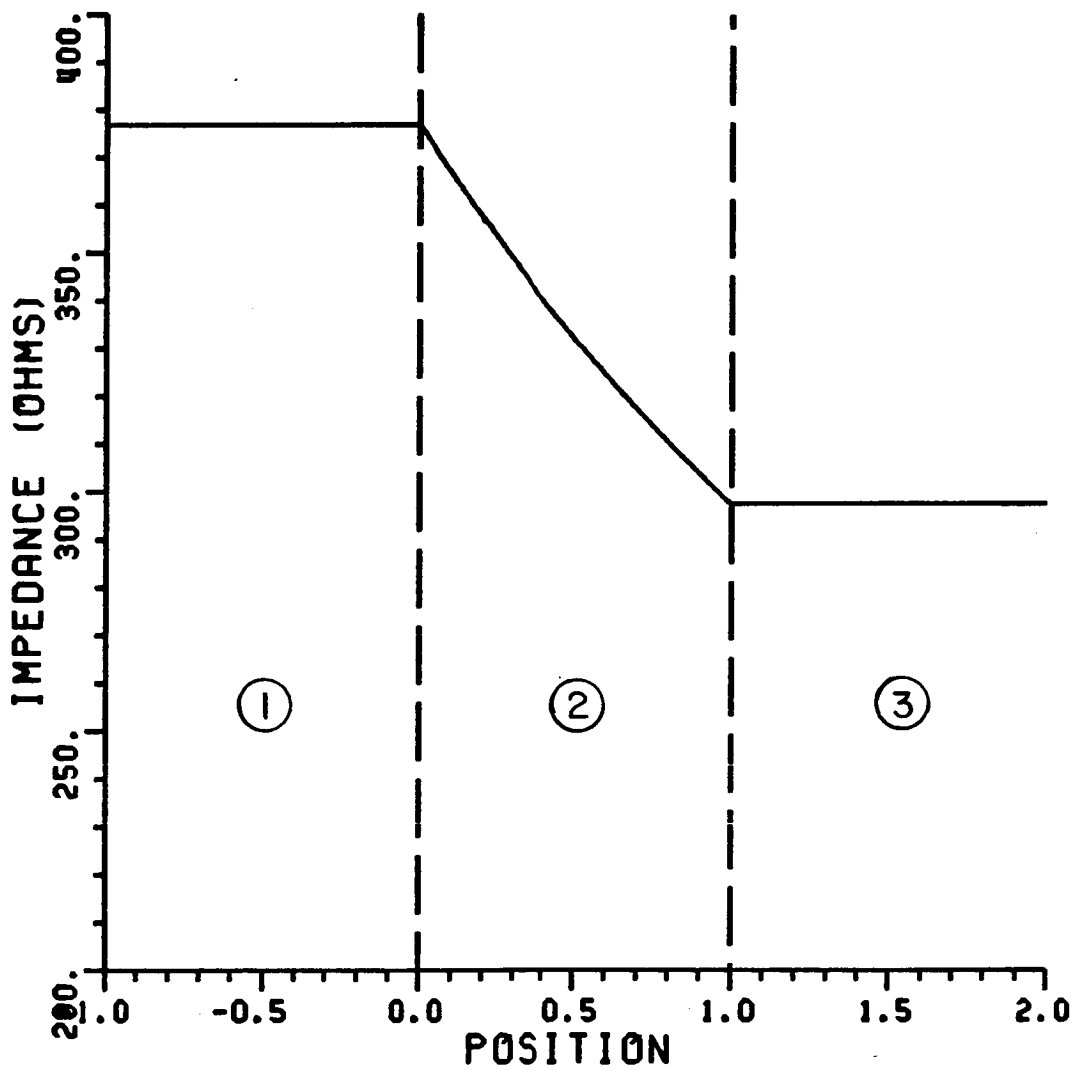
188

Figure 6.3. Impedance taper for dielectric wedge with ε_r=1.6.

Again taking h=1 and ε_r=1.6, the impedance taper for the pyramid is calculated as shown in Figure 6.4. The pyramidal absorber represents a linear taper in two directions so it is represented as a parabolic type curve connecting regions 1 and 3. Now the junction between regions 1 and 2 is much smoother than the wedge case but the junction between regions 2 and 3 shows no improvement. The junction between regions 2 and 3 is not as critical as 1 and 2 because some of the signal will be attenuated by the time the second junction is reached. Nevertheless, smoother junctions should improve the absorbers performance such as shown in Figure 6.5. Using this impedance taper a corresponding pyramid shape is calculated and appears in Figure 6.6. The performance of some alternate shapes are tested and compared against standard pyramid measurements in Section D.

C. HIGH FREQUENCY CONSIDERATIONS

The dominant mechanisms in the high frequency analysis of the scattering from the pyramid absorbers are identified in Chapter III as the tip and base diffraction, plus multiple reflected terms. The reduction of each of these will be considered separately.

The tip contribution theoretically can be reduced by making the tip more pointed and by reducing the dielectric constant of the material close to the tip. These changes show only a slight reduction in the tip contribution.

The base diffraction can theoretically be reduced greatly by reducing the interior wedge angle at the base of the pyramids or the
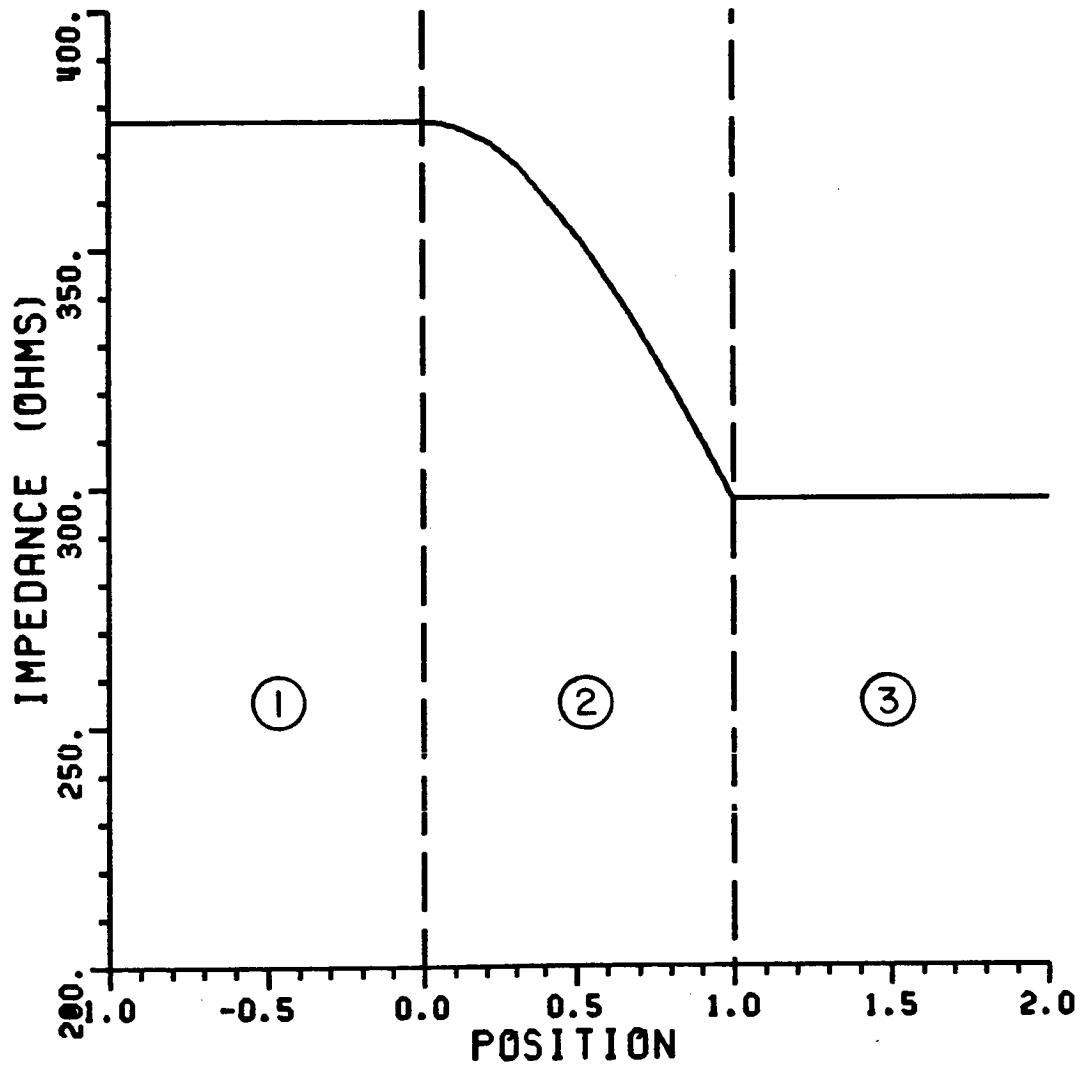
190

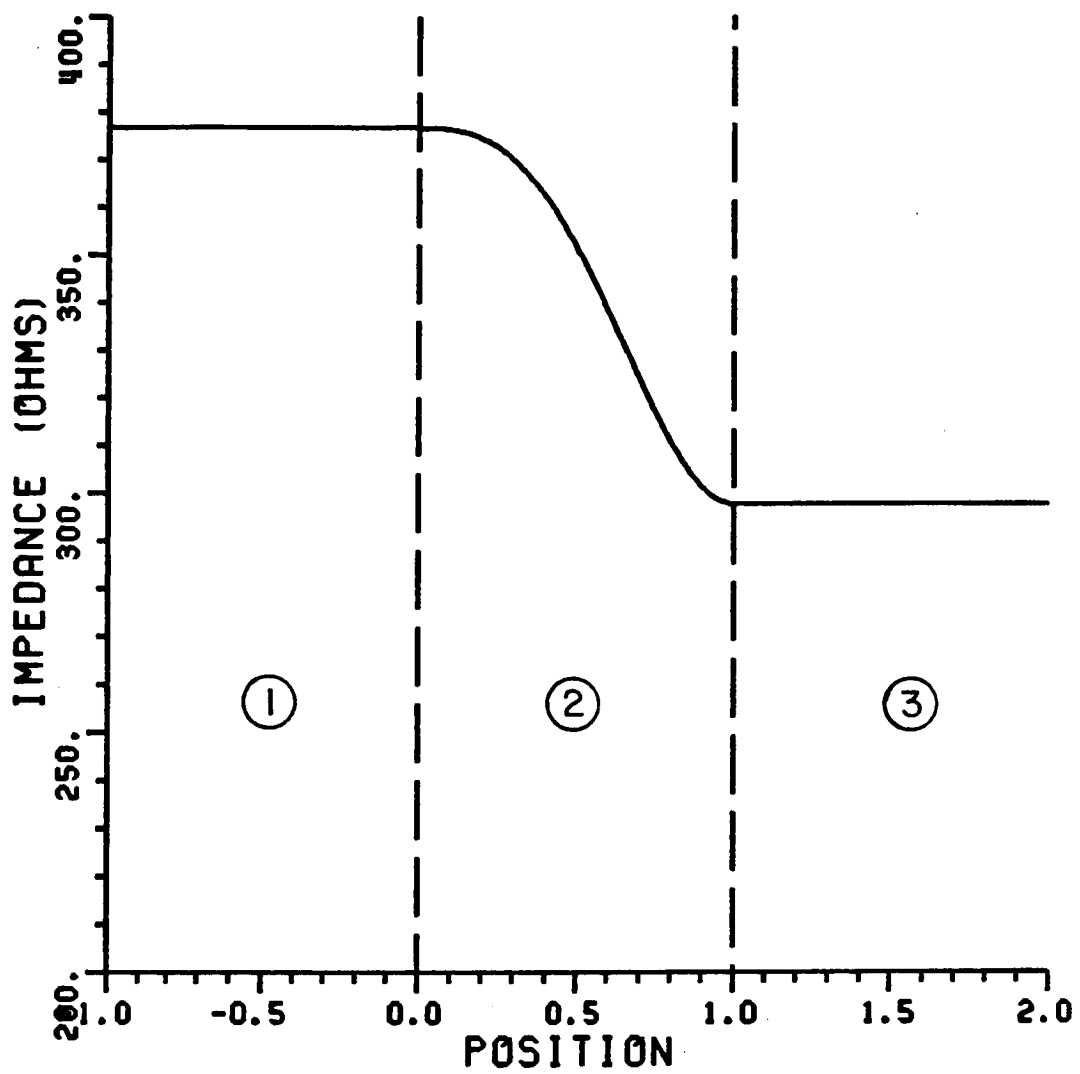Figure 6.4. Impedance taper for dielectric pyramid with $\varepsilon_r=1.6$.

191

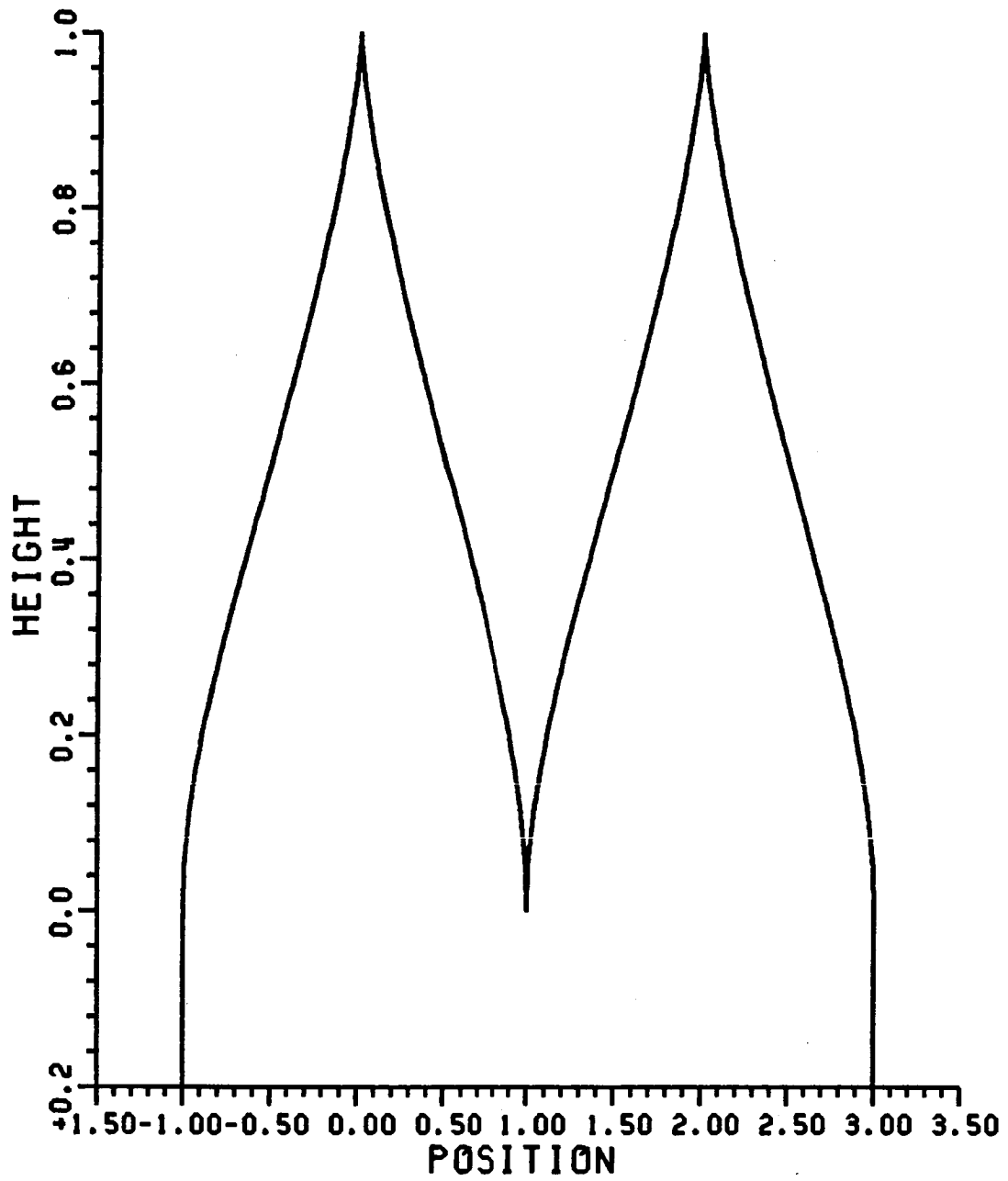Figure 6.5. Impedance taper to smooth junctions between regions.

Figure 6.6. Curved pyramid corresonding to impedance taper shown in Figure 6.5.

dielectric constant of the material. The base diffraction term has a multiple reflection coefficient which is highly dependent on both the material properties and interior wedge angle.

The reflected contribution is reduced by making the pyramids more pointed, reducing the dielectric constant, and replacing the straight edges of the pyramid with a slight curve to break up the reflected field.

From these considerations the sides of the pyramid are curved slightly as shown in Figures 6.7 and 6.8. A new high frequency term results from the changing curvature on the sides of the absorber but this term is very difficult to analyze because of the continuously changing curvature. Diffractions from a change in curvature are typically an order of magnitude smaller than a straight wedge structure so these terms should not dominate the scattered response.

It is very interesting that both the high frequency and low frequency methods arrive at similar conclusions in terms of the shape modifications.

D. MEASUREMENT OF NEW ABSORBER

Prototypes of curved pyramid absorber were made by Company D from the drawings shown in Figures 6.7 and 6.8. Company B made prototypes from Figure 6.6. The time and frequency domain data from two different samples of each prototype along with time and frequency domain data of standard pyramids from the same company are shown in Figure 6.9 through 6.28. The time domain plots were generated from frequency domain data

measured from 2 to 18 GHz in 10 MHz increments on a compact range. The frequency domain plots were generated by software gating the time domain response to eliminate the back edge contribution, then doing an inverse Fourier transform. In other words, the frequency domain plots represent the spectral content of the time domain signal between -3.0 nsec. and -0.5 nsec. only.

Consider first the time domain plots of scattering from Company D's standard pyramids. The scattering is, unfortunately, not solely from the tips, valleys, and back as in the data from Company C's 12" absorber displayed in Figure 5.2. This is probably due to some inhomogenities in Company D's material. This makes it harder to determine the exact effect of changing the shaping. Sample 1 has a very strong tip return compared to sample 2 while sample 2 has a stornger base return. (Note: Figure 5.2 was generated from frequency data between 6 and 18 GHz instead of 2 to 18 GHZ. Time domain plots generated from the 2 to 18 GHz data tend to have the tip, valleys, and back less clearly defined. However, using just the 6 to 18 GHz data Company D's absorber still displays stronger returns between the tips and bases.)

Company D's curved absorber has only slightly lower returns than their standard pyramids as can be seen in Figures 6.13 through 6.20. The absorber shape in Figure 6.7 had strong returns about 2" down the pyramid and at the valleys. The valley return may be partly due to the curved pyramids being separated from each other, leaving a very visible valley. This was not intended in the design but occurred during the manufacturing process. The bases in the absorber shaped like Figure 6.8 come out much closer together and show lower scattering levels. The

195

tips of this design are very pointed but get wider much faster but still show little improvement in tip scattering. This may be due to the previously mentioned material problem that may be overshadowing the tip returns.

The data for Company B's standard pyramids are shown in Figures 6.21 through 6.24 and the curved absorber in Figures 6.25 through 6.28. The curved absorber did not show an overall improvement over the straight pyramids. The tips of Company B's curved absorber were very pointed and the manufacturing process bent many of them. This may have adversely affected the tip returns. Both pieces of curved absorber show a large return about 2" in front of the valleys. There was a change in curvature close to this location that may have caused this return.

The backscatter for both Company D's curved absorber designs were measured at angles away from normal incidence and the results were very similar to that of the same size pyramids. There was some improvement in the curved absorbers near grazing incidence. This reduction may be from being normal to a curved face rather than a flat one, giving lower backscatter.

These measurements have shown that minor shaping changes can have an effect on the scattering signature of the absorber. However, the overall scattering level did not drop significantly in any of the curved pyramid designs. Each of the curved designs had flaws that could have been eliminated with closer controls in the manufacturing process, thus improving the results. The returns from inhomogenities in the material make it hard to determine the exact effect of the curved shaping and also limit possible improvement in performance.
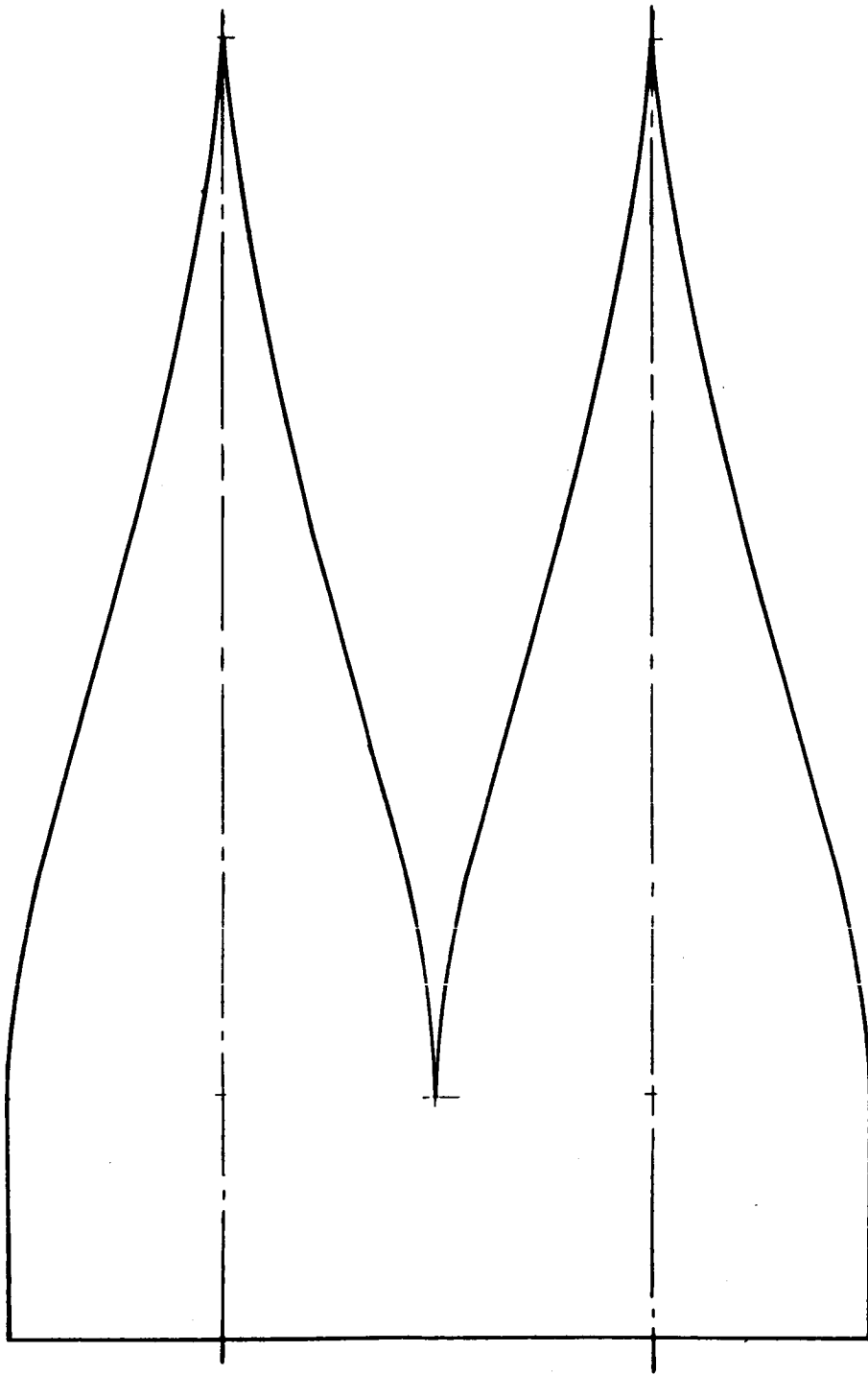
196

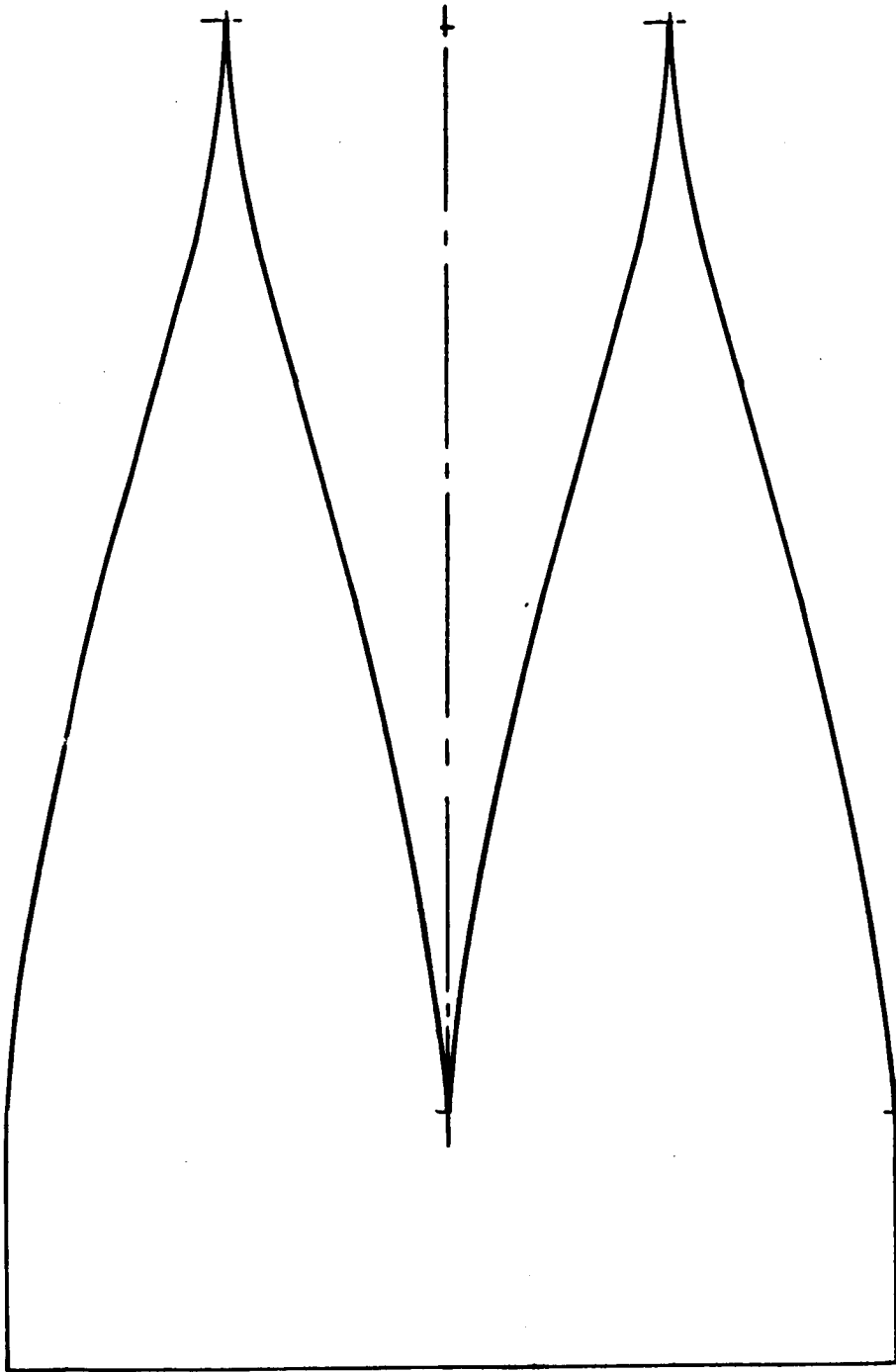Figure 6.7. Curved pyramid to minimize tip contribution.

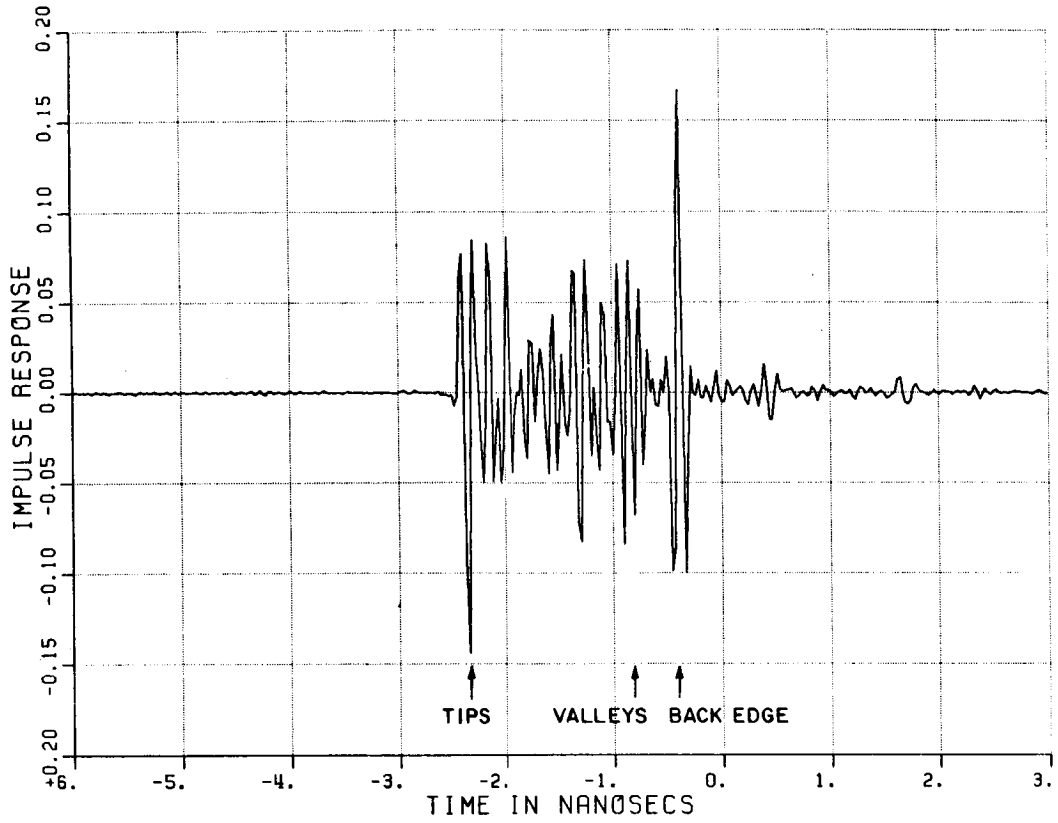Figure 6.8. Curved pyramid to minimize base contribution.

Figure 6.9. Time domain response from Sample 1 of Company D's standard 12" pyramid absorber.
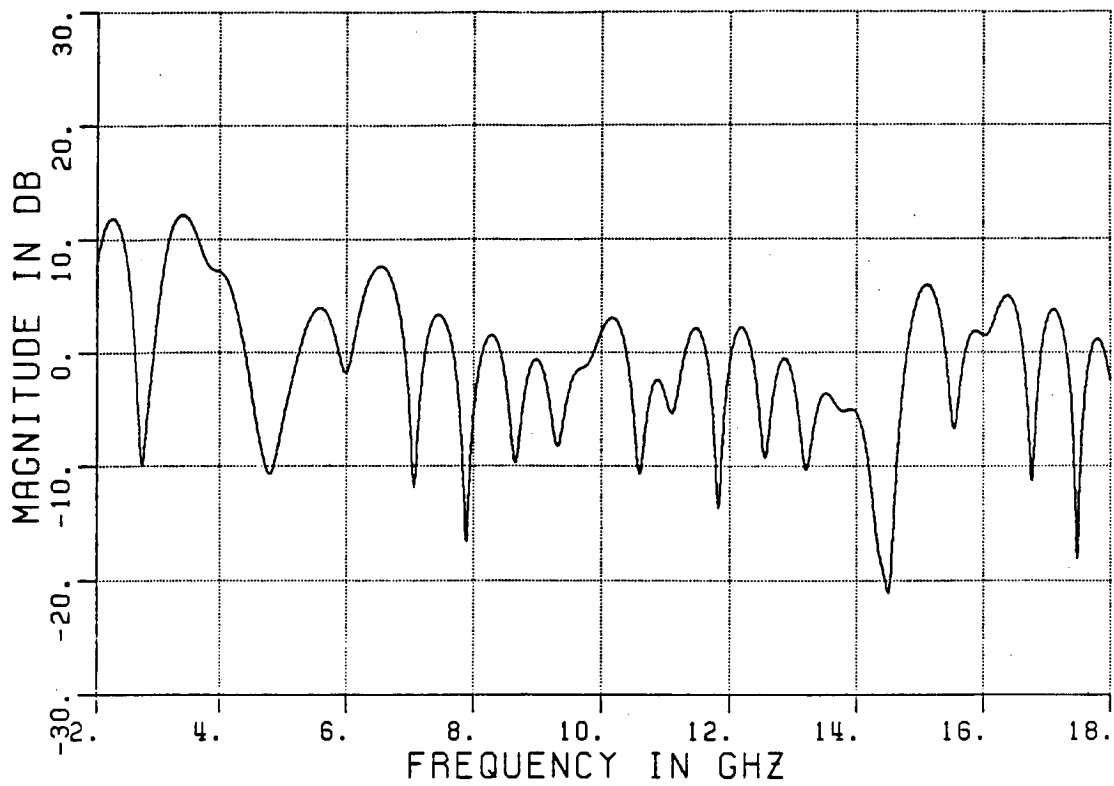
199

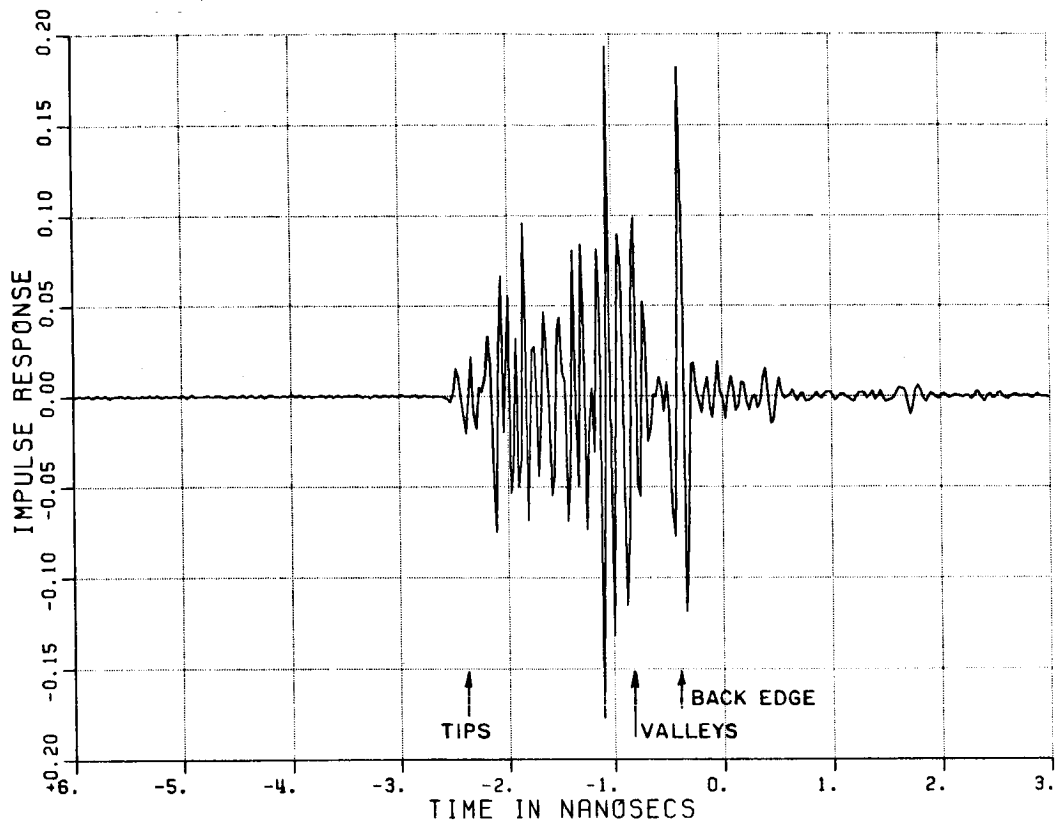Figure 6.10. Frequency domain data for Sample 1 of Company D's standard 12" pyramid absorber.

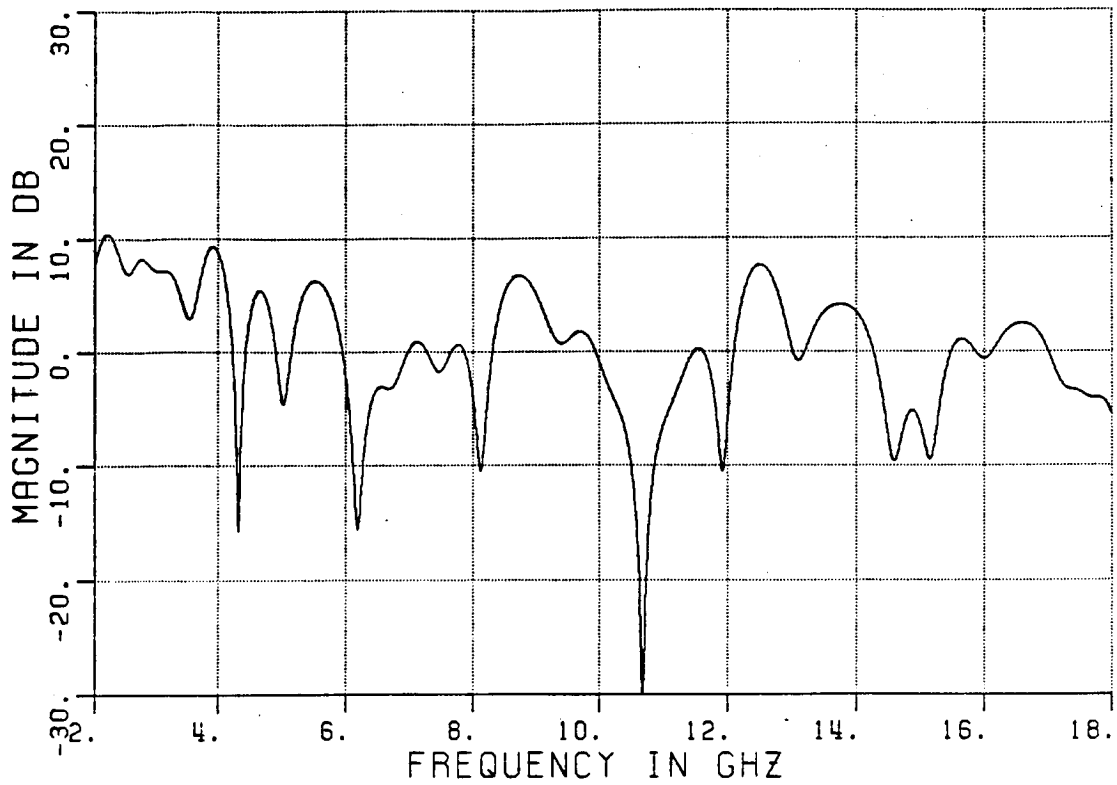Figure 6.11. Time domain response from Sample 2 of Company D's standard 12" pyramid absorber.

Figure 6.12. Frequency domain data for Sample 2 of Company D's standard 12" pyramid absorber.
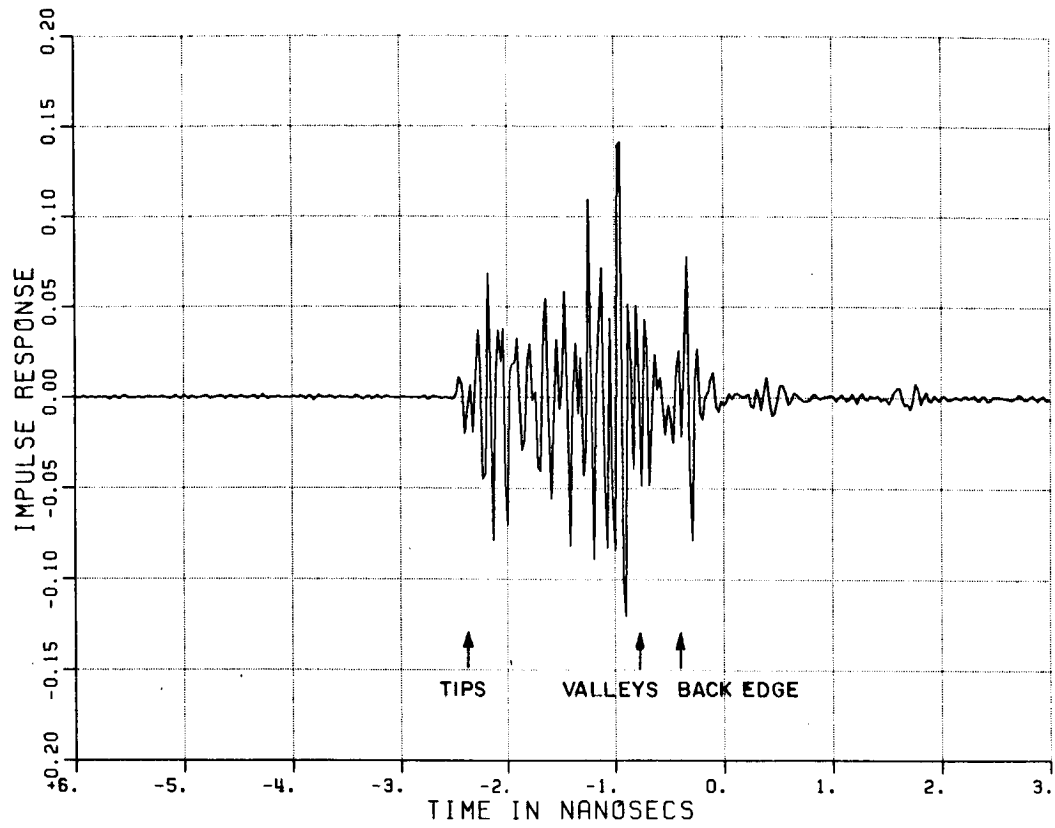
Figure 6.13. Time domain response from Sample 1 of absorber shaped like Figure 6.7 made by Company D.
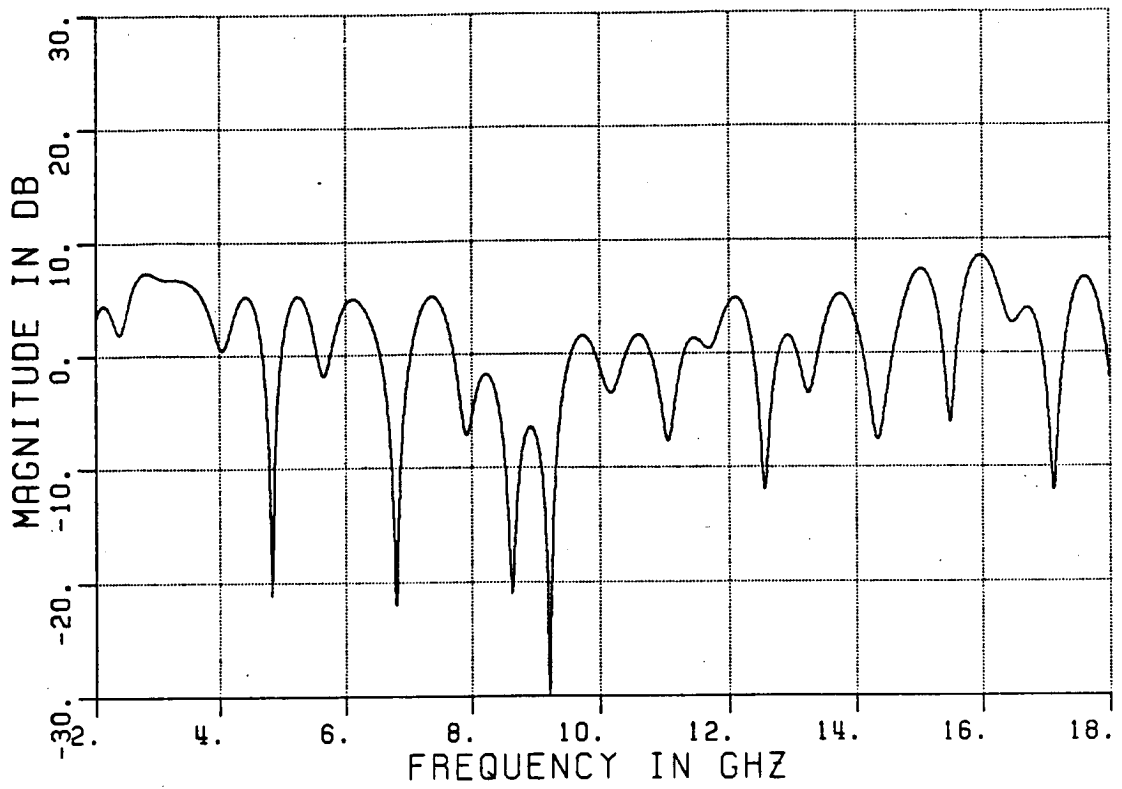
Figure 6.14. Frequency domain data for Sample 1 of absorber
shaped like Figure 6.7 made by Company D.

204

Figure 6.15. Time domain response from Sample 2 of absorber shaped like Figure 6.7 made by Company D.

Figure 6.16. Frequency domain data for Sample 2 of absorber
shaped like Figure 6.7 made by Company D.

206

Figure 6.17. Time domain response from Sample 1 of absorber shaped like Figure 6.8 made by Company D.

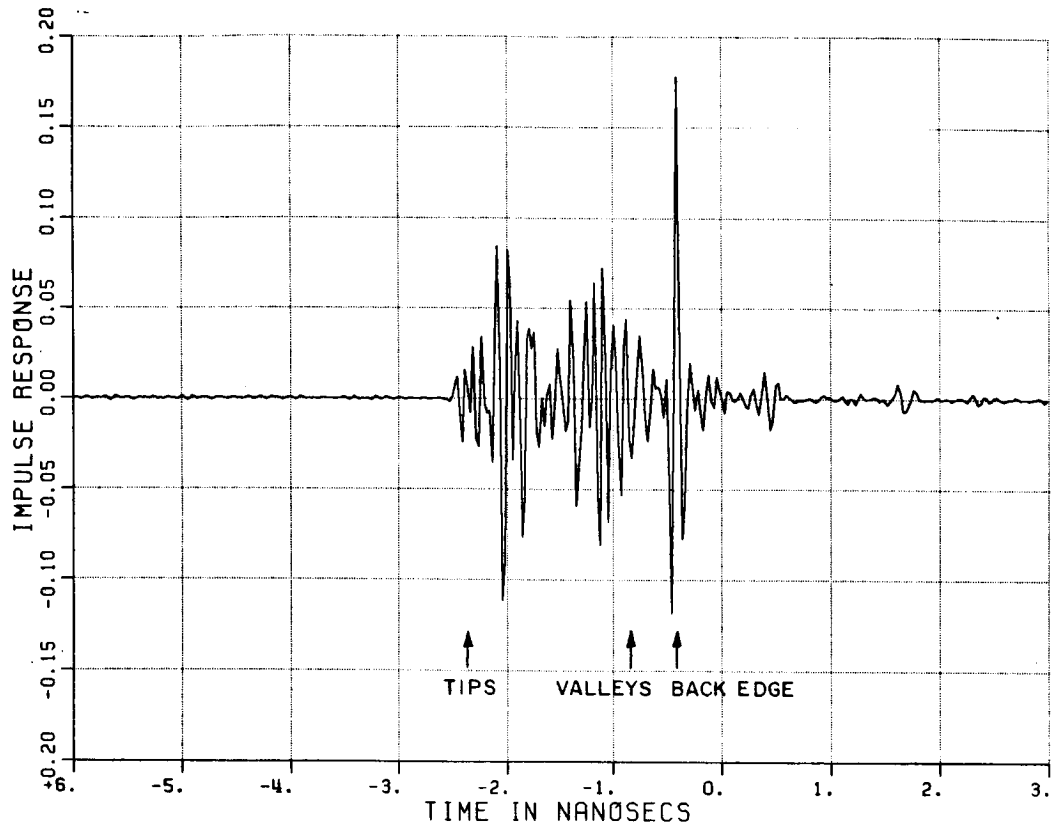Figure 6.18. Frequency domain data for Sample 1 of absorber shaped like Figure 6.8 made by Company D.

Figure 6.19. Time domain response from Sample 2 of absorber shaped like Figure 6.8 made by Company D.
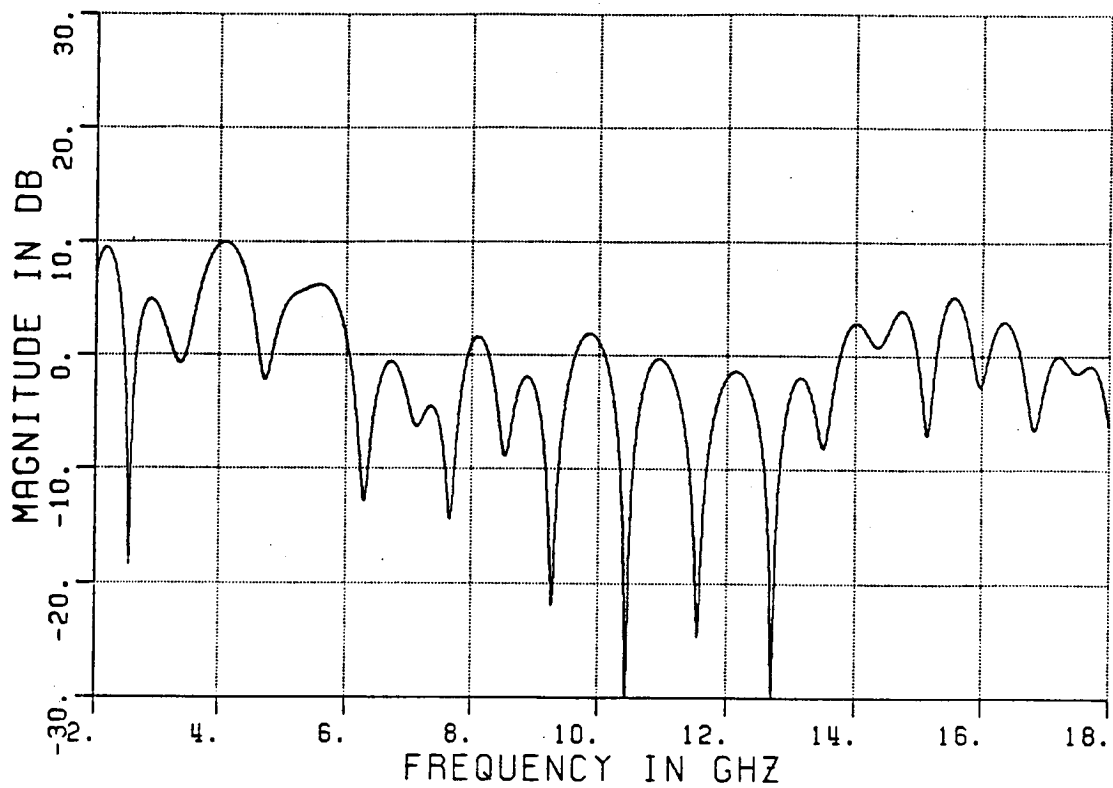
Figure 6.20. Frequency domain data for Sample 2 of absorber shaped like Figure 6.8 made by Company D.
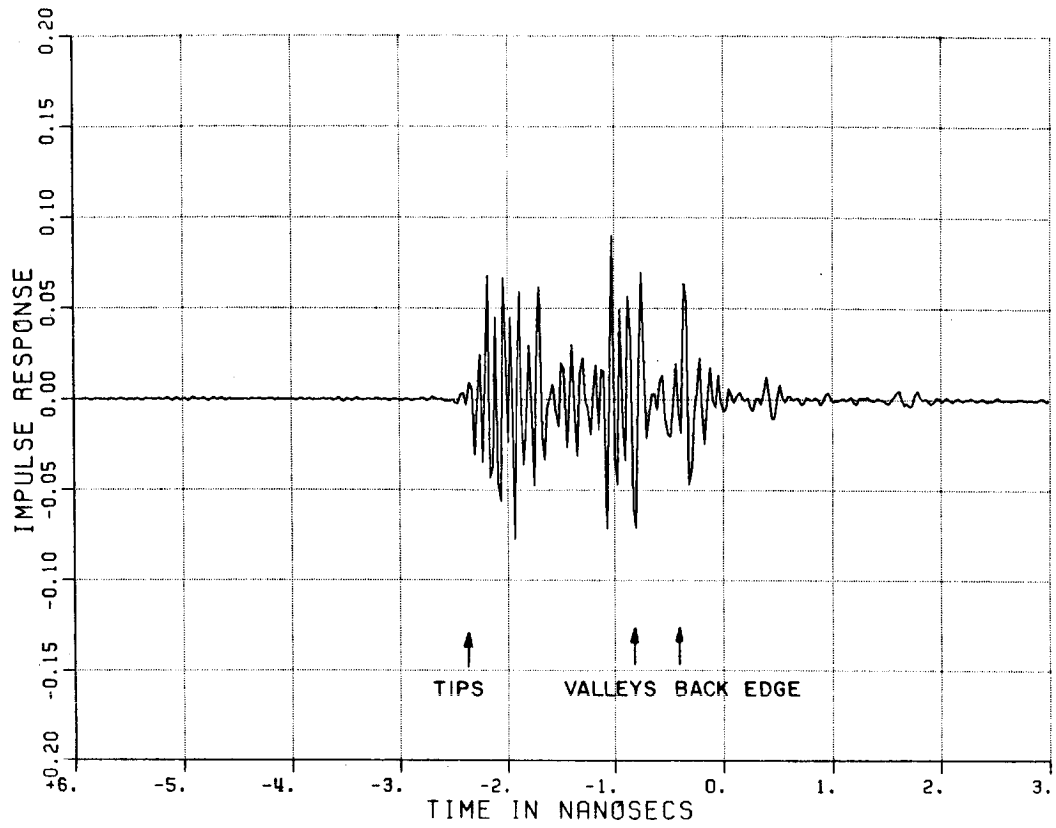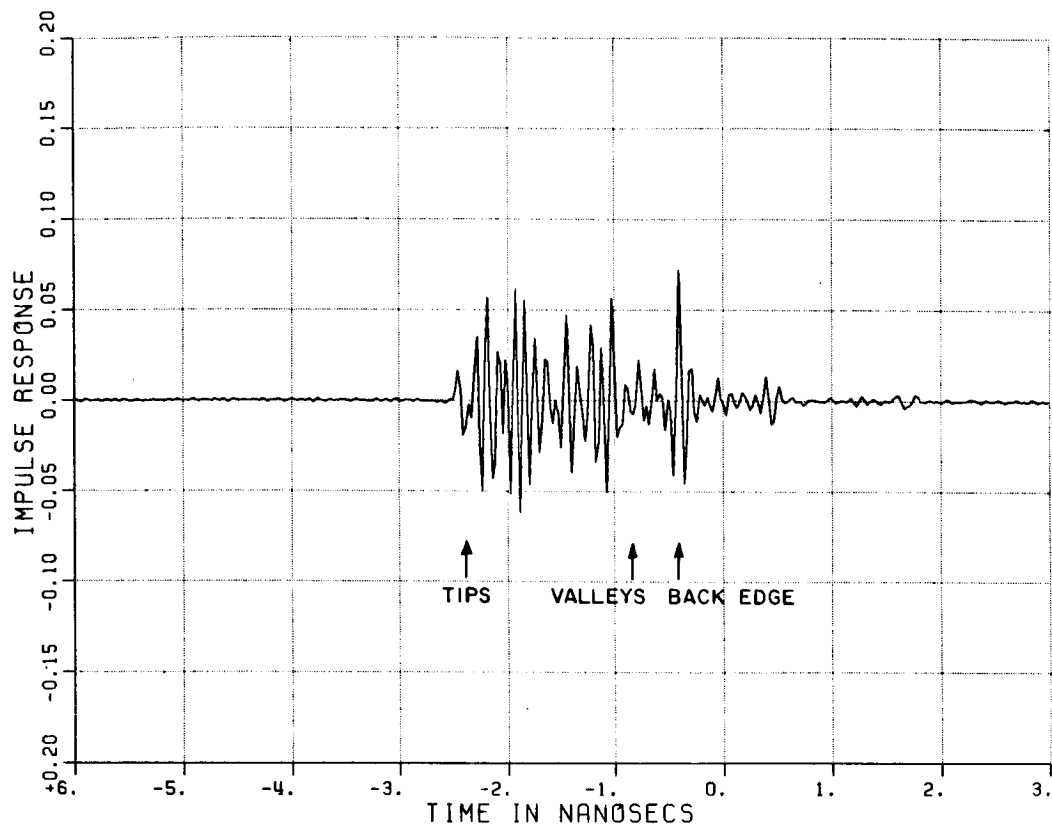
Figure 6.21. Time domain response from Sample 1 of Company B's standard 12" pyramid absorber.

211
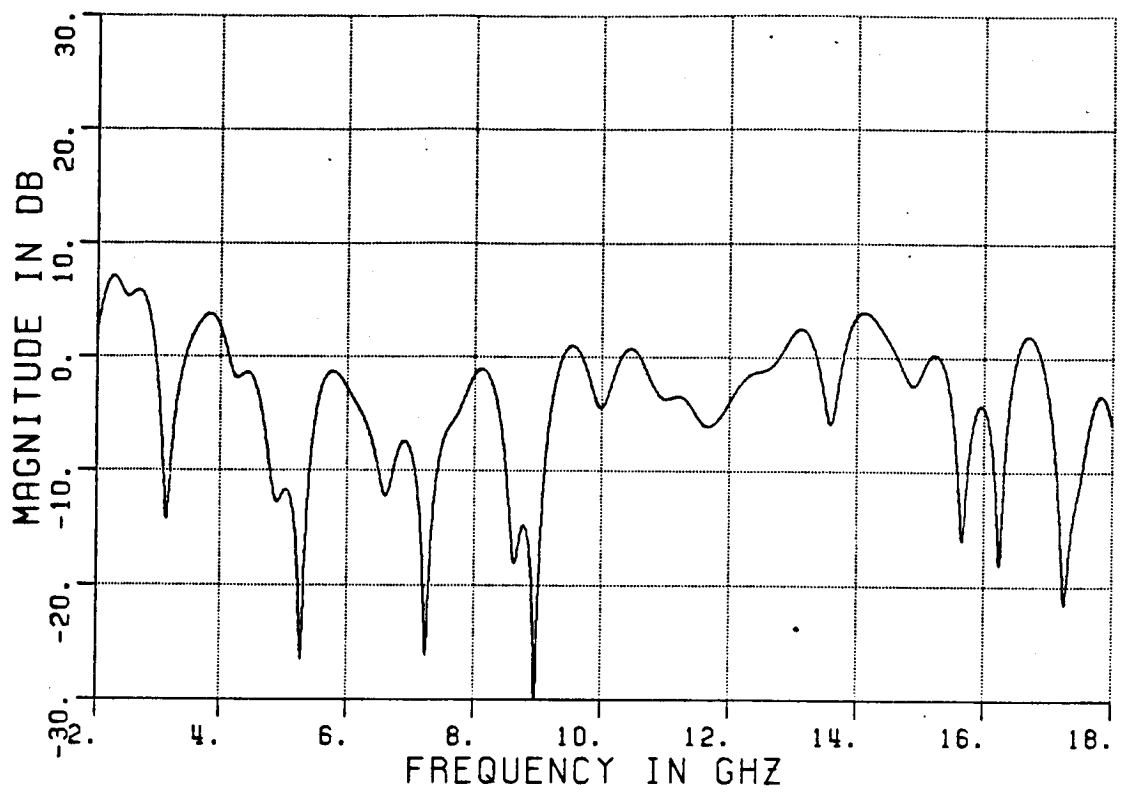
Figure 6.22. Frequency domain data for Sample 1 of Company B's standard 12" pyramid absorber.

212
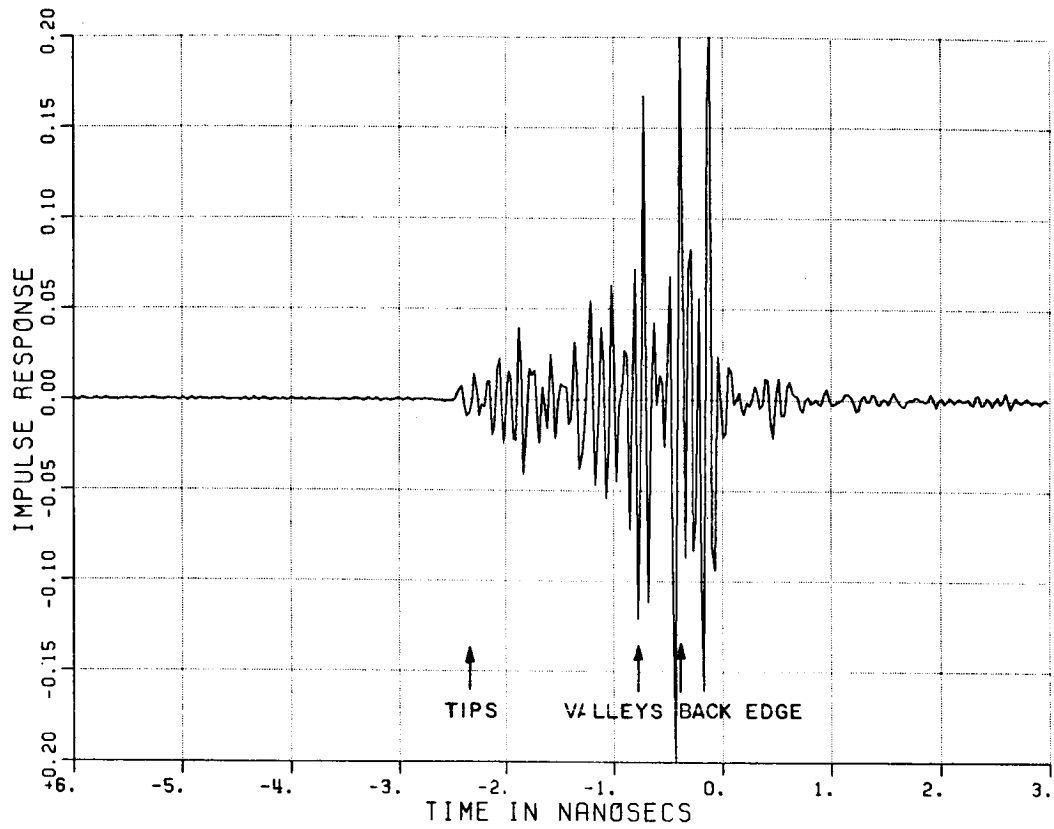
Figure 6.23. Time domain response from Sample 2 of Company B's standard 12" pyramid absorber.
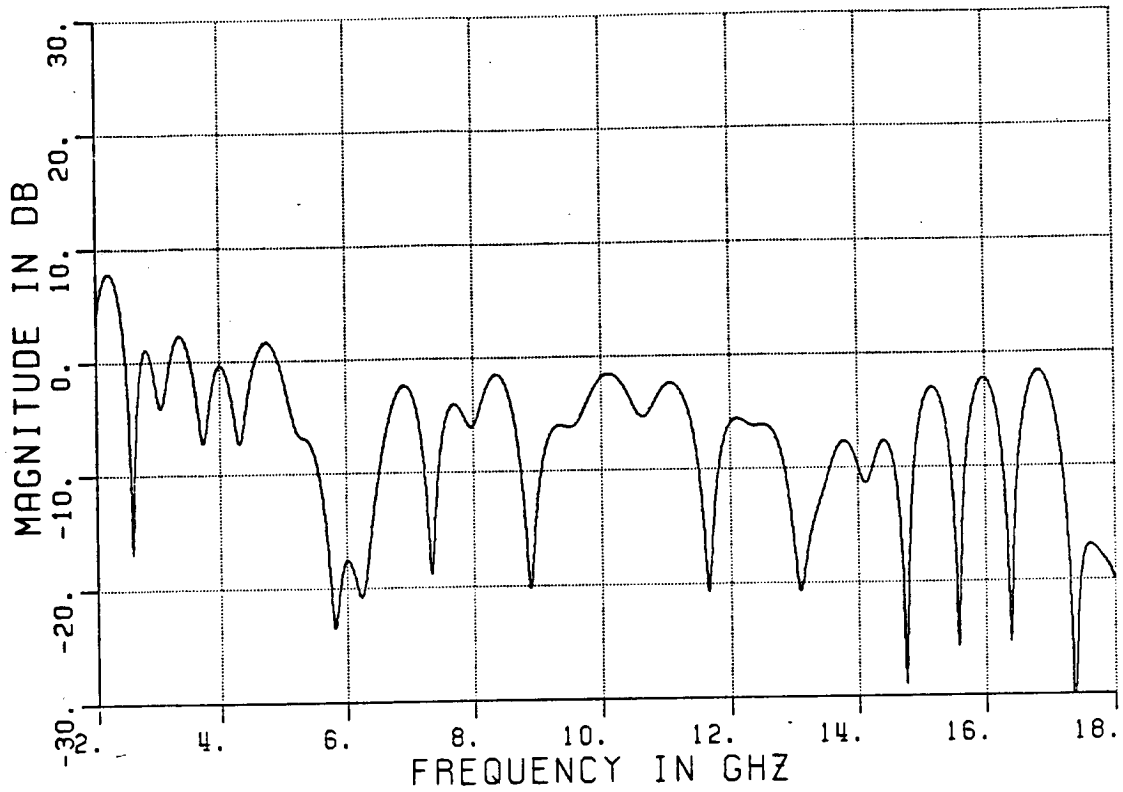
Figure 6.24. Frequency domain data for Sample 2 of Company B's standard 12" pyramid absorber.

214

Figure 6.25. Time domain response from Sample 1 of absorber shaped like Figure 6.6 made by Company B.

Figure 6.26.   Frequency domain data for Sample 1 of absorber
shaped like Figure 6.6 made by Company B.
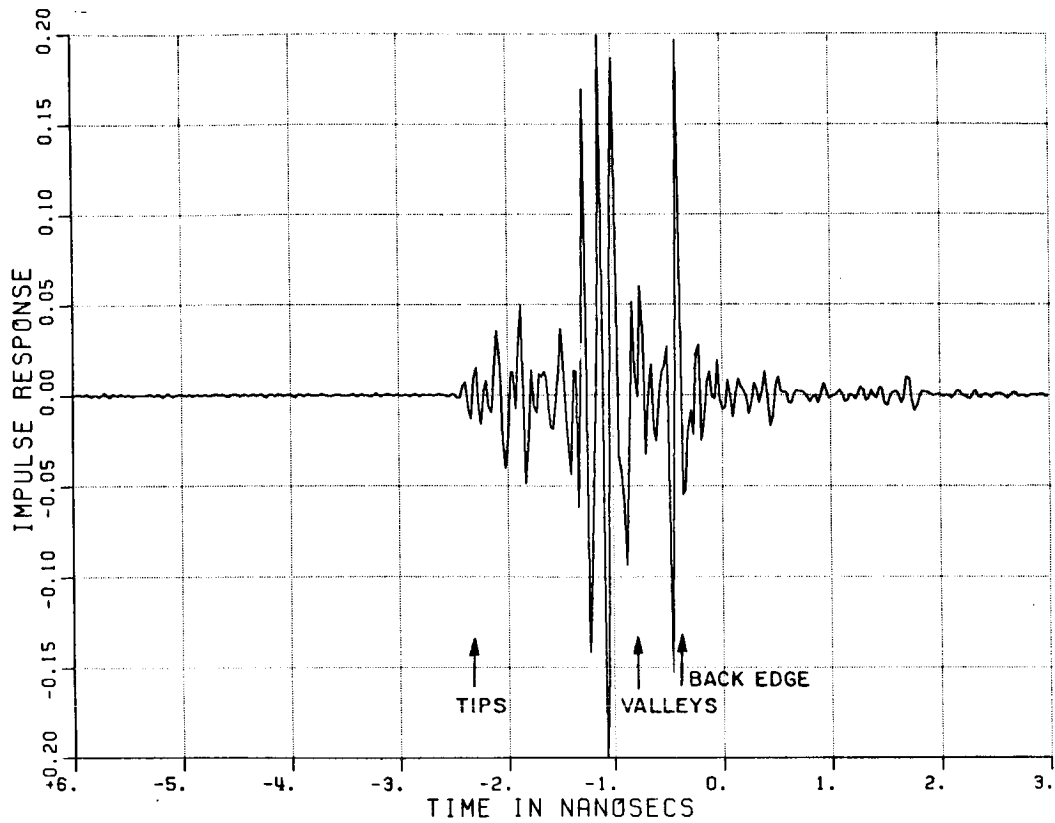
Figure 6.27. Time domain response from Sample 2 of absorber shaped like Figure 6.6 made by Company B.
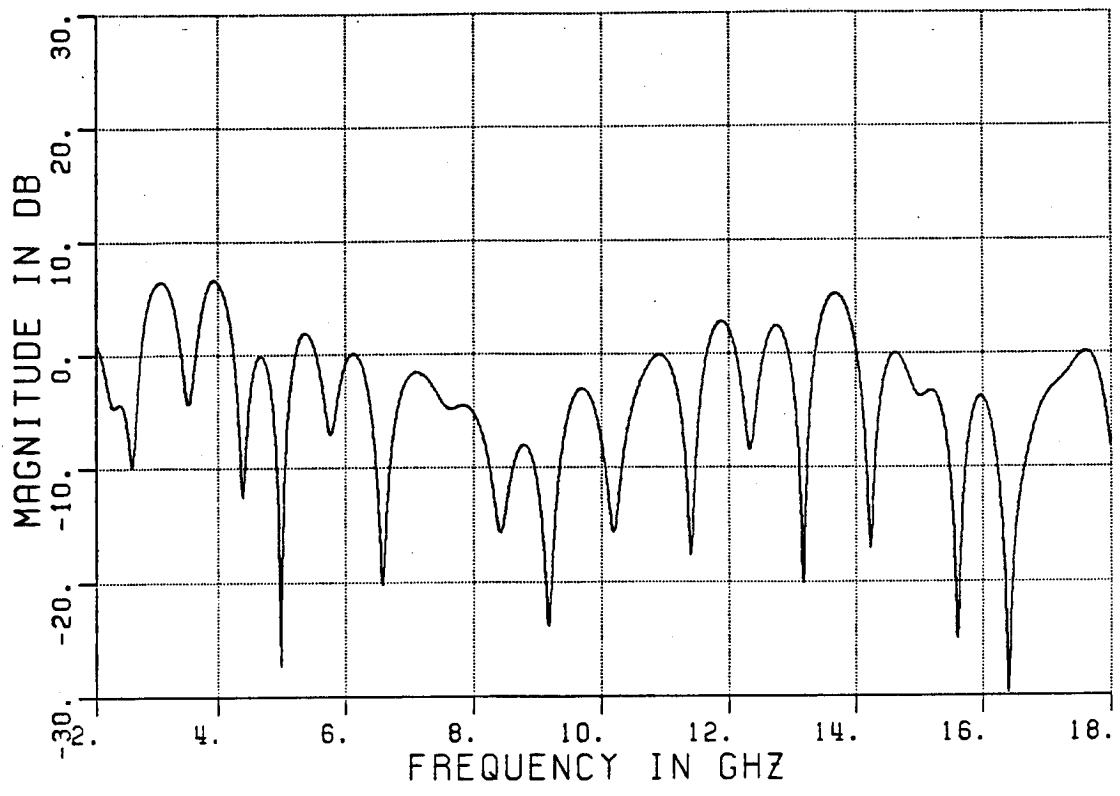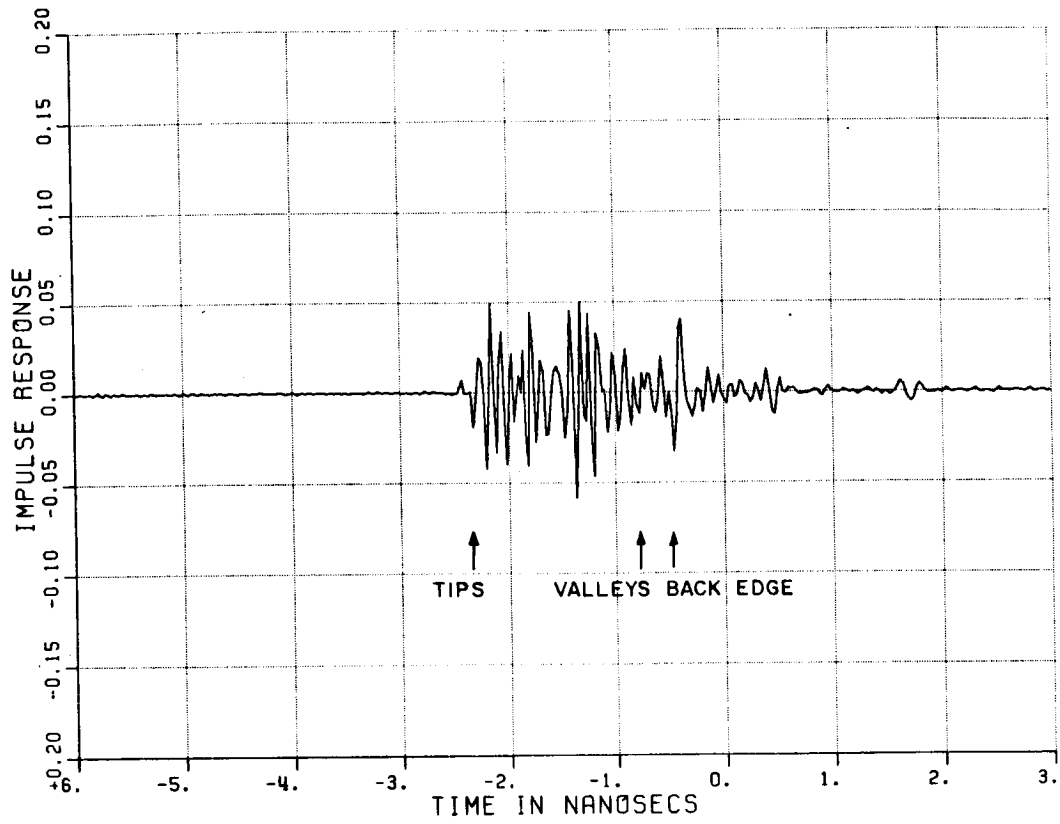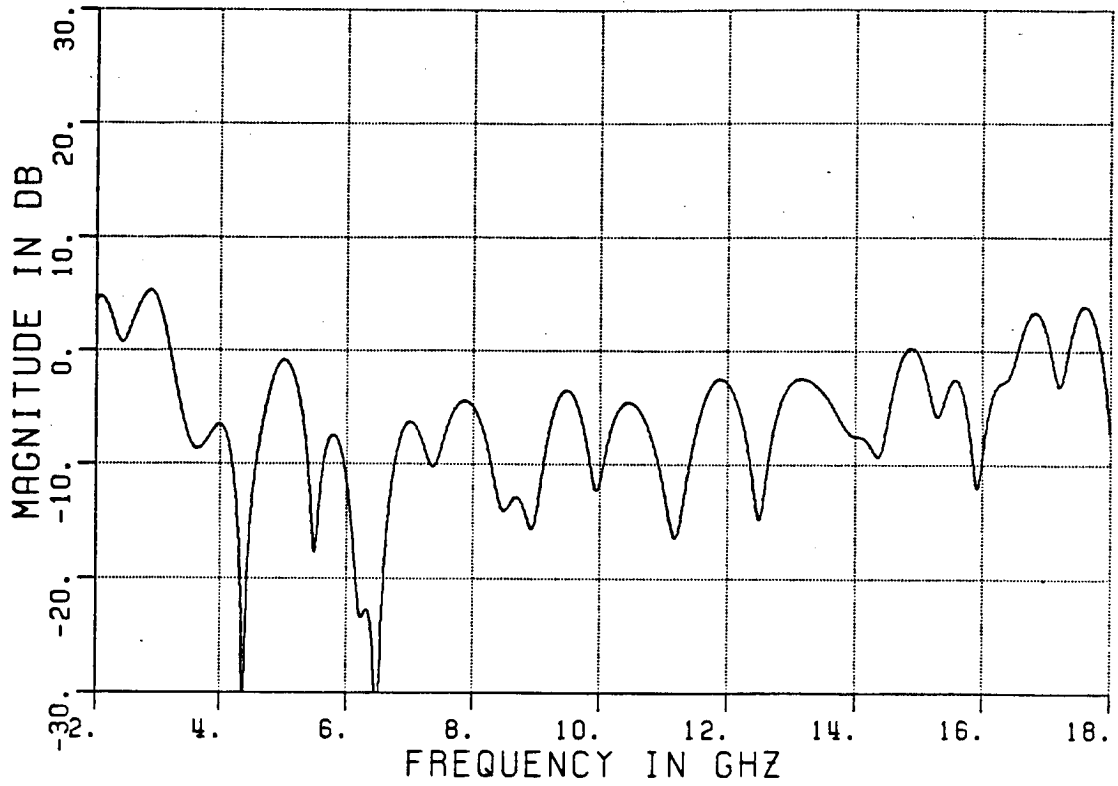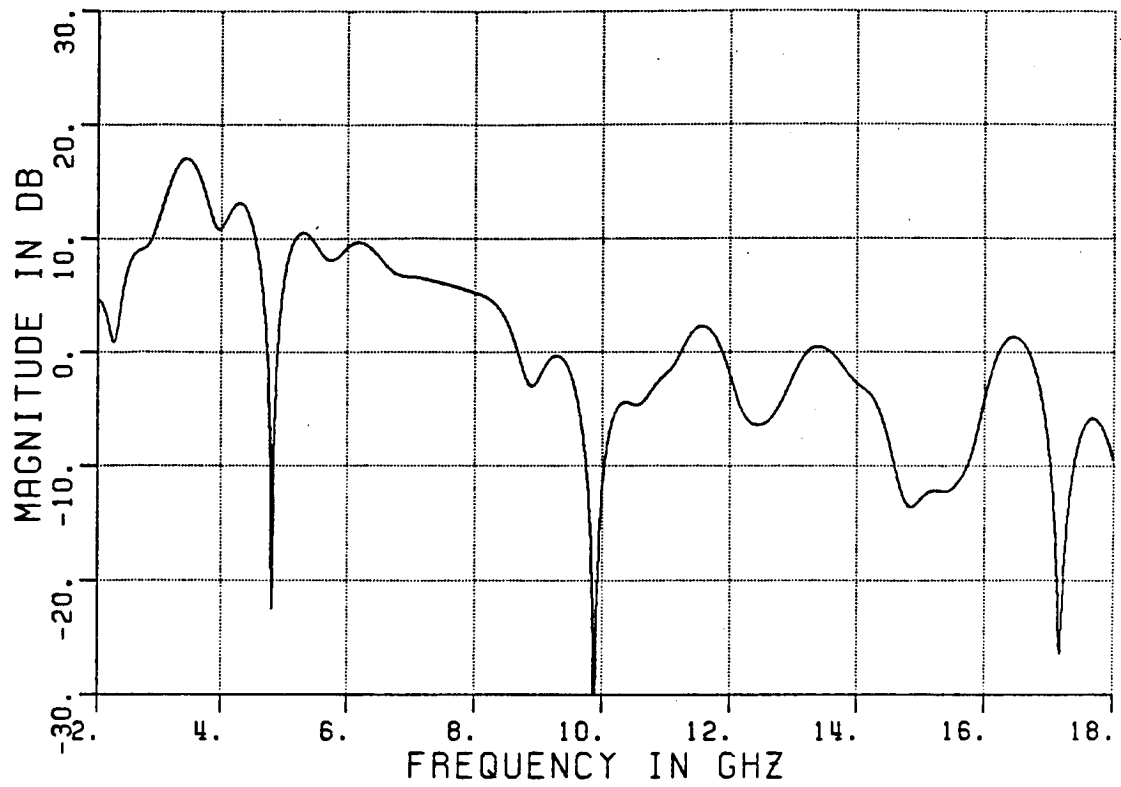
Figure 6.28. Frequency domain data for Sample 2 of absorber
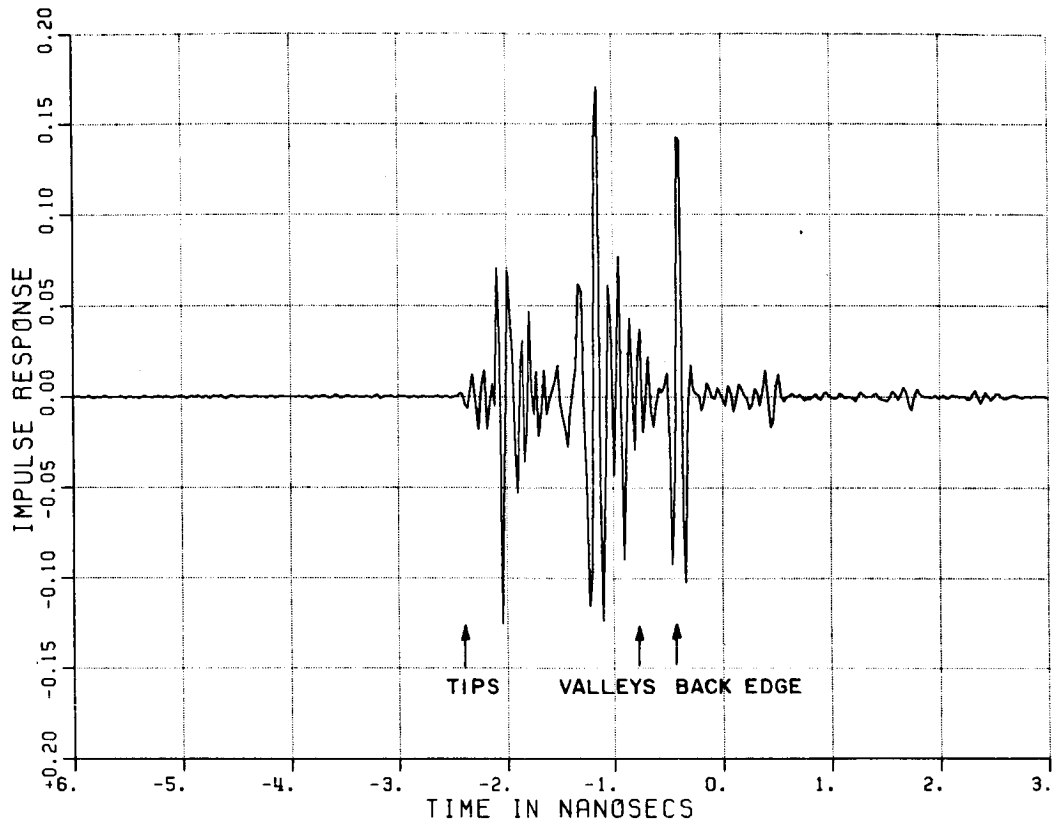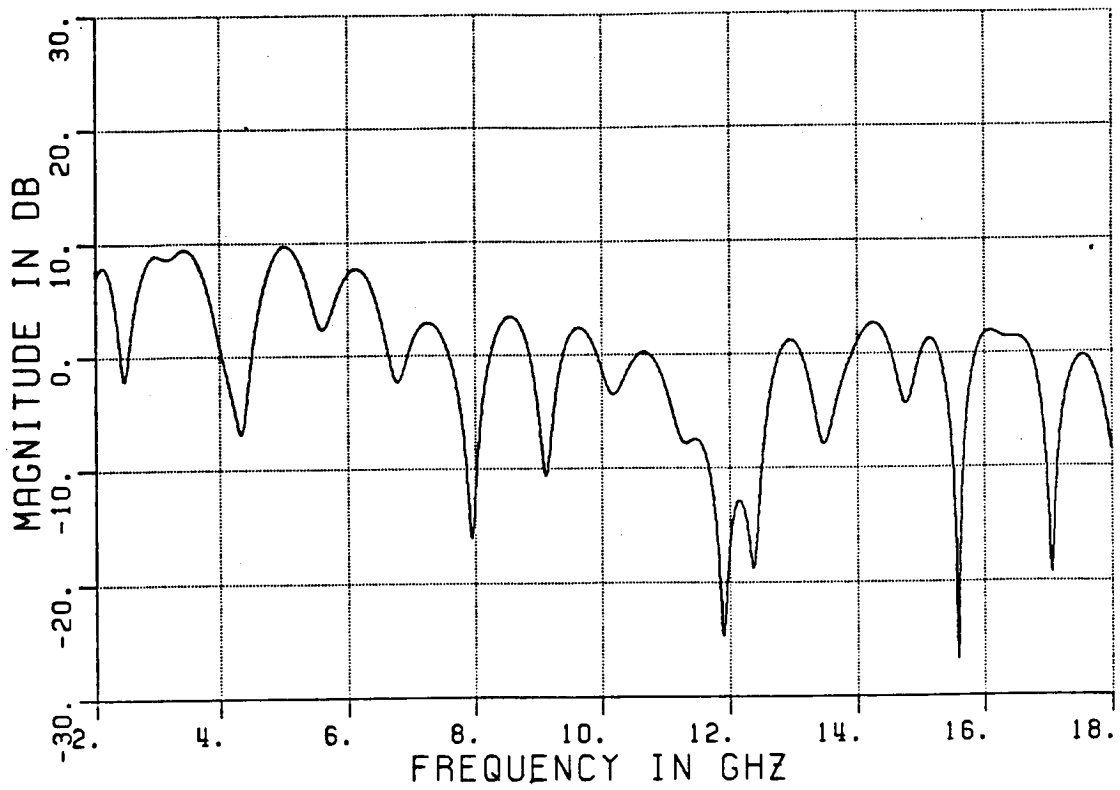shaped like Figure 6.6 made by Company B.

218

CHAPTER VII

SUMMARY AND CONCLUSIONS

By changing the reflection coefficient in the wedge diffraction equation a solution that approximates the scattering from a dielectric wedge is found. This solution agrees closely with the exact solution of Rawlins which is only valid for a few minor cases; nevertheless, it provides a nice set of check cases. Presently, the performance of the new wedge diffraction equation is unknown at angles and dielectric constants where Rawlins solution fails. It is suspected that the new solution will work well for cases where energy entering the dielectric is trapped thus eliminating transmission shadow boundries. The present solution only did poorly in scattered directions close to the dielectric boundary. More measured data or other solutions for the dielectric wedge are needed to compare against.

The high frequency scattering from an absorber pyramid can be predicted using a modified UTD corner diffraction, equivalent currents, and geometrical optics solutions. In the nose-on regions, both the reflected and diffracted terms are needed to model the absorber. With near grazing incidence, the backscattered field is dominated by a large return from tip diffraction.

The corner diffraction contribution can be reduced by lowering the dielectric constant of the absorber or by making slimmer pyramids. Both methods only reduce this term a few dB. Lowering the dielectric constant introduces additional problems with energy passing thru the absorber since the imaginary part of the dielectric constant tends to drop much faster than the real part with carbon impregnated polyerthane foam. The geometrical optics reflected terms are highly dependent on the dielectric constant.

Since tip diffraction is less dependent on the dielectric constant, for a given pyramid angle, tip diffraction will give the backscattered field's lower limit. The dielectric constant should then be chosen so that the reflected field, in the regions of interest, will be smaller than the tip diffraction. This will give the maximum performance for the absorber.

The scattering from one absorber pyramid can be used to model the scattering from a piece of absorber or an absorber wall. Since experimental results show that the absorber tends to act incoherently, the total result is found by simply adding the power scattered by each individual pyramid. Because of the adding in power effect, the reflectivity of absorbers decreases with the size measured.

Absorber reflectivity can be measured on a conventional far field range; however, the measurement is limited to the level of the edge effects which corrupt the results. To measure lower levels, a time gating system or an extended wall measurement with high gain collimated beam antennas is needed.

The wall scattering model has the limitations that the high frequency solution breaks down when the spacing between the rows of wedges or pyramid tips becomes less than a wavelength. Also, the shadowing effects of one pyramid partly shadowing the face of the next are not included making the solution singular when looking broadside to a pyramid face or edge.

Calculations show that by changing the shape of the pyramids, one can slightly reduce the scattered field. This change involves making the tips more pointed, curving the sides of the pyramid to break up the reflected fields, and making the base angle smaller. These changes have an overall effect of smoothing the transition between free space and the absorber material. Note that this modification can also be applied to wedge absorber. The curved pyramid prototypes built and tested did not show a significant improvement. This may be mostly due to the manufacturing process and the material inhomogenities.

With a better understanding of the scattering properties of absorber wedges and pyramids, one can expect better performance of absorber in anechoic chamber applications.

REFERENCES

[1] W.H. EMERSON, "Electromagnetic Wave Absorbers and Anechoic Chambers Through the Years," IEEE Trans. on Antennas and Propagation, Vol. AP-21, No. 4 , pp. 484-489, 1973.

[2] R.G. Kouyoumjian and P.H. Pathak, "A Uniform Geometrical Theory of Diffraction for an Edge in a Perfectly-Conducting Surface," Proc. IEEE, Vol. 62, November 1974, pp. 1448-1461.

[3] W.D. Burnside and K.W. Burgener, "High Frequency Scattering by a Thin Lossless Dielectric Slab," IEEE Trans. on Antennas and Propagation, Vol. AP-31, No.1, pp. 104-111, 1983.

[4] R.G. Rojas-Teran, "GTD Analysis of Airborne Antennas Radiating in the Presence of Lossy Dielectric Layers," Thesis, The Ohio State University Department of Electrical Engineering, 1981.

[5] C.E. Ryan, Jr. and L. Peters, Jr., "Evaluation of Edge-Diffracted Fields Including Equivalent Currents for the caustic Regions," IEEE Trans. on Antennas and Propagation, Vol. AP-17, No.3 , pp. 292-299, 1969. Also see correction, IEEE Trans. on Antennas and Propagation, Vol. AP-18, No. 2 , p. 275, 1970.

[6] F.A. Sikta, W.D. Burnside, T.T. Chu, and L. Peters, Jr., "First-Order Equivalent Current and Corner Diffraction Scattering from Flat Plate Structures," IEEE Trans. on Antennas and Propagation, Vol. AP-31, NO. 4, pp. 584-589, 1983.

[7] B.T. DeWitt, "Analysis of the Scattering by a Cone and Time Domain Scattering by a Flat Plate," Thesis, The Ohio State University ElectroScience Lab., Department of Electrical Engineering, 1983.

[8] R.J. Marhefka, RADAR CROSS SECTION STUDIES Final Report 714614-6, August 1984. The Ohio State U. ElectroScience Lab, prepared for the Department of the Navy Pacific Missile Test Center, Point Magu, California 93042.

[9] A. Michaeli, "Equivalent Edge Currents For Currents for Arbitrary Aspects of Observation," IEEE Trans. on Antennas and Propagation, Vol. AP-32, No. 3, pp. 252-258, 1984.

[10] E.H. Newman, "A Users Manual for: Electromagnetic Surface Patch Code (ESP)," Technical Report 713402-1, July 1981, The Ohio State University ElectroScience Lab., Department of Electrical Engineering, prepared under Grant No. DAA29-81-k-0020 for U.S. Army Research Office.

[11] J.A. Stratton, "Electromagnetic Theory," McGraw-Hill, pp. 500-505, 1941.

[12] T.B.A. Senior, "Diffraction by an Imperfectly Conducting wedge," The University of Michigan, Scientific Report No. 2, 1957. Sponsorship by Air Force Contract AF-19(604)-1949.

[13] A.D. Rawlins, "Diffraction by a Dielectric Wedge," J. Inst. Math. Appl., Vol. 19, pp. 261-279, 1977.

[14] S. Berntsen, "Diffraction of an Electric Polarized Wave by a Dielectric Wedge," SIAM J. Appl. Math., Vol 43, No. 1, pp. 186-211, 1983.

[15] C. Joo, J. Ra, and S. Shin, "Scattering by Right Angle Dielectric Wedge," IEEE Trans. on Antennas and Propagation, Vol. AP-32, No.1, pp. 61-69, 1984.

[16] O.M. Bucci and G. Franceschetti, "Scattering from Wedge-Tapered Absorbers'" IEEE Trans. on Antennas and Propagation, Vol. AP-19, No.1, pp. 96-104, 1971.

[17] H. Severin, "Nonreflecting Absorbers for Microwave Radiation," IRE Trans. on Antennas and Propagation, Vol. AP-4, pp. 385-392, 1956.

[18] H.E. King, F.I. Shimabukuro, and J.L. Wong, "94-Gc Measurements of Microwave Absorbing Material," Aerospace Corporation report #TR-669(6230-46)-5 prepared for Air Force Systems Command, report #SSD-TR-66-71, 1966.

[19] W.G. Swarner, E.K. Walton, W.D. Burnside, B. DeWitt, "FIFTH AND SIXTH STATUS REPORT ON CONTRACT OR-549651-B28 TO ELIZABETH STARK HUGHES AIRCRAFT COMPANY", 1985.

[20] E.K. Walton and J.D. Young, "The Ohio State University Compact Radar Cross-Section Measurement Range," IEEE Trans. on Antennas and Propagation, Vol. AP-32, No. 11, pp. 1218-1223, 1984.

[21] E.F. Knot, J.F. Shaeffer, M.T. Tuley, RADAR CROSS SECTION, Artech House, Dedham, MA 1985.